TOHOKU UNIVERSITY

Graduate School of Engineering

Theoretical and Experimental Studies of the Correlation Functions in Supercooled Liquids near the Glass Transition

(ガラス転移点近傍の過冷却液体状態での相関関数についての理論および実験による研究)

A dissertation submitted for the degree of Doctor of Philosophy (Engineering)

Department of Nanomechanics

by

Takayuki NARUMI

January 15, 2010

(Last minor update: February 15, 2010)

Theoretical and Experimental Studies of the Correlation Functions in Supercooled Liquids near the Glass Transition

Takayuki NARUMI

Abstract

In general, liquid crystallizes at the freezing temperature on cooling. However, if the crystallization is avoided by appropriate ways such as quench, mixture, externally applied field, and so on, it can become supercooled liquid followed by glass as the temperature decreases. The vitrification, so-called the glass transition, occurs at the glass transition point and has not been theoretically elucidated yet. This is one of the most challenging themes in condensed matter physics. It is believed that the glass transition is not a phase transition but a dynamical crossover from equilibrium to non-equilibrium state. This is one of main reasons why it is difficult to explain the mechanisms. Since one can treat supercooled liquids as equilibrium liquids, our strategy is paying attention to dynamics of the supercooled liquid in order to understand the glass transition.

It is considered that one of key ideas to understand the glass transition is the dynamical heterogeneity appearing in the supercooled liquids near the glass transition point. The dynamical heterogeneity means that mobile particles move cooperatively during corresponding time scale. Although the presence of it has been proved in three-dimensional particle behavior for experiments of poly-disperse colloidal suspensions, some points remain somewhat mysterious: How large is the dynamical heterogeneity? How does the size of the dynamical heterogeneity depend on systems? Which variables are important with respect to the dynamical heterogeneity? In order to understand the glass transition and the dynamical heterogeneity quantitatively, we have investigated some correlation functions near the glass transition point for several systems; binary colloidal mixtures (experiment), one-component Lennard-Jones systems (molecular dynamics simulation and numerical calculation), and Kob-Andersen type Lennard-Jones binary mixtures (molecular dynamics simulation and numerical calculation).

Colloidal suspensions have been studied well because they can be controlled even under not-special environments (i.e. atmospheric pressure and ambient temperature). For molecules, the dynamics of the particles is measured in the scattering experiments and obtained as data in the reciprocal lattice space, in general. We, thus, need to transform them in order to see it in the real space. However, for the colloidal particles, one can directly observe motion of the particles in the real space by using a microscopy

because the size of the colloidal particles is of the order of micrometer. We have studied concentrated binary colloidal suspensions in experiments. It is a model system which has a glass transition as the volume fraction ϕ of particles is increased. We used the confocal microscopy to directly observe three-dimensional particle motion within dense samples with ϕ ranging from 0.4 to 0.7. Our binary mixtures have a particle diameter ratio $d_S/d_L = 1/1.3$ and particle number ratio $N_S/N_L = 1.56$, which are chosen to inhibit crystallization and enable long-time observations. The glass transition occurs at $\phi_g \simeq 0.58$, with characteristic signs of aging observed for all samples with $\phi > \phi_g$. Near the glass transition point, we found that particle dynamics were heterogeneous in both space and time. The most mobile particles occur in spatially localized groups from snapshots. In order to characterize the dynamical heterogeneity quantitatively, we measured the two kinds of correlation functions; one of them is the vector correlation function corresponding to correlation of displacement and the other is the scalar correlation function corresponding to correlation of mobility fluctuation. Those correlation functions are originally temporal-spatial correlation functions, and then we fix the time scale as the time relating to the dynamical heterogeneity in order to investigate the dynamical spatial correlation. The spatial correlation decays in an exponential manner, so that we can predict the length scale ξ; the correlation length of the dynamical spatial correlation. The length scales characterizing these mobile regions (i.e. regions of the dynamical heterogeneity) grow slightly as the glass transition is approached, with the largest length scales seen being about three small particle diameters.

We have also carried out molecular dynamics simulations for the Lennard-Jones binary mixtures. One can trace motion of particles more correctly in the molecular dynamics simulations. It was needed to avoid crystallization in order to reach supercooled state near the glass transition, and hence that was why we have employed the binary systems as well as the binary colloidal mixtures. The Kob-Andersen model was employed as the parameters of the interaction; a diameter ratio $d_{\rm A}/d_{\rm B} = 1/0.88$ and particle number ratio $N_{\rm A}/N_{\rm B} = 4$. The control parameter is the temperature T. It should be noted that the simulation model does not directly correspond to the binary colloidal mixtures done by experiment, the Kob-Andersen model was originally developed to simulate $Ni_{80}P_{20}$ (A and B particles correspond to Ni and P, respectively). The model is much well-studied, and thus we can compare our results with enormous of previous studies. In addition, we can compare them with results of the binary colloidal mixtures from a viewpoint of binary mixtures. The specific heat at constant volume leaded us to determining the glass transition temperature in dimensionless value as $T_g \simeq 0.43$ which is close to the glass transition temperature determined by simulation results of the long-time self-diffusion coefficient. It is difficult to distinguish glassy state from liquid and supercooled liquid by existing static correlation

functions (e.g. the radial distribution function, the static structure factor, and so on.) Those existing functions do not much information enough to reflect structure of glass. The radial distribution function including size effect has been proposed and revealed the intermediate length order.

As well as the experiments for the binary colloidal mixtures, we have calculated the dynamical spatial correlation functions and those dynamical correlation lengths. The length from the vector correlation increases as temperature decreases in relatively high temperature region, but converges in the temperature far away from the glass transition point. On the other hand, the length from the scalar correlation increases toward the glass transition point, and has a maximum in the vicinity of the glass transition. It indicates that the scalar correlation plays a more important role than the vector one near the glass transition. The maximum length of the correlation of the mobility fluctuation is about two large particle diameters. We also calculated the dynamical spatial correlation functions for the one-component Lennard-Jones systems as before. Both the scalar and vector correlation functions in coexistence states between liquid and crystal are different from those of liquids. The scalar correlation in coexistence states is extremely larger than that in liquids, so that it might be significant for study of the crystal growth to investigate the relationship between the mobility fluctuation and the coexistence states. Moreover, we have predicted the correlation lengths from the both correlation functions. The both correlation lengths jump at the freezing point. The width of jump is much larger in the scalar correlation length than the vector correlation length. It is suggested by considering the influence of the periodical boundary conditions that the scalar correlation length diverges at the transition temperature. Furthermore, we have compared the results for one-component Lennard-Jones systems with those for Kob-Andersen type Lennard-Jones binary mixtures. The comparison suggests that the dynamics of supercooled liquids is different from that of coexistence states, although their configuration resembles each other.

In comparison between experimental and simulation results, the dynamical correlation length is several times of the particle diameter and does not diverge even near the glass transition point. The length is shorter than that of the one-component systems that is almost ten particle diameters near the glass transition point. Although the models that we employed in experiment and molecular dynamics simulation are different from each other, it can be suggested that the range of the dynamical heterogeneity do not need to get so large in the binary systems. It implies that the glass transition occurs even in little dynamical heterogeneity for the binary systems because binary systems have a priori spatial heterogeneity. We should consider the dynamical heterogeneity and spatial heterogeneity together for the future.

As mentioned above, we measured the dynamical correlation functions in experiments and molecular dynamics simulations. Then, one of natural next steps is to predict its behavior by theory. There are

some theories for glass and/or supercooled liquid. The mode-coupling theory is the most well-known to describe the dynamics of the supercooled liquid and predict the time correlation functions. Biroli and Bouchaud [Europhys. Lett. 67, 21 (2004)] suggested from the field-theoretical approach that the mode-coupling theory can develop the expression of a length scale of the dynamical heterogeneity. Note that the length scale estimated by the mode-coupling theory is different from the above dynamical correlation length obtained from the scalar and vector correlation functions. To estimate a length scale by the mode-coupling theory, they analyzed the four-body correlation function whose generating function is the same as that of the vector correlation function. Since it has been suggested from our simulation results that the scalar correlation functions is more distinguished near the glass transition, we should analyze the scalar one by the mode-coupling theory. However, the mode-coupling theory of itself has some problems. One of those is to underestimate the control parameters such as the inverse temperature, the volume fraction, and so on. We, therefore, carried out numerical calculations in the mode-coupling theory for the Kob-Andersen type binary mixtures in order to predict some dynamical variables such as the intermediate scattering function, the self-intermediate scattering function, the mean square displacement, the long-time self-diffusion coefficient, the non-Gaussian parameter. The equations predicted by the mode-coupling theory have complicated forms; non-linear differential-integral equations. The most difficult point in the numerical calculation is the convolution integral between the memory term and the physical variables, and we have employed a well thought out numerical algorithms. The numerical solutions revealed that the distinction was based on that of the intermediate time scale, so-called β time scale, from viewpoint of the mean-field theory.

We also have constructed an alternative mode-coupling theory to improve the conventional mode-coupling theory. The difference between them is the starting equation; that of the conventional theory is the convolution-type generalized Langevin equation but that of the alternative one is the product-type, so-called convolutionless, generalized Langevin equation. As well as the conventional mode-coupling theory, the alternative mode-coupling equations were calculated numerically. Although there remains distinction between the numerical solutions of the alternative mode-coupling theory and the simulation results, dynamics predicted by the alternative theory is improved than that by the original one in terms of the qualitative behavior. Some previous studies have shown that the product-type Langevin equation is compatible with nanoscale systems such as protein, those dominated by electron transfer, and so on. In nano-systems, dynamics interacting among several time and length scale is important, and our results show that the supercooled liquids is one of such systems.

The main results and findings are summarized as follows:

1. The dynamical heterogeneity of the mobility fluctuation is more significant than that of the displacement. Nowadays, study for the displacement is major (e.g. the mean square displacement). However, we should study the mobility fluctuation as well to understand the glass transition thorough the dynamical heterogeneity.

2. The size of the dynamical heterogeneity for binary systems is about 2 - 3 diameters of particles and is smaller than that of one-component systems. It implies that even less dynamical heterogeneity leads to the glass transition in the binary systems because they have a priori structural heterogeneity.

3. Although the static structure of the supercooled liquid resembles the coexistence state of liquid and crystal, the dynamics of them are much different from each other: the dynamical correlation lengths predicted by the scalar correlation diverges in the coexistence state but that does not diverge in the supercooled liquid. It corresponds to the difference between the critical phenomenon and the dynamical crossover.

4. The glass transition temperature of the Kob-Andersen type binary mixtures is determined by the specific heat at constant volume: $T_g \simeq 0.43$ which is much similar to the glass transition temperature defined by using results of the long-time self-diffusion coefficient.

5. The origin that the mode-coupling theory underestimates the control parameter is revealed; the theory does not correctly describe the cage dynamics.

6. The alternative mode-coupling theory, in which the starting equation is different from that of the conventional mode-coupling theory, is better in terms of qualitative behavior. However, the numerical solutions are not in quantitatively agreement with the simulation ones. We might improve the approximations that we employed.

Contents

Chapter 1

Introduction

1.1 Glass and Supercooled Liquid

One of the unsolved problems in the condensed matter physics is the glass transition [1]. As the temperature decreases, liquid becomes crystal at the freezing point. This is a phase transition and thermodynamical variables such as pressure, enthalpy, and something like that jumps at the melting point. However, if the crystallization is avoided by appropriate ways such as quench, mixture, external field and so on, liquid can become supercooled liquid followed by glass [2–5]. The crossover from the supercooled liquid to the glass is so-called the glass transition. As systems approach to the glass transition, the dynamic property such as the diffusion constant and the viscosity dramatically changes (i.e. slow dynamics) while the statics hardly changes.

Glasses have been used since ancient time and are very useful material, for example, window glass, liquid crystal display, optical fiber, and so on. In these days, metallic glasses attract technological attention [6]. They have outstanding mechanical properties; elastic characteristic, breaking strength, and so on. Moreover, because metallic glasses do not have slip surface which crystal has, a material made of them has smooth surface. Metallic glasses are applied for a face material of golf club and shaft of microscopical motor. Nevertheless, mechanisms of the glass transition have not been elucidated theoretically yet.

It is difficult to define a glassy state clearly. One definition of glass is liquid whose vis-

cosity is more than 10^{13} P [4, 7]. This corresponds to the relaxation time of human order (second $\sim$ hour). In other words, the glassy state is characterized by limit of our experiments. Alternatively, there is another method which uses the thermal expansion coefficient $[\partial \ln V/\partial T]_p$ [2]. The glass transition temperature depends on the way how to make (hysteresis)[1], and thus one can define not the transition point but the transition region. Because first derivations of thermodynamical energy (e.g. volume, pressure) do not diverge in the glass transition temperature, the glass transition was considered as the one of the second-order phase transitions. Nevertheless, second derivations of thermodynamical energy (e.g. specific heat) also do not diverge in the glass transition temperature. Nowadays, it is widely accepted that the glass transition is a dynamical crossover from supercooled liquid to glass. Therefore, glassy state should be characterized by the dynamics such as the viscosity, the diffusion coefficient, or something like that.

1.2 Dynamical Heterogeneity

In general, supercooled liquids are defined by the liquids undercooled below the melting point from a melt, and are ordinary metastable state. There are some cases in which the melting point cannot be determined. This can be a trivial problem because our interest is drawn to the glass transition. Tokuyama has proposed that supercooled liquid is clearly distinguished from ordinary liquid from a view of the dynamics [8]. In fact, the dynamics of the supercooled liquids show different behavior from that of liquids.

In these days, it is the central idea to measure time correlation functions for understanding properties of a system. Let consider an equilibrium state added perturbation. The response function Φ plays an important role in such systems because the function determines the mo-

[1] In practice, we can ignore the influence of quench rate because the temperature range is 3-5 K.

tion of physical variables. Here, in standpoint of the linear-response theory [9], the response function corresponds to the relaxation function Ψ by a relation

$$\Psi(\boldsymbol{r}, t) := \int_t^\infty \mathrm{d}s \Phi(\boldsymbol{r}, s). \tag{1.1}$$

In addition, it is known that the relaxation function is given by the time correlation function [9]. The time correlation function therefore determines "future" of systems.

What we should first do is to select appropriate physical variables, in particular, to pick up slow variables. If the variables can be regarded as macroscopic ones, the statistical physics can be applied. The number density is one of such slow variables. In particular, the time correlation of the Fourier transformed number density fluctuation is measurable by the scattering experiments and is called the intermediate scattering function $F(q, t)$, which is a central variable to study supercooled liquids.

As mentioned above, the glass transition is different from the critical phenomena. In the case of the critical phenomena, the dynamics is getting slow down at the vicinity of the critical point. It is called the critical slow down [10] and is understood that the relaxation time is getting longer as the temperature approaches to the critical point. On the other hand, the relaxation time also gets longer in the slow dynamics near the glass transition. The cage dynamics, however, appears as plateau of the intermediate scattering function in the intermediate time regime [11–16].

There are some empirical theories for the intermediate scattering function. Kohlrausch-Williams-Watts (KWW) function, which is also called the stretched exponential function, is one of such empirical fitting equations for the intermediate scattering function in the long-time regime. It is given by

$$F(q, t) \sim \exp\left[-(t/\tau)^\beta\right] \tag{1.2}$$

where τ denotes the relaxation time which depends on the wave number q and β an exponent given by fitting.

Supercooled liquid near the glass transition has some characteristic features. In particular, the dynamical heterogeneity is widely known as the most interesting property [17–22]. It is considered that this slow dynamics relates to dynamical heterogeneity. Weeks et.al reported that the dynamical heterogeneity is observed directly using confocal microscope in colloidal suspension [22].

The first theoretical approach to glass and supercooled liquid was proposed by Adam and Gibbs [23]. Their equation is explicitly considered the effect of the heterogeneity and is obtained as

$$\tau = \tau_0 \exp\left(\frac{C}{TS_c}\right) \tag{1.3}$$

where τ denotes the relaxation time, S_c the configurational entropy, T the temperature, and τ_0 and C are constants. According to this equation, slow dynamics is due to the decreasing the number of configurations.

1.3 Mode-Coupling Theory

The mode-coupling theory proposed by Kawasaki [24] is originally derived as a theory for critical phenomena [25]. In 1980s, the mode-coupling theory was applied for supercooled liquids [26, 27] and has succeeded in describing some aspects of dynamics of supercooled liquids qualitatively [28]. In particular, the prediction of the non-ergodic transition is outstanding achievement. In the non-ergodic state, the relaxation functions do not converge to zero, so that we can regard it as solid state.

In the mode-coupling theory, corrective motion plays an important role within the correlation length ξ because of a theory for critical phenomena. In vicinity of the critical point, ξ is

so large that the wave number that we have to consider is very small. On the other hand, no long correlations appear in supercooled liquids and glasses, and small range corresponding to the cage effect is significant. Therefore, the first-peak wave number q_m of the static structure factor, which relates with the diameter of a particle approximately, is important in supercooled liquids and glasses.

The mode-coupling theory for the supercooled liquids is successful in some aspects. However, needless to say, it is not perfect theory. Some numerical solutions of the mode-coupling theory have been already submitted for several models [29–36], leading to solving problems. One of the problems is the deviation of the control parameters. For example, the mode-coupling theory overestimates the temperature in models where the control parameter is the temperature. Although it is unclear whether or not the non-ergodic transition corresponds to the glass transition, the non-ergodic transition occurs in much higher temperature than the glass transition temperature [30].

Tokuyama has proposed that the origin of the problems is the starting equation of the mode-coupling theory [37]. In general, the equation of motion which has the fluctuation term is called the generalized Langevin equation. The starting equation is one of the generalized Langevin equations [38]

$$\dot{A}(t) = i\omega A(t) - \int_0^t \varphi(t-s)A(s)\mathrm{d}s + R(t), \tag{1.4}$$

where $A(t)$ denotes a physical variable, $i\omega$ denotes the mechanical coefficient, $\varphi(t)$ the memory function, and $R(t)$ the fluctuation term. The memory term connects with the physical variable by the convolution, so that the above equation is called the convolution type generalized Langevin equation. This type equation is successful. However, it is known that there are some cases in which phenomena can not described by the convolution type Langevin equation [39–42]. Although origin of the failure is still open problem, the convolution type tends

not to hold in mesoscale systems as Tokuyama has already discussed [37].

1.4 Purpose and Contents

Our final goal is to understand the mechanisms of the glass transition. In Ph. D. study, we carried out

1. experiments for binary colloidal suspensions,

2. molecular dynamics simulations for binary Lennard-Jones mixture,

3. numerical calculations for conventional and alternative mode-coupling theory.

In experiments (chapter 2), we measured three-dimension dynamics of binary colloidal mixtures by using the confocal microscopy. From the image analyses, we determined the position of the colloidal particles and measured some physical variables. A similar experiment has been done by Weeks [43] in single-component colloidal suspensions. We aim to characterize the dynamical heterogeneity in binary-mixtures. Snapshots in which the mobile particles are emphasized can qualitatively visualize the dynamical heterogeneity. In addition, the temporal–spatial correlation functions can show it quantitatively. We also predicted the correlation lengths from the temporal–spatial correlation functions. In the single-component colloidal suspensions, the correlation lengths is about ten particle diameters near the glass transition.

In molecular dynamics simulations (chapter 3), the temporal–spatial correlation functions were measured for the Kob–Andersen type Lennard-Jones binary mixtures [44]. This system does not correspond to the above binary colloidal mixtures directly, although their systems are similar. First of all, we clarify the glass transition temperature by using the specific heat. The temperature is in agreement with the glass transition temperature determined by the long-time self-diffusion coefficient. Next, the spatial correlation function including the exclusive volume

effect was proposed. While it is an interesting quantity to measure, the static information is not enough to characterize the supercooled liquids and the glass. Thus, the temporal–spatial correlation functions and their correlation lengths were measured. Our simulation data are plausible statistically, we could discuss which physical variables strongly corresponds to the dynamical heterogeneity.

In numerical calculations (chapter 4), we solved the mode-coupling equations numerically. From the standpoint of the mean-field theory, it was clarified that the conventional mode-coupling theory could not predict the dynamics in the intermediate time scale, so that it should be improved. One of the solutions, Tokuyama has proposed the alternative mode-coupling theory [45] and we solve the alternative theory numerically. Our solutions revealed that the alternative theory is closer to the simulation results in some aspects.

The last chapter will be devoted to conclusion followed by appendix, references, list of figures, achievement, and acknowledgement.

Chapter 2

Dynamical Spatial Correlation Functions in Experiments

In this chapter, our experimental study is summarized. We measured three-dimension particle dynamics by the confocal microscopy to characterize the heterogeneity, especially dynamical spatial correlation function and its characteristic length scale. This work was done with Prof. Eric R. Weeks (Emory University) and Prof. Scott V. Franklin (Rochester Institute of Technology) at Emory University.

2.1 Experimental Model

2.1.1 Colloidal suspension

Pusey and van Magen reported that the glass transition occurs in colloidal suspensions [46]. The colloidal glass transition is induced not by cooling but by increasing particle concentration (i.e. volume fraction). Colloidal glasses have many similar properties to molecular glasses. Although the dynamics is measured by scattering experiments, one can directly measure the dynamics of colloids by a microscopy because typical size of colloids are of order μm. In fact, the dynamical heterogeneity has been directly observed in colloidal materials [22].

The colloidal glass transition is regarded as the hard sphere glass transition. The control parameter is the volume fraction ϕ. It is known that the glass transition occurs at $\phi_g \simeq 0.58$

[46]. Because the melting volume fraction is $\phi \simeq 0.54$ in monodisperse colloidal suspensions, the polydisperse colloidal suspensions are employed in general to avoid crystallization.

2.1.2 Binary colloidal mixture

Another way to avoid crystallization is to employ binary colloidal mixtures. In fact, many simulations also study binary mixtures. A secondary reason is thus to facilitate comparisons with those simulations. In addition, parameters we can control increase due to binary mixtures. We can consider the ratio of the radii, for example. This is a significant merit for application.

2.1.3 Confocal microscopy

The confocal microscope enables direct visualization of the interior of the sample, and we follow the motion of several thousand colloidal particles within each sample [47]. It scans two-dimension layers and composes three-dimension images. It takes a little time to scan two-dimension images, but it is fast enough to neglect the time lag because our colloidal suspensions are dense. The data are analyzed by IDL [48], which is a software to capture the particle dynamics from images .

2.2 Detail of Experiment

Suspensions are prepared from poly-(methyl-methacrylate) (PMMA) colloids stabilized sterically by a thin layer of poly-12-hydroxystearic acid [49]. Mixtures are binary, with a large particle mean radius $a_L = 1.55 \pm 0.05$ μm and small particle mean radius $a_S = 1.18 \pm 0.05$ μm [50]. The number ratio of small particles to large particles is $N_S/N_L = 1.56$, resulting in a volume fraction ratio $\phi_S/\phi_L = 0.69$. The control parameter is the total volume fraction $\phi = \phi_S + \phi_L$. All particles are fluorescently dyed and suspended in a density- and index-matched mixture of decalin and cyclohexyl bromide to prevent sedimentation and allow us to see into the sample.

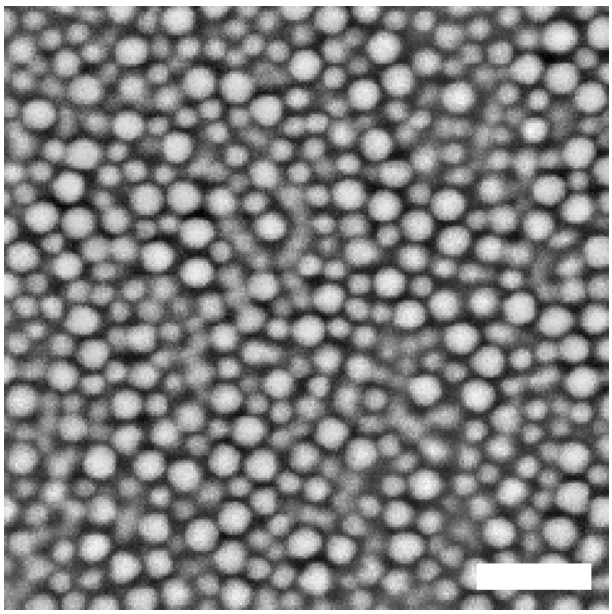

Figure 2.1: A two-dimensional image of our sample taken by a confocal microscope. The size of this image is 55×55 μm^2, and the scale bar represents 10 μm.

Particles are slightly charged as a result of the dying process. We note that crystallization and segregation were not observed to occur during the course of our measurements.

Suspensions are sealed in microscope chambers and confocal microscopy [47] is used to observe the particle dynamics at ambient temperature. A volume of $55 \times 55 \times 20$ μm^3 (Fig. 2.1) can be taken at speeds of up to 1 Hz. (As will be shown later, in these concentrated samples, particles do not move significantly on this time scale.) To avoid influences from the walls, we focus at least 25 μm away from the coverslip.

Within each three-dimensional image, we identify both large and small particles. In practice this is accomplished with a single convolution that identifies spherical, bright regions [48]; the convolution kernel is a three-dimensional Gaussian with a width chosen to match the size of the image of a large particle. The distribution of object sizes is typically bimodal, and the two peaks can be identified with small and large particles. This particular method is the same as is normally used to follow particle motion in two dimensions, which normally can achieve

sub-pixel resolution in particle positions [48]. However, given that a single convolution kernel is used to identify both particle types, in practice when applied to our binary samples in three dimensions, we do not achieve this accuracy. In practice, our uncertainty in locating particle positions is set by the pixel scale and is 0.2 μm in all three dimensions. However, we do achieve accurate discrimination between large and small particles with this method, with less than 1% of the particles misidentified.

2.3 Measurand

2.3.1 Dynamical Spatial Correlation Functions

Correlation that does not depend on $R = |\boldsymbol{X}_i(t_0) - \boldsymbol{X}_j(t_0)|$

We consider the following correlation function;

$$S_\Delta(\boldsymbol{q}, t) := \frac{1}{N^2} \sum_{i=1}^{N} \sum_{j=1}^{N} \left\langle e^{i\boldsymbol{q}\cdot(\Delta \boldsymbol{X}_i(t) - \Delta \boldsymbol{X}_j(t))} \right\rangle , \tag{2.1}$$

where $\Delta \boldsymbol{X}_i(t)$ denotes the displacement of i-th particle;

$$\Delta \boldsymbol{X}_i(t) := \boldsymbol{X}_i(t + t_0) - \boldsymbol{X}_i(t_0). \tag{2.2}$$

Moreover, we consider another correlation function

$$S_\delta(q, t) := \frac{1}{N^2} \sum_{i=1}^{N} \sum_{j=1}^{N} \left\langle e^{iq(\delta X_i(t) - \delta X_j(t))} \right\rangle = \frac{1}{N^2} \sum_{i=1}^{N} \sum_{j=1}^{N} \left\langle e^{iq(|\Delta \boldsymbol{X}_i(t)| - |\Delta \boldsymbol{X}_j(t)|)} \right\rangle , \tag{2.3}$$

where $\delta X_i(t)$ denotes the mobility of i-th particle;

$$\delta X_i(t) := |\Delta \boldsymbol{X}_i(t)| - \langle |\Delta \boldsymbol{X}_i(t)| \rangle . \tag{2.4}$$

When a system we consider is isotropic, the correlation functions reduce to

$$\begin{aligned} S_\Delta(q, t) &= \frac{1}{N^2} \sum_{i=1}^{N} \sum_{j=1}^{N} \left\langle \frac{\sin(q|\Delta \boldsymbol{X}_i(t) - \Delta \boldsymbol{X}_j(t)|))}{q|\Delta \boldsymbol{X}_i(t) - \Delta \boldsymbol{X}_j(t)|)} \right\rangle \\ &= 1 - \frac{q^2}{6N^2} \sum_{i=1}^{N} \sum_{j=1}^{N} \left\langle |\Delta \boldsymbol{X}_i(t) - \Delta \boldsymbol{X}_j(t)|^2 \right\rangle \end{aligned}$$

$$
\begin{aligned}
&+\frac{q^4}{120N^2}\sum_{i=1}^{N}\sum_{j=1}^{N}\left\langle|\Delta\boldsymbol{X}_i(t)-\Delta\boldsymbol{X}_j(t)|^4\right\rangle+O(q^6)\\
=:\;& 1-\frac{q^2}{3}\Xi_2^{\Delta}(t)+\frac{q^4}{60}\Xi_4^{\Delta}(t)+O(q^6)\\
\therefore\;& S_{\Delta}(q,t)=\exp\left[-\frac{q^2}{3}\Xi_2^{\Delta}(t)+\frac{1}{2}\left(-\frac{q^2}{3}\Xi_2^{\Delta}(t)\right)^2\alpha_2^{\Delta}(t)\right] \qquad (2.5)
\end{aligned}
$$

and

$$
S_{\delta}(q,t)=\exp\left[-q^2\Xi_2^{\delta}(t)+\frac{1}{2}\left\{-q^2\Xi_2^{\delta}(t)\right\}^2\alpha_2^{\delta}(t)\right], \qquad (2.6)
$$

where $\Xi_2^{\Delta}(t)$ is defined by

$$
\begin{aligned}
\Xi_2^{\Delta}(t) &:= \frac{1}{2N^2}\sum_{i=1}^{N}\sum_{j=1}^{N}\left\langle|\Delta\boldsymbol{X}_i(t)-\Delta\boldsymbol{X}_j(t)|^2\right\rangle\\
&= \frac{N-1}{N}M_2(t)-\frac{1}{N^2}\sum_{i=1}^{N}\sum_{j(\neq i)}^{N}\left\langle\Delta\boldsymbol{X}_i(t)\cdot\Delta\boldsymbol{X}_j(t)\right\rangle. \qquad (2.7)
\end{aligned}
$$

On the other hand, $\Xi_2^{\delta}(t)$ is defined by

$$
\begin{aligned}
\Xi_2^{\delta}(t) &:= \frac{1}{2N^2}\sum_{i=1}^{N}\sum_{j=1}^{N}\left\langle(\delta X_i(t)-\delta X_j(t))^2\right\rangle\\
&= \frac{N-1}{N^2}\sum_{i=1}^{N}\left\langle\delta X_i(t)^2\right\rangle-\frac{1}{N^2}\sum_{i=1}^{N}\sum_{j(\neq i)}^{N}\left\langle\delta X_i(t)\delta X_j(t)\right\rangle\\
&= \frac{N-1}{N}M_2(t)-\frac{N-1}{N^2}\sum_{i=1}^{N}\left\langle|\Delta\boldsymbol{X}_i(t)|\right\rangle^2-\frac{1}{N^2}\sum_{i=1}^{N}\sum_{j(\neq i)}^{N}\left\langle\delta X_i(t)\delta X_j(t)\right\rangle \qquad (2.8)\\
&= \frac{N-1}{N}M_2(t)-\frac{1}{N^2}\sum_{i=1}^{N}\sum_{j(\neq i)}^{N}\left\langle|\Delta\boldsymbol{X}_i(t)||\Delta\boldsymbol{X}_j(t)|\right\rangle. \qquad (2.9)
\end{aligned}
$$

where we use $\langle|\Delta\boldsymbol{X}_i(t)|\rangle = \langle|\Delta\boldsymbol{X}_j(t)|\rangle$. We regard $\Xi_2^{\Delta}(t)$ and $\Xi_2^{\delta}(t)$ as an extended mean-square displacement.

Correlation that depends on $R=|\boldsymbol{X}_i(t_0)-\boldsymbol{X}_j(t_0)|$

We consider two correlation functions which depends on $\boldsymbol{R}=\boldsymbol{X}_i(t_0)-\boldsymbol{X}_j(t_0)$. One of them is defined as

$$
G_{\Delta}(\Delta\boldsymbol{r},\boldsymbol{R},t):=\frac{1}{N\langle n\rangle}\sum_{i=1}^{N}\sum_{j(\neq i)}^{N}\left\langle\delta(\boldsymbol{R}-\boldsymbol{X}_i(t_0)+\boldsymbol{X}_j(t_0))\delta(\Delta\boldsymbol{r}-\Delta\boldsymbol{X}_i(t)+\Delta\boldsymbol{X}_j(t))\right\rangle \qquad (2.10)
$$

and another is

$$G_\delta(\delta r, \boldsymbol{R}, t) := \frac{1}{N\langle n\rangle}\sum_{i=1}^{N}\sum_{j(\neq i)}^{N}\langle\delta(\boldsymbol{R}-\boldsymbol{X}_i(t_0)+\boldsymbol{X}_j(t_0))\delta(\delta r-\delta X_i(t)+\delta X_j(t))\rangle \quad (2.11)$$

where V denotes the volume, N the number of particle, $\Delta\boldsymbol{X}_i$ the displacement vector of i-th particle defined as $\Delta\boldsymbol{X}_i(t) := \boldsymbol{X}_i(t+t_0) - \boldsymbol{X}_i(t_0)$ with the position vector $\boldsymbol{X}_i = \boldsymbol{X}_i(t_0)$, and δX_i the mobility of i-th particle defined as $\delta X_i(t) = |\Delta\boldsymbol{X}_i(t)| - \langle|\Delta\boldsymbol{X}_i(t)|\rangle$. We do not consider the case of $j = i$ because $R = 0$ has no physical meanings. The Fourier transforms with respect to $\Delta\boldsymbol{r}$ or δr of the correlation functions are

$$F_\Delta(\boldsymbol{q}, \boldsymbol{R}, t) := \int \mathrm{d}(\Delta\boldsymbol{r}) G_\Delta(\Delta\boldsymbol{r}, R, t) = \frac{V}{N^2}\sum_{i=1}^{N}\sum_{j(\neq i)}^{N}\left\langle e^{i\boldsymbol{q}\cdot(\Delta\boldsymbol{X}_i(t)-\Delta\boldsymbol{X}_j(t))}\delta(\boldsymbol{R}-\boldsymbol{X}_i+\boldsymbol{X}_j)\right\rangle, \quad (2.12)$$

$$F_\delta(q, \boldsymbol{R}, t) := \int \mathrm{d}(\delta r) G_\delta(\delta r, R, t) = \frac{V}{N^2}\sum_{i=1}^{N}\sum_{j(\neq i)}^{N}\left\langle e^{iq(\delta X_i(t)-\delta X_j(t))}\delta(\boldsymbol{R}-\boldsymbol{X}_i+\boldsymbol{X}_j)\right\rangle. \quad (2.13)$$

We consider isotropic systems to obtain[1]

$$\begin{aligned}
F_\Delta(q,R,t) &= \frac{V}{4\pi R^2N^2}\sum_{i=1}^{N}\sum_{j(\neq i)}^{N}\left\langle\frac{\sin q|\Delta\boldsymbol{X}_i(t)-\Delta\boldsymbol{X}_j(t)|}{q|\Delta\boldsymbol{X}_i(t)-\Delta\boldsymbol{X}_j(t)|}\delta(R-X_{ij})\right\rangle \\
&= g(R) + \frac{q^2V}{24\pi R^2N^2}\sum_{i=1}^{N}\sum_{j(\neq i)}^{N}\left\langle|\Delta\boldsymbol{X}_i(t)-\Delta\boldsymbol{X}_j(t)|^2\delta(R-X_{ij})\right\rangle + O(q^4) \\
&= g(R) + \frac{q^2V}{12\pi R^2N^2}\sum_{i=1}^{N}\sum_{j(\neq i)}^{N}\left[\langle\Delta\boldsymbol{X}_i(t)\cdot\Delta\boldsymbol{X}_j(t)\delta(R-X_{ij})\rangle\right. \\
&\qquad\left. -\left\langle|\Delta\boldsymbol{X}_i(t)|^2\delta(R-X_{ij})\right\rangle\right] + O(q^4) \\
&= g(R) + \frac{q^2V}{12\pi R^2N^2}\sum_{i=1}^{N}\sum_{j(\neq i)}^{N}\langle\Delta\boldsymbol{X}_i(t)\cdot\Delta\boldsymbol{X}_j(t)\delta(R-X_{ij})\rangle \\
&\qquad -\frac{q^2}{3}M_2(t)g(R) + O(q^4) \qquad (2.15) \\
\frac{F_\Delta(q,R,t)}{g(R)} &= 1 + \frac{q^2M_2(t)}{3}\left[\frac{V}{4\pi R^2N^2M_2(t)g(R)}\right.
\end{aligned}$$

[1] In the derivation, the following equation might be used;

$$\sum_{i=1}^{N}\sum_{j(\neq i)}^{N}\left[\langle|\Delta\boldsymbol{X}_i(t)|^2\delta(R-X_{ij})\rangle + \left\langle|\Delta\boldsymbol{X}_j(t)|^2\delta(R-X_{ij})\right\rangle\right] = 2\sum_{i=1}^{N}\sum_{j(\neq i)}^{N}\left\langle|\Delta\boldsymbol{X}_i(t)|^2\delta(R-X_{ij})\right\rangle. \quad (2.14)$$

$$\times \sum_{i=1}^{N}\sum_{j(\neq i)}^{N} \langle \Delta \boldsymbol{X}_i(t)\cdot\Delta\boldsymbol{X}_j(t)\delta(R-X_{ij})\rangle - 1\Bigg] + O(q^4)$$
$$= 1 + \frac{q^2 M_2(t)}{3}\left[\frac{g_\Delta(R,t)}{g(R)} - 1\right] + O(q^4) =: 1 + \frac{q^2 M_2(t)}{3}\Gamma_\Delta(R,t) + O(q^4) \tag{2.16}$$

where $X_{ij} = X_{ij}(t_0) := |\boldsymbol{X}_i(t_0) - \boldsymbol{X}_j(t_0)|$, $g(R)$ denotes the radial distribution function and

$$g_\Delta(R,t) := \frac{V}{4\pi R^2 N^2 M_2(t)} \sum_{i=1}^{N}\sum_{j(\neq i)}^{N} \langle \Delta \boldsymbol{X}_i(t)\cdot\Delta\boldsymbol{X}_j(t)\delta(R-X_{ij})\rangle\,. \tag{2.17}$$

Note that it is assumed that

$$\left\langle |\Delta\boldsymbol{X}_i(t)|^2\delta(R-X_{ij})\right\rangle = \left\langle |\Delta\boldsymbol{X}_i(t)|^2\right\rangle \langle\delta(R-X_{ij})\rangle = M_2(t)\,\langle\delta(R-X_{ij})\rangle \tag{2.18}$$

to obtain eq. (2.15).

We also obtain

$$\begin{aligned} F_\delta(q,R,t) &= g(R) + \frac{q^2 V}{4\pi R^2 N^2}\sum_{i=1}^{N}\sum_{j(\neq i)}^{N}\big[\langle\delta X_i(t)\delta X_j(t)\delta(R-X_{ij})\rangle \\ &\qquad - \left\langle\delta X_i(t)^2\delta(R-X_{ij})\right\rangle\big] + O(q^4) \\ &= g(R) + \frac{q^2 V}{4\pi R^2 N^2}\sum_{i=1}^{N}\sum_{j(\neq i)}^{N}\langle\delta X_i(t)\delta X_j(t)\delta(R-X_{ij})\rangle \\ &\qquad -q^2\left\langle\delta X_i(t)^2\right\rangle g(R) + O(q^4) \end{aligned}$$

$$\begin{aligned} \frac{F_\delta(q,R,t)}{g(R)} &= 1 + q^2\left\langle\delta X_i(t)^2\right\rangle\left[\frac{g_\delta(R,t)}{g(R)} - 1\right] + O(q^4) \\ &=: 1 + q^2\left\langle\delta X_i(t)^2\right\rangle\Gamma_\delta(R,t) + O(q^4), \end{aligned} \tag{2.19}$$

where

$$g_\delta(R,t) = \frac{V}{4\pi R^2 N^2\left\langle\delta X_i(t)^2\right\rangle}\sum_{i=1}^{N}\sum_{j(\neq i)}^{N}\langle\delta X_i(t)\delta X_j(t)\delta(R-X_{ij})\rangle\,. \tag{2.20}$$

Using the following relation

$$\sum_{i=1}^{N}\sum_{j(\neq i)}^{N}\langle\delta X_i(t)\delta X_j(t)\delta(R-X_{ij})\rangle = \sum_{i=1}^{N}\sum_{j(\neq i)}^{N}\langle|\Delta\boldsymbol{X}_i(t)||\Delta\boldsymbol{X}_j(t)|\delta(R-X_{ij})\rangle$$

$$- \langle |\Delta \boldsymbol{X}_i(t)| \rangle^2 \sum_{i=1}^{N} \sum_{j(\neq i)}^{N} \langle \delta(R - X_{ij}) \rangle \,, \quad (2.21)$$

eq. (2.19) reduces to

$$\begin{aligned} \frac{F_\delta(q,R,t)}{g(R)} &= 1 + \frac{q^2 V}{4\pi R^2 N^2 g(R)} \sum_{i=1}^{N} \sum_{j(\neq i)}^{N} \langle |\Delta \boldsymbol{X}_i(t)||\Delta \boldsymbol{X}_j(t)| \delta(R - X_{ij}) \rangle \\ &\quad -q^2 M_2(t) + O(q^4) \\ &= 1 + q^2 M_2(t) \left[\frac{g'_\delta(R,t)}{g(R)} - 1 \right] + O(q^4) \\ &=: 1 + q^2 M_2(t) \Gamma'_\delta(R,t) + O(q^4), \end{aligned} \quad (2.22)$$

where

$$g'_\delta(R,t) := \frac{V}{4\pi R^2 N^2 M_2(t)} \sum_{i=1}^{N} \sum_{j(\neq i)}^{N} \langle |\Delta \boldsymbol{X}_i(t)||\Delta \boldsymbol{X}_j(t)| \delta(R - X_{ij}) \rangle \,. \quad (2.23)$$

It should be noted that $g'_\delta(R,t)$ is slightly different from the "displacement-displacement" correlation function $g^{uu}(R,t)$ defined as [51]

$$\begin{aligned} g^{uu}(R,t) &:= \frac{V}{4\pi R^2 N^2 \langle |\Delta \boldsymbol{X}_i(t)| \rangle^2} \sum_{i=1}^{N} \sum_{j(\neq i)}^{N} \langle |\Delta \boldsymbol{X}_i(t)||\Delta \boldsymbol{X}_j(t)| \delta(R - X_{ij}) \rangle \\ &= \frac{M_2(t)}{\langle |\Delta \boldsymbol{X}_i(t)| \rangle^2} g'_\delta(R,t). \end{aligned} \quad (2.24)$$

We have already calculated the spatial-temporal correlation functions [43, 52]. The directional one is

$$S_\Delta(R,t) = \frac{1}{\langle \Delta \boldsymbol{X}_i(t)^2 \rangle} \sum_{i=1}^{N} \sum_{j(\neq i)}^{N} \langle \Delta \boldsymbol{X}_i(t) \cdot \Delta \boldsymbol{X}_j(t) \delta(R - X_{ij}) \rangle \,, \quad (2.25)$$

and the mobility one is

$$S_\delta(R,t) = \frac{1}{\langle \delta X_i(t)^2 \rangle} \sum_{i=1}^{N} \sum_{j(\neq i)}^{N} \langle \delta X_i(t) \delta X_j(t) \delta(R - X_{ij}) \rangle \,. \quad (2.26)$$

The direction and mobility correlation functions are related to g_Δ and g_δ, respectively, as

$$g_\Delta(R,t) = \frac{V}{4\pi R^2 N^2} S_\Delta(R,t) \;\;, \quad g_\delta(R,t) = \frac{V}{4\pi R^2 N^2} S_\delta(R,t). \quad (2.27)$$

F_Δ relates with χ_4 defined by [53, 54]

$$\chi_4(q,t) := \frac{1}{N}\sum_{i=1}^{N}\sum_{j=1}^{N}\left[\left\langle e^{i\boldsymbol{q}\cdot(\Delta\boldsymbol{X}_i(t)-\Delta\boldsymbol{X}_j(t))}\right\rangle - \left\langle e^{i\boldsymbol{q}\cdot\Delta\boldsymbol{X}_i}\right\rangle\left\langle e^{i\boldsymbol{q}\cdot\Delta\boldsymbol{X}_j}\right\rangle\right]. \tag{2.28}$$

The relationship is written by

$$\frac{N}{V}\int \mathrm{d}\boldsymbol{R}F_\Delta(q,\boldsymbol{R},t) = \chi_4(q,t) - 1 + NF_s(q,t)^2, \tag{2.29}$$

where $F_s(q,t)$ denotes the self intermediate scattering function.

2.4 Result and Discussion

2.4.1 Radial distribution function

It is difficult to measure the partial radial distribution function $g(r)$ separately in scattering measurements because it is difficult to distinguish each particle. However, the confocal microscopy makes it possible. Figure 2.2 shows the radial distribution function $g(r)$ of a sample with volume fraction $\phi = 0.57$. $g(r)$ relates to probability of finding a particle at a distance r away from a reference particle. The dotted line is for correlations between two small particles, with a peak at $\approx 2a_S = 2.36$ μm, confirming our small particle radius. Likewise the dashed line shows correlations between two large particles, peaking at $\approx 2a_L = 3.10$ μm. When $g(r)$ is calculated for all particles, regardless of size, the result is the solid line in fig. 2.2. A lower, slightly broader, peak is found near the average diameter of $a_L + a_S = 2.73$ μm.

There are some strange peaks appear around $r = 1.5$. We regard them as error in detecting particles. In fact, the similar strange peaks appear in single-component colloidal suspensions. It looks that we cannot neglect the error because of the peak height. However, we made sure that the number of particle with regard to the error is not so much.

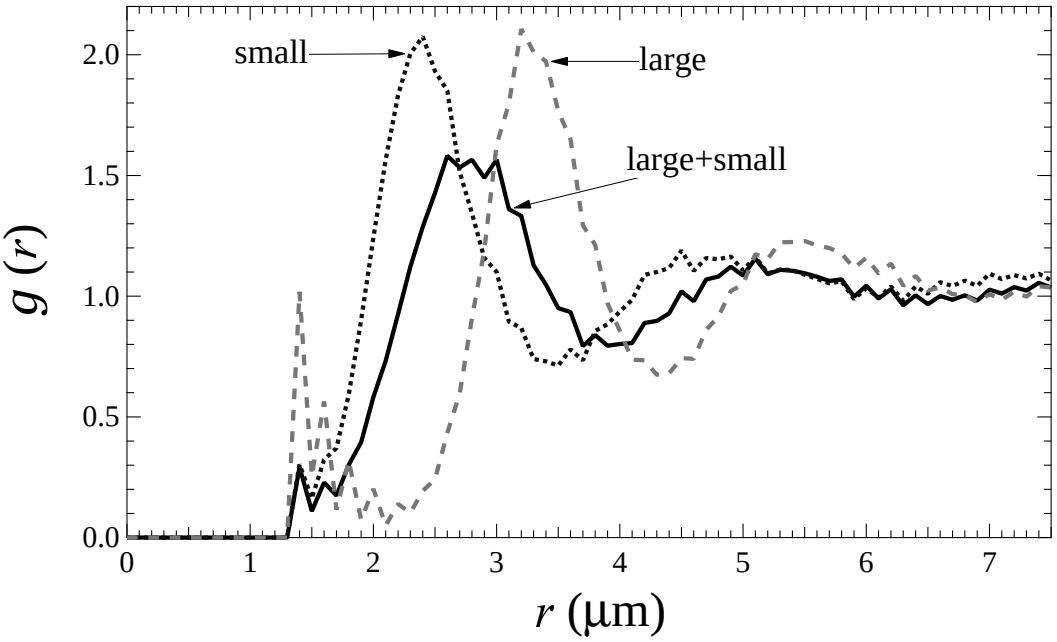

Figure 2.2: The pair correlation function $g(r)$ for a sample with volume fraction ϕ =0.57. The solid line represents $g(r)$ for both large and small particles combined; the dashed line that of large particles alone; and the dotted line that of small particles alone.

2.4.2 Dynamical slowing

We next consider how the motion of particles slows as the volume fraction increases and approaches the glass transition. Figures 2.3 and 2.4 show results of the mean square displacement $\langle \Delta \boldsymbol{r}_i{}^2 \rangle$ of large and small particles, respectively, where $\Delta \boldsymbol{r}_i = \Delta \boldsymbol{r}_i(\Delta t)$ denotes the displacement of i-th particle in time-lag Δt, and the angle brackets an average over all particles and times observed. Note that our resolution means we cannot measure mean square displacement values less than 0.1 μm^2, and thus the plateau height of curves for the highest volume fraction data is set by this limit, rather than the dynamics. The slight upturn for those curves at large values of Δt is above our resolution limit. Figures 2.3 and 2.4 show that as the volume fraction increases, particle motion slows significantly, as expected. At $\phi = 0.4$, small particles take tens of seconds to move a distance $a_S^2 = 1.4$ μm^2; at $\phi = 0.59$ the time has grown to more than 10^4 s. For the lowest volume fraction samples, comparing the two particle species, we find that

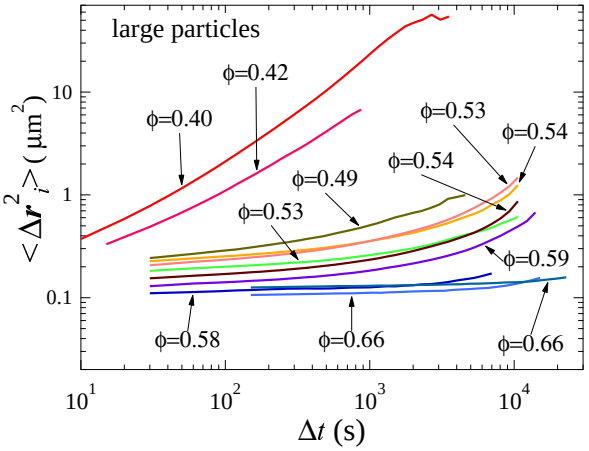

Figure 2.3: A log-log plot of mean square displacement versus time lag for large particles.

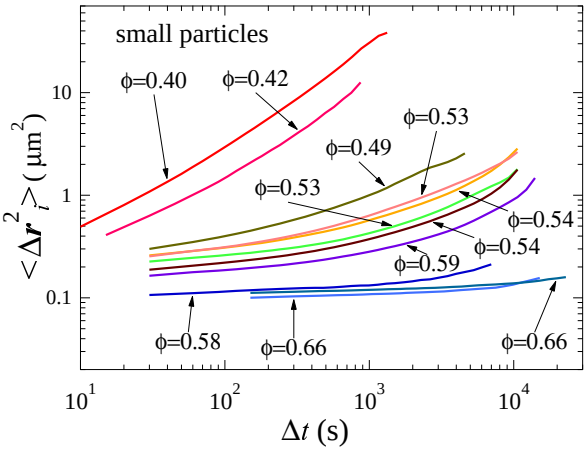

Figure 2.4: A log-log plot of mean square displacement versus time lag for small particles.

$\langle \Delta r_S^2 \rangle / \langle \Delta r_L^2 \rangle \approx a_L/a_S$, as expected from the Stokes-Einstein equation.

As the volume fraction increases, the plots of the mean square displacement show a characteristic plateau, interpreted as "cage trapping." Particles cannot diffuse freely, but instead are surrounded by their nearest neighbor particles which form a transient cage [11–16]. The upturn in the curve of the mean square displacement is identified with the rearrangements of the cage, allowing the particle within the cage to move to a new location, perhaps caged by different particles. Although the smaller particles move faster than the large particles, curves of the mean square displacement for both show upturns at similar time scales, indicating that their dynamics are strongly coupled [55].

For the samples with $\phi \geq \phi_g \approx 0.58$, the curves of the mean square displacement are nearly flat, suggesting that on our experimental time scales, these samples behave as glasses. Glasses are fundamentally non-equilibrium systems, so that physical properties for glasses depend on the preparation history in general and, in particular, the time since they were initially formed. This time-dependence is known as aging, and can be quantified by examining the mean square displacement at different times since the start of the experiment [55–57]. Figure 2.5 shows

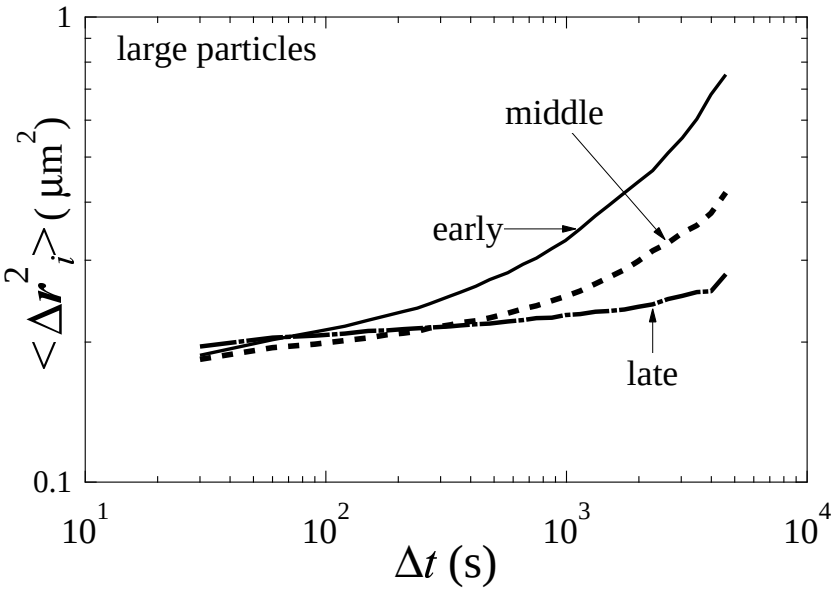

Figure 2.5: Plot of the mean square displacement taken of the same $\phi = 0.59$ sample from three different times (early, middle, late). The time-dependence of $\langle \Delta r^2 \rangle$ is clearly seen, indicating the presence of aging. As $\phi = 0.59$ is the lowest volume fraction in which this behavior is seen, we conclude that the glass transition occurs below at $\phi_g \approx 0.58$

data of the mean square displacement from $\phi = 0.59$. The top/middle/bottom curve is data from the motion over the first/second/third of the experimental run. The sample is most active immediately after being formed, and continues to slow down as time elapses. The aging of the mean square displacement appears in samples for $\phi \geq 0.58$, while no samples for $\phi < 0.58$ show aging. From the onset of aging, we conclude that the glass transition point is at volume fraction $\phi \approx 0.58$, similar to that seen for monodisperse samples [49]. Note that our particle size uncertainty of ± 0.02 μm (radius) leads to a systematic volume fraction uncertainty of $\pm 4\%$, so our estimate is $\phi_g = 0.58 \pm 0.02$ as a comparison with prior work.

Particles involved in a cage rearrangement event move significant distances compared to when they are caged, and prior work noted that the distribution of displacements is unusually broad on the time scale of the rearrangement [14, 58]. This is quantified by calculating the non-Gaussian parameter $\alpha_2(\Delta t)$, which for a one-dimensional distribution of displacements is

defined as

$$\alpha_2(\Delta t) = \frac{\langle \Delta x^4 \rangle}{3\langle \Delta x^2 \rangle} - 1, \tag{2.30}$$

where $\Delta x = \Delta x(\Delta t)$ denotes the one-dimension displacement for time lag Δt [59]. If the distribution of displacements Δx is Gaussian, then $\alpha_2 = 0$ by definition. If events with large displacements are more common than would be expected from a Gaussian distribution, then $\alpha_2 > 0$. Figures 2.6 and 2.7 show the results of the non-Gaussian parameter for one-dimension displacements of large and small particles. Note that we show only a few results because α_2 is sensitive to noise. The curves peak at time scales where cage rearrangements are most important [22,60], and thus coincides with the upturn of the curves of the mean square displacement. α_2 is fairly sensitive to experimental noise, and thus we only show a few curves in figs. 2.6 and 2.7. For example, the downturns at large Δt for the low volume fraction curves are probably not real.

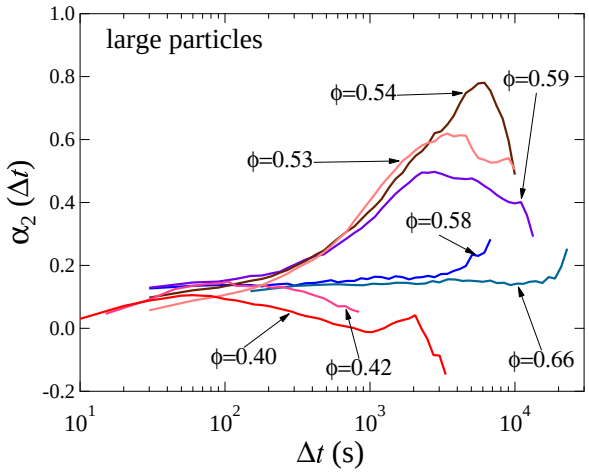

Figure 2.6: A semi-log plot of the non-Gaussian Parameter α_2 versus lag time for large particles.

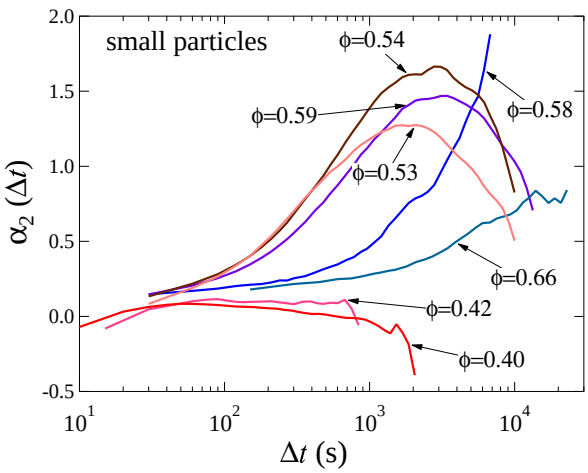

Figure 2.7: A semi-log plot of the non-Gaussian Parameter α_2 versus lag time for small particles.

Figures 2.6 and 2.7 also reveal that the motions of the small particles are more heterogeneous, with the maximum peaking of the non-Gaussian parameter above 1.5 for the small species but only reaching 0.8 for the large species. This is consistent with recent observations

of aging binary colloidal glasses, which likewise found the small particles had more "non-Gaussian" motion [55].

From figs. 2.3, 2.4, 2.6 and 2.7, we conclude that the dynamics of the large and small particles are qualitatively the same, although with small quantitative differences. In particular, the time scale over which particles escape cages is the same for both, as is the time of peak non-Gaussianity. In much of the subsequent analysis, therefore, we consider both species together in order to obtain better statistical validity.

2.4.3 Local environment influences mobility

We wish to understand the origins of dynamical heterogeneity. For a hard-sphere system, or an overdamped system such as our experimental colloidal suspension, the only variable is the local structure. Clearly structure has some relation with particle mobility [61], although this relationship may be difficult to see and not directly predictive in nature [62]. Prior work found that more disordered environments are weakly correlated with higher particle mobility [14, 57], and a recent study of aging binary colloidal glasses found a relation between the local composition and the mobility [55].

We quantify a particle's local environment by counting its nearest neighbors N_{NN}, defined as particles closer than the first minimum of the pair correlation function for the large particles, 3.8 μm (fig. 2.2), and distinguish between large and small neighbors. Figures 2.8 and 2.9 show that the number of neighbors of a given type has a strong influence on the mobility of a particle. Mobility is very sensitive to the number of large neighbors, decreasing sharply as the number of large neighbors increases. The number of smaller neighbors has a weaker, yet measurable, impact. Particles with more large neighbors have, on average, a lower mobility, while those with more small neighbors a larger mobility. These observations agree with studies

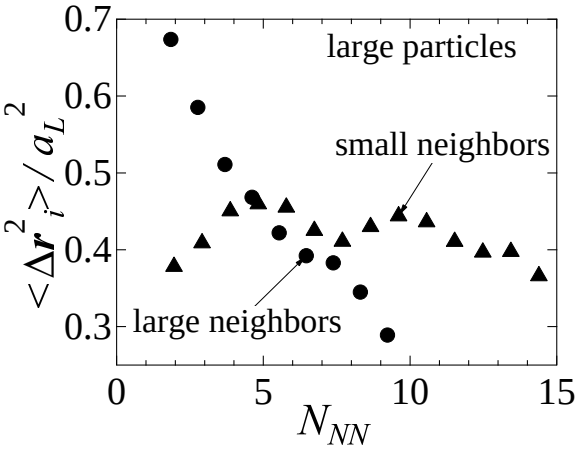

Figure 2.8: Large particle mobility as a function of the number of large and small nearest neighbors N_{NN}. These data are for volume fraction $\phi = 0.53$, using a time scale $\Delta t = 3780$ s to define displacements.

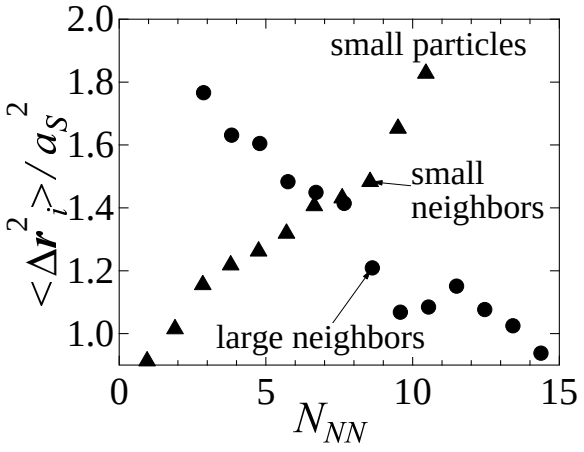

Figure 2.9: Small particle mobility as a function of the number of large and small nearest neighbors N_{NN}. These data are for volume fraction $\phi = 0.53$, using a time scale $\Delta t = 3780$ s to define displacements.

of aging in binary colloidal glasses, [55] and are reminiscent of prior rheological observations of binary suspensions [63–65] which noted that binary mixtures have lower viscosities than single-component samples with equivalent total volume fraction. The reason is that binary suspensions can in general be packed to higher volume fractions, and so have more free volume than monodisperse samples at the same volume fraction. Figures 2.8 and 2.9 suggest that the small particles indeed have much free volume and thus "lubricate" the large particles, as proposed previously [65]; although clearly with our data, the large particles seem to play a more important role. The lubricant effect for a large particle is less pronounced and this implies that the free volume is not enough for large particles. This agrees with prior observations of monodisperse suspensions which found that regions with slightly more free volume are slightly more mobile [14].

2.4.4 Cooperative motions

In dense supercooled liquids, it is known that the dynamics are anomalous, with the large displacements rare, but more common than a Gaussian distribution would predict. It is also clear

that, in many materials, the particles that have larger than average displacements are distributed in a spatially heterogeneous fashion [21,60]. In monodisperse colloidal systems, direct imaging using microscopy found that particles rearrange in cooperative groups [20, 22, 66]. Following the prior work, we characterize the cooperative nature of colloidal rearrangements by studying the dynamics over a time scale Δt^* that corresponds to the maximum of the non-Gaussian parameter [22, 60]. The maximum displacement of a particle over that time D_i is defined as

$$D_i(t) := \max_{t,t+\Delta t^*} (|\boldsymbol{r}_i(t_2) - \boldsymbol{r}_i(t_1)|) \tag{2.31}$$

where $\max_{t,t+\Delta t^*}(X)$ is the maximum value of X using times t_1, t_2 such that $t \leq t_1 < t_2 \leq t + \Delta t^*$. Taking the maximum displacement results in a quantity that is less sensitive to random Brownian motion than the ordinary displacement Δr. Following prior work, [22, 60] a threshold $D^*(\phi)$ is chosen such that on average, 5% of the particles at any given time have $D_i(t) > D^*$. These particles are termed "mobile particles" and generally are the ones undergoing cage rearrangements. (Note that at any particular time, the fraction of particles matching this definition is not required to be 5% [67]).

Figures 2.10, 2.11, 2.12 and 2.13 show snapshots of our system, highlighting the mobile particles. Clusters of these mobile particles are visible, in agreement with previous work which found similar mobile regions [22, 55, 60]. The clusters are somewhat smaller than those seen previously in single-component colloidal suspension [22]; apparently the dynamics in binary mixtures are less spatially heterogeneous. Our result is in agreement with the results of a simulation study for polydisperse hard-disk systems [68], which found that polydispersity reduces dynamic heterogeneity. It is also apparent in figures 2.10, 2.11, 2.12 and 2.13 that the number of mobile particles is similar for the two particle sizes. This reinforces are earlier decision to consider both large and small particles as one for statistical calculations.

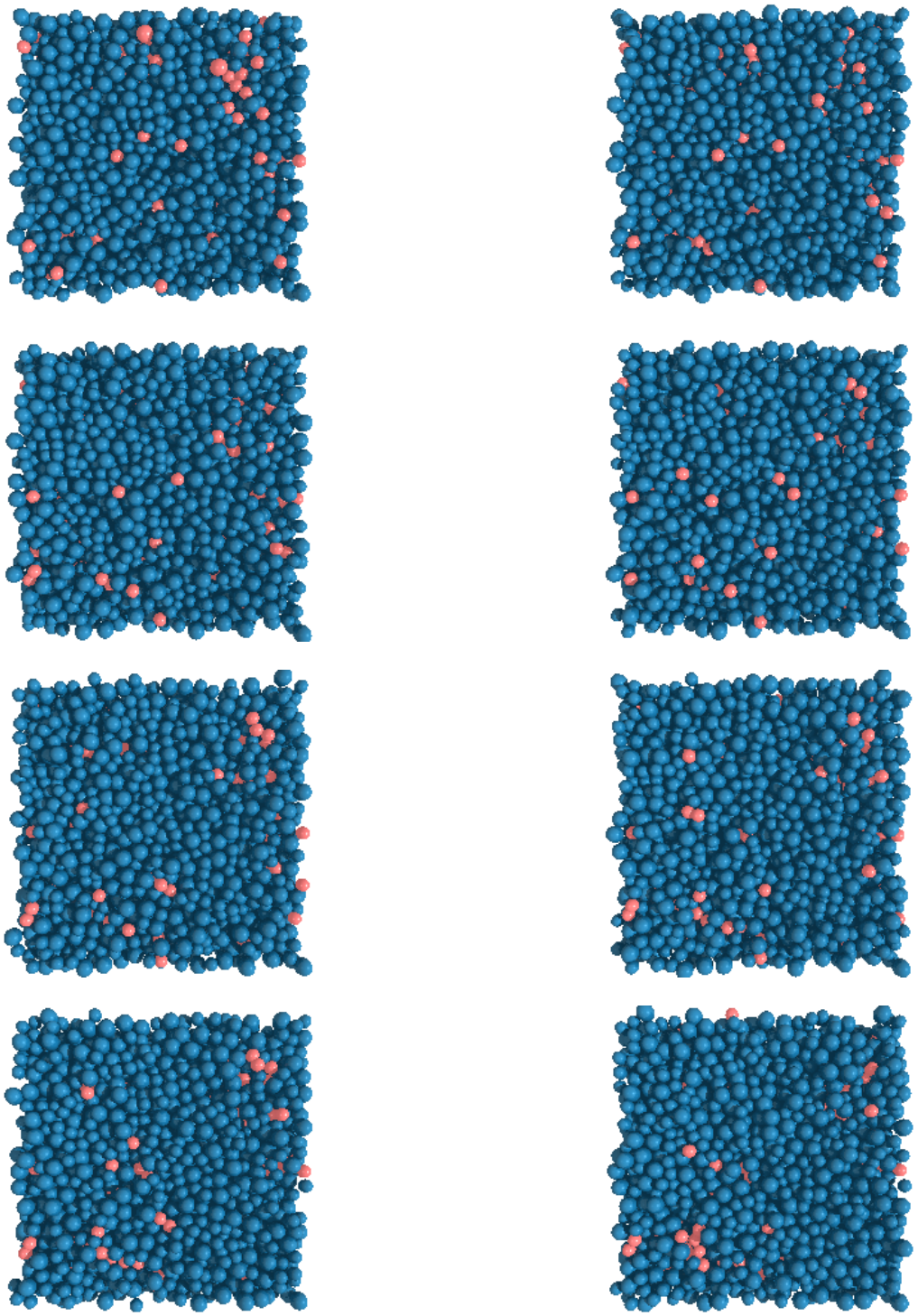

Figure 2.10: Snapshots of system for $\phi = 0.53$. The red particles are mobile, all other particles are blue. Mobile particles are defined as those making the largest displacements at this particular moment in time; see text for further details. We set the time lag for the displacement as the cage breaking time scale (the peak time of the non-Gaussian parameter t_{NGP}) which is Δt^* =3000 s for $\phi = 0.53$. The left upper figure is set as $t = 0$ and the right upper one $t = 300$ s, and the right bottom one $t = 2100$ s.

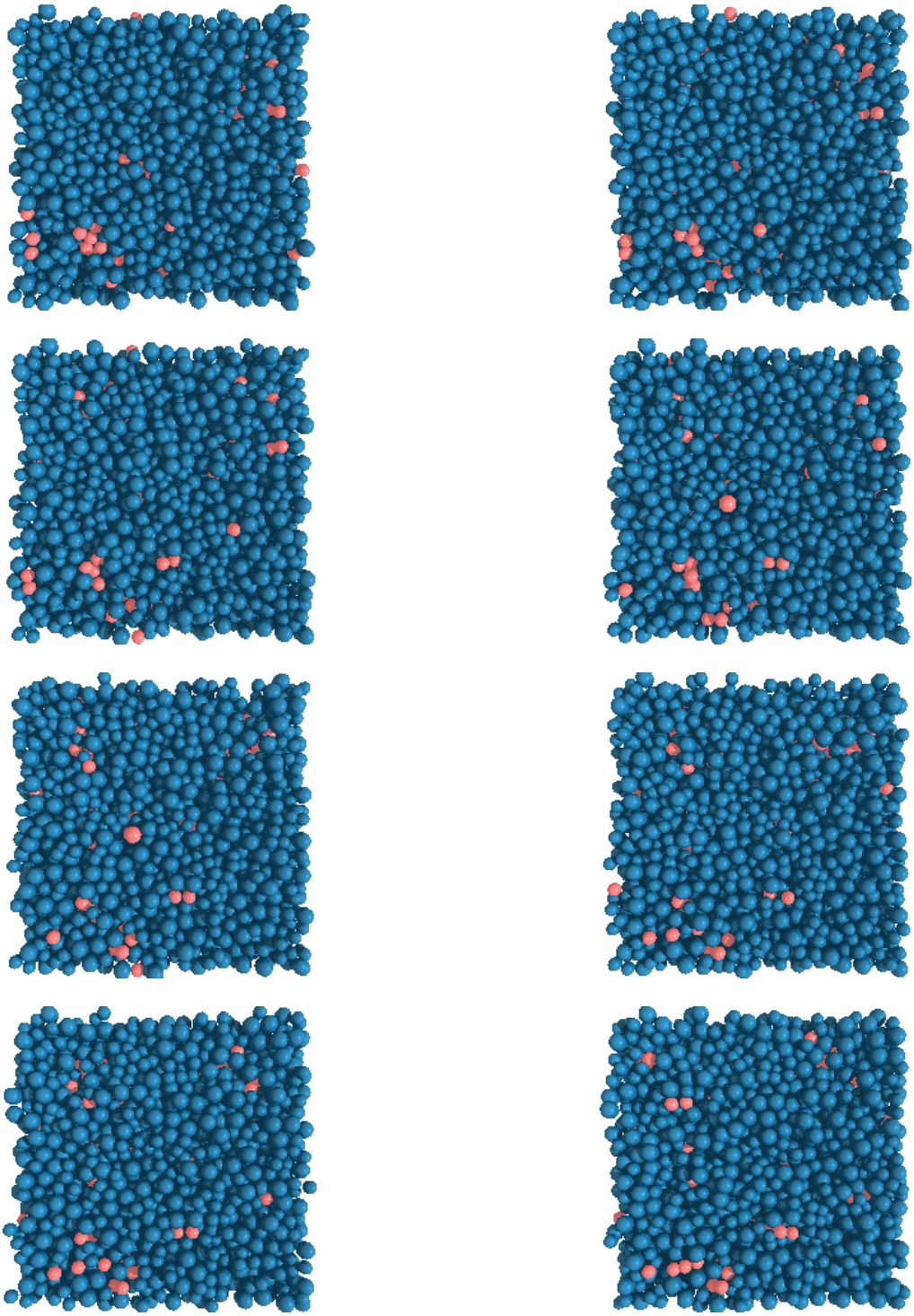

Figure 2.11: Snapshots of system for $\phi = 0.53$. The red particles are mobile, all other particles are blue. Mobile particles are defined as those making the largest displacements at this particular moment in time; see text for further details. We set the time lag for the displacement as the cage breaking time scale (the peak time of the non-Gaussian parameter τ_{NGP}) which is Δt^* =3000 s for $\phi = 0.53$. The left upper figure is set as $t = 2400$ s and the right upper one $t = 2700$ s, and the right bottom one $t = 4500$ s.

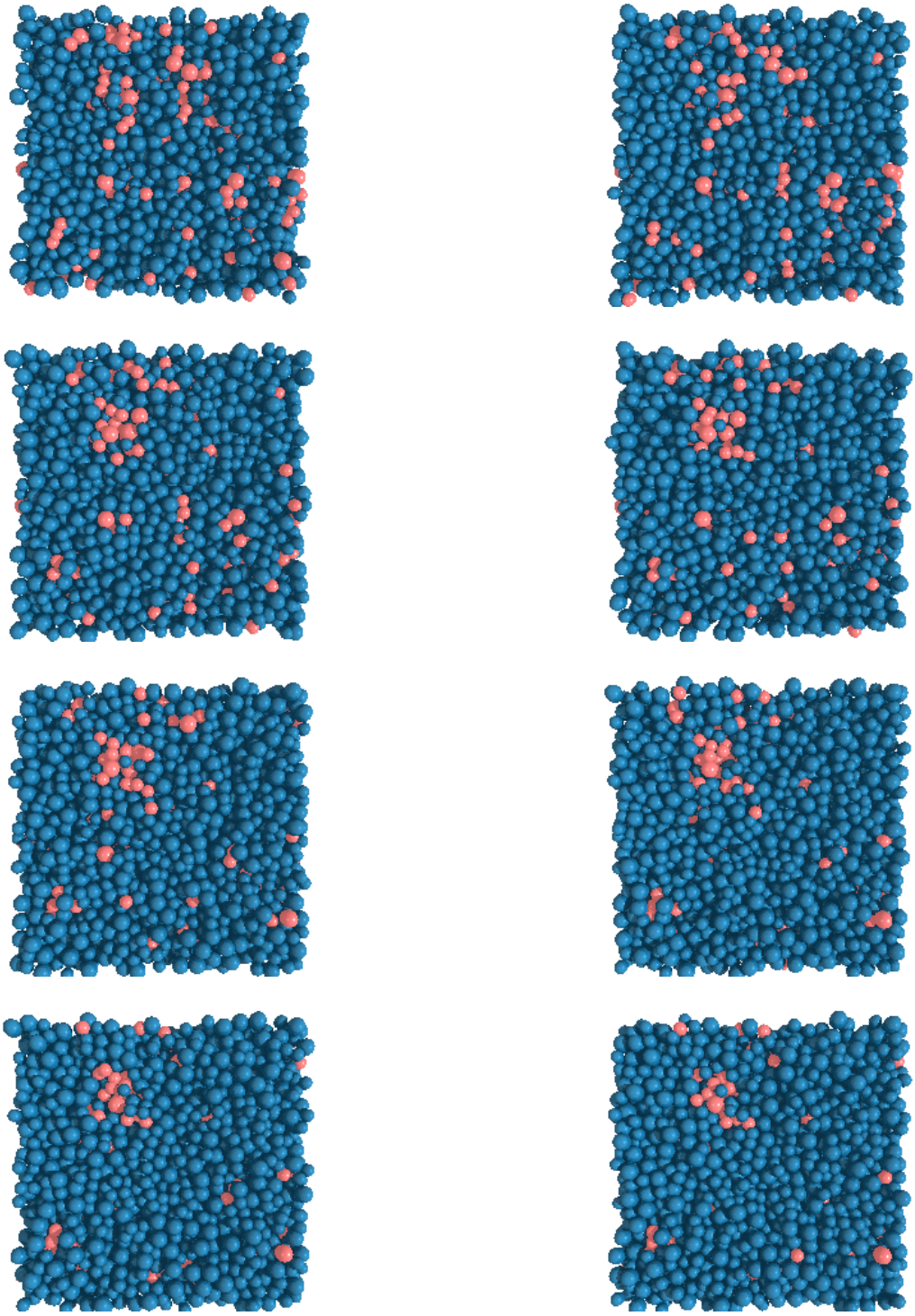

Figure 2.12: Snapshots of system for $\phi = 0.59$. The red particles are mobile, all other particles are blue. Mobile particles are defined as those making the largest displacements at this particular moment in time; see text for further details. We set the time lag for the displacement as the cage breaking time scale (the peak time of the non-Gaussian parameter τ_{NGP}) which is Δt^* =5070 s for $\phi = 0.59$. The left upper figure is set as $t = 0$ and the right upper one $t = 300$ s, and the right bottom one $t = 2100$ s.

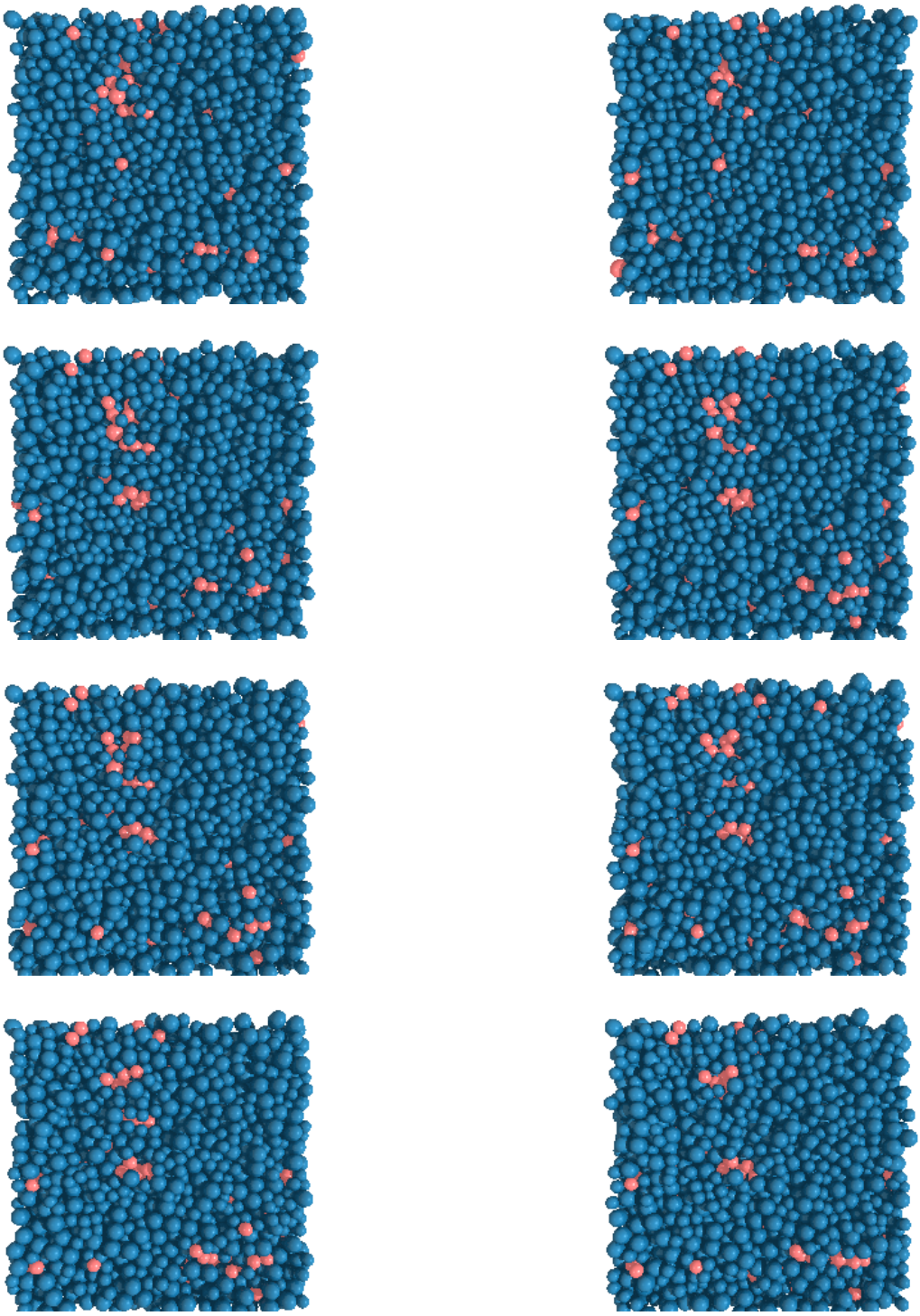

Figure 2.13: Snapshots of system for $\phi = 0.59$. The red particles are mobile, all other particles are blue. Mobile particles are defined as those making the largest displacements at this particular moment in time; see text for further details. We set the time lag for the displacement as the cage breaking time scale (the peak time of the non-Gaussian parameter τ_{NGP}) which is $\Delta t^* = 5070$ s for $\phi = 0.59$. The left upper figure is set as $t = 2400$ s and the right upper one $t = 2700$ s, and the right bottom one $t = 4500$ s.

2.4.5 Correlation functions and dynamic length scales

Pictures such as figures 2.10, 2.11, 2.12 and 2.13 are qualitative evidence of dynamical heterogeneity. For quantitative information, we consider the vector and scalar spatial-temporal correlation functions [52] $S_{\Delta \boldsymbol{r}}(R, \Delta t)$ and $S_{\delta r}(R, \Delta t)$ defined as eq. (2.25) and eq. (2.26). The vector function $S_{\Delta \boldsymbol{r}}(R, \Delta t)$ characterizes correlations in the vector displacements $\Delta \boldsymbol{r}_i = \boldsymbol{r}_i(t + \Delta t) - \boldsymbol{r}_i(t)$; the corresponding scalar function $S_{\delta \boldsymbol{r}}(R, \Delta t)$ uses the scalar distance $\delta r_i = |\Delta \boldsymbol{r}_i| - \langle |\Delta \boldsymbol{r}_i| \rangle$. The correlation function defined by eq. (2.25) indicates a vector correlation, and that defined by eq. (2.26) a scalar correlation. If particles correlate perfectly, the both correlation functions are unity. These correlation functions give information about spatial correlations for fixed lag time Δt, and about temporal dependence of the correlations for fixed separation R. We calculate these functions for all pairs of particles, without concern for the particle sizes, both to improve our statistics and because we do not find significant differences for large and small particles only.

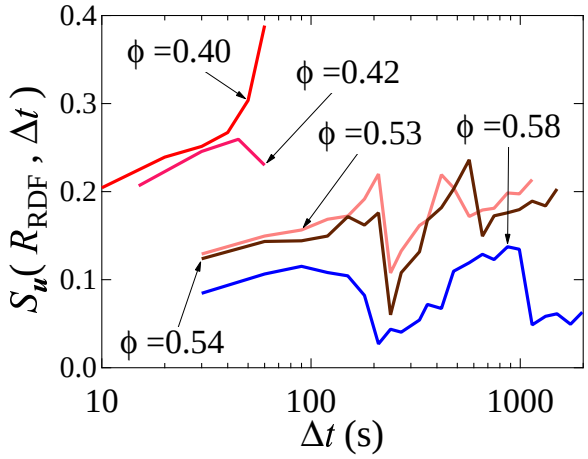

Figure 2.14: Semi-log plot of the vector correlation function (eq. (2.25)) in which the distance $R = 2.73$ μm is set as the first peak of the pair correlation function for all (large+small) particles.

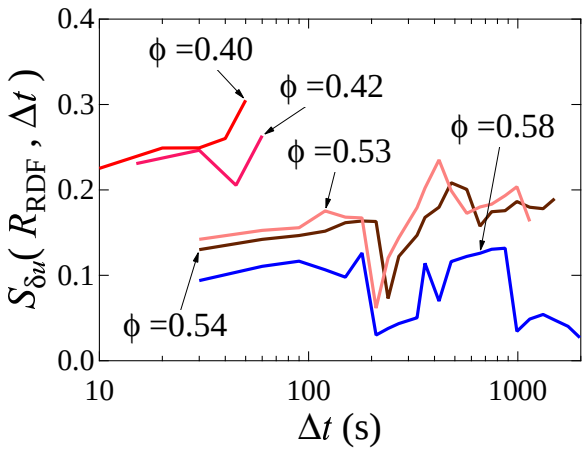

Figure 2.15: Semi-log plot of the scalar correlation function (eq. (2.26)) in which the distance $R = 2.73$ μm is set as the first peak of the pair correlation function for all (large+small) particles.

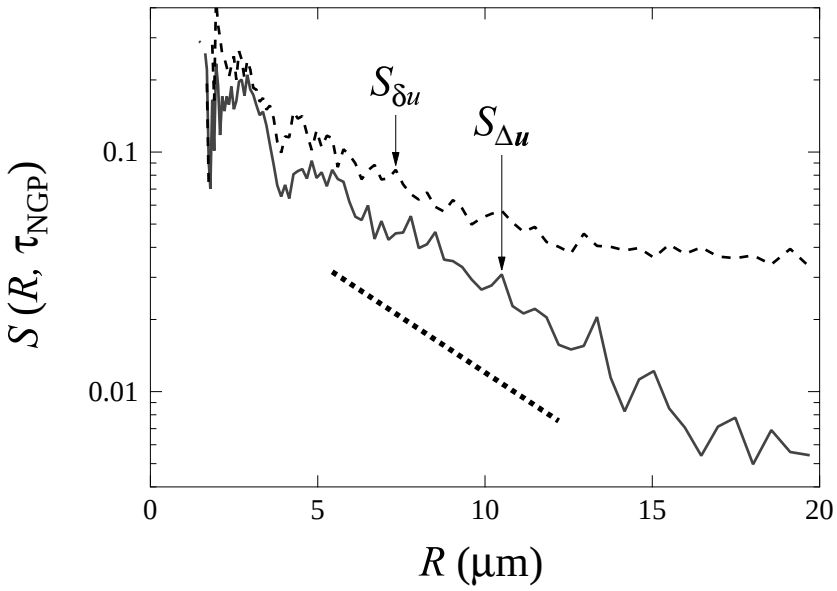

Figure 2.16: Semi-log plot of the spatial correlation functions of $\phi = 0.54$, where the time lag is set as $\tau_{\text{NGP}} = 3030$s. The dotted line represents an exponential function.

Figures 2.14 and 2.15 show the lag time dependence of these correlation functions, in which the distance R is set as the first peak distance of the pair correlation function $g(r)$ (see fig. 2.2). At time scales larger than those shown in figs. 2.14 and 2.15, the results become too uncertain, due to lack of data. In intermediate volume fraction region ($\phi < 0.6$), both correlation functions increase with Δt. In conjunction with figs. 2.3 and 2.4, this suggests that larger motions are more correlated with the motions of their neighboring particles. In particular, as $\Delta t \to \tau_{\text{NGP}}$, the scalar correlation is clearly important and thus cooperative motions are relevant for the relaxation. This agrees with prior experiments [22, 43].

For glassy samples ($\phi > 0.6$) the correlation functions show no real dependence on the lag time. Additionally, their values are small, suggesting that there is little correlation of the motion of neighbors. This is both because there is little overall motion in glassy samples (see figs. 2.3 and 2.4) and also the motion that does occur is dominated by Brownian motion within the cage, which is less correlated that the motions responsible for cage rearrangements [14].

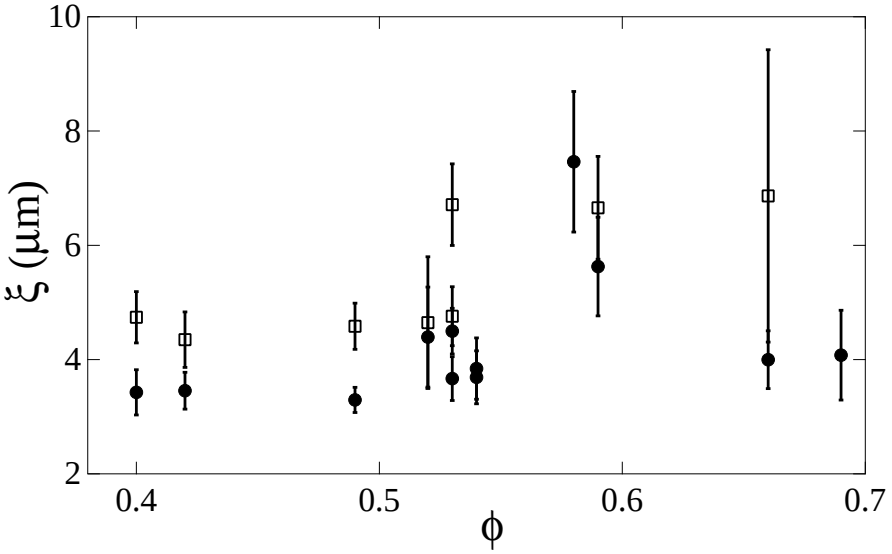

Figure 2.17: The relationship between the length scales and the volume fraction. The closed circles indicate the vector correlation lengths and the open squares the scalar ones. The symbols indicate the average value, and the error bars show the range of values found for different lag times Δt. These length scales are extracted from the vector correlation function for all particles (large + small). For volume fractions where data are missing, the scalar mobility correlation function did not decay exponentially and thus no length scale was determined.

To consider the spatial dynamical heterogeneity, we plot the correlation functions as a function of R in fig. 2.16 (for $\phi = 0.54$; results for other volume fractions are similar). For small separations around $R = 3.5$ μm, there is a dip in the correlation functions, which corresponds to the dip in the pair correlation function at the same position (fig. 2.2); the peak around $R = 2.8$ μm likewise corresponds to the peak of the pair correlation function. Thus, a particle's motion is correlated with that of its nearest neighbors, while particles separated by a less structurally favorable distance are less likely to have correlated motion.

We fit our data with an exponential function $S \simeq A\exp(-R/\xi)$ and extract the decay length ξ. Figure 2.17 shows both the vector (circles) and scalar (squares) decay lengths versus the volume fraction. Both length scales gradually increase as the volume fractions increase, although the increase is more pronounced for the scalar length. These lengths do not appear to diverge as the glass transition ($\phi_g \approx 0.58$) is approached, consistent with simulations of binary

Lennard-Jones mixtures [69]. The largest length scale seen is ≈ 7 μm$\approx 6a_S \approx 4.5a_L$, similar to prior studies of monodisperse colloids [43].

2.5 Conclusion

We have used confocal microscopy to study three-dimensional motion of particles in binary colloidal mixture. The volume fraction ϕ is varied from 0.4 - 0.7 and a glass transition, characterized by aging dynamics, is found at $\phi \simeq 0.58$. The dynamics of large and small particles are qualitatively similar. At volume fractions approaching the glass transition, both show an increase in motion at the same characteristic cage breaking time scale. This time scale also corresponds with the time over which the motion of both particles have the least Gaussian distribution. The number of mobile particle of large and small particle is also comparable. Particle motion is facilitated by the presence of small neighbors, and inhibited by large neighbors, consistent with the idea that small particles serve as lubricants. We have investigated the vector and scalar correlation functions and extracted specific length scales associated with the decay in correlation. This length slightly increases with volume fraction, although it does not appear to diverge as the glass transition is approached.

Chapter 3

Dynamical Spatial Correlation Functions in Molecular Dynamics Simulations

In this chapter, our study of molecular dynamics simulations is summarized. We measured the specific heat at constant volume to characterize the glass transition temperature. The radial distribution function including exclusive volume effect will be next discussed. Since the static information is not enough to characterize the supercooled liquids or the glasses, we measured the temporal-spatial correlation functions as well as the experiments for the binary colloidal mixtures. The correlation lengths were also extracted from the dynamical correlation functions. These simulation works are extended from my master course study.

3.1 Model

3.1.1 System

We consider a three-dimensional binary mixture system in which two kinds of particles, A and B, are dominated by the pair interactions. The volume V and the total number of particle N are invariant, leading to the constant number density $\rho = N/V$. The volume is large enough to neglect surface effects. We regard a simulation cell as a piece in bulk systems. Since we can not deal with the infinite space in computer simulations, we employ the periodical boundary condition as the boundary condition.

The control parameter is an inverse temperature $\beta = 1/k_B T$ because the control parameter should be a degree of the many-body effect in general. For example, the control parameter of hard-sphere systems (simulation) or colloidal suspensions (experiment) is the volume fraction. It is clear that influence of the many-body effect increases as the volume fraction increases. In fact, as the inverse temperature increases (i.e. the temperature decreases), the effect of the many-body effect increases because the kinetic energy decreases relatively.

3.1.2 Interaction

We consider a simple model called the Kob-Andersen model [44]. In this model, it is assumed that an only pair interaction acts between arbitrary two particles, and the pair interaction is represented by the binary-mixture Lennard-Jones potential

$$u(r) = 4\varepsilon_{\alpha\beta}\left[\left(\frac{\sigma_{\alpha\beta}}{r}\right)^{12} - \left(\frac{\sigma_{\alpha\beta}}{r}\right)^{6}\right], \tag{3.1}$$

where $\{\alpha, \beta\} = \{\mathrm{A}, \mathrm{B}\}$. According to real experimental values [70], the parameters are set as

$$\frac{\sigma_{\mathrm{AB}}}{\sigma_{\mathrm{AA}}} = 0.8, \quad \frac{\sigma_{\mathrm{BB}}}{\sigma_{\mathrm{AA}}} = 0.88, \quad \frac{\varepsilon_{\mathrm{AB}}}{\varepsilon_{\mathrm{AA}}} = 1.5, \text{ and } \frac{\varepsilon_{\mathrm{BB}}}{\varepsilon_{\mathrm{AA}}} = 0.5.$$

This model is widely studied, and then it is known that this system does not crystallize for long-time calculations. Therefore, it is suitable for the study of glass or supercooled liquid. Furthermore, the phase separation does not occur under appropriate initial conditions because the potential well $\varepsilon_{\mathrm{AB}}$ is the deepest.

In the present study, we also assume that the system is dominated by the classical dynamics, leading to the following two principal equations:

$$\frac{\mathrm{d}\boldsymbol{X}_i(t)}{\mathrm{d}t} = \boldsymbol{V}_i(t), \tag{3.2}$$

$$m_i \frac{\mathrm{d}\boldsymbol{V}_i(t)}{\mathrm{d}t} = -\sum_{j(\neq i)}^{N} \nabla_i u(X_{ij}), \tag{3.3}$$

where $\boldsymbol{X}_i(t)$ denotes the position vector of i-th particle, $\boldsymbol{V}_i(t)$ the velocity vector of i-th particle, m_i the mass of i-th particle, and $X_{ij} = |\boldsymbol{X}_i - \boldsymbol{X}_j|$. From the binary potential (3.1), the intermolecular force is given by

$$-\sum_{j(\neq i)}^{N} \nabla_i \phi(X_{ij}) = \frac{48\epsilon_{\alpha\beta}}{{\sigma_{\alpha\beta}}^2} \sum_{j(\neq i)}^{N} \left[\left(\frac{\sigma_{\alpha\beta}}{X_{ij}} \right)^{14} - \frac{1}{2} \left(\frac{\sigma_{\alpha\beta}}{X_{ij}} \right)^{8} \right] \boldsymbol{X}_{ij}(t). \tag{3.4}$$

The equations of motion is integrated with the velocity Verlet method.

3.1.3 Details of molecular dynamics simulations

We employ the Lennard-Jones units; length is scaled by σ_{AA} and energy by $\varepsilon_{\mathrm{AA}}$. Using the mass of particle m, time is scaled by $\tau_{\mathrm{LJ}} = \sigma_{\mathrm{AA}}\sqrt{m/48\varepsilon_{\mathrm{AA}}}$ and velocity by $\sqrt{48\varepsilon_{\mathrm{AA}}/m}$. We thus obtain dimensionless equations of motion

$$\frac{\mathrm{d}\hat{\boldsymbol{X}}_i(\hat{t})}{\mathrm{d}\hat{t}} = \hat{\boldsymbol{V}}_i(\hat{t}), \tag{3.5}$$

$$\frac{\mathrm{d}\hat{\boldsymbol{V}}_i(\hat{t})}{\mathrm{d}\hat{t}} = \hat{\epsilon}_{\alpha\beta} \sum_{j(\neq i)}^{N} \left(\frac{\hat{\sigma}_{\alpha\beta}^{12}}{\hat{X}_{ij}^{14}} - \frac{\hat{\sigma}_{\alpha\beta}^{6}}{2\hat{X}_{ij}^{8}} \right) \hat{\boldsymbol{X}}_{ij}, \tag{3.6}$$

where the hat symbol $\hat{}$ denotes dimensionless value. It should be noted here that the long-time self-diffusion constant is scaled by $d_0 = \sigma_{\mathrm{AA}}\sqrt{\varepsilon_{\mathrm{AA}}/m}$ from a view point of the mean-field theory [8].

In molecular dynamics simulations, $N_{\mathrm{A}} = 8780$, $N_{\mathrm{B}} = 2196$ and the length of simulation cell $L = 20.89\sigma_{\mathrm{AA}}$. The temperature first is adjusted by the velocity scaling method for equilibrating. After the simulation carries out in equilibrium, the velocity scaling method is not used. Our results thus are obtained under the microcanonical ensemble.

3.2 Measurand

3.2.1 Specific Heat

In the microcanonical ensemble, an equilibrium average of a certain physical variable $A(\Gamma)$, in which Γ denotes a point on the phase space, is represented by

$$\langle A(\Gamma)\rangle = \int \mathrm{d}\Gamma A(\Gamma)\delta(H(\Gamma)-E), \tag{3.7}$$

where $H(\Gamma)$ denotes the total energy of system. It is assumed that the $H(\Gamma)$ has

$$H(\Gamma) = \sum_i \frac{\boldsymbol{P}_i^2}{2m_i} + \Phi(\boldsymbol{X}), \tag{3.8}$$

where $\boldsymbol{X} = \{\boldsymbol{X}_i\}$ $(i = 1, 2, ..., N)$. The number of states $\Omega(E)$, which indicates the number of microscopic states less than E, is calculated by

$$\begin{aligned}
\Omega(E) &= \int^E \mathrm{d}E' \int \delta(H(\Gamma)-E')\mathrm{d}\Gamma \\
&= \int^E \mathrm{d}E' \int \mathrm{d}\boldsymbol{X} \int \mathrm{d}\boldsymbol{Y} \sqrt{\prod_i m_i}\, \delta\left(\sum_i Y_i^2 + \Phi(\boldsymbol{X}) - E'\right) \quad (\text{where } \boldsymbol{Y}_i = \boldsymbol{P}_i/\sqrt{m_i}) \\
&= C_{3N}\int^E \mathrm{d}E' \int \mathrm{d}\boldsymbol{X} \int_0^\infty \mathrm{d}y\, y^{3N-1}\delta(y^2 + \Phi(\boldsymbol{X}) - E') \quad (\text{where } y = |\boldsymbol{Y}_i| \text{ for } {}^\forall i) \\
&= C_{3N}\int^E \mathrm{d}E' \int \mathrm{d}\boldsymbol{X} \int \mathrm{d}y\, y^{3N-1}\frac{\delta(y - \sqrt{E' - \Phi(\boldsymbol{X})})}{2\sqrt{E' - \Phi(\boldsymbol{X})}} \\
&= C_{3N}\frac{1}{3N}\int \mathrm{d}\boldsymbol{X}(E - \Phi(\boldsymbol{X}))^{3N/2},
\end{aligned} \tag{3.9}$$

where $C_{3N} = 2\pi^{3N/2}\sqrt{\prod_i m_i}/\Gamma(3N/2)$ (appendix B.1).

The entropy S is defined by

$$S := k_B \ln\left[w(E)\Delta E\right], \tag{3.10}$$

where $w(E)\Delta E$ denotes the thermodynamic weight that indicates the number of microscopic states from E to $E + \Delta E$. We should note that the density of the number of states $w(E)$ is represented by

$$w(E)\Delta E = \Omega(E + \Delta E) - \Omega(E) \;\Leftrightarrow\; w(E) = \frac{\partial\Omega(E)}{\partial E} \;\; (\Delta E \ll 1).$$

If the state is normal[1] thermodynamically, for any $\Delta E(>0)$

$$\frac{\Omega(E)-\Omega(E-\Delta E)}{\Omega(E)} \simeq 1. \tag{3.11}$$

Thus, we can write

$$S \simeq k_B \ln \Omega(E) \tag{3.12}$$

in thermodynamically normal states. When the total energy is written by eq. (3.8), the entropy on the microcanonical ensemble is given by

$$S = k_B \ln \left[\frac{C_{3N}}{3N} \int \mathrm{d}\boldsymbol{X} (E - \Phi(\boldsymbol{X}))^{3N/2} \right]. \tag{3.13}$$

The statistical-mechanical definition of temperature[2] is

$$\frac{1}{T} := \left(\frac{\partial S}{\partial E} \right)_{V,N}, \tag{3.14}$$

thus,

$$\frac{1}{T} = \frac{3Nk_B}{2} \frac{\displaystyle\int \mathrm{d}\boldsymbol{X} (E-\Phi(\boldsymbol{X}))^{\frac{3N}{2}-1}}{\displaystyle\int \mathrm{d}\boldsymbol{X} (E-\Phi(\boldsymbol{X}))^{\frac{3N}{2}}} = \frac{3Nk_B}{2} \frac{1}{\langle H(\Gamma) - \Phi(\boldsymbol{X}) \rangle}, \tag{3.15}$$

where (ref. the derivation of eq.(3.9))

$$(E-\Phi(\boldsymbol{X}))^{\frac{3N}{2}-1} = \frac{2}{C_{3N}} \int \mathrm{d}\boldsymbol{P} \delta(H(\Gamma) - E).$$

eq.(3.15) denotes the law of equipartition of energy.

The pressure is defined by

$$P := T \left(\frac{\partial S}{\partial V} \right)_{E,N}. \tag{3.16}$$

[1] This "thermodynamically normal" means that the following limit exists:

$$\lim_{V\to\infty} \frac{1}{V} \log \Omega(E)$$

In this case, the number of states increases exponentially as the energy E increases.

[2] One can discuss other statements, e.g. one first defines the temperature, and then derives the entropy. However, we define the entropy by eq. (3.10), and then define the temperature by eq. (3.14).

It should be noted that the range of the integration in the representation of the entropy (3.13) depends on the volume. We replace X_i^α by $V^{1/3}x_i^\alpha$ where X_i^α denotes the α component of the position vector $\boldsymbol{X}_i$ of the i-th particle[3]. The entropy (3.13) reduces to

$$S = k_B \ln \left[\frac{C_{3N}}{3N} V^N \int_1 \mathrm{d}\boldsymbol{x} (E - \Phi(V^{1/3}\boldsymbol{x}))^{3N/2} \right], \tag{3.17}$$

where the range of this integration is independent on the volume. The differential with respect to the volume is thus given by

$$\begin{aligned} \frac{\partial}{\partial V} \int \mathrm{d}\boldsymbol{X} (E - \Phi(\boldsymbol{X}))^{3N/2} &= \frac{N}{V} \int \mathrm{d}\boldsymbol{X} (E - \Phi(\boldsymbol{X}))^{3N/2} \\ &\quad - \frac{1}{3V} \frac{3N}{2} \int \mathrm{d}\boldsymbol{X} \left(\sum_i \frac{\partial \Phi}{\boldsymbol{X}_i} \cdot \boldsymbol{X}_i \right) (E - \Phi(\boldsymbol{X}))^{\frac{3N}{2}-1}. \end{aligned} \tag{3.18}$$

Therefore, we obtain

$$P = \frac{N k_B T}{V} - \frac{1}{3V} \left\langle \sum_i \frac{\partial \Phi(\boldsymbol{X})}{\partial \boldsymbol{X}_i} \cdot \boldsymbol{X}_i \right\rangle. \tag{3.19}$$

This representation is the same equation as that derived from the virial theorem and the above form of the pressure is approved for any ensembles [71].

The specific heat at constant volume is defined by

$$C_V := \left(\frac{\partial E}{\partial T} \right)_V. \tag{3.20}$$

On the other hand,

$$\left(\frac{\partial^2 S}{\partial E^2} \right)_V = \left(\frac{\partial}{\partial E} \frac{1}{T} \right)_{V,N} = -\frac{1}{T^2} \left(\frac{\partial T}{\partial E} \right)_V, \tag{3.21}$$

$$C_V = -\frac{1}{T^2} \left(\frac{\partial^2 S}{\partial E^2} \right)_V^{-1}. \tag{3.22}$$

Here,

$$\left(\frac{\partial^2 S}{\partial E^2} \right)_V = \frac{3N k_B}{2} \left[\left(\frac{3N}{2} - 1 \right) \frac{\int \mathrm{d}\boldsymbol{X} (E - \Phi(\boldsymbol{X}))^{\frac{3N}{2}-2}}{\int \mathrm{d}\boldsymbol{X} (E - \Phi(\boldsymbol{X}))^{\frac{3N}{2}}} \right.$$

[3] Here, it is assumed that the system is cube. Since we consider $V \to \infty$ in the final analysis, any shape of the system can be allowed.

$$
\begin{aligned}
& \qquad\qquad -\frac{3N}{2}\frac{\left\{\int \mathrm{d}\boldsymbol{X}(E-\Phi(\boldsymbol{X}))^{\frac{3N}{2}-1}\right\}^2}{\left\{\int \mathrm{d}\boldsymbol{X}(E-\Phi(\boldsymbol{X}))^{\frac{3N}{2}}\right\}^2}\Bigg] \\
&= \frac{3Nk_B}{2}\left[\left(\frac{3N}{2}-1\right)\left\langle\frac{1}{K}\right\rangle\frac{1}{\langle K\rangle}-\frac{3N}{2}\frac{1}{\langle K\rangle^2}\right] \\
&= -\frac{1}{k_BT^2}\left[1-\left(1-\frac{2}{3N}\right)\left\langle\frac{1}{K}\right\rangle\langle K\rangle\right],
\end{aligned}
$$

$$
\therefore\ C_V = k_B\left[1-\left(1-\frac{2}{3N}\right)\left\langle\frac{1}{K}\right\rangle\langle K\rangle\right]^{-1}, \tag{3.23}
$$

where K denotes the kinetic energy. In case $N \gg 1$ and $\delta K/\langle K\rangle \ll 1$, the specific heat reduces to

$$
C_V \simeq k_B\left[\frac{2}{3N}-\frac{\langle\delta K^2\rangle}{\langle K\rangle^2}\right]^{-1} = \frac{3Nk_B}{2}\left[1-\frac{2\langle\delta\Phi^2\rangle}{3N(k_BT)^2}\right], \tag{3.24}
$$

where $1-\frac{2}{3N}\simeq 1$ and

$$
\left\langle\frac{1}{K}\right\rangle = \left\langle\frac{1}{\langle K\rangle+\delta K}\right\rangle = \frac{1}{\langle K\rangle}\left\langle 1-\frac{\delta K}{\langle K\rangle}+\frac{\delta K^2}{\langle K\rangle^2}+\cdots\right\rangle = \frac{1}{\langle K\rangle}+\frac{\langle\delta K^2\rangle}{\langle K\rangle^3}+\cdots.
$$

This approximation result (3.24) corresponds to the expression derived by Lebowitz et al. [71]. The relationship between the specific heat at constant volume C_V and that at constant pressure C_p is summarized in appendix B.2.

3.2.2 Alternative pair correlation function

A pair-correlation function is introduced by

$$
w(\boldsymbol{r}) := \int \mathrm{d}\boldsymbol{r}' n_\Delta(\boldsymbol{r}')n_\Delta(\boldsymbol{r}'+\boldsymbol{r})\Big/\int \mathrm{d}\boldsymbol{r}', \tag{3.25}
$$

where $n_\Delta(\boldsymbol{r})$ denotes the number density including size effect defined by

$$
n_\Delta(\boldsymbol{r}) = \frac{1}{4\pi}\sum_{i=1}^{N}\int \mathrm{d}\Omega_i \int \frac{\mathrm{d}\boldsymbol{k}}{(2\pi^3)}e^{i\boldsymbol{k}\cdot(\boldsymbol{r}-\boldsymbol{R}_i)} \tag{3.26}
$$

with $\boldsymbol{R}_i = \boldsymbol{R}_i(\Omega_i) = \boldsymbol{X}_i + \boldsymbol{a}_i(\Omega_i)$. In the following, we set $\int \mathrm{d}\boldsymbol{r}' =: V$. The pair-correlation function is calculated by

$$w(\boldsymbol{r}) = \frac{1}{(4\pi)^2(2\pi)^3 V} \sum_{i,j}^{N} \iint \mathrm{d}\Omega_i \mathrm{d}\Omega_j \int \mathrm{d}\boldsymbol{k} e^{-i\boldsymbol{k}\cdot(\boldsymbol{r}-\boldsymbol{R}_j+\boldsymbol{R}_i)}. \tag{3.27}$$

Considering isotropy of systems which we treat, eq. (3.27) reduces to

$$\begin{aligned} w(r) &= \frac{1}{2\pi^2 V r} \sum_{i=1}^{N} \frac{1}{a_i} \left[\sum_{j(\neq i)}^{N} \frac{1}{a_j X_{ij}} \int_0^\infty \mathrm{d}k \frac{\sin ka_i \sin ka_j \sin kr \sin kX_{ij}}{k^2} \right. \\ &\qquad \left. + \frac{1}{a_j} \int_0^\infty \mathrm{d}k \frac{\sin ka_i \sin ka_j \sin kr}{k} \right]. \end{aligned} \tag{3.28}$$

A radial distribution function $g'(r)$ including size effect is defined as

$$g'(r) := \frac{1}{2\pi^2 \bar{n}^2 V r} \sum_{i=1}^{N} \sum_{j(\neq i)}^{N} \frac{1}{a_i a_j X_{ij}} \int_0^\infty \mathrm{d}k \frac{\sin ka_i \sin ka_j \sin kr \sin kX_{ij}}{k^2}, \tag{3.29}$$

where $\bar{n}$ denotes the average number density

$$\bar{n} = \int \mathrm{d}\boldsymbol{r}' n(\boldsymbol{r}') \Big/ \int \mathrm{d}\boldsymbol{r}' = \frac{N}{V}. \tag{3.30}$$

The integrand reduces to

$$\begin{aligned} \frac{\sin ka_i \sin ka_j \sin kr \sin kX_{ij}}{k^2} &= \frac{1}{2} \frac{\sin ka_i \sin ka_j \cos k(r - X_{ij})}{k^2} \\ &\quad - \frac{1}{2} \frac{\sin ka_i \sin ka_j \cos k(r + X_{ij})}{k^2}. \end{aligned} \tag{3.31}$$

Thus,

$$g'(r) = \frac{V}{16\pi N^2 r} \sum_{i=1}^{N} \sum_{j(\neq i)}^{N} \frac{1}{a_i a_j X_{ij}} (g_{ij}^{(-)}(r) - g_{ij}^{(+)}(r)), \tag{3.32}$$

where

$$g_{ij}^{(\pm)}(r) = \begin{cases} 2\min(a_i, a_j) & 0 < |r \pm X_{ij}| < |a_i - a_j| \\ a_i + a_j - |r \pm X_{ij}| & |a_i - a_j| < |r \pm X_{ij}| < a_i + a_j \\ 0 & a_i + a_j < |r \pm X_{ij}| \end{cases} \tag{3.33}$$

In binary mixture systems where the number of A and B particle is N_A and N_B ($N_A + N_B = N$), respectively, the summation is divided as

$$\frac{1}{2} \sum_{i=1}^{N} \sum_{j(\neq i)}^{N} = \sum_{i=1}^{N_A - 1} \sum_{j=i+1}^{N_A} + \sum_{i=1}^{N_A} \sum_{j=N_A+1}^{N} + \sum_{i=N_A+1}^{N-1} \sum_{j=i+1}^{N}, \tag{3.34}$$

where the symmetry of i- and j-particle is assumed. The first term corresponds to A-A correlation, the second one A-B, and the third one B-B. Therefore, one can obtain

$$g'_{\mathrm{BM}}(r) = \frac{V}{8\pi N^2 r} \times \left[\frac{1}{{a_A}^2} \sum_{i=1}^{N_A-1} \sum_{j=i+1}^{N_A} + \frac{1}{a_A a_B} \sum_{i=1}^{N_A} \sum_{j=N_A+1}^{N} + \frac{1}{{a_B}^2} \sum_{i=N_A+1}^{N-1} \sum_{j=i+1}^{N} \right] \frac{g_{ij}^{(-)}(r) - g_{ij}^{(+)}(r)}{X_{ij}}, \tag{3.35}$$

where a_A and a_B denote the radius of A and B particle, respectively.

3.3 Result and Discussion

3.3.1 Specific heat at constant volume

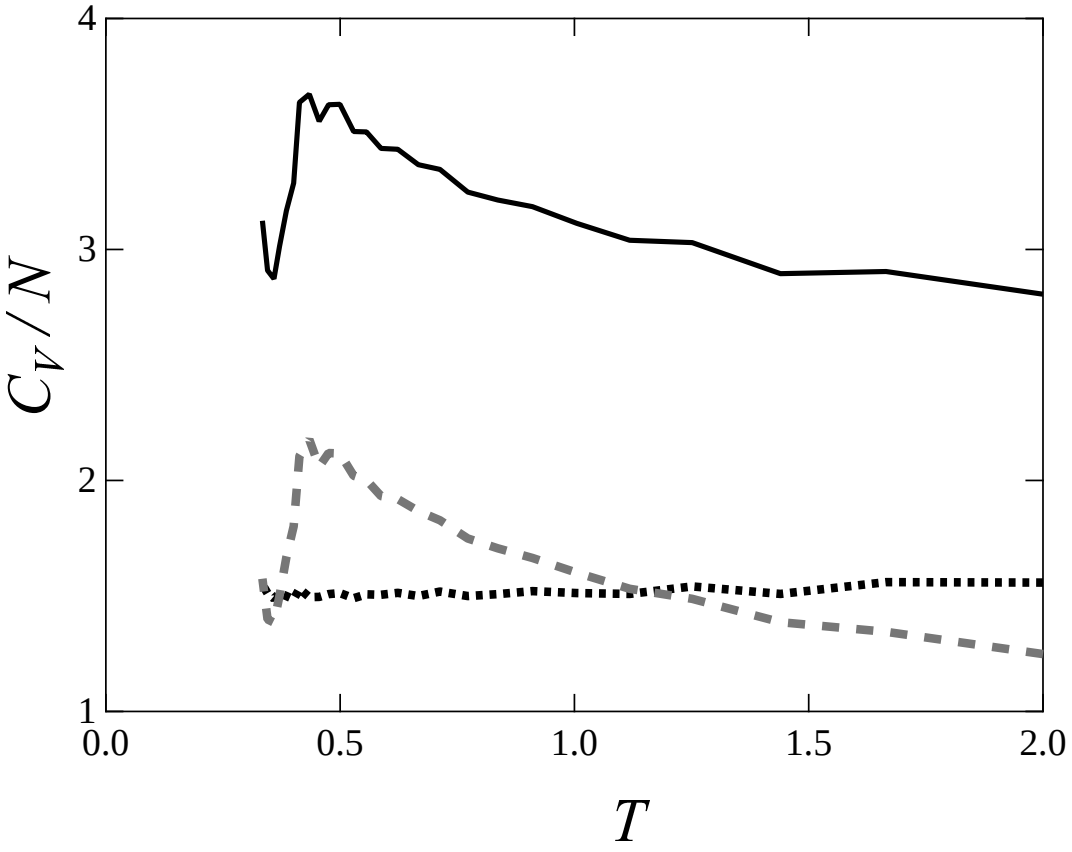

Figure 3.1: Plot of the specific heat per particle at constant volume versus the temperature. The solid line indicates the specific heat at constant volume, the dotted one that due to the kinetic energy, and the dashed gray one that due to the potential energy.

In the mean-field theory [8], glass is distinguished from supercooled liquid by the long-time self-diffusion coefficient D_S^L. Specifically, systems whose long-time self-diffusion coefficient holds $\log D_S^L/d_0 < -5.12$ are glass. Here, d_0 denotes an appropriate dimension; it must be $d_0 = \sigma_{\mathrm{AA}}\sqrt{\varepsilon_{\mathrm{AA}}/m}$. in binary Lennard-Jones mixtures. However, there are other definitions of the glass transition [2, 4] [4]. For instance, we can define the glass transition by paying attention to the specific heat. It is known that the specific heat rapidly decreases near the glass transition on cooling [72–74]. In other words, one can determine the glass transition point from the specific heat.

Figure 3.1 shows the results of the specific heat per particle at constant volume; $c_V = C_V/N$, where the results are scaled by the Boltzmann constant k_B. Note that the energy is average over $10^4\tau_{\mathrm{LJ}}$ to obtain credible data. The internal, kinetic, and potential energy are in steady-states even for $T < 0.434$, whereas the mean-square displacement is not.

The dimensionless specific heat c_V^K due to the kinetic energy is ideally a constant value of 1.5. It is reasonable because of the equipartition law of energy; $c_V^K = 3k_B/2$. Moreover, the specific heat due to the potential energy c_V^U should be $3k_B/2$ in the harmonic oscillator approximation, and thus one can obtain $c_V = 3k_B$ in solid states, which is known as the Dulong-Petit law[5]. On the other hand, they due to the internal and potential energy increase as the temperature decreases, but rapidly decrease below $T = 0.44$. The growth of the specific heat due to the potential energy represents the importance of the spatial structuring at the vicinity of the glass transition point.

The peak temperature $T \simeq 0.44$ is close to the glass transition point $T_g = 0.4376$ determined from the long-time self-diffusion coefficient [75]. It can be concluded that the definition

[4] It is not clear how each definition relates with the other ones.

[5] In ultralow temperature region, the Dulong-Petit law does not hold and the specific heat is a function of the square of the temperature (Debye model).

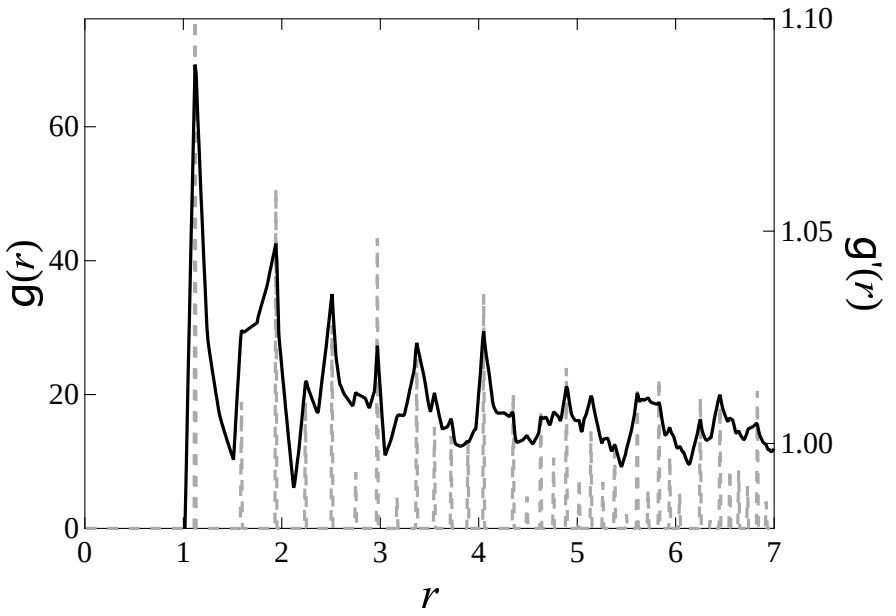

Figure 3.2: The result of $g(r)$ (dashed gray line) and $g'(r)$ (solid line) for the perfect FCC configuration. Left axis indicates value of the $g(r)$ and right axis that of the $g'(r)$.

of the glass transition by the long-time self-diffusion coefficient corresponds to that by the specific heat. The glass transition is regarded as the dynamical crossover, and thus the glass transition should be characterized by dynamical property. In the view point, the definition by the long-time self-diffusion coefficient is reasonable. However, we revealed that the specific heat, which is obtained from not dynamical but static information, relates with the dynamics near the glass transitions. It is consistent in view of the dynamical heterogeneity [21].

3.3.2 Radial distribution function including size effect

In order to understand physical meanings of an alternative pair correlation function defined by eq. (3.29), we first investigated it in one-component Lennard-Jones fluids. Unless stated, the number density of the one-component Lennard-Jones system is $N/V = 10976/23.0^3 \simeq 0.9$ in Lennard-Jones unit.

Figure 3.2 shows the results for the perfect FCC configuration of the ordinary radial distribution function $g(r)$ and the radial distribution function $g'(r)$ including size effect. Note that

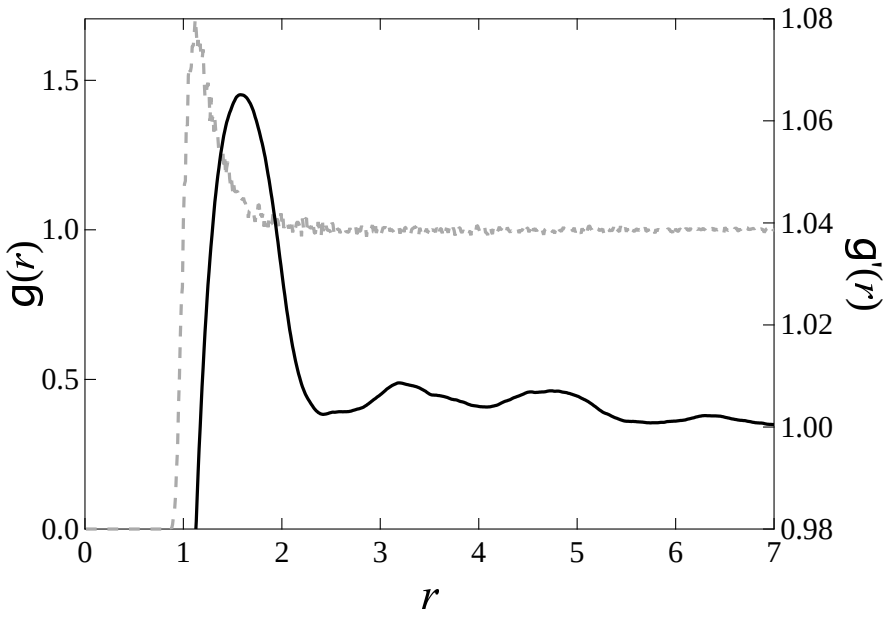

Figure 3.3: The result of $g(r)$ (dashed gray line) and $g'(r)$ (solid line) for very dilute Lennard-Jones system; $N/V \simeq 0.02$. Left axis indicates value of the $g(r)$ and right axis does that of the $g'(r)$.

the perfect FCC configuration is not achieved in molecular dynamics simulations because of the thermal fluctuation. The perfect FCC configuration was made artificially. The distance at which the both have peak extremely corresponds each other, but $g'(r)$ is broader because of the size effect. Moreover, the peak height of $g'(r)$ is much shorter than $g(r)$.

Figure 3.3 shows the results of $g(r)$ and $g'(r)$ for a dilute Lennard-Jones system; the number density is $N/V \simeq 0.02$. The result of $g(r)$ is averaged over 200 times results while that of $g'(r)$ is a single result. It implies that $g'(r)$ is more stable (less sensitive) than $g(r)$. The peak distance is slightly different. It might be because of the following reason. When two particles contact each other, the longest reactive distance of $g'(r)$ is twice diameter while that of $g(r)$ is diameter. In dilute systems, the three or more body collisions are safely neglected, so the two-body collision play an important role. Therefore, the peak distance of $g'(r)$ should be longer than that of $g(r)$.

Figures 3.4 and 3.5 show the results of the $g(r)$ and $g'(r)$ for a one-component LJ system

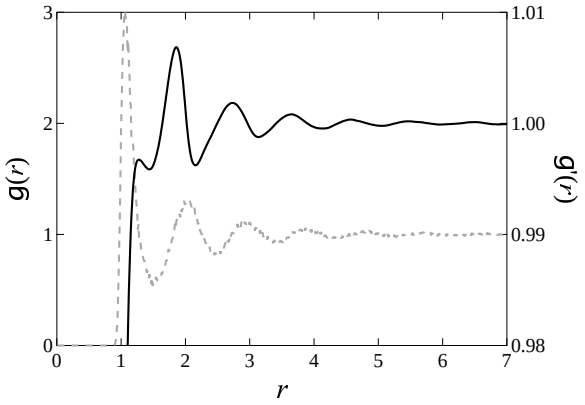

Figure 3.4: The result of $g(r)$ (dashed gray line) and $g'(r)$ (solid line) for one-component Lennard-Jones system at $T = 1.00$ (liquid). Left axis indicates value of the $g(r)$ and right axis does that of the $g'(r)$.

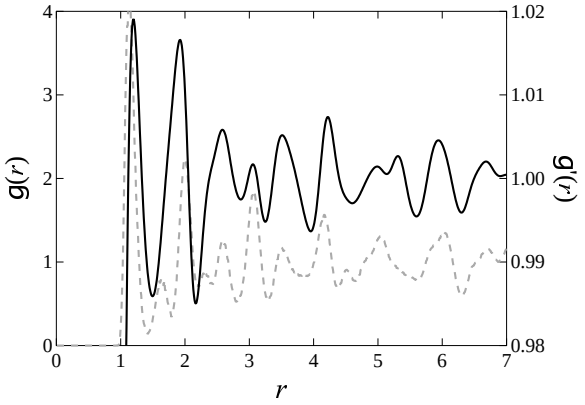

Figure 3.5: The result of $g(r)$ (dashed gray line) and $g'(r)$ (solid line) for one-component Lennard-Jones system in T=0.4000 (crystal). Left axis indicates value of the $g(r)$ and right axis does that of the $g'(r)$.

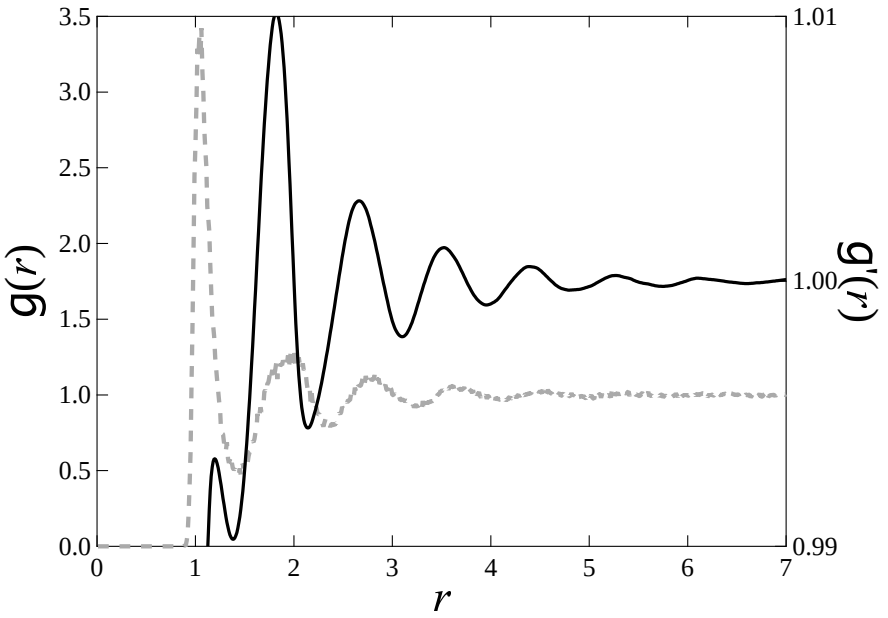

Figure 3.6: The result of $g(r)$ (dashed gray line) of A-A and $g'(r)$ (black line) of A-A for binary-mixture Lennard-Jones system at $T = 1.00$. Left axis indicates value of $g(r)$ and right axis that of $g'(r)$.

in $T = 1.00$ and 0.4000, respectively. The distances at which the radial distribution functions have peaks are different a little between $g(r)$ and $g'(r)$. The second peak is distinguished in crowded systems.

We next investigate $g'(r)$ for Lennard-Jones binary mixtures. Figure 3.6 shows the results

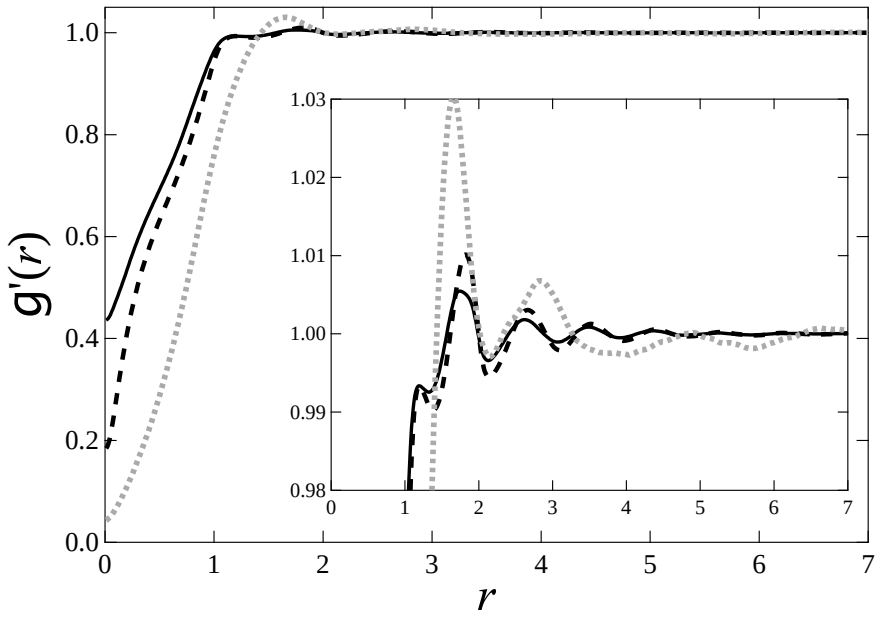

Figure 3.7: The results of $g'(r)$ of both (A+B) (solid line), only A (dashed line), and only B particle (dotted gray line) at $T = 1.00$. Inner panel is closeup.

of $g(r)$ and $g'(r)$ for $T = 1.00$ (liquid). As well as the one-component results, the peak distance of $g'(r)$ is a little different from that of $g(r)$ and the second peak is emphasized due to the size effect.

Figure 3.7 exhibits the results of $g'(r)$ of both (A+B), only A, and only B particle for $T = 1.00$. Although the $g'(r)$s of both (A and B) and only A particle have the small first peak, that of only B particle is taller than the others. The $g'(r)$ is not zero in the limit of $r \to 0$. Since $\sin x/x \to 1$ ($x \to 0$), we obtain

$$\begin{aligned} g'(0) &= \lim_{r\to 0} g'(r) \\ &= \frac{1}{2\pi^2\bar{n}^2 V}\sum_{i=1}^{N}\sum_{j(\neq 1)}^{N}\frac{1}{a_i a_j X_{ij}}\int_0^\infty \mathrm{d}k \frac{\sin ka_i \sin ka_j \sin kX_{ij}}{k} \\ &= \frac{1}{8\pi^2\bar{n}^2 V}\sum_{i=1}^{N}\sum_{j(\neq 1)}^{N}\frac{1}{a_i a_j X_{ij}}\left[I(-,+) - I(-,-) - I(+,+) + I(+,-)\right], \end{aligned} \tag{3.36}$$

where

$$I(\pm,\pm) := \int_0^\infty \mathrm{d}k \frac{\sin k(a_i \pm a_j \pm X_{ij})}{k} \quad \text{(double-sign corresponds)}. \tag{3.37}$$

Let us consider $I(\pm,\pm)$ individually. If $X_{ij} = a_j - a_i$, then $I(-,+) = 0$. Else if $X_{ij} > a_j - a_i$, then $I(-.+) = \pi/2$. Otherwise, $I(-,+) = -\pi/2$. Similarly, if $X_{ij} = a_i - a_j$, then $I(-,-) = 0$. Else if $X_{ij} > a_i - a_j$, then $I(-.-) = -\pi/2$. Otherwise, $I(-,-) = \pi/2$. However, it makes no sense at all that $X_{ij} \leq |a_i - a_j|$ because of the excluded volume effect. Therefore, we expect that $I(-,+) - I(-,-) = \pi$. Moreover, since $X_{ij} + a_i + a_j > 0$, it is concluded that $I(-,+) - I(-,-) - I(+,+) = \pi/2$. On the other hand, $I(+,-)$ requires extra attention. $I(+,-)$ is represented by

$$I(+,-) = \begin{cases} \pi/2 & (X_{ij} < a_i + a_j \Leftrightarrow \text{overlap}) \\ 0 & (X_{ij} = a_i + a_j \Leftrightarrow \text{contact}) \\ -\pi/2 & (X_{ij} > a_i + a_j \Leftrightarrow \text{no overlap}) \end{cases} . \tag{3.38}$$

Therefore, we can obtain the following relation

$$\lim_{r\to 0} g'(r) \begin{cases} > 0 & (\text{there are some overlap or contact.}) \\ = 0 & (\text{there are no overlap nor contact.}) \end{cases} . \tag{3.39}$$

In other words, the $g'(r)$ in the limit of $r \to 0$ indicates an index how many particles lap over or contact with other particles. In the hard-sphere system, it is predicted that the $g'(r)$ in the limit of $r \to 0$ is always zero because the hard-sphere particles never lap over and rarely contact with other particles.

Figure 3.8 shows the results of $g(r)$ and $g'(r)$ of A-A at $T = 0.455$ (supercooled liquid). Figure 3.8 is similar to those at $T = 1.00$. The ratio of the height of the first and second peak for $T = 0.455$ is less than that of $T = 1.00$. The temperature dependence of the ratio of the height of the first and second peak is interesting, but it is unclear what the ratio means. It is striking that there are no splits of the second peak in the $g'(r)$ of only A particle. The split might be hidden due to the size effect.

Figure 3.9 exhibits the results of $g'(r)$ of both (A+B), only A, and only B particle for $T = 0.455$. The behavior of the result of only B particle is very attractive; a split of the second

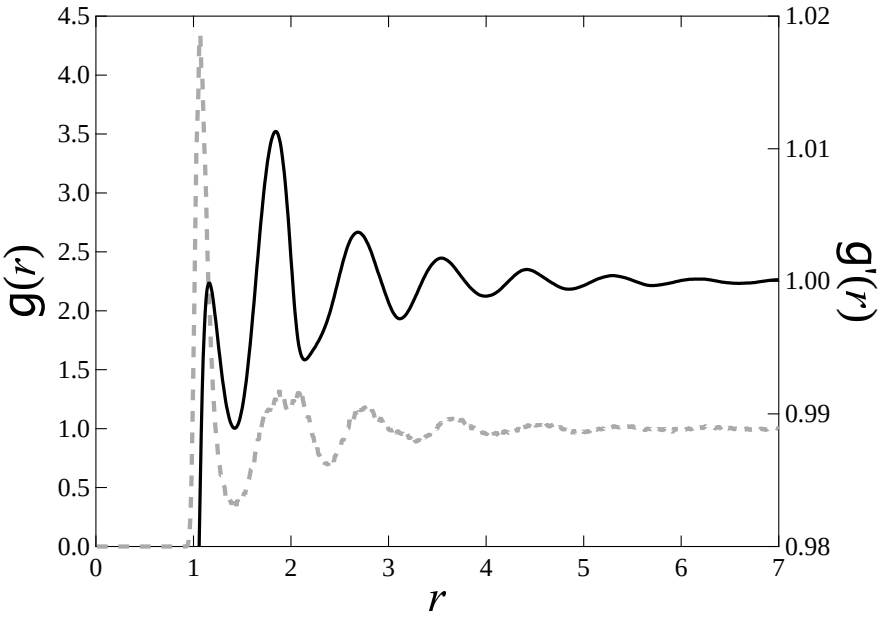

Figure 3.8: The result of $g(r)$ (dashed gray line) of A-A and $g'(r)$ (black line) of A-A for binary-mixture Lennard-Jones system at $T = 0.455$. Left axis indicates value of $g(r)$ and right axis that of $g'(r)$.

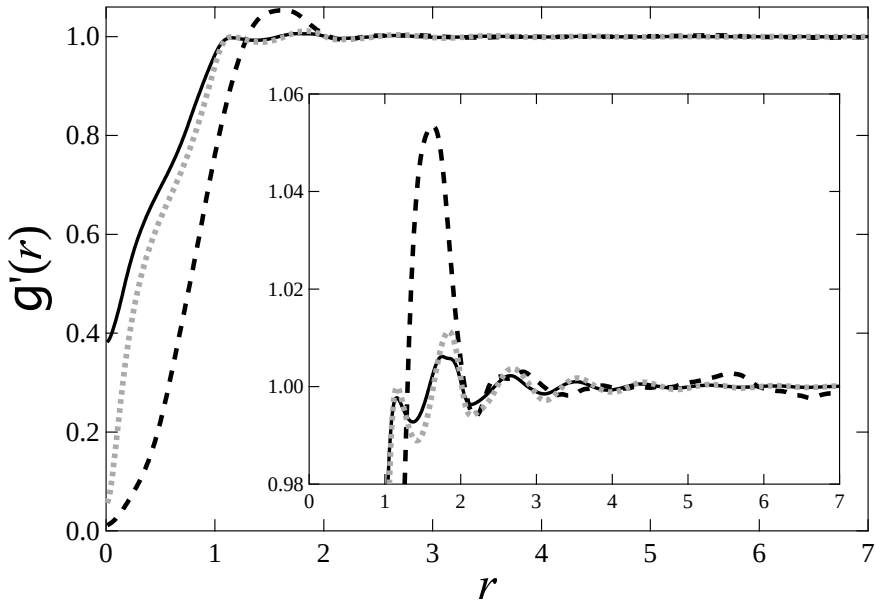

Figure 3.9: The results of $g'(r)$ of both (A+B) (solid line), only A (dashed line), and only B particle (dotted gray line) at $T = 0.455$. Inner panel is closeup.

peak of $g'(r)$ sharply appears at the third peak of $g'(r)$ for both or only A particles.

Figure 3.10 shows a result of $g(r)$ and $g'(r)$ of A-A at $T = 0.333$ (glass). The ratio of the height of the first and second peak for $T = 0.333$ looks smaller than that for $T = 0.455$. As

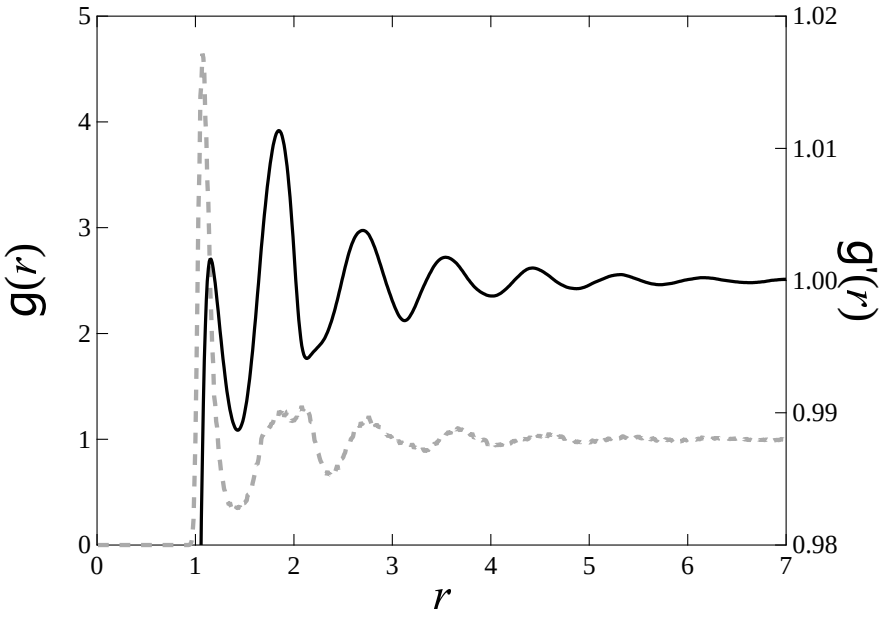

Figure 3.10: The result of $g(r)$ (dashed gray line) of A-A and $g'(r)$ (black line) of A-A for binary-mixture Lennard-Jones system at $T = 0.333$. Left axis indicates value of $g(r)$ and right axis that of $g'(r)$.

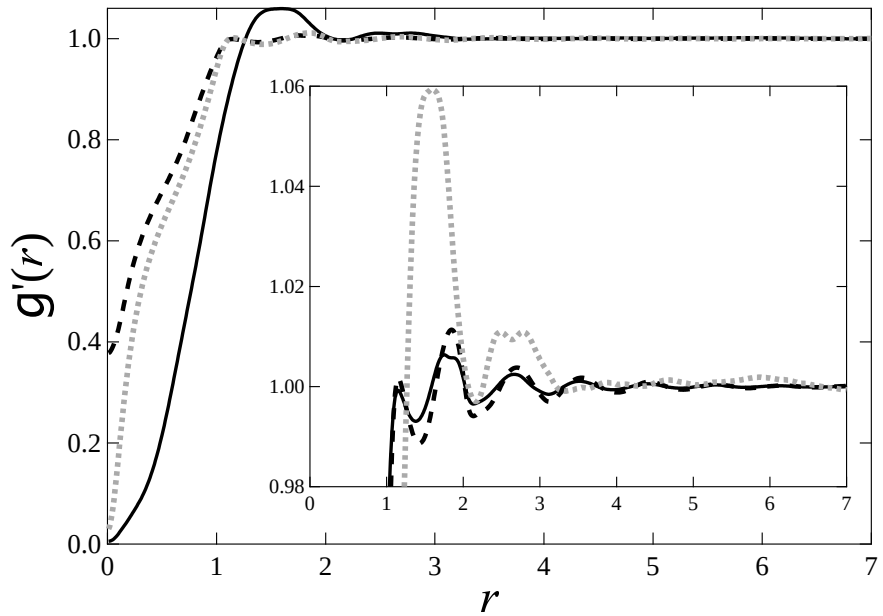

Figure 3.11: The results of $g'(r)$ of both (A+B) (solid line), only A (dashed line), and only B particle (dotted gray line) at $T = 0.333$. Inner panel is closeup.

well as the above results, the split of the second peak disappears in the result of only A particle, while we can see the split in the result of both (A and B) particle. In addition, fig. 3.11 exhibits

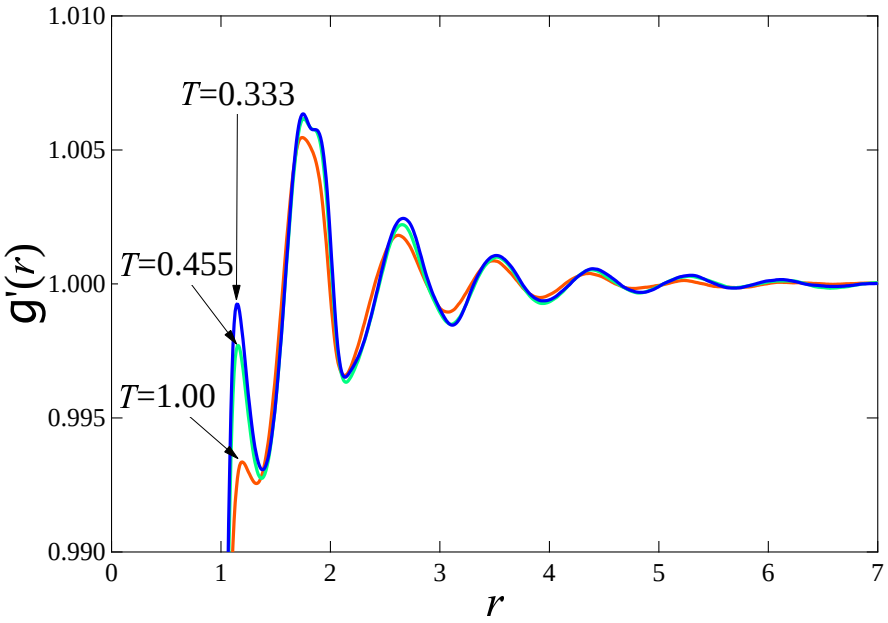

Figure 3.12: The results of the $g'(r)$ of both (A and B) particle for $T = 1.00$, 0.455, and 0.333.

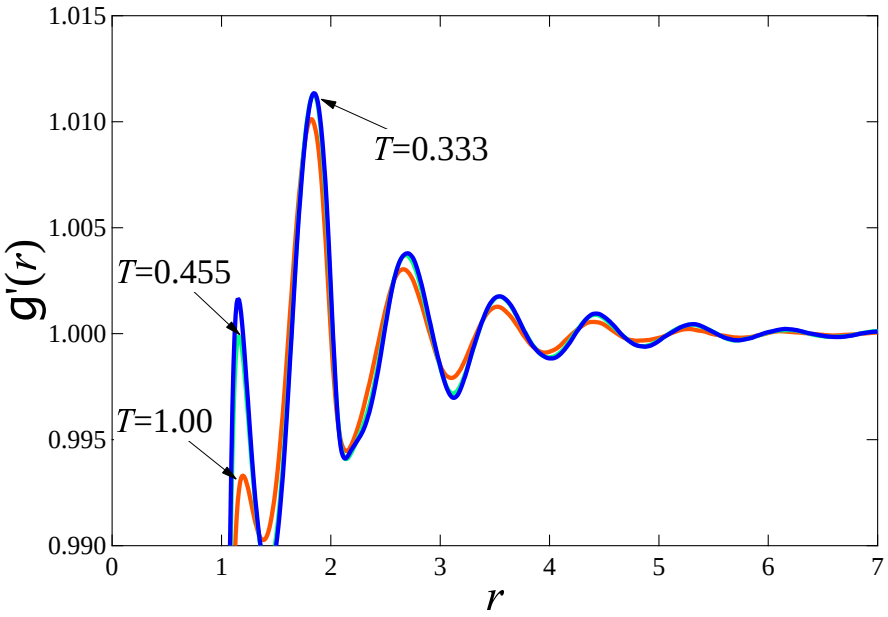

Figure 3.13: The results of the $g'(r)$ of A-A at $T = 1.00$, 0.455, and 0.333.

the results of $g'(r)$ of both (A and B), only A, and only B particle for $T = 0.333$. The tendency of the results for $T = 0.333$ (glass) is similar to that for $T = 0.455$ (supercooled liquid).

Figures 3.12, 3.13 and 3.14 show the results of the $g'(r)$ of total particles, only A, and only B, respectively. Each figure shows the results for T=1.00, 0.455, and 0.333. The result of B-B

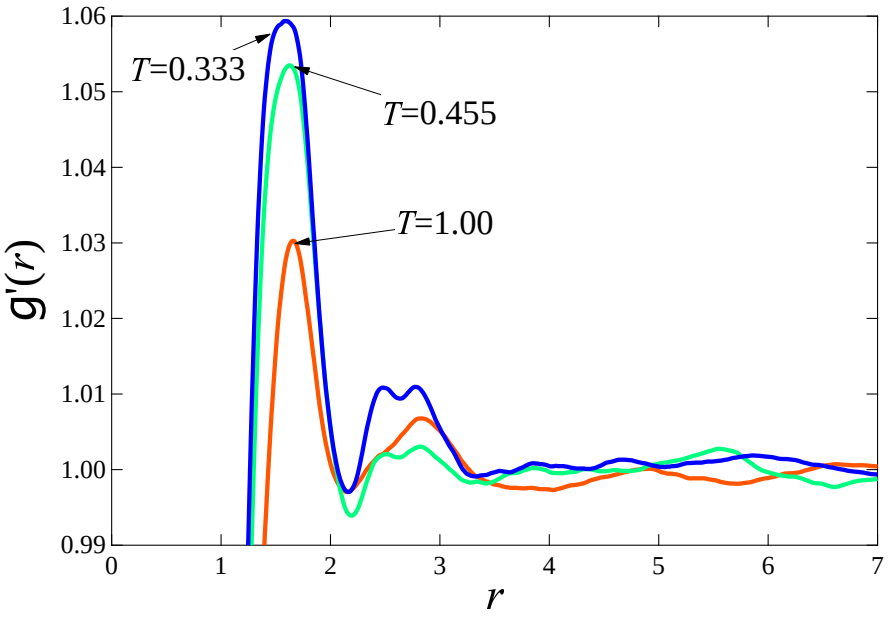

Figure 3.14: The results of the $g'(r)$ of B-B at $T = 1.00$, 0.455, and 0.333.

is characteristic.

3.3.3 Dynamic spatial correlation functions

We pay attention to the spatial correlation in the correlation functions, and then we fix the time lag Δt. Our purpose is to characterize the range of the correlation that relates with the dynamical heterogeneity. Thus, we should choose the time lag Δt corresponding to the dynamical heterogeneity. One of such time scales is τ_{NGP} at which the non-Gaussian parameter is maximum. In fact, particles escape from surrounding cage made by other neighbor particles in scale of τ_{NGP}, thus it is considered that the dynamical heterogeneity occurs in the time scale.

Figure 3.15 shows the temperature dependence of τ_{NGP} which is extracted from the non-Gaussian parameter for only A particle. τ_{NGP} rapidly increases as the temperature decreases. As shown in fig. 3.15, τ_{NGP} (i.e. the non-Gaussian parameter) is so sensitive, but the correlation functions are not so sensitive as τ_{NGP}.

Figures 3.16 and 3.17 show the results of the vector and scalar correlation functions, respec-

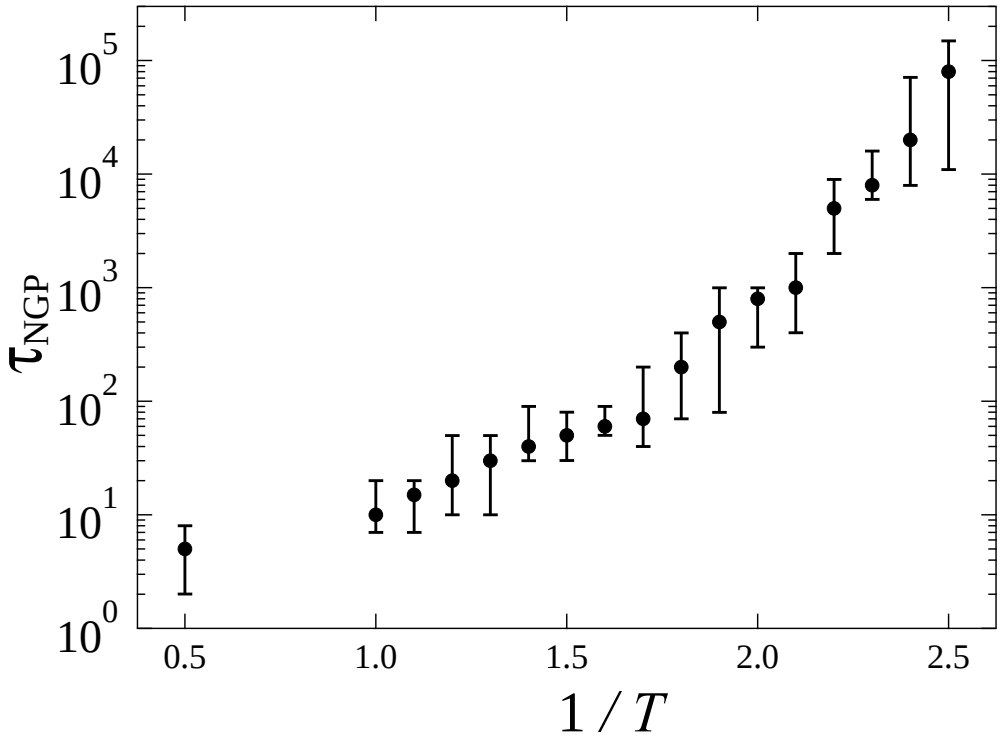

Figure 3.15: Semi–log plot of τ_{NGP} of A particle as a function of the inverse temperature. The circles represent the time we have employed to calculate the spatial correlation functions.

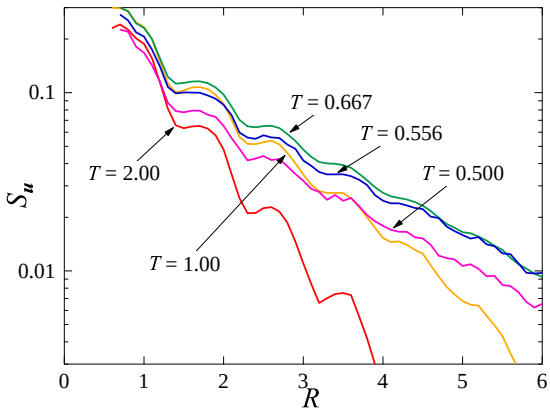

Figure 3.16: Semi–log plot of the vector correlation function versus the distance R. Red line indicates the result at $T = 2.00$, orange one at $T = 1.00$, green one at $T = 0.667$, blue one at $T = 0.556$, and purple one at $T = 0.500$.

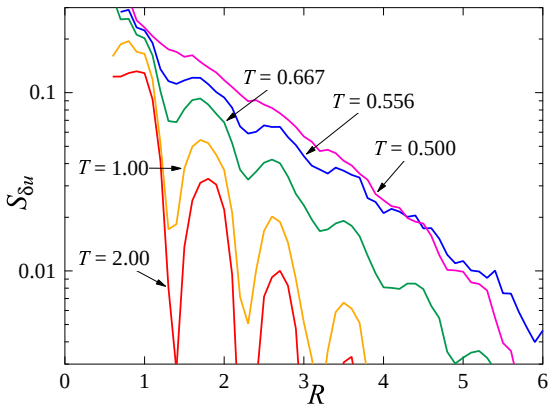

Figure 3.17: Semi–log plot of the scalar correlation function versus the distance R. Red line indicates the result at $T = 2.00$, orange one at $T = 1.00$, green one at $T = 0.667$, blue one at $T = 0.556$, and purple one at $T = 0.500$.

tively, for several temperatures. Those results oscillate, and the scalar correlation is influenced more than the vector correlation. The distance at which the dips appear corresponds to that

of the local minimum of the radial distribution function $g(r)$. Since $g(r)$ represents the ratio between the mean and local number density at the distance, the scalar correlation is more sensitive to existence of the particles than the vector correlation. This tendency is different from an experimental result of the colloidal mixtures [43]. It might be the influence of solvent. For example, we consider a couple of test particles. In case the distance of the two particles is r_{max} at which $g(r)$ has the first peak, there are a few particles in the range of r_{max} around the test particles. Since the test particles can go straight without interaction from the other particles in short time regime, the scalar correlation is high in molecular dynamics simulations. Although, in case the distance of the couple of test particles is r_{min} at which $g(r)$ has the first dip, it is highly possible that there are some particles in the range of r_{max} around the test particles. The test particle is interacted from the neighbor particles, so that the scalar correlation is low. On the other hand, the particles diffuse in colloidal experiments even in short time regime because of solvent. Thus, the scalar correlation in colloidal experiments is not so sensitive as in molecular dynamics simulations.

The amplitude of the correlation functions in high temperature is higher than in low temperature. This trend is also seen in colloidal mixture: The amplitude in the low volume fraction is higher than in the high volume fraction [43]. One of the reasons is the duration Δt. As mentioned above, the time duration Δt is τ_{NGP} and the time scale increases as the temperature decreases. No cage effects are represented in high temperature, and thus the correlation functions more strongly depend on the initial (i.e. $t = t_0$) spatial structure.

Although the strength of the scalar correlation is higher as the temperature decreases, that of the vector correlation does not show simple increment for change in temperature. In fact, the result of the vector correlation at $T = 0.667$ is the strongest in figure 3.16, and the results at T =0.556 and 0.500 are less strong. It suggests that the vector correlation is less to do with

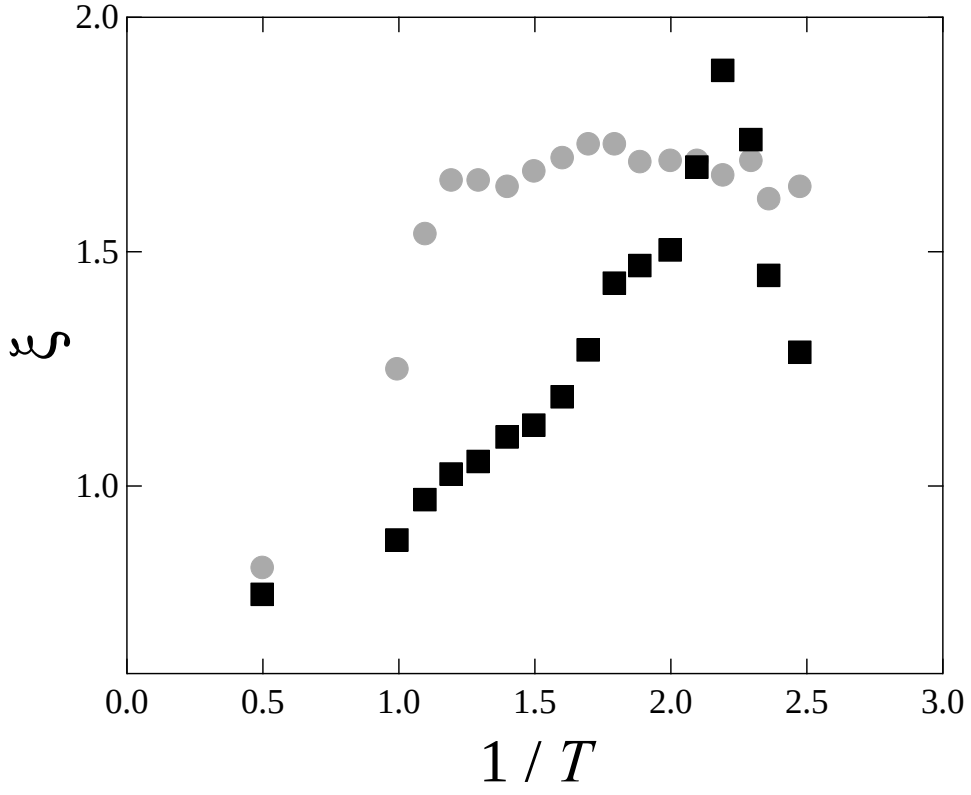

Figure 3.18: The each correlation length versus the inverse temperature. The circles represents the correlation length from the vector correlation, the gray squares that from the scalar correlation.

mechanisms of the glass transition.

We next discuss a length scale that relates with the correlation functions. As shown in figures 3.16 and 3.17, the dynamic spatial correlation functions are almost linear in the semi–log plot. It indicates that one can fit the results in an exponential function [43, 52] given by

$$S(R, \tau_{\mathrm{NGP}}) \simeq A(\tau_{\mathrm{NGP}}) \exp\left[-\frac{R}{\xi(\tau_{\mathrm{NGP}})}\right], \tag{3.40}$$

where S denotes the vector or scalar correlation, $A(\tau_{\mathrm{NGP}})$ a constant that is independent on R, and $\xi(\tau_{\mathrm{NGP}})$ the correlation length.

Figure 3.18 shows the results of the correlation lengths from the vector and scalar correlations. We have used the each peak value in the correlation function to fit the data in eq. (3.40). The first peak is, however, neglected because there are few particles in the region of the short

distance, and then the spatial correlation is strongly influenced from the fluctuation of the local number density [52].

As the temperature decreases, the correlation length from the vector correlation increases and converges to $\xi_{\boldsymbol{u}} \sim 1.7\sigma$ in low temperature. On the other hand, the length from the scalar correlation increases and has a maximum near the glass transition. It also indicates that mobility fluctuation relates the glass transition more than the displacement.

The scalar correlation increases, but the maximum value is $\xi_{\delta u} \sim 1.9\sigma$. If those correlation length corresponds to the region of the cooperative motion, the region contains only several particles. Furthermore, the maximum value is shorter than the result of one–component colloidal mixtures [43]. Our results imply that the dynamical heterogeneity is less. This suggestion agrees with the statement that polydispersity provides less dynamical heterogeneity [68, 76].

The results show that the scalar correlation is more significant than the vector correlation near the glass transition. Furthermore, we have predicted the correlation lengths from the correlation functions. The length from the vector correlation increases as temperature decreases in high temperature region, but converges far away from the glass transition point. On the other hand, that from the scalar correlation increases toward the glass transition point, and has a maximum near the glass transition. It also indicates that the scalar correlation plays an important role near the glass transition.

Unfortunately, it is unclear why the correlation length from the scalar correlation has a maximum near the glass transition. In order to understand it, one may propose a simple model. On the other hand, we can use the present results as a starting point to understand mechanisms of the glass transition.

Recently, Kawasaki et al. have suggested that the dynamical heterogeneity relates with the partially crystal–like structure [68]. As mentioned in their paper, it is possible that the crys-

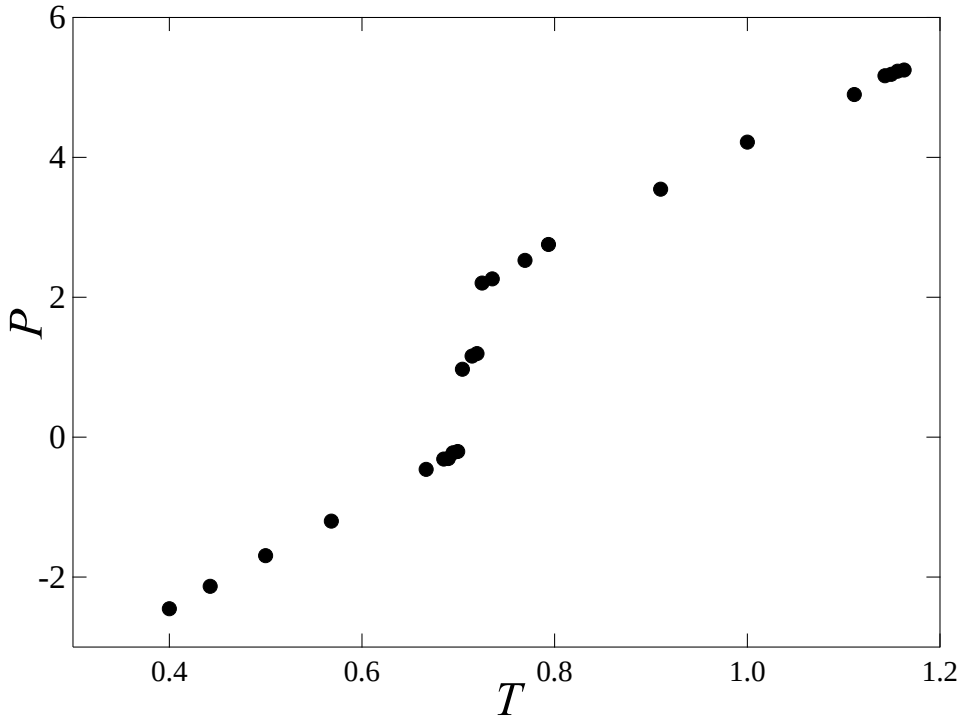

Figure 3.19: Plot of the temperature dependence of the pressure. The circles represent the simulation results for one–component Lennard-Jones fluids.

talline order is the origin of the glass transition. This idea is natural because the systems have to avoid crystallization to get glassy states. On the other hand, the coexistence state between liquid and crystal has a similar situation. One might not be able to distinguish a snapshot of supercooled states near the glass transition from that of coexistence states. We discuss the dynamical heterogeneity by measuring two types of spatial–temporal correlation functions in one–component Lennard–Jones fluids, which are obtained by performing the molecular dynamics simulations. An equilibrium supercooled liquid does not exist in single–component systems because the systems are easy to crystallize. We especially focus on the correlations in liquids and coexistence states. Furthermore, we compare the results of single–component systems to those of binary–mixtures [69].

We first discuss the pressure to characterize the first phase transition. Figure 3.19 shows the temperature dependence of the pressure. The results are time–averaged. As the temperature

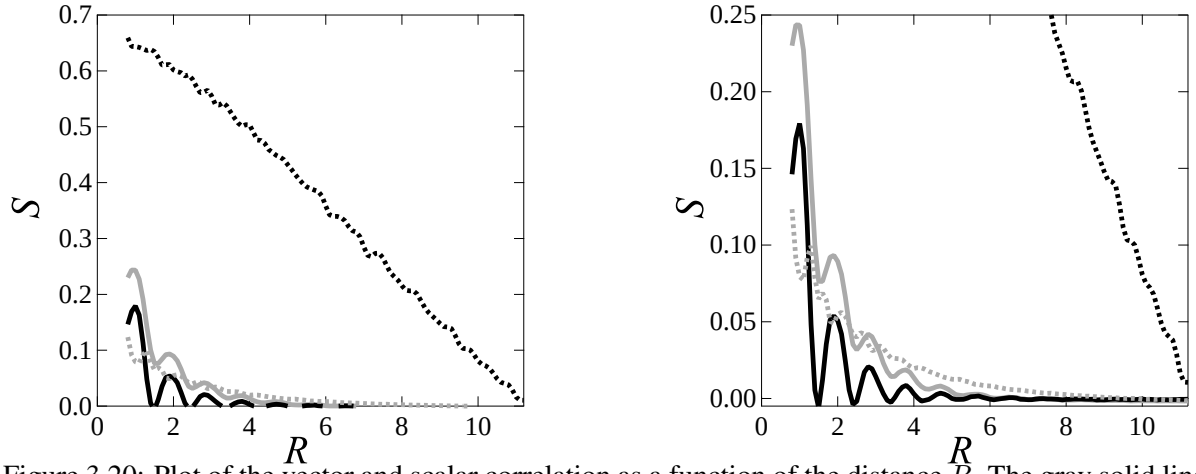

Figure 3.20: Plot of the vector and scalar correlation as a function of the distance R. The gray solid line indicates the vector correlation of liquid states at $T = 0.735$, the gray dotted one that of coexistence state at $T = 0.714$, the black solid one the scalar correlation of liquids at $T = 0.735$, and the black dashed line that of coexistence state at $T = 0.714$. The time lags (i.e. peak time of the non-Gaussian parameter) are approximately $\tau_{\rm NGP} = 10\tau_{\rm LJ}$ and $500\tau_{\rm LJ}$ at T =0.735 and 0.714, respectively. The right plot is a closeup figure of the left one.

decreases, the pressure decreases monotonically. The pressure jump is seen at some temperature at which crystallization occurs. The freezing point is $T_{\rm f} \sim 0.724$ and the melting point $T_{\rm m} \sim 0.699$. According to the results of the radial distribution function, the long range order appears at the temperatures lower than the melting point while it does not at the temperatures higher than the freezing point. Since the results between the freezing and the melting temperature are in intermediate value of the pressure jump, they are thought to be coexistence states between liquids and crystals. Note that it does not matter that the pressure in crystals is negative because the system size is fixed.

The two types of dynamic spatial correlation functions are next discussed. The time lag Δt must be fixed so as to pay attention to the dynamical spatial correlation in the correlation functions, and then it is chosen by a time scale corresponding to the dynamical heterogeneity. One of such time scales is a time scale $\tau_{\rm NGP}$ as well as the binary mixture cases. Figure 3.20 shows the vector and scalar correlation functions. Those results are averaged over 100 samples. We do not show the results of the spatial correlations in crystals because $\tau_{\rm NGP}$ cannot be defined

in crystals.

The both correlations in liquids converge to zero at a long distance. The correlations in liquids rapidly converge more than those in coexistence states. This corresponds to the fact that liquids do not have long–range order. The vector correlation functions in coexistence states converges as well. However, we do not know whether the scalar correlation function in coexistence state converges to zero or not. The result in fig. 3.20 decreases toward zero as the distance is larger, but there is possibility that the decrease is influenced by the periodical boundary condition. We cannot obtain the spatial correlation in longer distance than the half of the system size at the most.

The vector correlation in coexistence states is smaller than that in liquids in short range order but it is larger in long range order. It indicates that the vector correlation in crystals is smaller than that in liquids but has a long range correlation. Liquids can be rearranged but crystals move independently, so that the vector correlation in crystals is smaller than that in liquids. Moreover, the vector correlation in liquids has short–range order because the rearrangement occurs only in neighbor particles. On the other hand, the scalar correlation in coexistence states is extremely higher than that in liquids. It indicates that the correlation of the mobility fluctuation plays an important role in the coexistence state.

We now fit the results obtained above by an exponential function eq. (3.40). We can compare each correlation function in different states (i.e. liquid and coexistence state) but cannot do in different correlation functions (i.e. the vector and scalar correlation) in the same state. Nevertheless, we can compare different correlation functions by using the correlation lengths.

Figure 3.21 shows the temperature dependence of the correlation length from both the vector and scalar correlations. In fitting the data by eq. (3.40), we have used each peak positions of the spatial correlation.

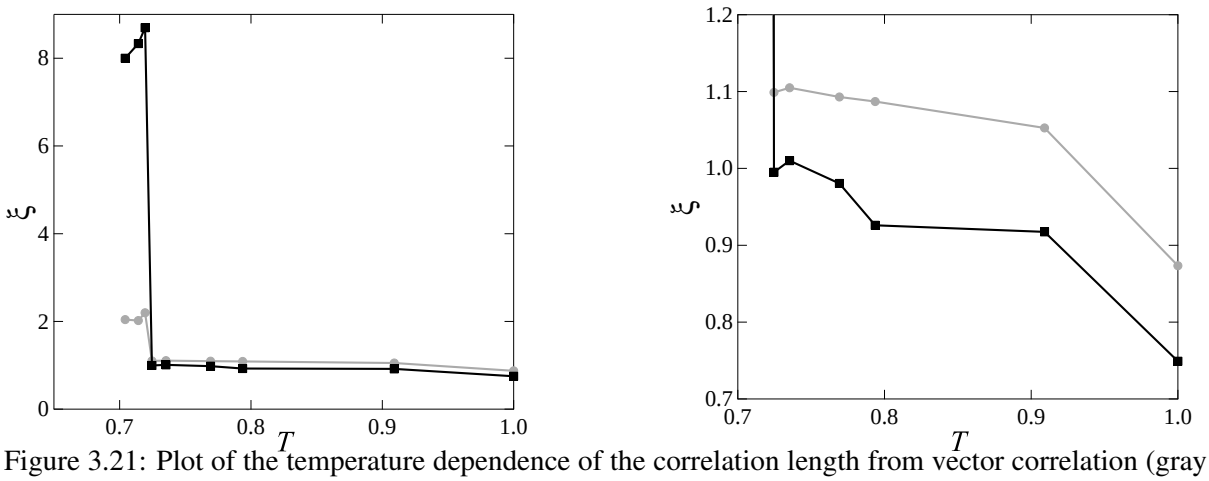

Figure 3.21: Plot of the temperature dependence of the correlation length from vector correlation (gray circles) and that from scalar correlation (squares) for one–component Lennard–Jones fluids. The right plot is a closeup figure of the left one.

The correlation length from the vector correlation is slightly longer than that from the scalar one in higher temperature than the freezing point. At the freezing point, the both correlation lengths suddenly increase. Especially, the length from the scalar correlation has large value. Considering again that we employ the periodical boundary condition, we can trust the data in the distance less than about 10 σ because the edge might be influenced by the boundary condition. Therefore, the correlation length from the scalar correlation might be larger if the system in simulations is bigger. On the other hand, the length from the vector correlation is not influenced by the boundary condition because the length of the coexistence states is about 2.0σ.

The correlation lengths are measured in Lennard–Jones binary mixtures for Kob–Andersen type. Figure 3.22 shows the correlation lengths in Lennard–Jones binary mixtures as a function of the temperature. In the binary mixtures, the length from the vector correlation converges as the temperature decreases. On the other hand, that from the scalar correlation increases toward the glass transition point $T_g \simeq 0.43$. No divergence of the correlation length appears even in vicinity of the glass transition point as well as experiments [43, 76]. This finiteness has originated as the frozen spatial configuration. In high temperature region (e.g. near the

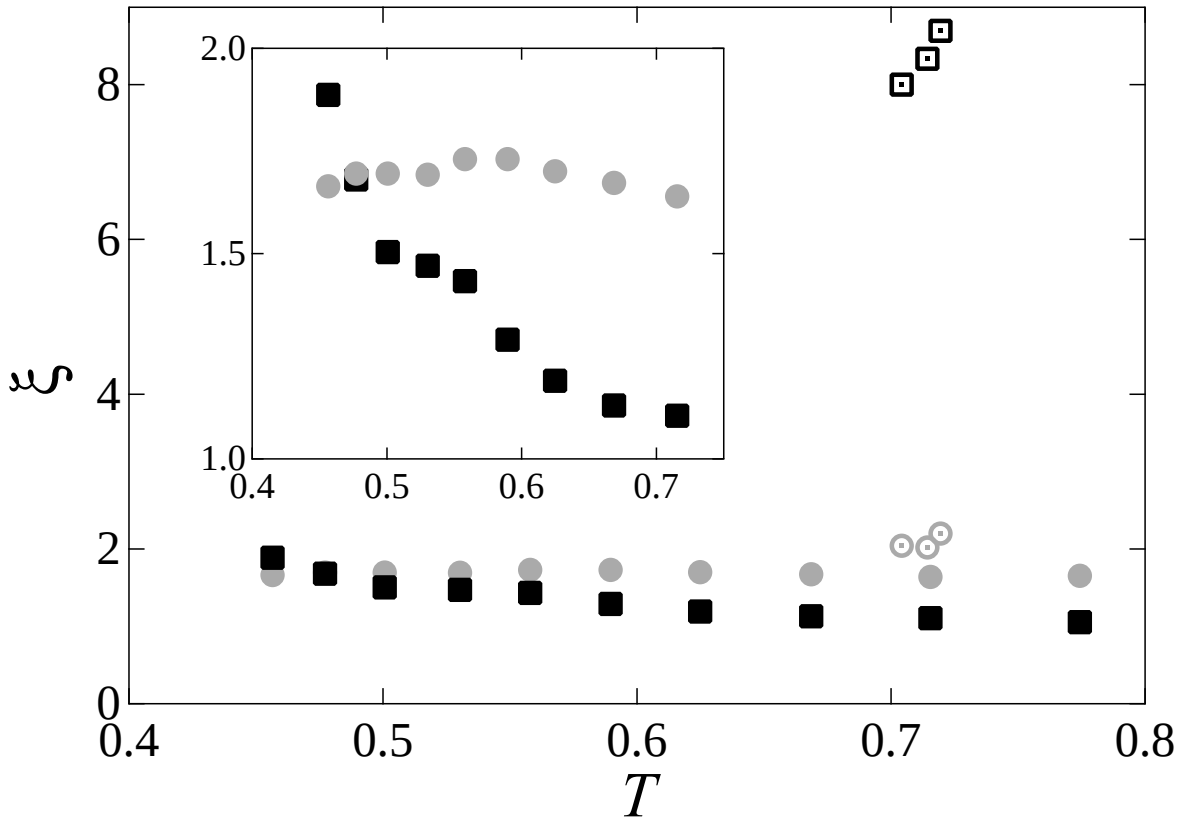

Figure 3.22: Plot of the correlation length from the vector correlation (gray circles) and that from the scalar correlation (squares) for one–component Lennard–Jones fluids (open symbols) and Lennard–Jones binary mixtures (closed symbols). The inner plot is drawn in different scale.

melting point), the increase of the correlation length causes ordering. However, it is inhibited because it takes long time for configuration to rearrange in low temperature region. It products some domains in which correlation times are different and leads to the dynamical heterogeneity. Note that it is possible that the correlation length we have measured does not reflect the glass transition perfectly. Thus, the maximum value of the length might not be significant, but it is important that the correlation length does not diverge even near the glass transition point.

Comparing the length of coexistence states for single–component Lennard–Jones fluids to that of supercooled liquids near the glass transition for Lennard–Jones binary mixtures, the length from the vector correlation of coexistence states is similar to that of supercooled liquids for Lennard–Jones binary mixtures. The results are different from each other but it might

be because of the difference in the number density ($N/V = 0.902\sigma^{-3}$ for single–component systems and $N/V = 1.20{\sigma_{AA}}^{-3}$ for binary–mixtures). However, the lengths from the scalar correlation do not resemble each other. That of supercooled liquids is $2.0\sigma_{AA}$ at the most, where σ_{AA} denotes a parameter of binary Lennard–Jones potential and corresponds to σ in the ordinary Lennard–Jones potential. It implies that the supercooled liquids and glasses have similar configuration in coexistence states but the dynamics is quite different.

3.4 Conclusion

We have carried out molecular dynamics simulations for the Kob-Andersen binary mixtures. The specific heat at constant volume and the long-time self-diffusion coefficient have been investigated. When we regard the long-time self-diffusion coefficient as an universal parameter, the glass transition coefficient is $D_g = 9.16 \times 10^{-6}$ from the mean-field theory. In the Kob-Andersen model, D_g corresponds to $T = 0.43$ which is in agreement with the glass transition temperature obtained from the specific heat at constant volume. The glass transition is regarded as the dynamical crossover, and thus the glass transition should be characterized by dynamical property. In the view point, the definition by the long-time self-diffusion coefficient is reasonable. However, we revealed that the specific heat, which is obtained from not dynamical but static information, relates with the dynamics near the glass transitions. It is consistent in view of the dynamical heterogeneity.

We have proposed the radial distribution function including size effect, $g'(r)$. This function emphasizes on structure around the intermediate length order (i.e. the second peak of the radial distribution function). In addition, it can estimate how particles lap over other particles.

As well as the experiments for the binary colloidal mixtures, we have calculated the dynamical spatial correlation functions for the Kob-Andersen binary mixtures. Furthermore, we have

predicted the correlation lengths from the correlation functions. The length from the vector correlation increases as temperature decreases in high temperature region, but converges far away from the glass transition point. On the other hand, that from the scalar correlation increases toward the glass transition point, and has a maximum near the glass transition. It indicates that the scalar correlation plays a more important role than the vector one near the glass transition. The maximum length of the correlation of the mobility fluctuation is $\xi \sim 1.9\sigma_{\mathrm{AA}}$.

We also calculated the dynamical spatial correlation functions for the one-component Lennard-Jones systems. Both scalar and vector correlation functions in coexistence states between liquid and crystal are different from those of liquids. The scalar correlation in coexistence states is extremely larger than that in liquids, so that it might be significant for study of the crystal growth to investigate the relationship between the mobility fluctuation and the coexistence states. Moreover, we have predicted the correlation length of the both correlation functions. The both correlation lengths jump at the freezing point. The width of jump is larger in the scalar correlation length than the vector correlation length. It is suggested by considering the influence of the periodical boundary conditions that the scalar correlation length diverges at the transition temperature. Finally, we have compared the results for one-component systems to those for Lennard-Jones binary mixtures. The comparison suggests that the dynamics of supercooled liquids is different from that of coexistence states, while their configuration resembles each other.

Chapter 4

Temporal Correlation Function in Numerical Calculations

The temporal correlation functions have been measured in molecular dynamics simulations and calculated in the mode-coupling theory. First of all, general remarks of the mode-coupling theory is introduced. After the explanation of the model in our molecular dynamics simulations and details of numerical calculations for the mode-coupling theory, the simulation and numerical results is shown and compared in standpoint of the mean-field theory.

4.1 Mode-Coupling Theory

> Mode coupling theory is the *worst* theory of colloidal glasses - apart from all the others that have been tried from time to time. – M. E. Cates [77]

4.1.1 What is "Mode-Coupling"?

We first consider the one-dimensional heat equation as a simple linear differential equation;

$$\partial_t f = \kappa \partial_x^2 f \tag{4.1}$$

with appropriate boundary condition, where $f = f(x,t)$ denotes the heat quantity at position x and time t; and κ the thermal conductivity. Note that it is assumed that the thermal conductivity is constant everywhere.

One of useful methods to obtain solutions is the way of Fourier series. A periodical function in which the cycle is $2L$ can be expanded to Fourier series;

$$f(x,t) = \sum_{n=-\infty}^{\infty} c_n(t) \exp\left[i\frac{n\pi}{L}x\right], \tag{4.2}$$

where $c_n(t)$ (for $n = ..., -2, -1, 0, 1, 2, ...$) are time-dependent series coefficients. The integer n corresponds to each wave and is called mode of wave. Substituting the Fourier series into eq. (4.1), we can obtain

$$\sum_{n=-\infty}^{\infty} \dot{c}_n(t) \exp\left[i\frac{n\pi}{L}x\right] = -\kappa \sum_{n=-\infty}^{\infty} \left(\frac{\pi n}{L}\right)^2 c_n(t) \exp\left[i\frac{n\pi}{L}x\right]. \tag{4.3}$$

Because of orthogonality of trigonometrical functions, we can obtain

$$\frac{\mathrm{d}c_n(t)}{\mathrm{d}t} = -\kappa \left(\frac{\pi n}{L}\right)^2 c_n(t) \tag{4.4}$$

for arbitrary integer n. We can show that any linear differential equation as well as the heat equation can reduce to mode-independent differential equations. It implies that the mode-coupling is one of representation for the nonlinearity. The mode is defined by one of waves in the above example. However, the concept of "mode" is generalized and means not only waves but also physical variables.

4.1.2 MCT for critical phenomena

MCT is originally a theory for critical phenomena [25] proposed by Kawasaki [24]. In the linear response theory, a transport coefficient L is represented by using the corresponding fluctuation $J(t)$ of the generalized flux, such as the velocity, the heat flux and so on, as

$$L = \frac{1}{V}\int_0^{\infty} \mathrm{d}t \left\langle J(t)J(0)\right\rangle, \tag{4.5}$$

where V denotes the volume of system. The representation for L is meaningful only when convergence of the integrand is fast enough for the integral to converge to zero quickly. If $J(t)$

holds

$$\langle J(t)A(t)\rangle = \langle JA\rangle = 0, \tag{4.6}$$

the integral converge safely because the above relationship implies that the flux is a fast variable in comparison with $A(t)$. It should be noted here that the above equation holds for linear A, so that $\langle Jf(A)\rangle \neq 0$, in general, where $f(A)$ denotes a function of A.

4.1.3 Generalized Langevin Equation

We start from the Newton equation. We can derive the canonical equations

$$\frac{\partial \boldsymbol{q}}{\partial t} = \frac{\partial \mathcal{H}}{\partial \boldsymbol{p}} \quad , \quad \frac{\partial \boldsymbol{p}}{\partial t} = -\frac{\partial \mathcal{H}}{\partial \boldsymbol{q}}, \tag{4.7}$$

where $\mathcal{H}$ denotes the Hamiltonian, $\boldsymbol{q}$ the generalized position, and $\boldsymbol{p}$ the generalized momentum. The equation of motion for physical variables $\boldsymbol{A}(t) = \boldsymbol{A}(\boldsymbol{q}(t), \boldsymbol{p}(t)) = \boldsymbol{A}(\boldsymbol{q}, \boldsymbol{p}; t)$ is therefore described by

$$\dot{\boldsymbol{A}}(t) = [\mathcal{H}, \boldsymbol{A}(t)] =: i\mathcal{L}\boldsymbol{A}(t), \tag{4.8}$$

where the solid bracket denotes the Poisson bracket, $i\mathcal{L}$ the Liouville operator. Note that the above solid bracket denotes the commutator in quantum cases. The above equation is called the Heisenberg equation which is equivalent to the Newton or Shrödinger equation.

We can derive the linear equation of motion for $A(t)$ from the Heisenberg equation. One of the most useful ways to derive it is the method of the projection-operator technics [38]. Using the Mori identity, we can derive the generalized Langevin equation as

$$\dot{\boldsymbol{A}} = i\omega \cdot \boldsymbol{A} - \int_0^t \mathrm{d}s \varphi(t-s) \cdot \boldsymbol{A}(s) + \boldsymbol{R}(t), \tag{4.9}$$

where $i\omega$ denotes the mechanical coefficient, $\varphi(t)$ the memory function, and $\boldsymbol{R}(t)$ the fluctuation term. The fluctuation-dissipation relation holds;

$$\varphi(t) = \left\langle \boldsymbol{R}(t)\boldsymbol{R}^\dagger \right\rangle \cdot \left\langle \boldsymbol{A}\boldsymbol{A}^\dagger \right\rangle^{-1}. \tag{4.10}$$

The fluctuation term includes the nonlinearity of $\boldsymbol{A}$, and thus the memory term also does. Although the fluctuation term is sometimes treated as noise, the polynomials of A are extracted from the memory term in the mode-coupling scheme. It should be noted here that the memory function connects to $\boldsymbol{A}(t)$ by convolution integral and the convolution form of eq. (4.9) is naturally derived for the one-dimensional Brownian motion with the harmonic potential (ref. [78] and appendix B.3).

The above separation method is useful, but one can consider other separation methods. Let us consider, for example, the model described by

$$\dot{x}(t) = i\omega(t)x(t). \tag{4.11}$$

We divide $\omega(t)$ into the average part $\bar{\omega}$ and the fluctuating part $\Delta\omega(t)$, where the overbar means an average. It is assumed that $\overline{\Delta\omega} = 0$, $\overline{\Delta\omega(t_0)\Delta\omega(t_0+t)} = \omega_0^2\psi(t)$, and $\overline{f(x(0))g(\Delta\omega(t))} = \overline{f(x(0))} \cdot \overline{g(\Delta\omega(t))}$ with arbitrary functions f and g. The differential equation can be solved easily to obtain

$$x(t) = x(0)\exp\left[i\bar{\omega}t + i\int_0^t \Delta\omega(\tau)\mathrm{d}\tau\right]. \tag{4.12}$$

The time correlation function is thus represented as

$$\overline{x(t)x(0)} = e^{i\bar{\omega}t}\overline{x(0)^2}\overline{\exp\left[i\int_0^t \Delta\omega(\tau)\mathrm{d}\tau\right]}. \tag{4.13}$$

Using the cumulant expansion, we can obtain

$$\overline{x(t)x(0)} = e^{i\bar{\omega}t}\overline{x(0)^2}\exp\left[-\omega_0^2\int_0^t \psi(\tau)(t-\tau)\mathrm{d}\tau\right]. \tag{4.14}$$

This representation implies that the convolutionless generalized Langevin equation exists because the time differential reduces to

$$\frac{\mathrm{d}}{\mathrm{d}t}\overline{x(t)x(0)} = i\bar{\omega}\overline{x(t)x(0)} - \omega_0^2\int_0^t \mathrm{d}\tau\psi(\tau)\overline{x(t)x(0)}. \tag{4.15}$$

The above equation corresponds to the convolutionless generalized Langevin equation

$$\frac{\mathrm{d}}{\mathrm{d}t}x(t) = i\bar{\omega}x(t) - \omega_0^2 \int_0^t \mathrm{d}\tau\psi(\tau)x(t) + R_T(t), \tag{4.16}$$

where $R_T(t)$ denotes the fluctuating term. In this case, the memory term connects to physical variables by not convolution integral but just product. This type generalized Langevin equation is called the convolutionless type proposed by Tokuyama [79]

$$\dot{\boldsymbol{A}} = i\omega \cdot \boldsymbol{A} - \int_0^t \mathrm{d}s\psi(s) \cdot \boldsymbol{A}(t) + \boldsymbol{R}_T(t), \tag{4.17}$$

where $\psi(t)$ denotes the memory function and $R_T(t)$ the fluctuation term in the convolutionless generalized Langevin equation. The above example also implies that we can separate multiplicative noises into additive noises by using the convolutionless type projection method. More details are summarized in appendix B.7.

4.1.4 Partial Intermediate Scattering Function

We employ the fluctuation of the number density and its flux as the physical variables $\boldsymbol{A}(t)$. Because our model is binary mixtures, we should consider the partial temporal correlation functions. We set $\boldsymbol{A}(t)$ as

$$\boldsymbol{A}(t) := \begin{pmatrix} \boldsymbol{\delta\rho}_q(t) \\ \boldsymbol{j}_q^L(t) \end{pmatrix} := \begin{pmatrix} \delta\rho_q^{(A)}(t) \\ \delta\rho_q^{(B)}(t) \\ j_q^{L(A)}(t) \\ j_q^{L(B)}(t) \end{pmatrix} \tag{4.18}$$

as dynamical variables, where $\delta\rho_q^{(\alpha)}(t)$ denotes the number density fluctuation of particle $\alpha \in \{A, B\}$ defined by

$$\delta\rho_q^{(\alpha)}(t) := \frac{1}{\sqrt{N_\alpha}}\sum_i^{(\alpha)} e^{i\boldsymbol{q}\cdot\boldsymbol{X}_i(t)} - \frac{\rho_\alpha}{\sqrt{N_\alpha}}(2\pi)^3\delta(\boldsymbol{q}) \tag{4.19}$$

with $\rho_\alpha = N_\alpha/V$, $j_q^{L(\alpha)}(t)$ denotes the longitudinal flux of the density of particle α defined by

$$j_q^{L(\alpha)}(t) := \frac{1}{\sqrt{N_\alpha}}\sum_i^{(\alpha)} \tilde{\boldsymbol{q}} \cdot \boldsymbol{V}_i(t) e^{i\boldsymbol{q}\cdot\boldsymbol{X}_i(t)}, \tag{4.20}$$

$\tilde{\boldsymbol{q}}$ the unit vector of $\boldsymbol{q}$, and $\sum^{(\alpha)}$ means the summation for α particle.

Using the definition (4.19) of the density fluctuation, the partial intermediate scattering functions is calculated as

$$F^{(\alpha\beta)}(q,t) = \frac{1}{\sqrt{N_\alpha N_\beta}}\sum_i^{(\alpha)}\sum_j^{(\beta)}\left\langle e^{i\boldsymbol{q}\cdot(\boldsymbol{X}_i(t)-\boldsymbol{X}_j)}\right\rangle - (2\pi)^3\frac{\sqrt{N_\alpha N_\beta}}{V}\delta(\boldsymbol{q}), \quad (4.21)$$

where $\delta(\boldsymbol{q})\delta(\boldsymbol{q}) = V(2\pi)^{-3}\delta(\boldsymbol{q})$. The partial static structure factor is

$$S^{(\alpha\beta)}(q) = \frac{1}{\sqrt{N_\alpha N_\beta}}\sum_i^{(\alpha)}\sum_j^{(\beta)}\left\langle e^{i\boldsymbol{q}\cdot(\boldsymbol{X}_i-\boldsymbol{X}_j)}\right\rangle - (2\pi)^3\frac{\sqrt{N_\alpha N_\beta}}{V}\delta(\boldsymbol{q}). \quad (4.22)$$

It reduces to

$$\begin{aligned} S^{(\alpha\beta)}(q) &= \frac{1}{\sqrt{N_\alpha N_\beta}}\iint \mathrm{d}\boldsymbol{r}\mathrm{d}\boldsymbol{r}' e^{i\boldsymbol{q}\cdot(\boldsymbol{r}-\boldsymbol{r}')}\sum_i^{(\alpha)}\sum_j^{(\beta)}\langle\delta(\boldsymbol{r}-\boldsymbol{X}_i)\delta(\boldsymbol{r}'-\boldsymbol{X}_j)\rangle \\ &\quad -(2\pi)^3\frac{\sqrt{N_\alpha N_\beta}}{V}\delta(\boldsymbol{q}). \end{aligned} \quad (4.23)$$

In case of $\alpha = \beta$, we can obtain

$$S^{(\alpha\alpha)}(q) = 1 + \frac{N_\alpha}{V}\int \mathrm{d}\boldsymbol{r} e^{i\boldsymbol{q}\cdot\boldsymbol{r}}[g^{(\alpha\alpha)}(\boldsymbol{r}) - 1], \quad (4.24)$$

where

$$\rho_\alpha\rho_\alpha g^{(\alpha\alpha)}(\boldsymbol{r}-\boldsymbol{r}') := \sum_i^{(\alpha)}\sum_{j(\neq i)}^{(\alpha)}\langle\delta(\boldsymbol{r}-\boldsymbol{X}_i)\delta(\boldsymbol{r}'-\boldsymbol{X}_j)\rangle\,.$$

On the other hand, in case of $\alpha \neq \beta$, we can also obtain

$$S^{(\alpha\beta)}(q) = \frac{\sqrt{N_\alpha N_\beta}}{V}\int \mathrm{d}\boldsymbol{r} e^{i\boldsymbol{q}\cdot\boldsymbol{r}}[g^{(\alpha\beta)}(\boldsymbol{r}) - 1], \quad (4.25)$$

where

$$\rho_\alpha\rho_\beta g^{(\alpha\beta)}(\boldsymbol{r}-\boldsymbol{r}') := \sum_i^{(\alpha)}\sum_j^{(\beta)}\langle\delta(\boldsymbol{r}-\boldsymbol{X}_i)\delta(\boldsymbol{r}'-\boldsymbol{X}_j)\rangle\,. \quad (4.26)$$

In general, we can write them by

$$S^{(\alpha\beta)}(q) = \delta_{\alpha\beta} + \frac{\sqrt{N_\alpha N_\beta}}{V}\int \mathrm{d}\boldsymbol{r} e^{i\boldsymbol{q}\cdot\boldsymbol{r}}[g^{(\alpha\beta)}(\boldsymbol{r}) - 1]. \quad (4.27)$$

When system is isotropic, the partial static structure factor is represented by the partial radial distribution function $g^{(\alpha\beta)}(r)$ as

$$S^{(\alpha\beta)}(q) = \delta_{\alpha\beta} + \frac{4\pi\sqrt{N_\alpha N_\beta}}{qV}\int_0^\infty \mathrm{d}r[g^{(\alpha\beta)}(r) - 1]r\sin(qr). \tag{4.28}$$

The partial radial distribution function is represented as

$$g^{(\alpha\beta)}(r) = \frac{V}{4\pi r^2 N_\alpha N_\beta}\sum_i^{(\alpha)}\sum_j^{(\beta)}\langle\delta(r - X_{ij})\rangle \tag{4.29}$$

in case of $\alpha \neq \beta$.

4.1.5 Convolutionless Type Mode-Coupling Theory

The start equation of the conventional mode-coupling theory is the convolution generalized Langevin equation (4.9). That is summarized in appendix A. Here, the convolutionless type mode-coupling theory in which the start equation is the convolutionless Langevin equation (4.17) is introduced [45].

First of all, we discuss the relationship of the memory term between the convolution and convolutionless type equations. The fluctuating term in convolution type generalized Langevin equation

$$R(t) = e^{t\mathcal{Q}i\mathcal{L}}\mathcal{Q}i\mathcal{L}A \tag{4.30}$$

and $R_T(t)$ that in convolutionless type one

$$R_T(t) = e^{t\mathcal{Q}i\mathcal{L}}\left[1 - \mathcal{Q}\left\{1 - e^{-ti\mathcal{L}}e^{t\mathcal{Q}i\mathcal{L}}\right\}\right]^{-1}\mathcal{Q}i\mathcal{L}A. \tag{4.31}$$

The fluctuating term $R_T(t)$ reduces to [79]

$$\begin{aligned} R_T(t) &= e^{t\mathcal{Q}i\mathcal{L}}\left[1 - \mathcal{Q}\mathcal{S}(t)\left(1 - \mathcal{P}\mathcal{S}(t)\right)^{-1}\right]\mathcal{Q}i\mathcal{L}A \\ &= R(t) - e^{t\mathcal{Q}i\mathcal{L}}\mathcal{Q}\mathcal{S}(t)\left(1 - \mathcal{P}\mathcal{S}(t)\right)^{-1}\mathcal{Q}i\mathcal{L}A =: R(t) - \Delta R_T(t). \end{aligned} \tag{4.32}$$

where

$$\mathcal{S}(t) := 1 - e^{-t\mathcal{Q}i\mathcal{L}}e^{ti\mathcal{L}}. \tag{4.33}$$

Since

$$\mathcal{T}(t) = -\mathcal{S}(t)\left[1 - \mathcal{P}\mathcal{S}(t)\right]^{-1}$$

$$\Leftrightarrow \quad \frac{\mathrm{d}\mathcal{T}(t)}{\mathrm{d}t} = \left[1 - \mathcal{S}(t)\mathcal{P}\right]^{-1}\exp\left(-t\mathcal{Q}i\mathcal{L}\right)\mathcal{P}i\mathcal{L}e^{ti\mathcal{L}}[1 - \mathcal{P}\mathcal{S}(t)]^{-1}, \tag{4.34}$$

the remainder term $\Delta R_T(t)$ reduces to

$$\begin{aligned}
\Delta R_T(t) &= -e^{t\mathcal{Q}i\mathcal{L}}\mathcal{Q}\int_0^t \mathrm{d}\tau\left(1 - \mathcal{S}(\tau)\mathcal{P}\right)^{-1} e^{-\tau\mathcal{Q}i\mathcal{L}}\mathcal{P}i\mathcal{L}R_T(\tau) \\
&= e^{t\mathcal{Q}i\mathcal{L}}\mathcal{Q}\int_0^t \mathrm{d}\tau\psi(\tau)\cdot\phi(\tau)\cdot\left(1 - \mathcal{S}(\tau)\mathcal{P}\right)^{-1} e^{-\tau\mathcal{Q}i\mathcal{L}}A \\
&= e^{t\mathcal{Q}i\mathcal{L}}\mathcal{Q}\int_0^t \mathrm{d}\tau\psi(\tau)\cdot\left[e^{-\tau\mathcal{Q}i\mathcal{L}}\phi(\tau)\cdot A + \mathcal{S}(\tau)A\right] \\
&= -\int_0^t \mathrm{d}\tau\int_0^\tau \mathrm{d}s\psi(\tau)\cdot\phi(s)\cdot R(t-s)
\end{aligned} \tag{4.35}$$

where $\phi(t)$ denotes the normalized time-correlation function defined by

$$\phi(t) := \left\langle A(t)A^\dagger\right\rangle\cdot\left\langle AA^\dagger\right\rangle^{-1} \tag{4.36}$$

Note that the following relationships are used (the former [79] and the latter [38]);

$$\left(1 - \mathcal{S}(\tau)\mathcal{P}\right)^{-1}X = X + \left\langle XA^\dagger\right\rangle\cdot\left\langle A(\tau)A^\dagger\right\rangle^{-1}\cdot\mathcal{S}(\tau)A \tag{4.37}$$

and

$$A(t) = \mathcal{P}A(t) + \mathcal{Q}A(t) = \phi(t)\cdot A + \int_0^t \mathrm{d}\tau\phi(\tau)\cdot R(t-\tau). \tag{4.38}$$

Therefore, we can obtain

$$R(t) = R_T(t) - \int_0^t \mathrm{d}\tau\int_0^\tau \mathrm{d}s\psi(\tau)\cdot\phi(s)\cdot R(t-s), \tag{4.39}$$

and then

$$\varphi(t) = \psi(t)\cdot\phi(t) - \int_0^t \mathrm{d}\tau\int_0^\tau \mathrm{d}s\psi(\tau)\cdot\phi(s)\cdot\varphi(t-s). \tag{4.40}$$

The memory term $\psi(t)$ in convolutionless-type equation is represented by

$$\begin{aligned}\psi(t) &= \varphi(t)\cdot\phi^{-1}(t) + \int_0^t \mathrm{d}\tau \int_0^\tau \mathrm{d}s\psi(\tau)\cdot\phi(s)\cdot\varphi(t-s)\cdot\phi^{-1}(t) \\ &= \varphi(t)\cdot\phi^{-1}(t) + O(\varphi^2). \end{aligned} \tag{4.41}$$

As mentioned above, our starting equation is the convolutionless generalized Langevin equation [79]

$$\frac{\mathrm{d}}{\mathrm{d}t}\phi(t) = i\overleftrightarrow{\omega}\cdot\phi(t) - \int_0^t \mathrm{d}s\psi(s)\cdot\phi(t), \tag{4.42}$$

where the coefficient of the mechanical term is calculated by

$$i\omega := \begin{pmatrix} 0 & iq \\ \dfrac{iq}{m\beta S(q)} & 0 \end{pmatrix}. \tag{4.43}$$

The convolutionless type memory function thus reduces to

$$\psi(t) \simeq \left\langle \boldsymbol{R}_q(t)\boldsymbol{R}_q^\dagger \right\rangle \cdot \left\langle \boldsymbol{A}_q(t)\boldsymbol{A}_q^\dagger \right\rangle^{-1}, \tag{4.44}$$

where $\boldsymbol{R}_q(t)$ denotes the fluctuation term in convolution type representation. We consider only zeroth order of the memory function in $\left\langle \boldsymbol{A}_q(t)\boldsymbol{A}_q^\dagger \right\rangle^{-1}$ because we can safely neglect second order terms of the memory function within the approach of the mode-coupling theory. Equation (4.42) can be solved to obtain

$$\left\langle \boldsymbol{A}_q(t)\boldsymbol{A}_q^\dagger \right\rangle = \exp\left[i\omega t - \int_0^t \mathrm{d}\tau \int_0^\tau \mathrm{d}s\psi(s) \right] \cdot \left\langle \boldsymbol{A}_q\boldsymbol{A}_q^\dagger \right\rangle = \exp\left[i\omega t\right] \cdot \left\langle \boldsymbol{A}_q\boldsymbol{A}_q^\dagger \right\rangle + O(\psi). \tag{4.45}$$

Therefore,

$$\left\langle \boldsymbol{A}_q(t)\boldsymbol{A}_q^\dagger \right\rangle^{-1} \simeq \left\langle \boldsymbol{A}_q\boldsymbol{A}_q^\dagger \right\rangle^{-1} \cdot \exp\left[-i\omega t\right]. \tag{4.46}$$

It is straightforward to obtain

$$(i\omega)^{2n} = (-1)^n \Omega(q)^{2n} \mathbf{1} \tag{4.47}$$

$$(i\omega)^{2n+1} = \frac{(-1)^n}{\Omega(q)} \Omega(q)^{2n+1}\, i\omega, \tag{4.48}$$

where $\Omega(q)$ is defined by

$$\Omega(q)^2 := \frac{q^2}{m\beta S(q)}. \tag{4.49}$$

One can obtain

$$\begin{aligned}
\exp\left[-i\omega t\right] &= \sum_{n=0}^{\infty} \frac{t^{2n}}{(2n)!}(i\omega)^{2n} - \sum_{n=0}^{\infty} \frac{t^{2n+1}}{(2n+1)!}(i\omega)^{2n+1} \\
&= \cos\Omega(q)t\mathbf{1} - \frac{\sin\Omega(q)t}{\Omega(q)}\, i\omega \\
&= \begin{pmatrix} \cos\Omega(q)t & -\frac{iq}{\Omega(q)}\sin\Omega(q)t \\ -\frac{iq}{m\beta S(q)\Omega(q)}\sin\Omega(q)t & \cos\Omega(q)t \end{pmatrix}.
\end{aligned} \tag{4.50}$$

In conclusion, the equation of motion for the intermediate scattering function is described by

$$\begin{aligned}
&\partial_t^2 F(q,t) + \int_0^t \mathrm{d}s \cos\left(s\Omega(q)\right) K(q,s)\partial_t F(q,t) \\
&\quad +\Omega(q)^2\left[1 + \frac{1}{\Omega(q)}\int_0^t \mathrm{d}s \sin\left(s\Omega(q)\right) K(q,s)\right] F(q,t) = 0,
\end{aligned} \tag{4.51}$$

where $K(q,t)$ denotes the approximated memory function.

As well as the intermediate scattering function, we can derive the equation of motion for the self intermediate scattering function as

$$\begin{aligned}
&\partial_t^2 F_s(q,t) + \int_0^t \mathrm{d}s \cos\left(s\Omega_s(q)\right) K_s(q,s)\partial_t F_s(q,t) \\
&\quad +\Omega_s(q)^2\left[1 + \frac{1}{\Omega_s(q)}\int_0^t \mathrm{d}s \sin\left(s\Omega_s(q)\right) K_s(q,s)\right] F_s(q,t) = 0,
\end{aligned} \tag{4.52}$$

where $K_s(q,t)$ denotes the approximated memory term in connection with the self intermediate scattering function and $\Omega_s(q)^2 = q^2/m\beta$.

Substituting

$$F_s(q,t) = 1 - \frac{q^2}{6}M_2(t) + O(q^4) \tag{4.53}$$

to the equation of motion for the self intermediate scattering function, we can obtain the equation of motion for the mean-square displacement as

$$\partial_t^2 M_2(t) + \int_0^t \mathrm{d}s K_0(s)\partial_t M_2(t) - \frac{6}{m\beta}\left[1 + \int_0^t \mathrm{d}s\; sK_0(s)\right] = 0 \tag{4.54}$$

with

$$K_0(t) := \lim_{q\to 0} K_s(q,t). \tag{4.55}$$

We impose one more assumption that the memory function safely converges to zero in the not so long time scale. Under the assumption, the convolutionless type mode-coupling equations are represented by

$$\partial_t^2 F(q,t) + \int_0^t \mathrm{d}s K(q,s)\partial_t F(q,t) + \Omega(q)^2 F(q,t) = 0, \tag{4.56}$$

$$\partial_t^2 F_s(q,t) + \int_0^t \mathrm{d}s K_s(q,s)\partial_t F_s(q,t) + \Omega_s(q)^2 F_s(q,t) = 0, \tag{4.57}$$

$$\partial_t^2 M_2(t) + \int_0^t \mathrm{d}s K_0(s)\partial_t M_2(t) - \frac{6}{m\beta} = 0, \tag{4.58}$$

and so on.

4.2 Numerical Calculation

The numerical calculation of the convolutionless mode-coupling theory is basically similar to that of conventional one (appendix A). The main difference is the discretized equation to obtain physical variables.

4.2.1 Discretized equation

The discretized equation for the intermediate scattering function is represented by

$$A_T F_J = -B_T \hat{M}_J + C_T, \tag{4.59}$$

where $F_J = F(q, J\Delta t)$, $\hat{M}_J = \hat{M}(q, J\Delta t)$, and

$$A_T = \frac{2}{(\Delta t)^2} + \frac{3}{2}\left(\frac{1}{2}\hat{M}_0 + \sum_{j=1}^{J-1}\hat{M}_j\right) + \frac{3}{4}\hat{M}_J + \frac{q^2 T}{48S(q)}, \tag{4.60}$$

$$B_T = \frac{1}{4}F_{J-2} - F_{J-1}, \tag{4.61}$$

$$C_T = \frac{1}{(\Delta t)^2}\left(F_{J-3} - 4F_{J-2} + 5F_{J-1}\right) - 2\left(\frac{1}{2}\hat{M}_0 + \sum_{j=1}^{J-1}\hat{M}_j\right) B_T. \tag{4.62}$$

Similarly, we can obtain the discretized equation for the self-intermediate scattering function as

$$A_{s,T}F_{s,J} = -B_{s,T}\hat{M}_{s,J} + C_{s,T}, \tag{4.63}$$

where $F_{s,J} = F_s(q, J\Delta t)$, $\hat{M}_{s,J} = \hat{M}_s(q, J\Delta t)$, and

$$A_{s,T} = \frac{2}{(\Delta t)^2} + \frac{3}{2}\left(\frac{1}{2}\hat{M}_{s,0} + \sum_{j=1}^{J-1}\hat{M}_{s,j}\right) + \frac{3}{4}\hat{M}_{s,J} + \frac{q^2T}{48}, \tag{4.64}$$

$$B_{s,T} = \frac{1}{4}F_{s,J-2} - F_{s,J-1}, \tag{4.65}$$

$$C_{s,T} = \frac{1}{(\Delta t)^2}\left(F_{s,J-3} - 4F_{s,J-2} + 5F_{s,J-1}\right) - 2\left(\frac{1}{2}\hat{M}_{s,0} + \sum_{j=1}^{J-1}\hat{M}_{s,j}\right)B_{s,T}. \tag{4.66}$$

4.2.2 Initial condition: Static structure factor

The convolutionless type mode-coupling equations as well as the conventional mode-coupling theory can be numerically solved from only the static structure factor $S(q)$, which we can obtain from molecular dynamics simulations. We can also employ $S(q)$ analytically calculated from appropriate approximations. One of approximations is the Percus-Yevick approximation for the hard-sphere systems (appendix B.9).

Since analytical forms of the static structure factor such as obtained from the Percus-Yevick approximation are idealized situation, no analytical forms exist in almost all interesting systems so far. The Lennard-Jones fluid is one of them. We prepare the static structure factor from the molecular dynamics simulations. Figures 4.1 and 4.2 show the static structure factor for the one–component Lennard–Jones fluids. In addition, figs. 4.3, 4.4, 4.5, 4.6, 4.7, and 4.8 show that for binary mixture Lennard–Jones fluids. The static structure factor was calculated from the Fourier transform of the radial distribution function (correctly, the Fourier transform of the total correlation function) and was averaged out in at least 100 times. Since the simulation box is finite, $S(q)$ in small wave number region is not meaningful. Our data are extrapolated with

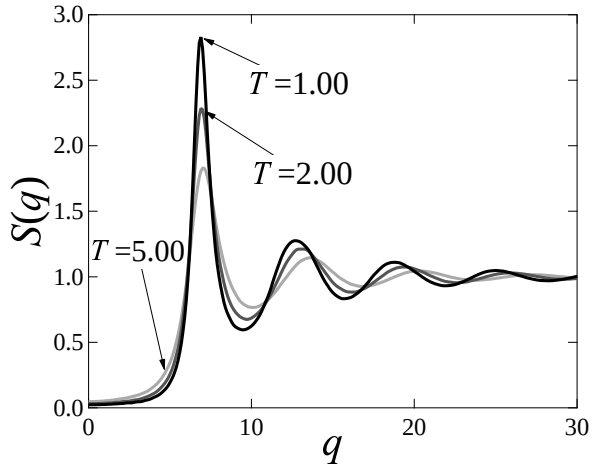

Figure 4.1: Plot of the static structure factor calculated in one–component Lennard–Jones systems by molecular dynamics simulations at $T = 5.00, 2.00$, and 1.00 (from light gray to black). The wave number q is normalized by the inverse diameter of a particle.

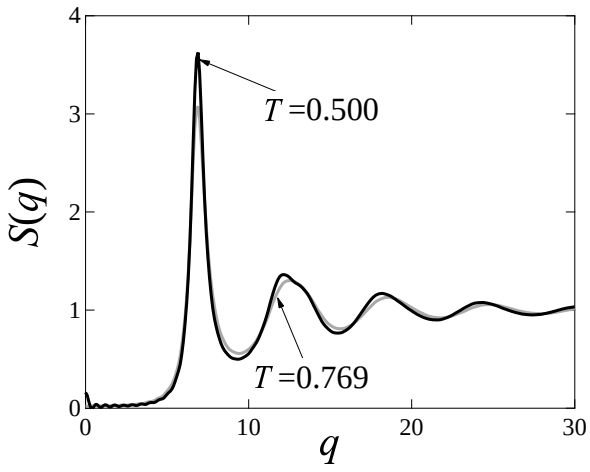

Figure 4.2: Plot of the static structure factor calculated in one–component Lennard–Jones systems by molecular dynamics simulations at $T = 0.769$ (gray) and 0.500 (black). The wave number q is normalized by the inverse diameter of a particle.

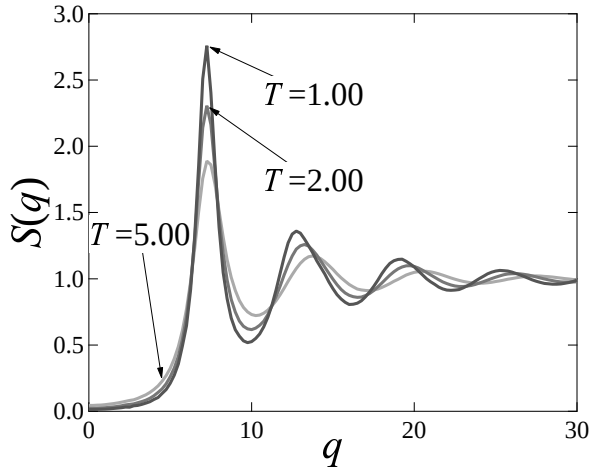

Figure 4.3: Plot of the static structure factor in one–component Lennard–Jones systems calculated by molecular dynamics simulations at $T = 5.00, 2.00$, and 1.00 (from light gray to black). The wave number q is normalized by the inverse diameter of a A particle.

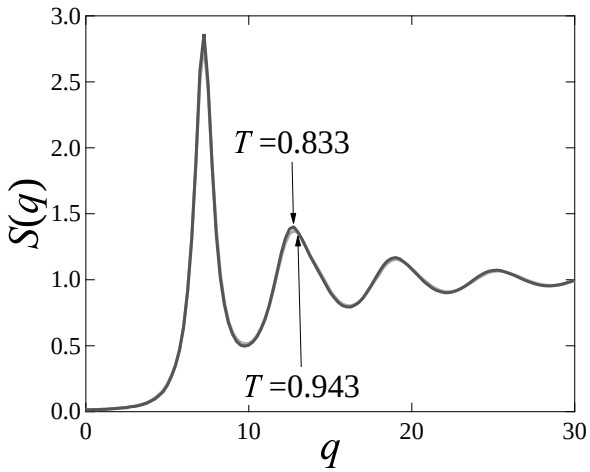

Figure 4.4: Plot of the static structure factor in one–component Lennard–Jones systems calculated by molecular dynamics simulations at $T = 0.943$ (gray) and 0.833 (black). The wave number q is normalized by the inverse diameter of a A particle.

quadratic function to approximate them. Note that the three-body direct correlation $c_3(\boldsymbol{q}, \boldsymbol{k})$ can be safely neglected in the Kob-Andersen model [32].

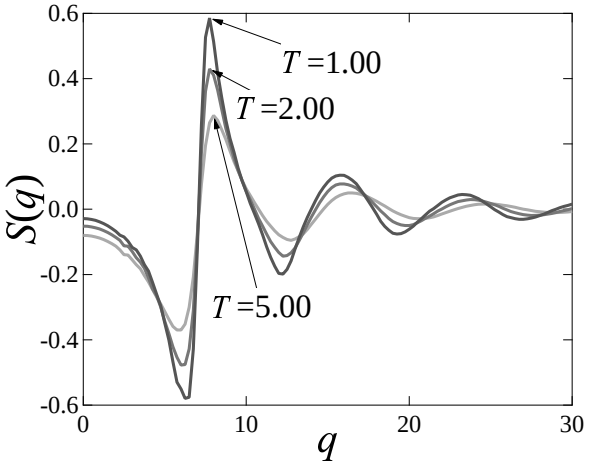

Figure 4.5: Plot of the static structure factor in one–component Lennard–Jones systems calculated by molecular dynamics simulations at $T = 5.00, 2.00$, and 1.00 (from light gray to black). The wave number q is normalized by the inverse diameter of a A particle.

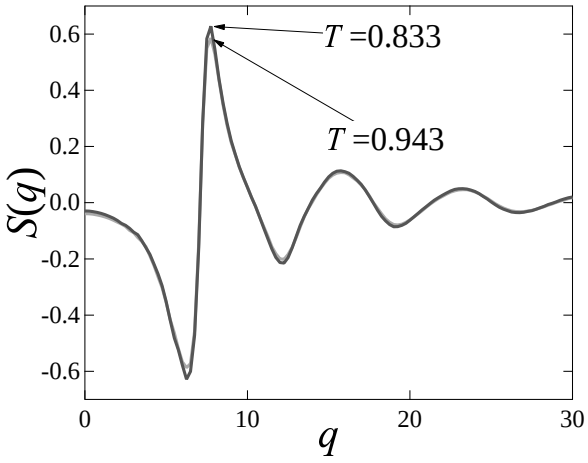

Figure 4.6: Plot of the static structure factor in one–component Lennard–Jones systems calculated by molecular dynamics simulations at $T = 0.943$ (gray) and 0.833 (black). The wave number q is normalized by the inverse diameter of a A particle.

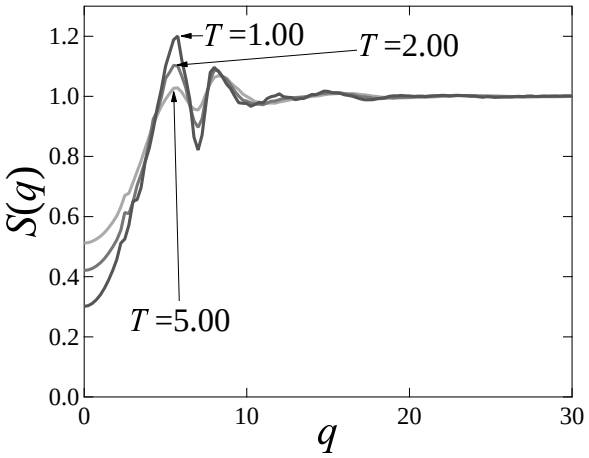

Figure 4.7: Plot of the static structure factor in one–component Lennard–Jones systems calculated by molecular dynamics simulations at $T = 5.00, 2.00$, and 1.00 (from light gray to black). The wave number q is normalized by the inverse diameter of a A particle.

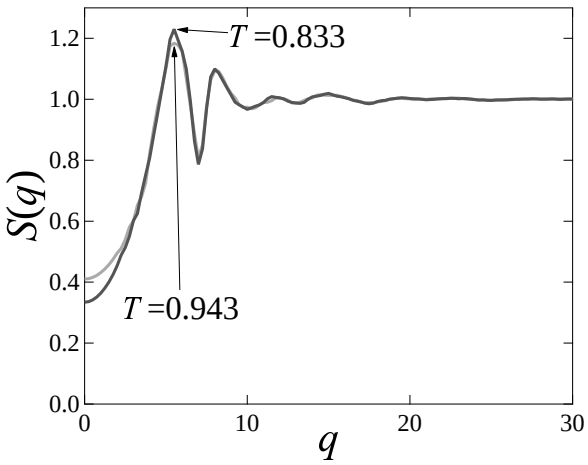

Figure 4.8: Plot of the static structure factor in one–component Lennard–Jones systems calculated by molecular dynamics simulations at $T = 0.943$ (gray) and 0.833 (black). The wave number q is normalized by the inverse diameter of a A particle.

4.2.3 Detail of numerical calculation

The step of the wave number is $\Delta q = 0.25/\sigma_{\mathrm{AA}}$. Note that $\Delta q L < 2\pi$, which L denotes the length of the simulation box; $V = L^3$. The upper limit of the integral is $q_{\mathrm{max}} = 60/\sigma_{\mathrm{AA}}$. In

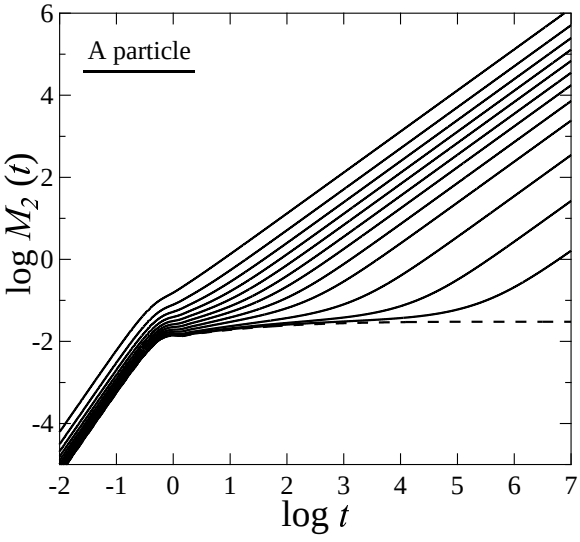

Figure 4.9: Log-log plot of the mean-square displacement of A particle versus the time for $T =$ 10.0, 5.00, 3.33, 2.50, 2.00, 1.67, 1.43, 1.25, 1.11, 1.00, 0.943, 0.929, and 0.909 (from left to right). The results in $T < T_{\mathrm{MCT}}$ are indicated by dashed lines.

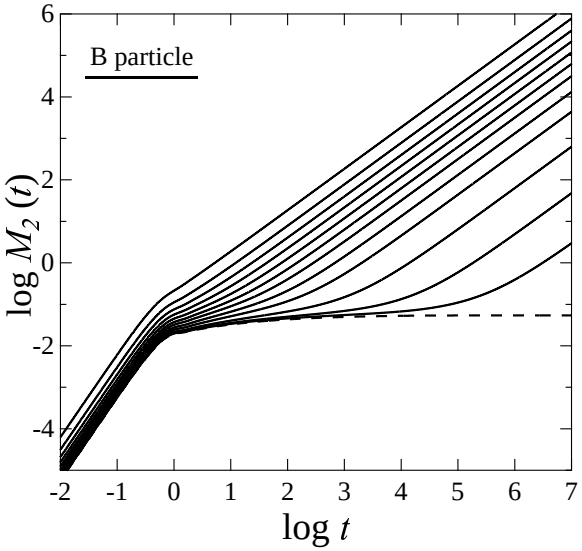

Figure 4.10: Log-log plot of the mean-square displacement for B particle versus the time for $T =$ 10.0, 5.00, 3.33, 2.50, 2.00, 1.67, 1.43, 1.25, 1.11, 1.00, 0.943, 0.929, and 0.909 (from left to right). The results in $T < T_{\mathrm{MCT}}$ are indicated by dashed lines.

order to carry out the double integral with regard to the wave number correctly, we should set q_{max} as $c_2(q) \simeq 0$ for $q > q_{\mathrm{max}}$. We set $q_{\mathrm{max}} = 60/\sigma_{\mathrm{AA}}$ which is large enough to hold the above condition in each temperature. The time step Δt doubles every 256 calculation steps, and the initial time step is $\Delta t = 10^{-5}\tau_{\mathrm{LJ}}$, where $\tau_{\mathrm{LJ}} = \sqrt{m{\sigma_{\mathrm{AA}}}^2/48\varepsilon_{\mathrm{AA}}}$.

4.3 Result and Discussion

4.3.1 Conventional mode-coupling theory

First of all, numerical solutions of the conventional mode-coupling theory are shown to discuss its deviation from real systems.

Figures 4.9 and 4.10 show numerical solutions of the mean-square displacement of A and B particle, respectively, calculated by using eq. (A.116). The diffusive motion disappears below $T_{\mathrm{MCT}} \approx 0.922$ already suggested by Nauroth et al. [30, 31], and it implies that the non-ergodic transition occurs around T_{MCT}. The results of both particles are the same qualitatively while B

particle is more mobile than A particle. It is reasonable because we can regard that B particle is smaller than A particle from the parameters of the potential.

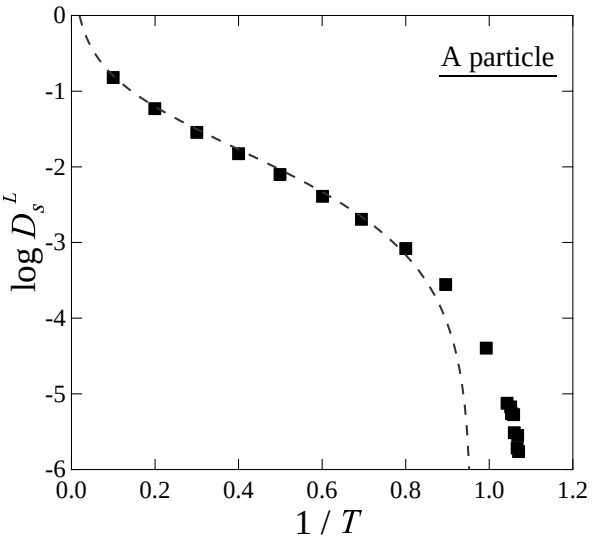

Figure 4.11: Semi-log plot of the long-time self-diffusion constant for A particle versus the inverse temperature. The squares represent results of A particle and the dashed line the theoretical line (4.67). The fitting parameters are (κ, T_c)=(48, 1.07)

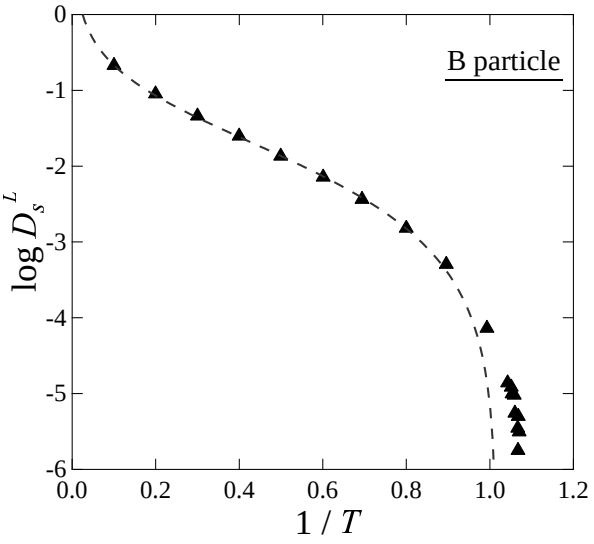

Figure 4.12: Semi-log plot of the long-time self-diffusion constant for B particle versus the inverse temperature. The triangles those of B particle and the dashed line the theoretical line (4.67). The fitting parameters are (κ, T_c)=(38.57, 0.984)

Figures 4.11 and 4.12 show numerical solutions of the long-time self-diffusion coefficient D_S^L for A and B particle, respectively. It is scaled by a universal unit $d_0 = \sigma_{\mathrm{AA}}\sqrt{\varepsilon_{\mathrm{AA}}/m}$ [8]. D_S^L rapidly decreases as the system approaches to the singular temperature T_{MCT} and becomes zero at T_{MCT}.

Tokuyama has suggested a theoretical equation [80] as

$$\frac{D_S^L}{d_0} = \kappa^{-1}\left(\frac{\lambda_c}{\lambda}\right)\left(1-\frac{\lambda}{\lambda_c}\right)^2, \tag{4.67}$$

where λ denotes the control parameter which is the inverse temperature in this paper, and κ and λ_c parameters. One of the parameters κ can be theoretically determined for some systems including the system we employ [80]. The parameter should be $\kappa = 48$ for A particle and

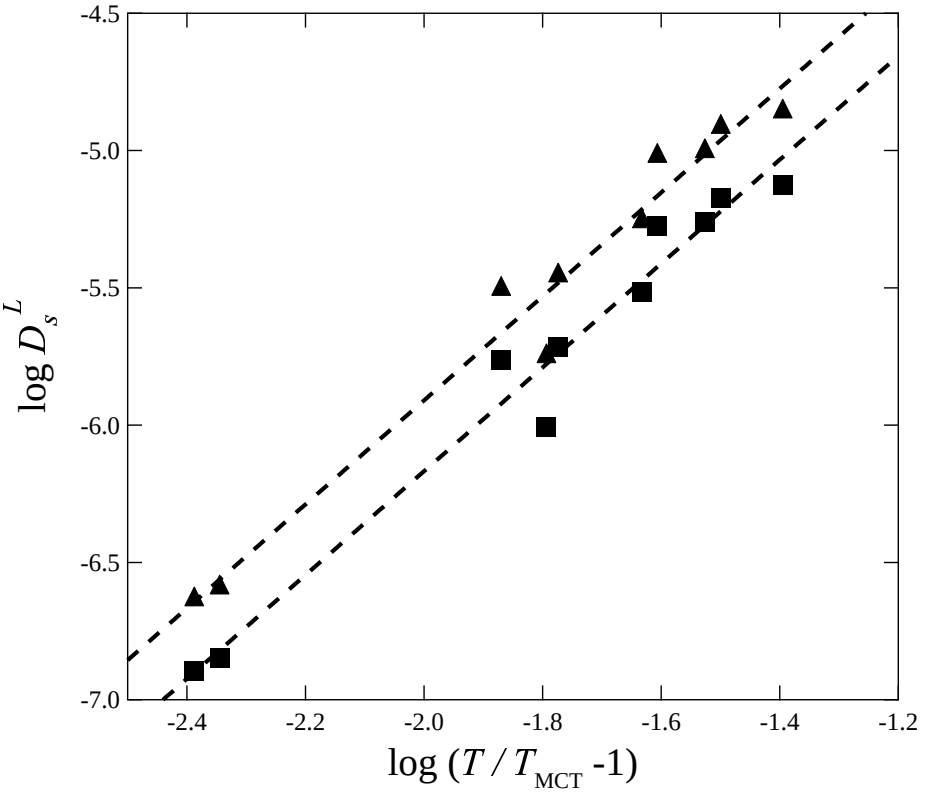

Figure 4.13: Log-log plot of the long-time self-diffusion constant versus the difference between the temperature and the singular temperature T_{MCT}. The squares represent results of A particle, the triangles those of B particle, and the dashed lines guide to power law fitting. The long-time self-diffusion coefficient is scaled by $\sigma_{\mathrm{AA}}\sqrt{\varepsilon_{\mathrm{AA}}/m}$ and the temperature by $\varepsilon_{\mathrm{AA}}/k_B$. The exponents are 1.8922 ± 0.117 for A particle and 1.8904 ± 0.118 for B particle.

$\kappa = 38.57$ for B particle according to Ref. [80]. In fact, the fitting lines with those parameters are in agreement with the numerical solution except in lower temperature region. In the lower temperature region, the theoretical line deviates from the numerical results. The theory also does not describe the molecular dynamics simulation results in the lower temperature region [81, 82]. As mentioned in ref. [81], we need a theory including effects of the dynamical heterogeneity to predict results correctly even in lower temperature.

The behavior in vicinity of T_{MCT} holds the power law $D_S^L \sim (T/T_{\mathrm{MCT}} - 1)^\gamma$ and the power γ is 1.8922 ± 0.117 for A particle and 1.8904 ± 0.118 for B particle as shown in fig. 4.13. The mode-coupling theory can describe dramatic change of dynamics (i.e. non-ergodic transition)

from slight difference of the statics (i.e. the static structure factor). The numerical solutions are thus much sensitive to the initial condition in the vicinity of the crossover temperature. Nevertheless, our results show reasonable power law. We do not overlook not only the sensitivity of the initial condition but also the error with the numerical integral. The error is estimated as $O(\Delta t^2)$. We must calculate for the long time region in lower temperatures, and then the error might be accumulated. Although the error is highly visible in a log-log plot, the magnitude is extremely small.

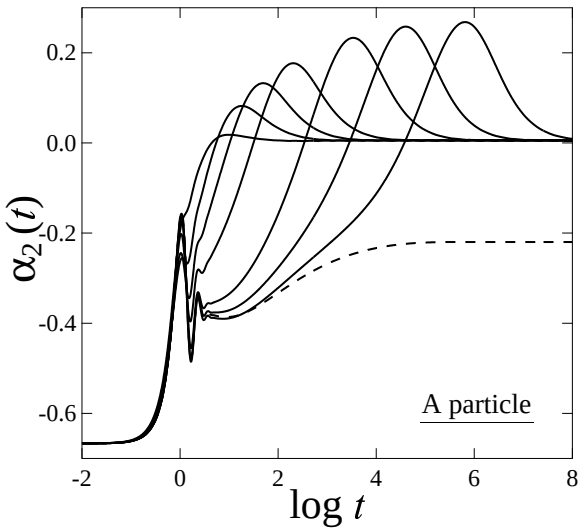

Figure 4.14: Semi-log plot of the non-Gaussian parameter for A particle versus the time for $T = 5.00$, 2.50, 1.67, 1.25, 1.00, 0.943, 0.929, and 0.909 (from left to right). The result in $T < T_{\mathrm{MCT}}$ is indicated by dashed lines.

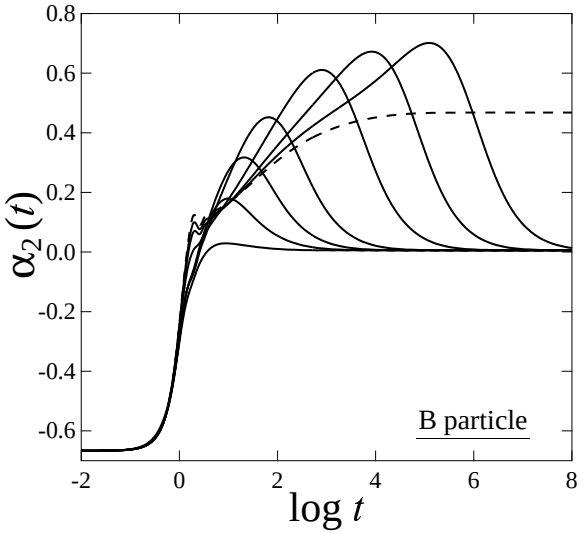

Figure 4.15: Semi-log plot of the non-Gaussian parameter for B particle versus the time for $T = 5.00$, 2.50, 1.67, 1.25, 1.00, 0.943, 0.929, and 0.909 (from left to right). The result in $T < T_{\mathrm{MCT}}$ is indicated by dashed lines.

It is known that the displacement of a tagged particle is not Gaussian in low temperature. We can estimate the deviation from the Gaussian by using the non-Gaussian parameter ;

$$\alpha_2(t) = \frac{3M_4(t)}{5M_2(t)^2} - 1. \tag{4.68}$$

As predicted from eqs. (A.116) and (A.117), the initial results are not zero but -0.667. However, the particles follow a ballistic course in the short-time regime, so that the non-Gaussian

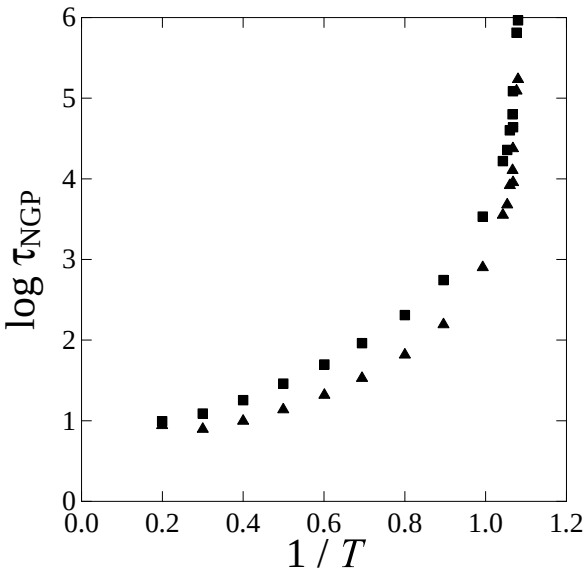

Figure 4.16: Semi-log plot of the peak time τ_{NGP} of the non-Gaussian parameter versus the inverse temperature. The squares represent results of A particle and the triangles those of B particle.

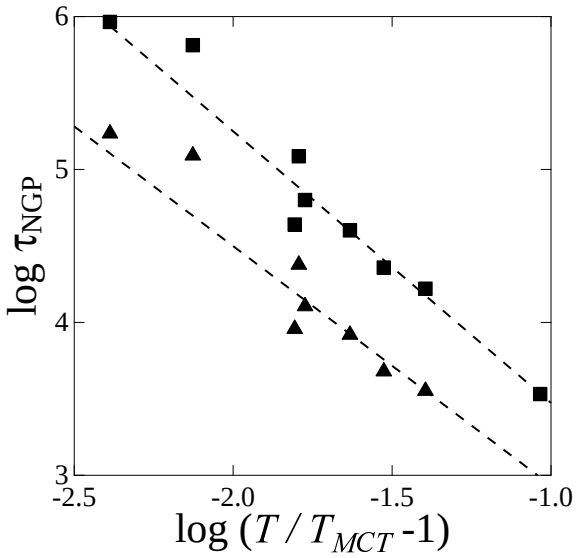

Figure 4.17: This plot shows τ_{NGP} versus the difference between the temperature and the singular temperature T_{MCT}. The exponents are -1.7758 $\pm$ 0.0508 for A particle and -1.5651 $\pm$ 0.0629 for B particle.

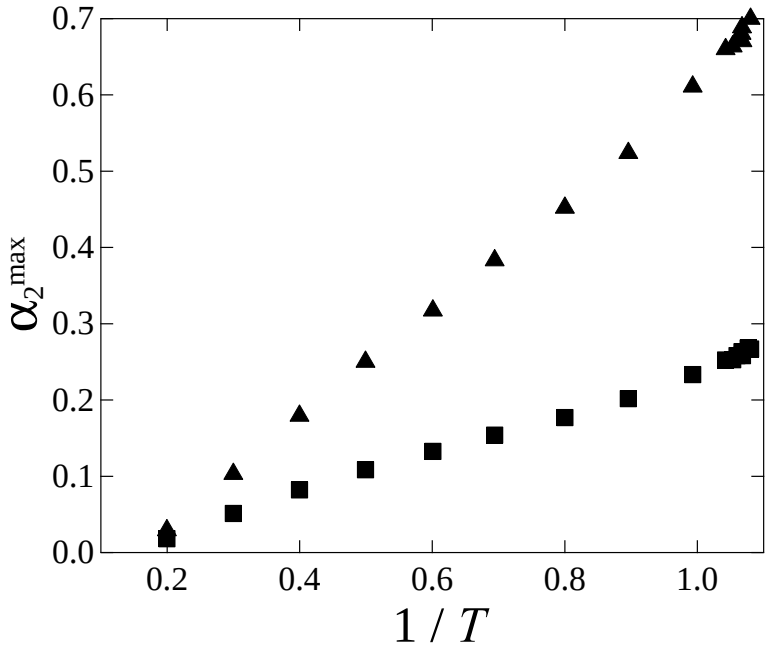

Figure 4.18: Plot of the peak height of the non-Gaussian parameter versus the inverse temperature. The squares represent results of A particle and the triangles those of B particle.

parameter should be zero. This is known as one of problems of idealized mode-coupling theory [83]. It is possible to approximate $\ddot{M}_4(t)$ by $t^{-1}\dot{M}_4(t)$ to set the initial the non-Gaussian parameter as zero. However, we pay attention to the peak height and peak time which do not relate to the initial behavior.

Numerical results show the initial behavior as predicted from the equations. On the other hand, they converge to zero in the long-time region except non-ergodic state. Strictly speaking, the long-time limit is slightly different from zero. We however regard them as numerical error as well as Flenner and Szamel [36]. The non-Gaussian parameter has maximum near the crossover from motion in cage to diffusive motion. Figure 4.16 shows how the maximum time τ_{NGP} depends on the inverse temperature. As the temperature approaches to T_{MCT}, τ_{NGP} diverges. The divergence shows the power law and the exponents are -1.7758 $\pm$ 0.0508 for A particle and -1.5651 $\pm$ 0.0629 for B particle as shown in fig. 4.17. The exponents of the non-Gaussian parameter are different between different kinds of particle while the exponents of the long-time self-diffusion coefficient are almost same. Considering τ_{NGP} corresponds to time when cages are broken, it implies that property of cages depends on the components of particles.

Although τ_{NGP} diverges at T_{MCT}, the peak heights α_2^{max} of the non-Gaussian parameter do not diverge but increase lineally (fig. 4.18). It is known that peak height of the non-Gaussian parameter corresponds to the dynamical heterogeneity and rapidly increases in vicinity of the glass transition. Our results suggest at least two possibilities; one of them is that the mode-coupling theory does not reflect the dynamical heterogeneity perfectly and another is that the non-ergodic crossover in the mode-coupling theory is different from the glass transition qualitatively. The former however seems wrong because some have suggested the mode-coupling theory calculation for the length scale corresponds to the dynamical heterogeneity [53, 54].

4.3.2 Deviation in conventional mode-coupling theory

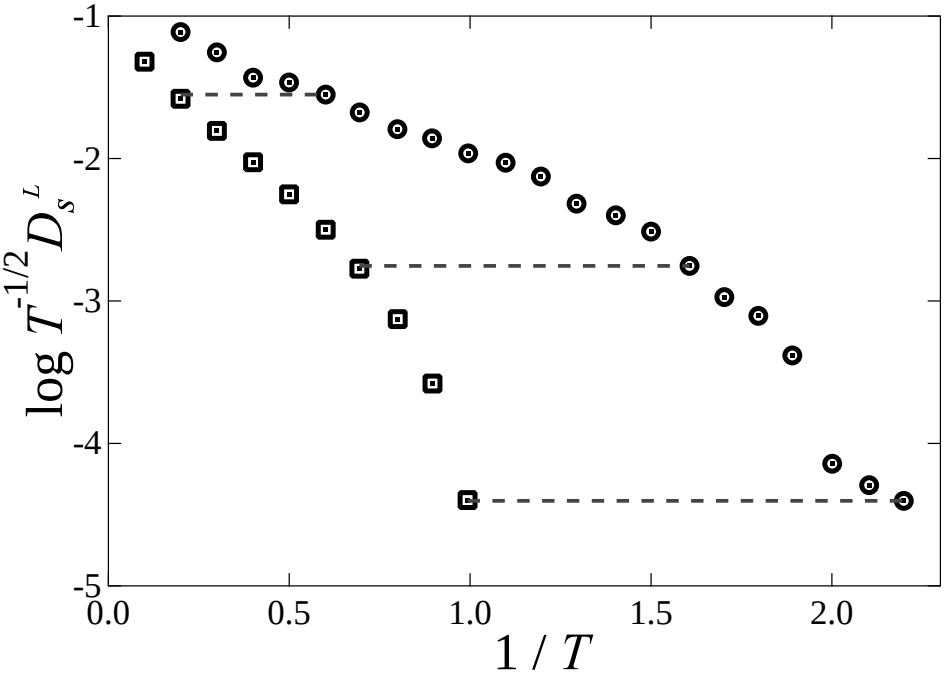

Figure 4.19: Semi-log plot of the long-time self-diffusion constant compensated by the temperature versus the inverse temperature. The squares represent numerical results of A particle, the circles results of the molecular dynamics simulations [82].

From the standpoint of the mean-field theory by Tokuyama, one can distinguish liquid, supercooled liquid, and glass by using the long-time self-diffusion coefficient scaled by appropriate unit [8, 81]. We rescale the long-time self-diffusion coefficient by $\sigma_{\mathrm{AA}}\sqrt{\varepsilon_{\mathrm{AA}}/mT}$ to eliminate the influence of the ballistic motion. Figure 4.19 shows that rescaled the long-time self-diffusion coefficient of A particle in numerical calculation and the molecular dynamics simulation [82]. We select three temperature couples of the mode-coupling theory and molecular dynamics which have almost same LSD; (MCT, MD)=(5.00, 1.67), (1.43, 0.625), and (1.00, 0.455).

As shown in fig. 4.20, results of the three couples agree in short-time regime, respectively, because we have eliminated temperature dependence. Our results imply that the mode-coupling

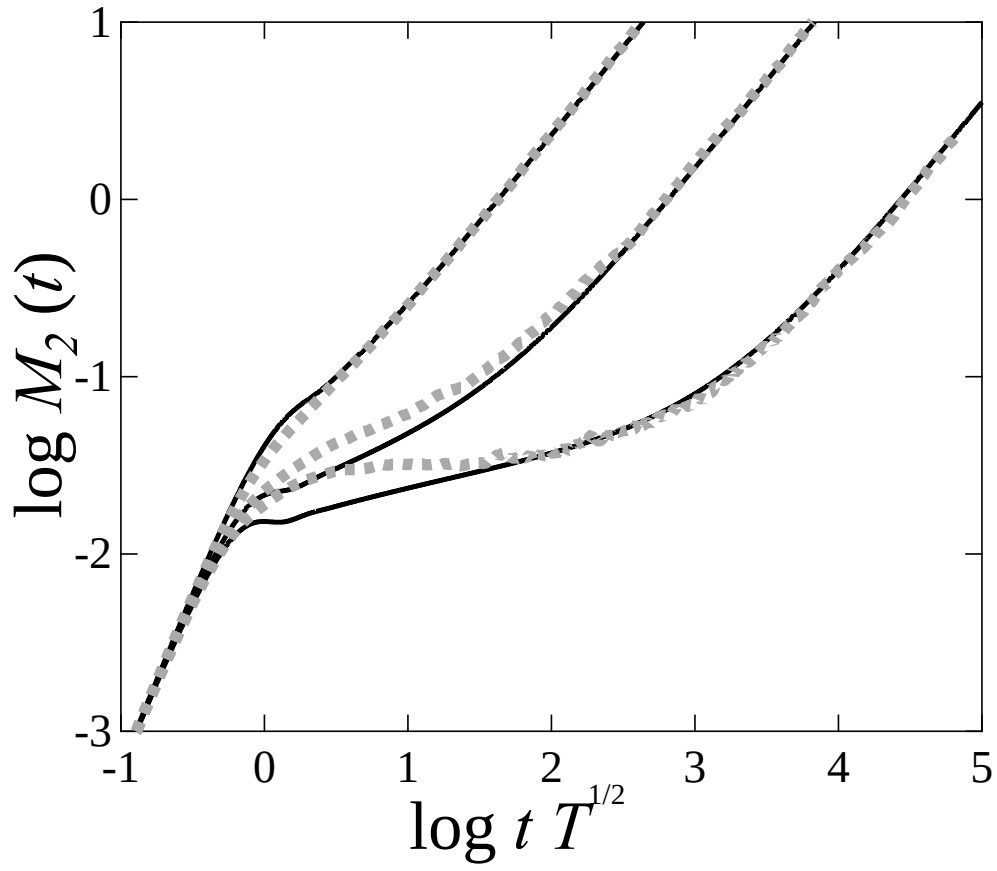

Figure 4.20: Log-log plot of the mean-square displacement of A particle versus the time compensated by the temperature at the temperature (MCT, MD)=(5.00, 1.67), (1.43, 0.625), and (1.00, 0.455) (from left to right). The solid black lines represents results of the mode-coupling theory and the dashed gray ones molecular dynamics results. The time is scaled by τ_{LJ}.

theory tends to drag the short-time behavior to the β relaxation time scale. The result of the mode-coupling theory thus overshoots in the β relaxation time scale In the highest temperature couples (MCT, MD) = (5.00, 1.67). On the other hand, the mode-coupling theory results do not approach molecular dynamics results in the lower temperature couples (MCT, MD) = (1.43, 0.625) and (1.00, 0.455). It is indicated as the kinetic energy is not much enough to move at the dip of the potential surface made by cage particles. It is concluded that the cage size evaluated by the mode-coupling theory is smaller than that in real systems.

Tokuyama has proposed that the starting equation of the mode-coupling theory, that is the

convolution type generalized Langevin equation, be not suitable for the supercooled liquids [37] and lead the deviation in the β relaxation time scale. In addition, we suggest that the non-Gaussian parameter influence to the β relaxation time scale. The non-Gaussian parameter originally corresponds to the α relaxation time scale and looks independent on the mean-square displacement. However, it connects with the mean-square displacement by the intermediate scattering function and the self-intermediate scattering function (eqs. (A.116) and (A.117)).

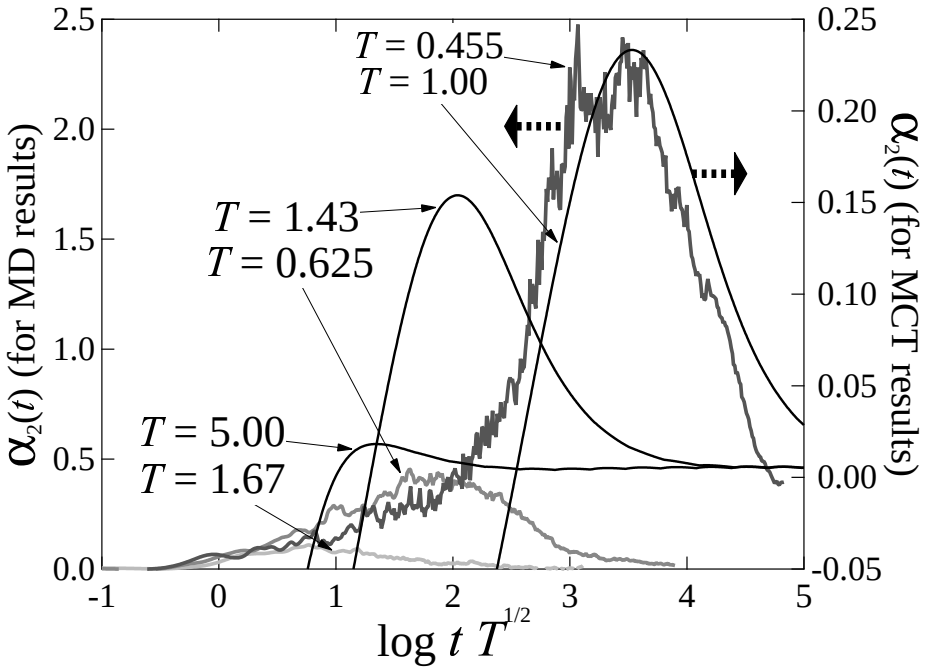

Figure 4.21: Semi-log plot of the non-Gaussian parameter of A particle versus the time compensated by the temperature at the temperature (MCT, MD)=(5.00, 1.67), (1.43, 0.625), and (1.00, 0.455) (from left to right).

Numerical results of the non-Gaussian parameter are shown in fig. 4.21 with corresponding molecular dynamics results. Although the peak heights of the mode-coupling theory are much smaller than those of molecular dynamics, the peak times τ_{NGP} are same order. It means the mode-coupling theory predicts the time scale of cage breaking correctly in the standpoint of the mean-field theory. The peak heights of the non-Gaussian parameter in numerical calculations are of the order of those in molecular dynamics simulations as shown in fig. 4.23. It suggests

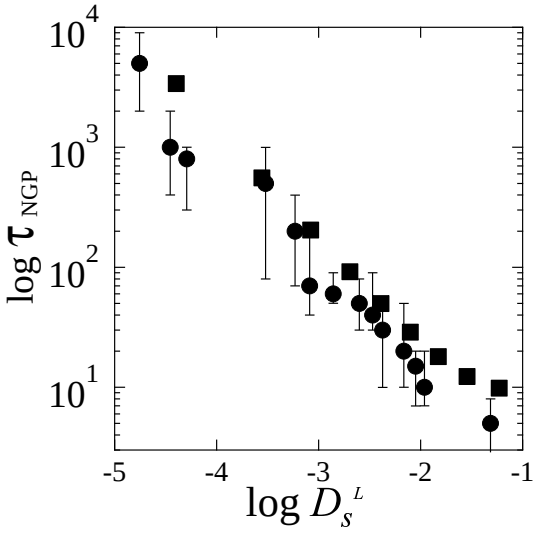

Figure 4.22: Log-log plot of τ_{NGP} versus the long-time self-diffusion coefficient. The squares indicates results of the mode-coupling theory and the circles with error bar those of the molecular dynamics simulation.

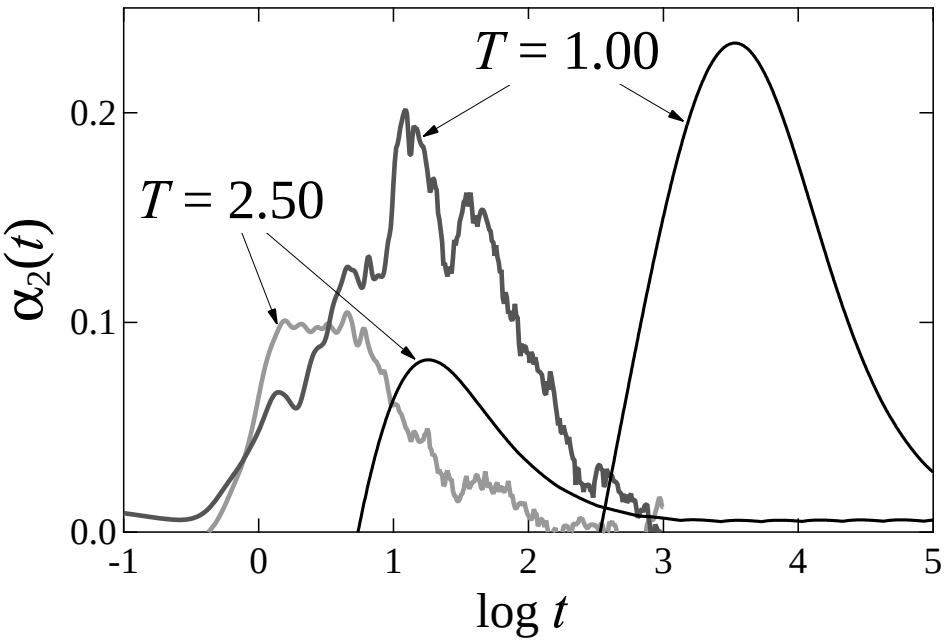

Figure 4.23: Semi-log plot of the non-Gaussian parameter of A particle versus the time at the temperature $T = 2.50$ and $T = 1.00$. The black (smooth) lines indicates results of the mode-coupling theory and the gray (rough) ones those of the molecular dynamics simulations.

that the peak heights strongly depend on static information. In order to obtain higher peak height which corresponds to real systems, we therefore substitute the static structure factor at

lower temperature. It is however impossible in the idealized mode-coupling theory because the non-ergodic crossover occurs at much higher temperature.

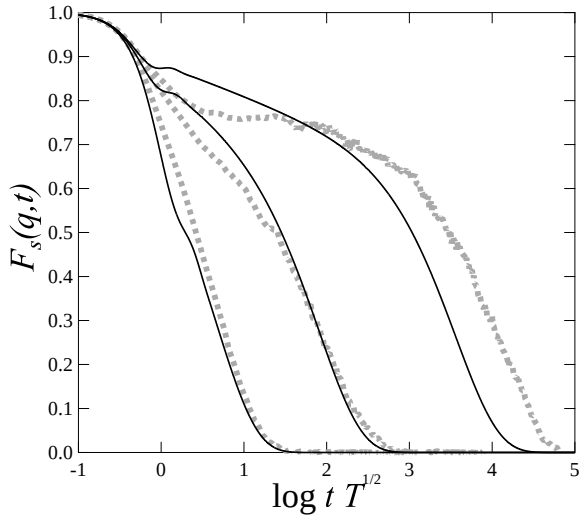

Figure 4.24: Semi-log plot of the self intermediate scattering function of A particle versus the time compensated by the temperature at the temperature (MCT, MD)=(5.00, 1.67), (1.43, 0.625), and (1.00, 0.455) (from left to right). The solid black lines represents results of the mode-coupling theory and the gray dashed ones molecular dynamics results. The wave number is fixed at $q_{\mathrm{w}} = 7.25{\sigma_{\mathrm{AA}}}^{-1}$.

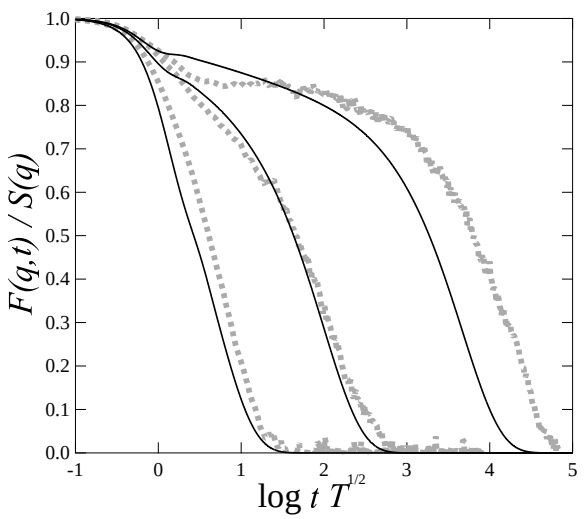

Figure 4.25: Semi-log plot of the normalized intermediate scattering function of A-A particle versus the time compensated by the temperature at the temperature (MCT, MD)=(5.00, 1.67), (1.43, 0.625), and (1.00, 0.455) (from left to right). The solid black lines represents results of the mode-coupling theory and the gray dashed ones molecular dynamics results. The wave number is fixed at $q_{\mathrm{w}} = 7.25{\sigma_{\mathrm{AA}}}^{-1}$.

We next discuss the self-intermediate scattering function in fig. 4.24. Note that the wave number is fixed at $q_w = 7.25{\sigma_{\mathrm{AA}}}^{-1}$ at which the partial static structure factor of A-A has maximum. As the temperature is lower, the deviation in the long-time regime is outstanding. These trends correspond to the fact that numerical results of the non-Gaussian parameter are smaller than real systems. If the non-Gaussian parameter was larger, the relaxation would get slower and then the mode-coupling theory results would be close to molecular dynamics results. As well as the mean-square displacement, the numerical and molecular dynamics results deviate in the intermediate time regime.

Dynamics of the tagged particle was mentioned in the above. We finally discuss coherent

dynamics by using the intermediate scattering function. As shown in fig. 4.25, the molecular dynamics and numerical results do not agree. As mentioned above, Tokuyama has suggested that the starting equation of the mode-coupling theory is not suitable for incoherent dynamics of supercooled liquids [37]. Our comparison mentions that the conventional mode-coupling theory is not acceptable for coherent dynamics too.

4.3.3 Analysis of the conventional mode-coupling theory from standpoint of the mean-field theory

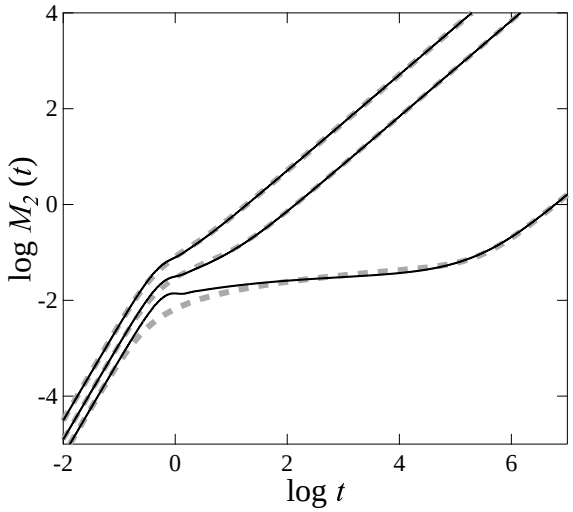

Figure 4.26: Log-log plot of the mean-square displacement of A particle versus the time for $T = 5.00$, 2.00, and 0.929 (from left to right). The solid lines represent the numerical solutions of the mode-coupling theory and the gray dashed lines the theoretical line predicted by the mean-field theory.

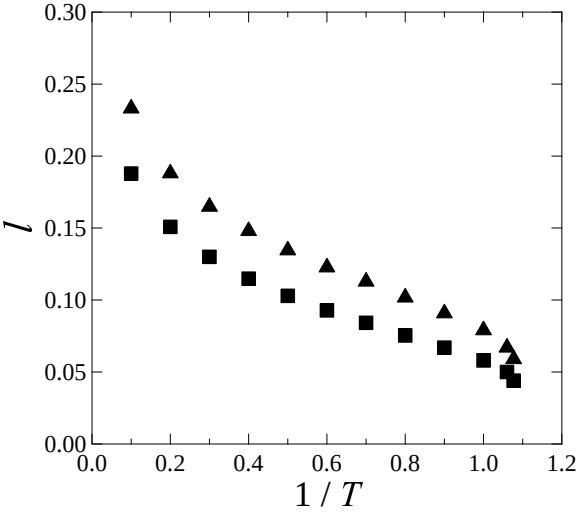

Figure 4.27: Numerical solutions of the mean-free path versus the inverse temperature. The squares represent results of A particle and the triangles those of B particle.

The analysis of $M_2^{(\mathrm{A})}(t)$ for A particle by the mean-field theory is shown in fig. 4.26. The same analysis can be also done for $M_2^{(\mathrm{B})}(t)$ of B particle. Although the mean-field predictions are in agreement with solutions of the mode-coupling theory in high temperature region, they deviate in low temperature region. The numerical solutions in low temperature region show bump in the intermediate time scale, while any results of the molecular dynamics simulations

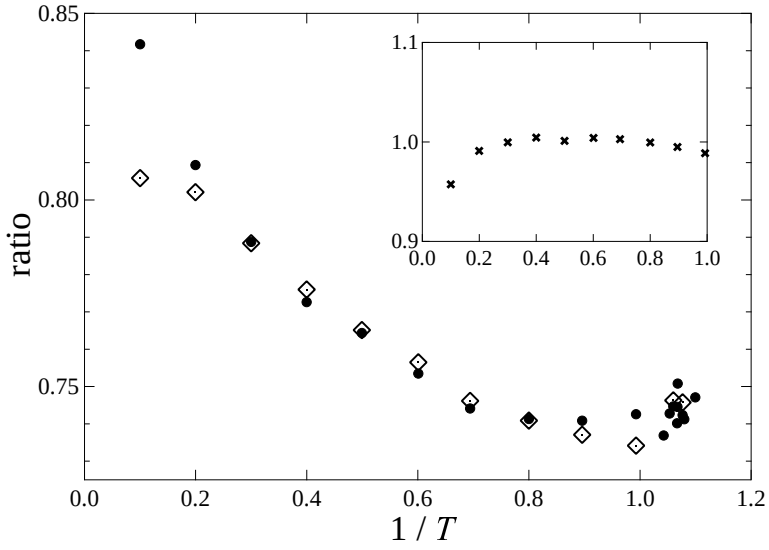

Figure 4.28: The two types of ratio are shown as function of the inverse temperature. Open diamonds represent the ratio $l^{(\mathrm{A})}/l^{(\mathrm{B})}$; and filled circles the square root of the ratio $\lim_{t\to\infty}\sqrt{M_2^{(\mathrm{A})}/M_2^{(\mathrm{B})}}$. The ratio of the above two ratios is shown in the inner plot and is almost one except in high temperature.

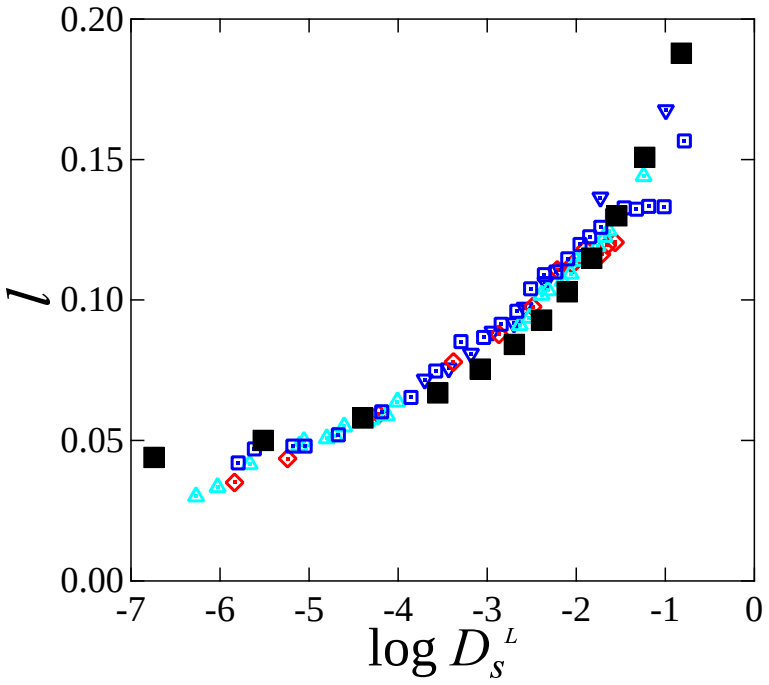

Figure 4.29: Plot of the mean-free path of A particle versus the long-time self-diffusion coefficient. The filled black squares represent results of the mode-coupling theory, blue squares results of Kob-Andersen binary mixtures [82], red diamonds those of a 15% poly-disperse hard sphere system [84], aqua triangles those of a 6% poly-disperse hard sphere system [85], and confined Lennard-Jones binary mixtures [86].

do not [82]. The bump means that the trapped particles intrude into cage. On the other hand, it does not appear in fitting by the mean-field theory.

The mean-free path $l^{(\mathrm{A})}$ is obtained by the mean-field analysis and shown in fig. 4.27. As the temperature decreases, $l^{(\mathrm{A})}$ decreases gradually. We note that the mean-free path $l^{(\mathrm{B})}$ of B particle is longer than $l^{(\mathrm{A})}$ at each temperature.

Figure 4.28 shows a couple of ratios $l^{(\mathrm{A})}/l^{(\mathrm{B})}$ and

$$\lim_{t\to\infty}\sqrt{M_2^{(\mathrm{A})}/M_2^{(\mathrm{B})}}.$$

As shown in the inner plot of fig. 4.28, the ratio of the mean-square displacement in long-time limit is almost same as that of the mean-free path especially in low temperature. This suggests a relationship between MFP and LSD. This result supports a universality predicted by Tokuyama [8, 87].

We finally discuss a universality. In fig. 4.29, the mean-free paths for different systems are plotted versus $\log D_S^L$. It is shown that the mean-free paths among different systems obey a master function of D_S^L [8]. However, results of the mode-coupling theory slightly deviate from such a master curve, where they are always smaller than the mean-free paths obtained by simulations in super-cooled region; $-2.6 > \log D_S^L > -5.1$ [8]. Since l is a length corresponding to the cage size, the result indicates the mode-coupling theory underestimates the cage size [87]. This agrees with our suggestion in ref. [88].

4.3.4 Numerical solutions of the alternative mode-coupling theory

In this subsection, the numerical results calculated by the alternative mode-coupling theory are shown for one-component Lennard-Jones systems.

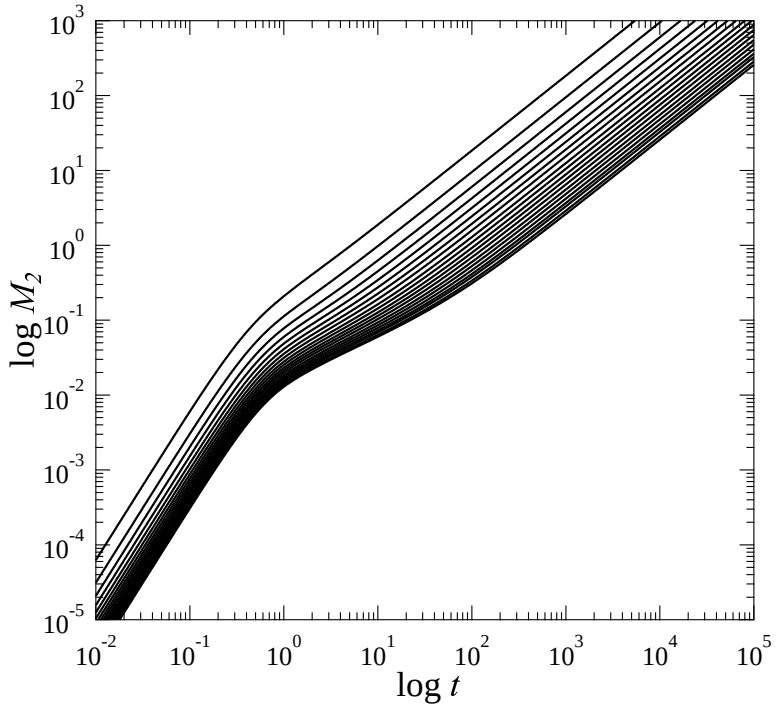

Figure 4.30: Log-log plot of the mean square displacement for one-component Lennard-Jones systems as function of the time for $T = 10.0$, 5.00, 3.33, 2.50, 2.00, 1.67, 1.43, 1.25, 1.11, 1.00, 0.909, 0.833, 0.769, 0.714, 0.667, 0.625, 0.588, 0.556, 0.526, and 0.500 (from left to right).

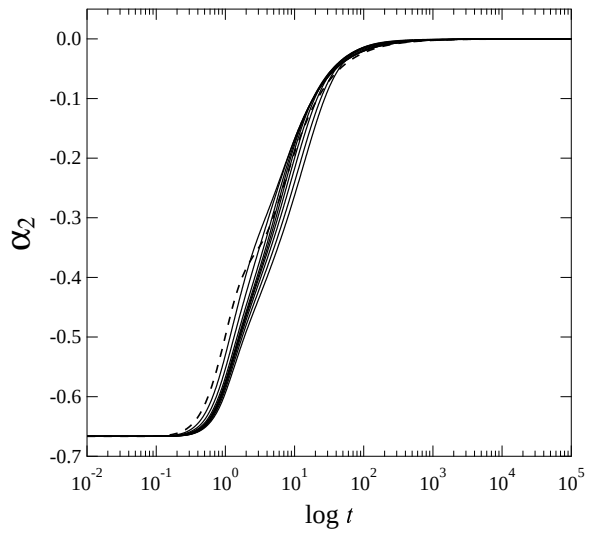

Figure 4.31: Semi-log plot of the non-Gaussian parameter for one-component Lennard-Jones systems as function of the time for $T = 10.0$ (dotted line), 5.00, 3.33, 2.50, 2.00, 1.67, 1.43, 1.25, 1.11, and 1.00 (from left to right).

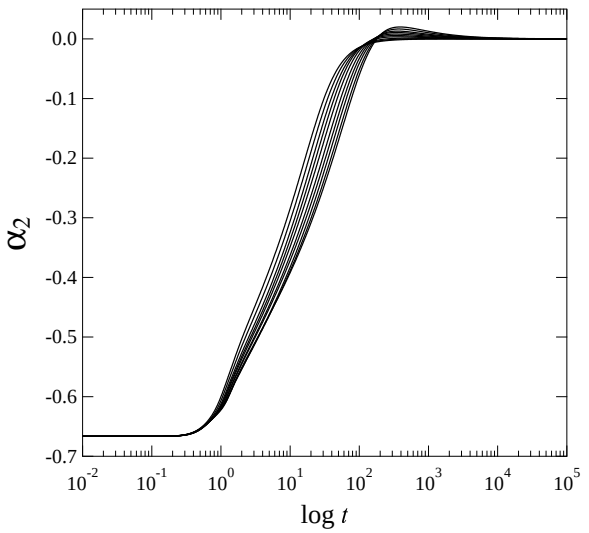

Figure 4.32: Semi-log plot of the non-Gaussian parameter for one-component Lennard-Jones systems as function of the time for $T = 0.909$, 0.833, 0.769, 0.714, 0.667, 0.625, 0.588, 0.556, 0.526, and 0.500 (from left to right).

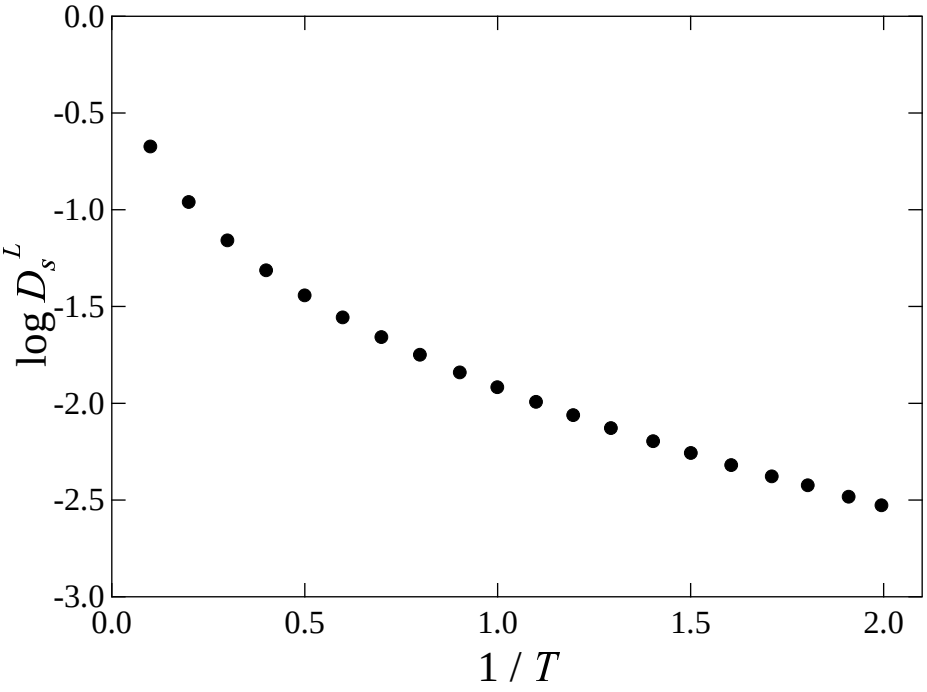

Figure 4.33: Semi-log plot of the long-time self-diffusion coefficient for one-component Lennard-Jones systems as function of the temperature.

Figure 4.30 shows results of the mean square displacement. No oscillation appearing in solutions of the conventional mode-coupling theory in the intermediate time scale is there.

Figures 4.31 and 4.32 show results of the non-Gaussian parameter. The non-Gaussian parameter is -0.667 as well as the conventional mode-coupling theory in the short-time limit, and it converges to zero in the long-time limit. The result of the highest temperature $T = 10.0$ (dotted line in fig. 4.31) gets across the lower temperature results near the crossover from ballistic to diffusion motion and it still is unclear. The peak heights of the non-Gaussian parameter in the alternative mode-coupling theory are small compared with that in the conventional one and simulation results. Considering that the three and more body effects are neglected in the mode-coupling theory, our results look reasonable because the non-Gaussian parameter without three and more body effects should be zero.

Figure 4.33 shows results of the long-time self-diffusion coefficient as function of the inverse temperature. Those decay as the temperature decreases but the decay rate is gentler by comparison with that of the conventional mode-coupling theory.

4.3.5 Comparison between conventional and alternative mode-coupling theory

We compare results between molecular dynamics simulations and numerical calculations. Figure 4.34 shows the comparison of the long-time self-diffusion coefficient.

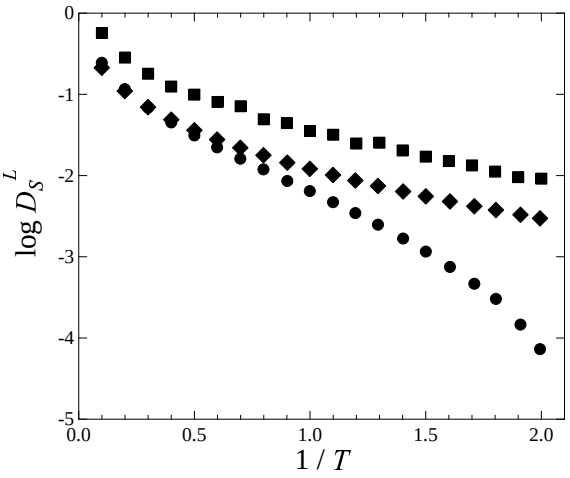

Figure 4.34: Semi-log plot of the long-time self-diffusion coefficient for one-component Lennard-Jones systems as function of the temperature. Circles represent results of the conventional mode-coupling theory, diamonds those of the alternative one, and squares those of the molecular dynamics simulations.

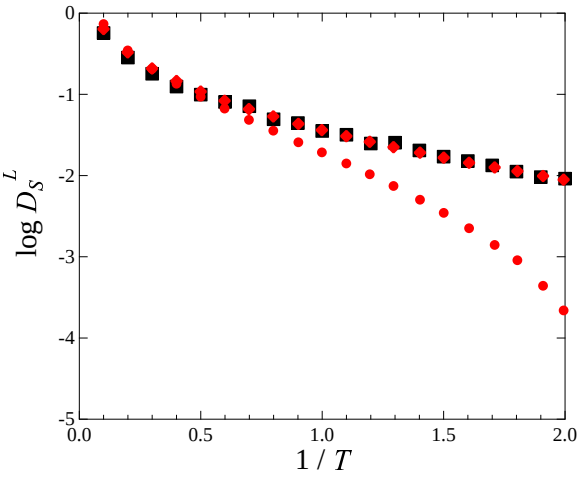

Figure 4.35: Semi-log plot of the long-time self-diffusion coefficient for one-component Lennard-Jones systems as function of the temperature. Red circles represent results of the conventional mode-coupling theory multiplied by factor three, Red diamonds those of the alternative one multiplied by factor three, and black squares those of the molecular dynamics simulations.

In high temperature regions, the results of the conventional and alternative mode-coupling theory are in agreement. It is reasonable because the memory term can be approximated to the delta function (i.e. Markov case) for both theory. As the temperature decreases, the long-time self-diffusion coefficient of the conventional theory decays. One of the problems of the conventional mode-coupling theory is underestimating the control parameter (e.g. the inverse

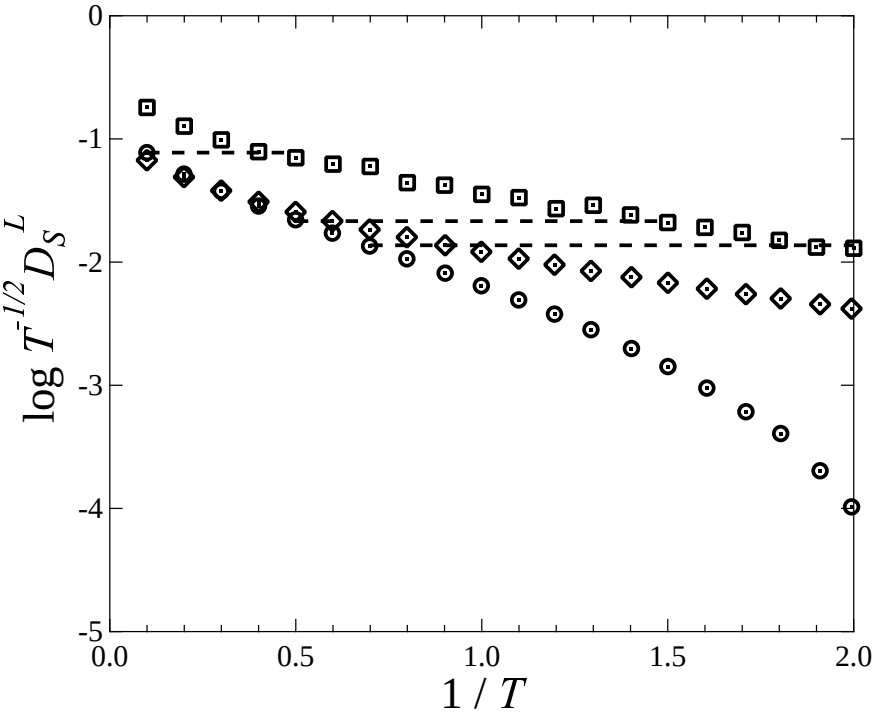

Figure 4.36: Semi-log plot of the compensated long-time self-diffusion coefficient for one-component Lennard-Jones systems as function of the temperature. Circles represent results of the conventional mode-coupling theory, diamonds those of the alternative one, squares those of the molecular dynamics simulations, and the three dashed lines shows the same compensated long-time self-diffusion coefficient to compare results.

temperature, the volume fraction, and so on). From this viewpoint, results of the alternative theory look better than those of the conventional one. Although results of the alternative theory are similar to those of the simulation results qualitatively, those do not agree quantitatively. Note that if results of the alternative mode-coupling theory are multiplied by factor three, those are surprisingly in agreement with the simulation results (shown in fig. 4.35), but it is no reason for the factor.

We next compare the mean square displacement in viewpoint of the mean-field theory in which the long-time self-diffusion coefficient is the universal control parameter. Figure 4.36 shows the compensated long-time self-diffusion coefficient by the temperature. We compare the mean square displacement at the same compensated long-time self-diffusion coefficient. It

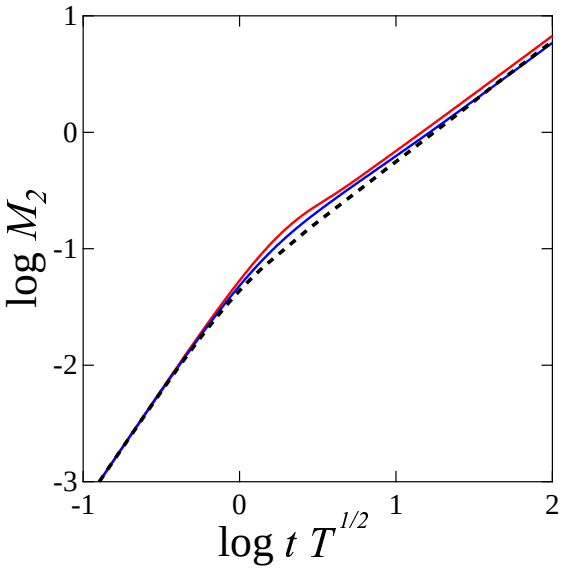

Figure 4.37: Log-log plot of the mean square displacement for one-component Lennard-Jones systems as function of the time. Dotted line represents the simulation result at $T = 2.0$, solid red line the result of the conventional mode-coupling theory at $T = 10.0$, and solid blue one that of the alternative one at $T = 10.0$.

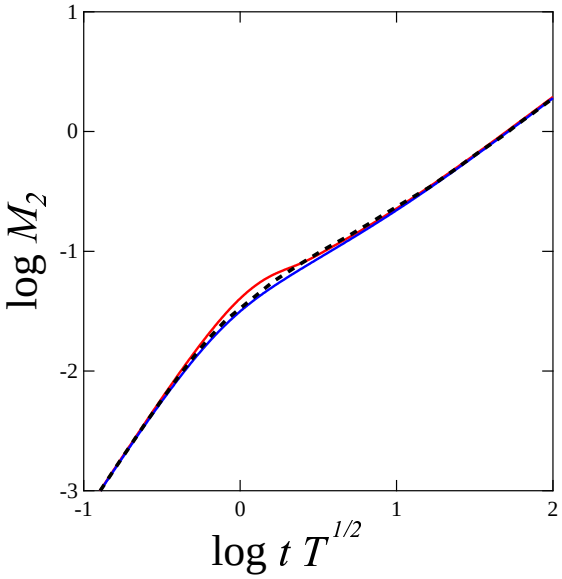

Figure 4.38: Log-log plot of the mean square displacement for one-component Lennard-Jones systems as function of the time. Dotted line represents the simulation result at $T = 0.667$, solid red line the result of the conventional mode-coupling theory at $T = 2.00$, and solid blue one that of the alternative one at $T = 1.67$.

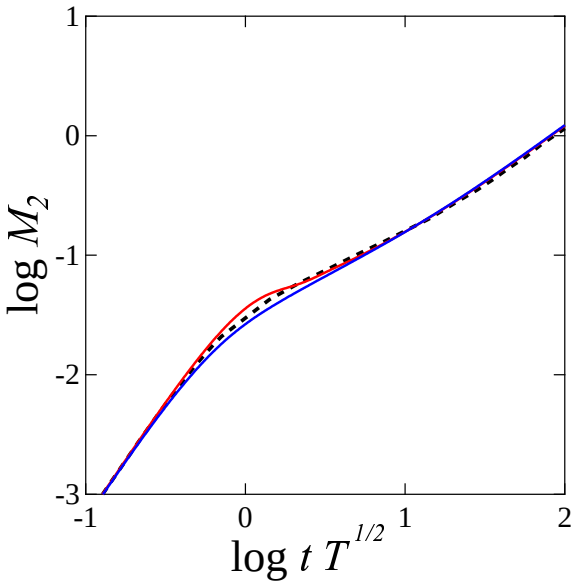

Figure 4.39: Log-log plot of the mean square displacement for one-component Lennard-Jones systems as function of the time. Dotted line represents the simulation result at $T = 0.500$, solid red line the result of the conventional mode-coupling theory at $T = 1.43$, and solid blue one that of the alternative one at $T = 1.11$.

is equivalent to the following temperature; (conventional MCT, alternative MCT, MD) = (10.0, 10.0, 2.00), (2.00, 1.67, 0.667), and (1.43, 1.11, 0.5) shown in fig. 4.36.

In the highest temperature (i.e. the largest long-time self-diffusion coefficient, fig. 4.37), in which the non-Gaussian parameter calculated from the mode-coupling theory is strange behavior, the numerical solutions overshoot comparing by the simulation result. It implies that the mode-coupling theory might do not describe dynamics of liquid far from the glass transition. In the middle long-time self-diffusion coefficient (fig. 4.37), the behavior calculated from the alternative theory is in agreement with the simulation result, although there is distinction between numerical solution from the conventional theory and the simulation result. However, in the lowest long-time self-diffusion coefficient (fig. 4.39), the numerical solution calculated from the alternative mode-coupling theory undershoots comparing by the simulation result, although that from the conventional theory overshoots. It implies that approximations that we employed in obtaining the alternative mode-coupling theory might be not appropriate to describe real situations.

4.4 Conclusion

We have solved the mode-coupling theory numerically to test it by comparing with results of molecular dynamics simulations for the Kob-Andersen type Lennard-Jones binary mixtures. Our results show that the distinction was based on that of the intermediate time scale, so-called β time scale, from viewpoint of the mean-field theory. We also have constructed an alternative mode-coupling theory to improve the conventional mode-coupling theory. The difference between them is the starting equation; that of the conventional theory is the convolution-type generalized Langevin equation but that of the alternative one is the product-type, so-called convolutionless, generalized Langevin equation. As well as the conventional mode-coupling

theory, the alternative mode-coupling equations were calculated numerically. Although there remains distinction between the numerical solutions of the alternative mode-coupling theory and the simulation results, dynamics predicted by the alternative theory is improved than that by the original one in terms of the qualitative behavior. Furthermore, the non-Gaussian parameter predicted from the alternative mode-coupling theory is more reasonable than that of the conventional theory because only two-body effect does not make the peak height of the non-Gaussian parameter higher. Some previous studies have shown that the product-type Langevin equation is compatible with nanoscale systems such as protein, those dominated by electron transfer, and so on. In nano-systems, dynamics interacting among several time and length scale is important, and our results show that the supercooled liquids is one of such systems. There remain some problems about approximation for the memory functions; the comparison between numerical solutions of the alternative mode-coupling theory and molecular dynamics simulations suggests that the approximation for the memory function might is not appropriate, and hence this is a future task what we should get rid of.

Chapter 5

Concluding Remarks

In this chapter, we briefly summarize our statements mentioned in this Ph. D thesis.

5.1 Which variables are important with respect to the dynamical heterogeneity?

We have employed two kinds of correlation functions; one of them is the vector correlation corresponding to the displacement correlation and the other is the scalar correlation corresponding to correlation of the mobility fluctuation. The correlation functions intrinsically depend on both time and distance, and we fix the time as the peak time of the non-Gaussian parameter to regard them as the dynamical correlation functions characterizing the dynamical heterogeneity. We can also extract the dynamical correlation lengths from the dynamical correlation functions. In the experiments for the binary colloidal mixtures, the detail behavior of the lengths did not get clear because the experimental data have much noise. On the other hand, in the molecular dynamics simulations for the Kob-Andersen type binary mixtures, although the vector correlation length converges at the temperature far away the glass transition point, the scalar correlation length increases toward the glass transition point and has a maximum in the vicinity of the glass transition. Although the largeness is almost same between the vector and scalar correlation lengths, the behavior suggests that the scalar correlation (i.e. correlation of the mobility fluctuation) influences to the glass transition more strongly than the vector correla-

tion (i.e. the displacement correlation). We, needless to say, should investigate much more correlations. Nevertheless, we got one guidepost to understand the glass transition: Study for the displacement (e.g. the mean square displacement) has mass apeak, although that of the mobility fluctuation does not. We also have to investigate the mobility fluctuation.

5.2 How large is the dynamical heterogeneity for binary mixtures?

The snapshot pictures for binary colloidal mixtures have shown the dynamical heterogeneity qualitatively. Furthermore, the dynamical correlation lengths can quantitatively estimate how large the dynamical heterogeneity is. Our results are that the range is several $(2 \sim 3)$ particle diameter even near the glass transition point for the binary colloidal mixtures and Kob-Andersen binary mixtures.

5.3 How does the size of the dynamical heterogeneity depend on systems?

Weeks et al. have carried out experiments for the poly-disperse one-component colloidal suspensions, and obtained the dynamical correlation lengths with about 10 particle diameter near the glass transition [43]. It is much larger than that of the binary cases. It implies that even less dynamical heterogeneity leads to the glass transition in the binary systems because the binary systems have a priori structure heterogeneity, and this statement is in agreement with previous study [68].

5.4 Is supercooled liquid the same as the coexistence of liquid and crystal?

Supercooled liquid resembles coexistence state of liquid and crystal from a viewpoint of statics [68]. However, the dynamics of them are much different from each other. The dynamical correlation length obtained from the scalar correlation diverges at the transition point for the

coexistence state, although that of the supercooled liquid does not. It also is shown that the scalar correlation and its correlation length might be a good physical variable to study crystal growth because the length diverges at the freezing point.

5.5 Glass transition temperature of the Kob-Andersen binary mixtures

The specific heat at constant volume leads us to obtaining the glass transition temperature for the Kob-Andersen type binary mixtures: $T_g \simeq 0.43$ which is close to the glass transition temperature defined by results of the long-time self-diffusion coefficient in a viewpoint of the mean-field theory. The specific heat is static (i.e. thermodynamics) quantity but the long-time self-diffusion coefficient is a dynamical variable. Since the glass transition is not a transition but a crossover, we should determine the glass transition point by using dynamical variables. Our results, however, indicate that the statics and dynamics strongly relate with each other in terms of the glass transition.

5.6 Origin of distinction in the mode-coupling theory

It is known that the mode-coupling theory underestimates the control parameter such as the inverse temperature, the volume fraction, and so on. We have identified that the distinction has its origin in the intermediate time region, called β time region: The mode-coupling theory do not correctly describe the cage dynamics qualitatively.

5.7 Adequacy of the alternative mode-coupling theory

We have constructed the alternative mode-coupling theory. The starting equation of the alternative theory, product-type generalized Langevin equation, is different from that of the conventional theory, convolution-type generalized Langevin equation. In order to build a closure relation, the memory term is approximated and converges to zero in the β time region. The

comparison of the mean square displacement between the numerical solutions and the simulation results shows that the approximation might be not appropriate and this is an interesting task what we should get rid of in the future. However, the qualitative behavior gets better from the results of the mean square displacement and the long-time self-diffusion coefficient. In addition, the non-Gaussian parameter looks nicer because only two-body effect does not make the peak height of the non-Gaussian parameter higher.

5.8 Estimation of the size of the dynamical heterogeneity by the mode-coupling theory

One of natural steps is to predict behavior of the dynamical correlation functions by the mode-coupling theory. Biroli and Bouchaud have suggested from the field-theoretical approach that the mode-coupling theory can develop the expression of a length scale of the dynamical heterogeneity [89]. Note that the length scale estimated by the mode-coupling theory is different from the above dynamical correlation length obtained from the scalar and vector correlation functions. To estimate a length scale by the mode-coupling theory, they analyzed the four-body correlation function whose generating function is the same as that of the vector correlation function. Since it has been suggested from our simulation results that the scalar correlation functions is more distinguished near the glass transition, we should analyze the scalar one by the mode-coupling theory.

Appendix A

Conventional (Mori type) Mode-Coupling Theory

A.1 Algorithm of the Intermediate Scattering Function in Binary Mixture

A.1.1 Exact equation of motion

Let $\mathcal{P}$ denote a projection operator defined as

$$\mathcal{P}\boldsymbol{X} := \left\langle \boldsymbol{X}\boldsymbol{A}^{\dagger} \right\rangle \cdot \overleftrightarrow{\phi}^{-1} \cdot \boldsymbol{A}, \tag{A.1}$$

where the correlation tensor $\overleftrightarrow{\phi}(t)$ is represented by

$$\overleftrightarrow{\phi}(t) := \begin{pmatrix} \langle \boldsymbol{\delta\rho}_q(t)\boldsymbol{\delta\rho}_{-q}\rangle & -\left\langle \boldsymbol{\delta\rho}_q(t)\boldsymbol{j}^L_{-q}\right\rangle \\ \left\langle \boldsymbol{j}^L_q(t)\boldsymbol{\delta\rho}_{-q}\right\rangle & -\left\langle \boldsymbol{j}^L_q(t)\boldsymbol{j}^L_{-q}\right\rangle \end{pmatrix} = \begin{pmatrix} \mathsf{F}(q,t) & -\left\langle \boldsymbol{\delta\rho}_q(t)\boldsymbol{j}^L_{-q}\right\rangle \\ \frac{1}{iq}\partial_t\mathsf{F}(q,t) & -\left\langle \boldsymbol{j}^L_q(t)\boldsymbol{j}^L_{-q}\right\rangle \end{pmatrix}, \tag{A.2}$$

with the intermediate scattering tensor $\mathsf{F}(q,t)$ that contains the partial intermediate scattering functions $F^{(\alpha\beta)}(q,t) = \left\langle \delta\rho^{(\alpha)}_q(t)\delta\rho^{(\beta)}_{-q}\right\rangle$. Note that $\delta\rho^{(\alpha)}_q(t)^{\dagger} = \delta\rho^{(\alpha)}_{-q}(t)^{\mathrm{T}}$ and $j^{L(\alpha)}_q(t)^{\dagger} = -j^{L(\alpha)}_{-q}(t)^{\mathrm{T}}$. Since the initial correlation $\overleftrightarrow{\phi}$ is represented by

$$\overleftrightarrow{\phi} = \begin{pmatrix} \mathsf{S}(q) & 0 \\ 0 & (m\beta)^{-1}\mathbf{1}_2 \end{pmatrix}, \tag{A.3}$$

the inverse tensor of the initial correlation is

$$\overleftrightarrow{\phi}^{-1} = \begin{pmatrix} \mathsf{S}^{-1}(q) & 0 \\ 0 & m\beta\mathbf{1}_2 \end{pmatrix}, \tag{A.4}$$

where $\mathsf{S}(q)$ denotes the static structure factor extended to binary systems that contains the partial scattering functions $S^{(\alpha\beta)}(q,t) := F^{(\alpha\beta)}(q,0)$ and $\mathbf{1}_n$ the $n \times n$ unit tensor. Using Mori type projection method, we obtain an equation for correlation function $\overleftrightarrow{\phi}(q,t)$ as

$$\partial_t \overleftrightarrow{\phi}(q,t) = i\overleftrightarrow{\omega} \cdot \overleftrightarrow{\phi}(q,t) - \int_0^t \mathrm{d}s \overleftrightarrow{\varphi}(q,t-s) \cdot \overleftrightarrow{\phi}(q,s), \tag{A.5}$$

Thus,

$$i\overleftrightarrow{\omega} = \begin{pmatrix} \left\langle \dot{\boldsymbol{\delta\rho}}_q \boldsymbol{\delta\rho}_{-q} \right\rangle & -\left\langle \dot{\boldsymbol{\delta\rho}}_q \boldsymbol{j}^L_{-q} \right\rangle \\ \left\langle \dot{\boldsymbol{j}}^L_q \boldsymbol{\delta\rho}_{-q} \right\rangle & -\left\langle \dot{\boldsymbol{j}}^L_q \boldsymbol{j}^L_{-q} \right\rangle \end{pmatrix} \cdot \overleftrightarrow{\phi}^{-1} = iq \begin{pmatrix} 0 & \mathbf{1}_2 \\ (m\beta)^{-1}\mathsf{S}^{-1}(q) & 0 \end{pmatrix}. \tag{A.6}$$

The initial random term $\boldsymbol{R} = \mathcal{Q}i\mathcal{L}\boldsymbol{A}$ is represented by

$$\boldsymbol{R} = \begin{pmatrix} \mathbf{0} \\ \dot{\boldsymbol{j}}^L_q - \dfrac{iq}{m\beta}\mathsf{S}^{-1}(q) \cdot \boldsymbol{\delta\rho}_q \end{pmatrix} =: \begin{pmatrix} \mathbf{0} \\ \boldsymbol{R}_q \end{pmatrix}. \tag{A.7}$$

Defining $\boldsymbol{R}_q(t)$ as $\boldsymbol{R}_q(t) := e^{t\mathcal{Q}i\mathcal{L}}\boldsymbol{R}_q$, the memory tensor is represented by

$$\overleftrightarrow{\varphi}(t) = \begin{pmatrix} 0 & 0 \\ 0 & \left\langle \boldsymbol{R}_q(t)\boldsymbol{R}^\dagger_q \right\rangle \end{pmatrix} \cdot \overleftrightarrow{\phi}^{-1} = \begin{pmatrix} 0 & 0 \\ 0 & m\beta \left\langle \boldsymbol{R}_q(t)\boldsymbol{R}^\dagger_q \right\rangle \end{pmatrix}. \tag{A.8}$$

Therefore, we obtain an exact differential equation for binary systems as

$$\partial_t^2 \mathsf{F}(q,t) + \frac{q^2}{m\beta}\mathsf{S}^{-1}(q) \cdot \mathsf{F}(q,t) + m\beta \int_0^t \mathrm{d}s \left\langle \boldsymbol{R}_q(t-s)\boldsymbol{R}^\dagger_q \right\rangle \cdot \partial_s \mathsf{F}(q,s) = 0. \tag{A.9}$$

A.1.2 Approximative equation of motion in MCT

We introduce a new projection operator defined by

$$\mathcal{P}_2 \boldsymbol{X} = \sum_{k_1,k_2,k_3,k_4} \left\langle \boldsymbol{X}\mathsf{B}^\dagger_{1,2} \right\rangle \cdot \left\langle \mathsf{B}_{1,2}\mathsf{B}^\dagger_{3,4} \right\rangle^{-1} \cdot \mathsf{B}_{3,4}, \tag{A.10}$$

where $\mathsf{B}_{1,2} := \boldsymbol{\delta\rho}_{k_1}\boldsymbol{\delta\rho}^{\mathrm{T}}_{k_2}$ and $\mathsf{B}^\dagger_{1,2} := \boldsymbol{\delta\rho}_{-k_2}\boldsymbol{\delta\rho}^{\mathrm{T}}_{-k_1}$. The $\left\langle \mathsf{B}_{1,2}\mathsf{B}^\dagger_{3,4} \right\rangle$ is a fourth-rank tensor and the inverse tensor $\left\langle \mathsf{B}_{1,2}\mathsf{B}^\dagger_{3,4} \right\rangle^{-1}$ is defined as

$$\sum_{k_3,k_4} \left\langle \mathsf{B}_{1,2}\mathsf{B}^\dagger_{3,4} \right\rangle^{-1} \cdot \left\langle \mathsf{B}_{3,4}\mathsf{B}^\dagger_{5,6} \right\rangle = \delta_{k_1,k_5}\delta_{k_2,k_6} =: \delta_{1,5}\delta_{2,6}. \tag{A.11}$$

We operate the projection operator to the random term $\boldsymbol{R}_q$ to obtain

$$\mathcal{P}_2 \boldsymbol{R}_q = \sum_{k_3,k_4} \mathsf{V}_q(3,4) \cdot \mathsf{B}_{3,4}, \tag{A.12}$$

where $\mathsf{V}_q(3,4)$ denotes the vertex tensor, which is a third-rank tensor, defined as

$$\mathsf{V}_q(3,4) := \sum_{k_1,k_2} \left\langle \boldsymbol{R}_q \mathsf{B}^\dagger_{1,2} \right\rangle \cdot \left\langle \mathsf{B}_{1,2} \mathsf{B}^\dagger_{3,4} \right\rangle^{-1}. \tag{A.13}$$

Note that $\mathsf{V}_q(3,4) = \delta_{4,q-3}\mathsf{V}_q(3,4)$ from the definition. The term $\left[\left\langle \boldsymbol{R}_q \mathsf{B}^\dagger_{1,2} \right\rangle\right]^{(\alpha\beta\gamma)}$ reduces to

$$\begin{aligned}
\left[\left\langle \boldsymbol{R}_q \mathsf{B}^\dagger_{1,2} \right\rangle\right]^{(\alpha\beta\gamma)} &= \left\langle \left(i\mathcal{L} j_q^{L(\alpha)}\right) \delta\rho^{(\beta)}_{-2} \delta\rho^{(\gamma)}_{-1} \right\rangle - \frac{iq}{m\beta} \sum_{\epsilon} \left[\mathsf{S}^{-1}(q)\right]^{(\alpha\epsilon)} \left\langle \delta\rho^{(\epsilon)}_q \delta\rho^{(\beta)}_{-2} \delta\rho^{(\gamma)}_{-1} \right\rangle \\
&= \frac{i\delta_{2,q-1}}{m\beta\sqrt{N_\alpha}} \tilde{\boldsymbol{q}} \cdot \boldsymbol{k}_1 S^{(\alpha\beta)}(k_2) \left\{\delta_{\alpha\gamma} - S^{(\alpha\gamma)}(k_1)\right\} \\
&\quad + \frac{i\delta_{2,q-1}}{m\beta\sqrt{N_\alpha}} \tilde{\boldsymbol{q}} \cdot \boldsymbol{k}_2 S^{(\alpha\gamma)}(k_1) \left\{\delta_{\alpha\beta} - S^{(\alpha\beta)}(k_2)\right\},
\end{aligned} \tag{A.14}$$

where the convolution approximation [32]

$$\left\langle \delta\rho^{(\epsilon)}_q \delta\rho^{(\beta)}_{-2} \delta\rho^{(\gamma)}_{-1} \right\rangle \simeq \delta_{2,q-1} \sum_{\xi} \frac{1}{\sqrt{N_\xi}} S^{(\epsilon\xi)}(q) S^{(\beta\xi)}(k_2) S^{(\gamma\xi)}(k_1) \tag{A.15}$$

has been employed. Furthermore, $\delta_{2,q-1}\left[\left\langle \mathsf{B}_{1,2} \mathsf{B}^\dagger_{3,4} \right\rangle\right]^{(\alpha\beta\gamma\epsilon)}$ reduces to

$$\begin{aligned}
\delta_{2,q-1}\left[\left\langle \mathsf{B}_{1,2} \mathsf{B}^\dagger_{3,4} \right\rangle\right]^{(\alpha\beta\gamma\epsilon)} &= \delta_{2,q-1}\delta_{4,q-3} \left\langle \delta\rho^{(\alpha)}_1 \delta\rho^{(\beta)}_{q-1} \delta\rho^{(\gamma)}_{3-q} \delta\rho^{(\epsilon)}_{-3} \right\rangle \\
&\simeq \delta_{2,q-1}\delta_{4,q-3} \left[\delta_{3,q-1} S^{(\alpha\gamma)}(k_1) S^{(\beta\epsilon)}(k_2) + \delta_{3,1} S^{(\alpha\epsilon)}(k_1) S^{(\beta\gamma)}(k_2)\right],
\end{aligned} \tag{A.16}$$

where the decoupling approximation has been employed. It is difficult to treat with the inverse fourth-rank tensor directly. Instead of eq. (A.13), we consider the equation given by

$$\sum_{k_3,k_4} \mathsf{V}_q(3,4) \cdot \left\langle \mathsf{B}_{3,4} \mathsf{B}^\dagger_{5,6} \right\rangle = \left\langle \boldsymbol{R}_q \mathsf{B}^\dagger_{5,6} \right\rangle. \tag{A.17}$$

From the above equation, we can obtain

$$\delta_{6,q-5}\left\{V_q^{(\xi\beta\alpha)}(6,5)+V_q^{(\xi\alpha\beta)}(5,6)\right\}=-\frac{i\delta_{6,q-5}}{m\beta\sqrt{N_\xi}}\left\{\tilde{\boldsymbol{q}}\cdot\boldsymbol{k}_5\delta_{\xi\alpha}c_2^{(\xi\beta)}(k_5)+\tilde{\boldsymbol{q}}\cdot\boldsymbol{k}_6\delta_{\xi\beta}c_2^{(\xi\alpha)}(k_6)\right\}, \tag{A.18}$$

where $\mathsf{c}_2(q)$ denotes the direct correlation matrix defined by

$$c_2^{(\alpha\beta)}(q):=\delta_{\alpha\beta}-\left[\mathsf{S}^{-1}(q)\right]^{(\alpha\beta)}. \tag{A.19}$$

Because of the definition of the vertex, $V_q^{(\xi\beta\alpha)}(6,5)=V_q^{(\xi\alpha\beta)}(5,6)$. Therefore, the vertex is represented as

$$V_q^{(\xi\alpha\beta)}(5,6)=-\frac{i\delta_{6,q-5}}{2m\beta\sqrt{N_\xi}}\left\{\tilde{\boldsymbol{q}}\cdot\boldsymbol{k}_5\delta_{\xi\alpha}c_2^{(\xi\beta)}(k_5)+\tilde{\boldsymbol{q}}\cdot\boldsymbol{k}_6\delta_{\xi\beta}c_2^{(\xi\alpha)}(k_6)\right\}. \tag{A.20}$$

We employ two approximations here; one is $\boldsymbol{R}_q\simeq\mathcal{P}_2\boldsymbol{R}_q$, and another is $\boldsymbol{R}_q(t)\simeq e^{i\mathcal{L}t}\boldsymbol{R}_q$. We can thus calculate the memory term as

$$\left[\left\langle\boldsymbol{R}_q(t)\boldsymbol{R}_q^\dagger\right\rangle\right]^{(ij)}\simeq\left[\left\langle\left(e^{i\mathcal{L}t}\mathcal{P}_2\boldsymbol{R}_q\right)\left(\mathcal{P}_2\boldsymbol{R}_q\right)^\dagger\right\rangle\right]^{(ij)}$$

$$\simeq\frac{1}{2(m\beta)^2\sqrt{N_iN_j}}\sum_{\boldsymbol{k}}\sum_{\alpha,\alpha',\beta,\beta'}\tilde{V}_q^{(i\alpha\beta)}(\boldsymbol{k})\tilde{V}_q^{(j\beta'\alpha')}(\boldsymbol{q}-\boldsymbol{k})F^{(\alpha\alpha')}(|\boldsymbol{q}-\boldsymbol{k}|,t)F^{(\beta\beta')}(k,t), \tag{A.21}$$

where

$$\tilde{V}_q^{(i\alpha\beta)}(\boldsymbol{k}):=\tilde{\boldsymbol{q}}\cdot\boldsymbol{k}\delta_{i\alpha}c_2^{(i\beta)}(k)+\tilde{\boldsymbol{q}}\cdot(\boldsymbol{q}-\boldsymbol{k})\delta_{i\beta}c_2^{(i\alpha)}(|\boldsymbol{q}-\boldsymbol{k}|). \tag{A.22}$$

Therefore, we get an approximative MCT equation for binary mixtures as

$$\partial_t^2F^{(\alpha\beta)}(q,t)+\sum_\gamma\frac{q^2}{m\beta}\left[\mathsf{S}^{-1}(q)\right]^{(\alpha\gamma)}F^{(\gamma\beta)}(q,t)+\int_0^t\mathrm{d}s\sum_\gamma K^{(\alpha\gamma)}(\boldsymbol{q},t-s)\partial_sF^{(\gamma\beta)}(q,s)=0, \tag{A.23}$$

where the memory tensor $\mathsf{K}(\boldsymbol{q},t)$ is defined as

$$K^{(ij)}(\boldsymbol{q},t):=$$

$$\frac{V}{2m\beta\sqrt{N_iN_j}}\int\frac{\mathrm{d}\boldsymbol{k}}{(2\pi)^3}\sum_{\alpha,\alpha',\beta,\beta'}\tilde{V}_q^{(i\alpha\beta)}(\boldsymbol{k})\tilde{V}_q^{(j\beta'\alpha')}(\boldsymbol{q}-\boldsymbol{k})F^{(\alpha\alpha')}(|\boldsymbol{q}-\boldsymbol{k}|,t)F^{(\beta\beta')}(k,t). \tag{A.24}$$

A.1.3 Numerical algorithm of memory term

The approximative memory term in MCT equation for binary mixtures is represented as[1]

$$K^{(ij)}(\boldsymbol{q},t)=\frac{V}{2m\beta\sqrt{N_iN_j}}\int\frac{\mathrm{d}\boldsymbol{k}}{(2\pi)^3}\tilde{V}_q^{(i\alpha\beta)}(\boldsymbol{k})\tilde{V}_q^{(j\beta'\alpha')}(\boldsymbol{q}-\boldsymbol{k})F^{(\alpha\alpha')}(|\boldsymbol{q}-\boldsymbol{k}|,t)F^{(\beta\beta')}(k,t), \tag{A.25}$$

where $\tilde{V}_q^{(i\alpha\beta)}(\boldsymbol{k})$ is defined by eq. (A.22).

In order to solve the approximative MCT equation numerically, we rewrite the memory term in a symmetrized form. We change the variable of integration from $\boldsymbol{k}$ to $\boldsymbol{p}=\boldsymbol{k}-\boldsymbol{q}/2$ to obtain

$$\begin{aligned}K^{(ij)}(\boldsymbol{q},t) &= \frac{V}{8\pi^2m\beta\sqrt{N_iN_j}}\int_0^\infty\mathrm{d}p\int_0^\pi\mathrm{d}\theta p^2\sin\theta\\ &\quad\times\tilde{V}_q^{(i\alpha\beta)}\left(\frac{\boldsymbol{q}}{2}+\boldsymbol{p}\right)\tilde{V}_q^{(j\beta'\alpha')}\left(\frac{\boldsymbol{q}}{2}-\boldsymbol{p}\right)F^{(\alpha\alpha')}\left(\left|\frac{\boldsymbol{q}}{2}-\boldsymbol{p}\right|,t\right)F^{(\beta\beta')}\left(\left|\frac{\boldsymbol{q}}{2}+\boldsymbol{p}\right|,t\right).\end{aligned} \tag{A.26}$$

The z-component of $\boldsymbol{p}$ points to the same direction as $\boldsymbol{q}$, and $\mathsf{V}_q(\boldsymbol{q}/2\pm\boldsymbol{p})$ actually depends on p and θ that is the angle between $\boldsymbol{q}$ and $\boldsymbol{p}$. Furthermore, using

$$x=\left|\frac{\boldsymbol{q}}{2}+\boldsymbol{p}\right|\quad\text{and}\quad y=\left|\frac{\boldsymbol{q}}{2}-\boldsymbol{p}\right|,$$

the memory term reduces to

$$K^{(ij)}(\boldsymbol{q},t) = \frac{V}{32\pi^2m\beta\sqrt{N_iN_j}q^3}\int_0^\infty\mathrm{d}x\int_{|x-q|}^{x+q}\mathrm{d}yxy$$

[1] In what follows, we employ the Einstein notation.

$$\times \bar{V}_q^{(i\alpha\beta)}(x,y)\bar{V}_q^{(j\alpha'\beta')}(x,y)F^{(\alpha\alpha')}(y,t)F^{(\beta\beta')}(x,t), \tag{A.27}$$

where $\bar{V}_q^{(i\alpha\beta)}(x,y)$ is defined as

$$\bar{V}_q^{(i\alpha\beta)}(x,y) = (q^2+x^2-y^2)\delta_{i\alpha}c_2^{(i\beta)}(x) + (q^2-x^2+y^2)\delta_{i\beta}c_2^{(i\alpha)}(y), \tag{A.28}$$

the Jacobian is represented by

$$\mathcal{J} = \left| \begin{array}{cc} \dfrac{\partial x}{\partial p} & \dfrac{\partial x}{\partial \theta} \\ \dfrac{\partial y}{\partial p} & \dfrac{\partial y}{\partial \theta} \end{array} \right| = \left| \begin{array}{cc} \dfrac{1}{x}(p+\dfrac{q}{2}\cos\theta) & -\dfrac{pq\sin\theta}{2x} \\ \dfrac{1}{y}(p-\dfrac{q}{2}\cos\theta) & \dfrac{pq\sin\theta}{2y} \end{array} \right| = \frac{qp^2\sin\theta}{xy} \tag{A.29}$$

and

$$\boldsymbol{q}\cdot\left(\frac{\boldsymbol{q}}{2}\pm\boldsymbol{p}\right) = \frac{q^2\pm(x^2-y^2)}{2}. \tag{A.30}$$

Derivation of the integral range of x and y is explained in subsection B.4.

Flenner et al. have suggested that the above calculation does not give right results when q is too small [36]. However, we check that the error is small enough to neglect it in our calculations.

In the Kob–Andersen model, the length is scaled with σ_{AA} the time with $\tau_{LJ} = \sigma_{AA}\sqrt{m/48\varepsilon_{AA}}$, and the temperature with $T_{LJ} = \epsilon_{AA}/k_B$. We thus obtain the dimensionless vertex as

$$\begin{aligned} \bar{V}_q^{(i\alpha\beta)}(x,y) &= \frac{1}{{\sigma_{AA}}^2}\left\{(\hat{q}^2+\hat{x}^2-\hat{y}^2)\delta_{i\alpha}\hat{c}_2^{(i\beta)}(\hat{x}) + (\hat{q}^2-\hat{x}^2+\hat{y}^2)\delta_{i\beta}\hat{c}_2^{(i\alpha)}(\hat{y})\right\} \\ &:= \frac{1}{{\sigma_{AA}}^2}\hat{\bar{V}}_{\hat{q}}^{(i\alpha\beta)}(\hat{x},\hat{y}). \end{aligned} \tag{A.31}$$

Similarly, the dimensionless memory term is written as

$$\begin{aligned} K^{(ij)}(\boldsymbol{q},t) &= \frac{\hat{T}\hat{V}}{32\pi^2\sqrt{N_iN_j}\hat{q}^3}\frac{\varepsilon_{AA}}{m{\sigma_{AA}}^2}\int_0^\infty \mathrm{d}\hat{x}\int_{|\hat{x}-\hat{q}|}^{\hat{x}+\hat{q}}\mathrm{d}\hat{y}\hat{x}\hat{y} \\ &\quad \times\hat{\bar{V}}_{\hat{q}}^{(i\alpha\beta)}(\hat{x},\hat{y})\hat{\bar{V}}_{\hat{q}}^{(j\alpha'\beta')}(\hat{x},\hat{y})\hat{F}^{(\alpha\alpha')}(\hat{y},\hat{t})\hat{F}^{(\beta\beta')}(\hat{x},\hat{t}) \end{aligned}$$

$$=: \quad \frac{\hat{T}\hat{V}}{1536\pi^2\sqrt{N_iN_j}\hat{q}^3}\frac{1}{{\tau_{LJ}}^2}\hat{K}^{(ij)}(\hat{\boldsymbol{q}},\hat{t}) =: \frac{1}{{\tau_{LJ}}^2}\hat{M}^{(ij)}(\hat{\boldsymbol{q}},\hat{t}). \tag{A.32}$$

This result leads us to rewrite eq. (A.23) as

$$\partial_{\hat{t}}^2\mathsf{F}(\hat{q},\hat{t}) + \frac{\hat{q}^2\hat{T}}{48}\mathsf{S}^{-1}(\hat{q})\cdot\mathsf{F}(\hat{q},\hat{t}) + \int_0^{\hat{t}}\mathrm{d}\hat{s}\hat{\mathsf{M}}(\hat{q},\hat{t}-\hat{s})\cdot\partial_{\hat{s}}\mathsf{F}(\hat{q},\hat{s}) = 0. \tag{A.33}$$

The lag of the wave number Δq should be small enough to obtain correct results. However, too small Δq makes calculation time longer. When we want data at q_w we set $q_w = n\Delta q + q_c$, where n denotes a certain integer. In what follows, it is assumed that $q_c\sigma_{AA} \ll 1$ for sake of simplicity. The memory term

$$\hat{K}^{(ij)}(\boldsymbol{q},t) = \hat{K}^{(ij)}(q,t) =: \int_0^\infty \mathrm{d}xx\int_{|q-x|}^{|q+x|}\mathrm{d}yyQ_q^{(ij)}(x,y). \tag{A.34}$$

reduces to

$$\hat{K}^{(ij)}(q+q_c,t) = \int_0^\infty \mathrm{d}xx\int_{|q+q_c-x|}^{q+q_c+x}\mathrm{d}yyQ_{q+q_c}^{(ij)}(x,y). \tag{A.35}$$

We cannot treat infinity number in numerical calculations. Thus, we have to set the ceiling of the integral q_m. In order to carry out the double integral with regard to the wave number correctly, we should set q_m as $c_2(q) \simeq 0$ for $q > q_m$. We next divide the range of integral into two parts;

$$\hat{K}^{(ij)}(q+q_c,t) = \int_0^{q_c}\mathrm{d}xx\int_{|q+q_c-x|}^{q+q_c+x}\mathrm{d}yyQ_{q+q_c}^{(ij)}(x,y) + \int_{q_c}^{q_m+q_c}\mathrm{d}xx\int_{|q+q_c-x|}^{q+q_c+x}\mathrm{d}yyQ_{q+q_c}^{(ij)}(x,y). \tag{A.36}$$

The first term of RHS of eq. (A.36) reduces to

$$\begin{aligned}\int_0^{q_c}\mathrm{d}xx\int_{|q+q_c-x|}^{q+q_c+x}\mathrm{d}yyQ_{q+q_c}^{(ij)}(x,y) &\simeq \frac{{q_c}^2}{2}\int_q^{q+2q_c}\mathrm{d}yyQ_{q+q_c}^{(ij)}(q_c,y)\\ &= \frac{{q_c}^2}{2}\int_{q-q_c}^{q+q_c}\mathrm{d}y'(y'+q_c)Q_{q+q_c}^{(ij)}(q_c,y'+q_c)\\ &\simeq \frac{{q_c}^2}{2}\cdot 2q_c(q+q_c)Q_{q+q_c}^{(ij)}(q_c,q+q_c).\end{aligned} \tag{A.37}$$

On the other hand, the second term of RHS of eq. (A.36) reduces to

$$\begin{aligned}
&\int_{q_c}^{q_m+q_c} \mathrm{d}x x \int_{|q+q_c-x|}^{q+q_c+x} \mathrm{d}y y Q^{(ij)}_{q+q_c}(x,y) \\
= &\int_0^{q_m} \mathrm{d}x'(x'+q_c) \int_{|q-x'|-q_c}^{q+x'+q_c} \mathrm{d}y'(y'+q_c) Q^{(ij)}_{q+q_c}(x'+q_c, y'+q_c) \\
\simeq &\int_0^{q_m} \mathrm{d}x'(x'+q_c) q_c(|q-x'|+q_c) Q^{(ij)}_{q+q_c}(x'+q_c, |q-x'|+q_c) \\
&+ \int_0^{q_m} \mathrm{d}x'(x'+q_c) \int_{|q-x'|}^{q+x'} \mathrm{d}y'(y'+q_c) Q^{(ij)}_{q+q_c}(x'+q_c, y'+q_c) \\
&+ \int_0^{q_m} \mathrm{d}x'(x'+q_c) q_c(q+x'+q_c) Q^{(ij)}_{q+q_c}(x'+q_c, q+x'+q_c). \qquad \text{(A.38)}
\end{aligned}$$

We employ the composite Simpson's rule (see subsection B.6) to solve the dimensionless memory term numerically.

A.1.4 Convolution integral

We need to treat with the convolution integral represented by

$$\int_0^t \mathrm{d}s M^{(\alpha\gamma)}(q, t-s) \partial_s F^{(\gamma\beta)}(q,s). \qquad \text{(A.39)}$$

We can obtain

$$\begin{aligned}
\int_0^t \mathrm{d}s M^{(\alpha\gamma)}(q,t-s)\partial_s F^{(\gamma\beta)}(q,s) &= M^{(\alpha\gamma)}(q,t-t^*)F^{(\gamma\beta)}(q,t^*) - M^{(\alpha\gamma)}(q,t)S^{(\gamma\beta)}(q) \\
&\quad - \int_0^{t^*} \mathrm{d}s \left\{\partial_s M^{(\alpha\gamma)}(q,t-s)\right\} F^{(\gamma\beta)}(q,s) \\
&\quad - \int_0^{t-t^*} \mathrm{d}s M^{(\alpha\gamma)}(q,s)\partial_s F^{(\gamma\beta)}(q,t-s). \qquad \text{(A.40)}
\end{aligned}$$

with an arbitrary time t^*. Moreover, we employ an approximation represented as

$$\int_0^t \mathrm{d}\tau \{\partial_\tau X(t-\tau)\} Y(\tau) = \sum_{j=1}^{J} \int_{t_{j-1}}^{t_j} \mathrm{d}\tau \{\partial_\tau X(t-\tau)\} Y(\tau)$$

$$\simeq \frac{1}{\Delta t}\sum_{j=1}^{J}\{X(t-t_j)-X(t-t_{j-1})\}\int_{t_{j-1}}^{t_j}\mathrm{d}\tau Y(\tau), \quad \text{(A.41)}$$

where Δt denotes the time step defined by $\Delta t := t_j - t_{j-1}$ for $j = 1, 2, ..., J$ and J is equal to $t/\Delta t$. Thus, eq. (A.40) reduces to

$$\begin{aligned}\text{(A.40)} \;=\; & M^{(\alpha\gamma)}(q,t-t^*)F^{(\gamma\beta)}(q,t^*) - M^{(\alpha\gamma)}(q,t)S^{(\gamma\beta)}(q) \\ & -\sum_{j=1}^{J^*}\left\{M^{(\alpha\gamma)}(q,t-t_j)-M^{(\alpha\gamma)}(q,t-t_{j-1})\right\}\mathrm{d}F_j^{(\gamma\beta)}(q) \\ & -\sum_{j=1}^{J-J^*}\mathrm{d}M_j^{(\alpha\gamma)}(q)\left\{F^{(\gamma\beta)}(q,t-t_j)-F^{(\gamma\beta)}(q,t-t_{j-1})\right\}, \quad \text{(A.42)}\end{aligned}$$

where

$$\mathrm{d}M_j^{(\alpha\gamma)}(q) := \frac{1}{\Delta t}\int_{t_{j-1}}^{t_j}\mathrm{d}sM^{(\alpha\gamma)}(q,s), \quad \text{(A.43)}$$

$$\mathrm{d}F_j^{(\gamma\beta)}(q) := \frac{1}{\Delta t}\int_{t_{j-1}}^{t_j}\mathrm{d}sF^{(\gamma\beta)}(q,s). \quad \text{(A.44)}$$

A.1.5 Discretized equation

What we do next is to discretized the dimensionless mode-coupling equation (A.33). In what follows, we omit q-dependence in the memory term and the intermediate scattering function for sake of simplification. In addition, we employ time-step representation; $F(q,t_j)$ is represented by F_j with $t_j = j\Delta t$.

A second order differential is discretized by

$$\ddot{f}_j = \frac{1}{(\Delta t)^2}\{2f_j - 5f_{j-1} + 4f_{j-2} - f_{j-3}\} + O((\Delta t)^2). \quad \text{(A.45)}$$

We thus obtain

$$\frac{1}{(\Delta t)^2}\left[2F_J^{(\alpha\beta)} - 5F_{J-1}^{(\alpha\beta)} + 4F_{J-2}^{(\alpha\beta)} - F_{J-3}^{(\alpha\beta)}\right] + \frac{q^2T}{48}\left[\mathsf{S}^{-1}(q)\right]^{(\alpha\gamma)}F_J^{(\gamma\beta)}$$

$$+M_{J-J^*}^{(\alpha\gamma)}F_{J^*}^{(\gamma\beta)} - M_J^{(\alpha\gamma)}S^{(\gamma\beta)}(q)$$

$$- \left(M_{J-1}^{(\alpha\gamma)} - M_J^{(\alpha\gamma)} \right) \mathrm{d}F_1^{(\gamma\beta)} - \mathrm{d}M_1^{(\alpha\gamma)} \left(F_{J-1}^{(\gamma\beta)} - F_J^{(\gamma\beta)} \right)$$

$$- \sum_{j=2}^{J^*} \left(M_{J-j}^{(\alpha\gamma)} - M_{J-j+1}^{(\alpha\gamma)} \right) \mathrm{d}F_j^{(\gamma\beta)} - \sum_{j=2}^{J-J^*} \mathrm{d}M_j^{(\alpha\gamma)} \left(F_{J-j}^{(\gamma\beta)} - F_{J-j+1}^{(\gamma\beta)} \right) = 0,$$

$$\Leftrightarrow \quad F_J^{(\alpha\beta)} = \left[\mathsf{A}^{-1} \right]^{(\alpha\epsilon)} M_J^{(\epsilon\gamma)} B^{(\gamma\beta)} + \left[\mathsf{A}^{-1} \right]^{(\alpha\epsilon)} C^{(\epsilon\beta)}, \tag{A.46}$$

where

$$\mathsf{A} := \frac{2}{(\Delta t)^2} \mathbf{1} + \frac{q^2 T}{48} \mathsf{S}^{-1}(q) + \mathrm{d}\mathsf{M}_1 \tag{A.47}$$

$$\mathsf{B} := \mathsf{S}(q) - \mathrm{d}\mathsf{F}_1 \tag{A.48}$$

$$\begin{aligned} \mathsf{C} := & \frac{1}{(\Delta t)^2} \left(5\mathsf{F}_{J-1} - 4\mathsf{F}_{J-2} + \mathsf{F}_{J-3} \right) - \mathsf{M}_{J-J^*} \cdot \mathsf{F}_{J^*} + \mathsf{M}_{J-1} \cdot \mathrm{d}\mathsf{F}_1 + \mathrm{d}\mathsf{M}_1 \cdot \mathsf{F}_{J-1} \\ & + \sum_{j=2}^{J^*} \left(\mathsf{M}_{J-j} - \mathsf{M}_{J-j+1} \right) \cdot \mathrm{d}\mathsf{F}_j + \sum_{j=2}^{J-J^*} \mathrm{d}\mathsf{M}_j \cdot \left(\mathsf{F}_{J-j} - \mathsf{F}_{J-j+1} \right). \end{aligned} \tag{A.49}$$

Note that we set $J^* = J/2$ in case that J is even or $J^* = (J+1)/2$ in case that J is odd.

We can solve the mode-coupling equation by Taylor expansion in the short time region. The second derivative of the intermediate scattering function reduces to

$$\partial_t^2 \mathsf{F}(q,t) = \frac{1}{t^2} [\mathsf{F}(q,t) - 2\mathsf{F}(q,t-\Delta t) + \mathsf{F}(q,t-2\Delta t)] + O(t), \tag{A.50}$$

and the second term of the MCT equation to

$$\frac{q^2 T}{48} \mathsf{S}^{-1}(q) \cdot \mathsf{F}(q,t) = \frac{q^2 T}{48} \mathbf{1} + O(t). \tag{A.51}$$

Furthermore, the integral including the memory term is calculated as

$$\int_0^t \mathrm{d}s \mathsf{M}(q,t-s) \partial_s \mathsf{F}(q,s) = [\mathsf{M}(q,0) + \mathsf{O}(t)] \cdot \int_0^t \mathrm{d}s \partial_s \mathsf{F}(q,s)$$

$$= \mathsf{M}(q,0)\cdot[\mathsf{F}(q,t)-\mathsf{S}(q)]+O(t), \tag{A.52}$$

where $\mathsf{O}(t)$ denotes a matrix in which each element is $O(t)$. Therefore, the MCT equation approximatively reduces to

$$\frac{1}{t^2}[\mathsf{F}(q,t)-2\mathsf{F}(q,t-\Delta t)+\mathsf{F}(q,t-2\Delta t)]+\frac{q^2T}{48}\mathbf{1}+\mathsf{M}(q,0)\cdot[\mathsf{F}(q,t)-\mathsf{S}(q)]=O(t),$$

$$\therefore\ \mathsf{F}(q,t)=2F(q,t-\Delta t)-F(q,t-2\Delta t)+O(t^2). \tag{A.53}$$

If it is assumed that $F(q,\Delta t)=S(q)$, then we obtain

$$\mathsf{F}(q,J\Delta t)=\mathsf{S}(q)\ (^\forall J\in\mathbb{N}) \tag{A.54}$$

where $\mathbb{N}$ denotes the set of integer greater or equal zero. Needless to say, the above equation is correct in quite short time region. In the time region, the memory term is also equal to initial value;

$$\mathsf{M}(q,J\Delta t)=\mathsf{M}(q,0)\ (^\forall J\in\mathbb{N}). \tag{A.55}$$

In addition, the following equations hold;

$$\mathrm{d}\mathsf{F}_J=\mathrm{d}\mathsf{F}_1\ ,\ \ \mathrm{d}\mathsf{M}_J=\mathrm{d}\mathsf{M}_1\ (^\forall(J-1)\in\mathbb{N}). \tag{A.56}$$

For $N_t/2+1<J\le N_t$, F_J is calculated by using eq. (A.46). If one continued to calculate under time step Δt, CPU would run out of memory immediately. In order to avoid this inconvenience, we make time-step Δt longer [36], and therein we replace $\{\mathrm{d}\mathsf{F}_j,\mathrm{d}\mathsf{M}_j\}$ $(j=1,2,\ldots,N_t)$ by

$$\left.\begin{array}{ll}\dfrac{1}{2}(\mathrm{d}\mathsf{F}_{2j}+\mathrm{d}\mathsf{F}_{2j-1}) & \left(0\le j\le\dfrac{N_t}{4}\right)\\ \dfrac{1}{6}(\mathsf{F}_{2j}+4\mathsf{F}_{2j-1}+\mathsf{F}_{2j-2}) & \left(\dfrac{N_t}{4}<j\le\dfrac{N_t}{2}\right)\end{array}\right\}\ \to\ \mathrm{d}\mathsf{F}_j \tag{A.57}$$

$$\left.\begin{array}{ll}\dfrac{1}{2}(\mathrm{d}\mathsf{M}_{2j}+\mathrm{d}\mathsf{M}_{2j-1}) & \left(0\le j\le\dfrac{N_t}{4}\right)\\ \dfrac{1}{6}(\mathsf{M}_{2j}+4\mathsf{M}_{2j-1}+\mathsf{M}_{2j-2}) & \left(\dfrac{N_t}{4}<j\le\dfrac{N_t}{2}\right)\end{array}\right\}\ \to\ \mathrm{d}\mathsf{K}_j, \tag{A.58}$$

$\{\mathsf{F}_j, \mathsf{M}_j\}$ by

$$\mathsf{F}_{2j} \to \mathsf{F}_j \ , \ \mathsf{M}_{2j} \to \mathsf{M}_j, \tag{A.59}$$

and the time step by $\Delta t \to 2\Delta t$. One can calculate F_J for $N_t/2 < J \leq N_t$ by using eq. (A.46) again, in which the new set of variables for $0 \leq J \leq N_t/2$ is employed as input.

A.2 Algorithm of the Self-Intermediate Scattering Function in Binary Mixture

A.2.1 Exact equation of motion

We consider an equation of the self intermediate scattering function for binary mixtures. The single-particle density $\boldsymbol{\rho}_{s,q}(t)$ and the longitudinal flux $\boldsymbol{j}^L_{s,q}(t)$ are employed as physical variables and time development of those is projected on subspace spanned by $\boldsymbol{\rho}_{s,q} := \boldsymbol{\rho}_{s,q}(0)$ and $\boldsymbol{j}^L_{s,q} := \boldsymbol{j}^L_{s,q}(0)$, where

$$\boldsymbol{\rho}_{s,q}(t) := \begin{pmatrix} e^{i\boldsymbol{q}\cdot\boldsymbol{X}_{i_A}(t)} \\ e^{i\boldsymbol{q}\cdot\boldsymbol{X}_{i_B}(t)} \end{pmatrix} , \ \boldsymbol{j}^L_{s,q}(t) := \begin{pmatrix} \tilde{\boldsymbol{q}}\cdot\boldsymbol{V}_{i_A}(t)e^{i\boldsymbol{q}\cdot\boldsymbol{X}_{i_A}(t)} \\ \tilde{\boldsymbol{q}}\cdot\boldsymbol{V}_{i_B}(t)e^{i\boldsymbol{q}\cdot\boldsymbol{X}_{i_B}(t)} \end{pmatrix}.$$

Using the Mori type projection method, we obtain an equation for correlation function $\overleftrightarrow{\phi}_s(q,t)$ as

$$\partial_t \overleftrightarrow{\phi}_s(q,t) = i\overleftrightarrow{\omega}_s \cdot \overleftrightarrow{\phi}_s(q,t) - \int_0^t \mathrm{d}s\, \overleftrightarrow{\psi}_s(q,t-s)\cdot\overleftrightarrow{\phi}_s(q,s), \tag{A.60}$$

where

$$\begin{aligned} \overleftrightarrow{\phi}_s(q,t) &= \begin{pmatrix} \langle\boldsymbol{\rho}_{s,q}(t)\boldsymbol{\rho}_{s,-q}\rangle & -\langle\boldsymbol{\rho}_{s,q}(t)\boldsymbol{j}^L_{s,-q}\rangle \\ \langle\boldsymbol{j}^L_{s,q}(t)\boldsymbol{\rho}_{s,-q}\rangle & -\langle\boldsymbol{j}^L_{s,q}(t)\boldsymbol{j}^L_{s,-q}\rangle \end{pmatrix} \\ &=: \begin{pmatrix} \mathsf{F}^{(s)}(q,t) & -\langle\boldsymbol{\rho}_{s,q}(t)\boldsymbol{j}^L_{s,-q}\rangle \\ \frac{1}{iq}\partial_t\mathsf{F}^{(s)}(q,t) & -\langle\boldsymbol{j}^L_{s,q}(t)\boldsymbol{j}^L_{s,-q}\rangle \end{pmatrix}, \end{aligned} \tag{A.61}$$

$$i\overleftrightarrow{\omega}_s = \begin{pmatrix} \langle\dot{\boldsymbol{\rho}}_{s,q}\boldsymbol{\rho}_{s,-q}\rangle & -\langle\dot{\boldsymbol{\rho}}_{s,q}\boldsymbol{j}^L_{s,-q}\rangle \\ \langle\dot{\boldsymbol{j}}^L_{s,q}\boldsymbol{\rho}_{s,-q}\rangle & -\langle\dot{\boldsymbol{j}}^L_{s,q}\boldsymbol{j}^L_{s,-q}\rangle \end{pmatrix} \cdot \overleftrightarrow{\phi}^{-1}_s(q,0), \tag{A.62}$$

and

$$\overleftrightarrow{\psi}_s(q,t) = \langle\boldsymbol{R}_s(t)\boldsymbol{R}_s{}^\dagger\rangle \cdot \overleftrightarrow{\phi}^{-1}_s(q,0) \tag{A.63}$$

with

$$\boldsymbol{R}_s(t) = e^{i\mathcal{Q}\mathcal{L}t} i\mathcal{Q}\mathcal{L} \begin{pmatrix} \boldsymbol{\rho}_{s,q} \\ \boldsymbol{j}^L_{s,q} \end{pmatrix}.$$

$\mathsf{F}^{(s)}(q,t)$ is represented by

$$\begin{aligned} \mathsf{F}^{(s)}(q,t) &:= \begin{pmatrix} \left\langle \rho^{(A)}_{s,q}(t)\rho^{(A)}_{s,-q} \right\rangle & \left\langle \rho^{(A)}_{s,q}(t)\rho^{(B)}_{s,-q} \right\rangle \\ \left\langle \rho^{(B)}_{s,q}(t)\rho^{(A)}_{s,-q} \right\rangle & \left\langle \rho^{(B)}_{s,q}(t)\rho^{(B)}_{s,-q} \right\rangle \end{pmatrix} \\ &= \begin{pmatrix} F^{(A)}_s(q,t) & \frac{1}{\sqrt{N_A N_B}} F^{(AB)}(q,t) \\ \frac{1}{\sqrt{N_A N_B}} F^{(BA)}(q,t) & F^{(B)}_s(q,t) \end{pmatrix}, \end{aligned} \tag{A.64}$$

where $F^{(\alpha\beta)}(q,t)$ denotes the partial intermediate scattering function[2] defined by

$$F^{(\alpha\beta)}(q,t) := \frac{1}{\sqrt{N_\alpha N_\beta}} \sum_i^{(\alpha)} \sum_j^{(\beta)} \left\langle e^{i\boldsymbol{q}\cdot(\boldsymbol{X}_i - \boldsymbol{X}_j)} \right\rangle, \tag{A.65}$$

and $F^{(\alpha)}_s(q,t)$ denotes the self-intermediate scattering function of α component defined by

$$F^{(\alpha)}_s(q,t) := \left\langle e^{i\boldsymbol{q}\cdot(\boldsymbol{X}_i(t) - \boldsymbol{X}_i)} \right\rangle = \frac{1}{N_\alpha} \sum_i^{(\alpha)} \left\langle e^{i\boldsymbol{q}\cdot(\boldsymbol{X}_i(t) - \boldsymbol{X}_i)} \right\rangle. \tag{A.66}$$

It should be noted that we can identify $F^{(s)(\alpha\beta)}(q,t)$ as $\delta_{\alpha\beta} F^{(\alpha)}_s(q,t)$ in the thermodynamic limit.

The initial correlation $\overleftrightarrow{\phi}_s(q,0)$ is represented by

$$\overleftrightarrow{\phi}_s(q,0) = \begin{pmatrix} \mathsf{F}^{(s)}(q,0) & 0 \\ 0 & (m\beta)^{-1}\mathbf{1}_2 \end{pmatrix}. \tag{A.67}$$

Considering that $F^{(\alpha)}_s(q,0) = 1$, the initial correlation reduces to

$$\overleftrightarrow{\phi}_s(q,0) = \begin{pmatrix} \mathbf{1}_2 & 0 \\ 0 & (m\beta)^{-1}\mathbf{1}_2 \end{pmatrix} \tag{A.68}$$

in the thermodynamic limit. We can obtain the inverse matrix of $\overleftrightarrow{\phi}_s(q,0)$ as

$$\overleftrightarrow{\phi}^{-1}_s(q,0) = \begin{pmatrix} \mathbf{1}_2 & 0 \\ 0 & m\beta\mathbf{1}_2 \end{pmatrix}. \tag{A.69}$$

[2] We do not consider $q = 0$ here.

Therefore,

$$i\overleftrightarrow{\omega}_s = iq \begin{pmatrix} 0 & \mathbf{1}_2 \\ (m\beta)^{-1}\mathbf{1}_2 & 0 \end{pmatrix}, \tag{A.70}$$

that is,

$$i\overleftrightarrow{\omega}_s \cdot \overleftrightarrow{\phi}_s(t) = \begin{pmatrix} \partial_t \mathsf{F}^{(s)}(q,t) & \cdots \\ \frac{iq}{m\beta}\mathsf{F}^{(s)}(q,t) & \cdots \end{pmatrix}. \tag{A.71}$$

In addition, the initial random term reduces to

$$\boldsymbol{R}_q = i\mathcal{Q}\mathcal{L} \begin{pmatrix} \boldsymbol{\rho}_{s,q} \\ \boldsymbol{j}^L_{s,q} \end{pmatrix} = \begin{pmatrix} \mathbf{0} \\ i\mathcal{L}\boldsymbol{j}^L_{s,q} - \frac{iq}{m\beta}\boldsymbol{\rho}_{s,q} \end{pmatrix} := \begin{pmatrix} \mathbf{0} \\ \boldsymbol{R}_{s,q} \end{pmatrix}. \tag{A.72}$$

It leads us to

$$\overleftrightarrow{\psi}_s(t) = \begin{pmatrix} 0 & 0 \\ 0 & m\beta \left\langle \boldsymbol{R}_{s,q}(t) {\boldsymbol{R}_{s,q}}^\dagger \right\rangle \end{pmatrix}, \tag{A.73}$$

that is,

$$\overleftrightarrow{\psi}_s(t-s) \cdot \overleftrightarrow{\phi}_s(s) = \begin{pmatrix} 0 & 0 \\ \frac{m\beta}{iq} \left\langle \boldsymbol{R}_{s,q}(t-s) {\boldsymbol{R}_{s,q}}^\dagger \right\rangle \cdot \partial_s \mathsf{F}^{(s)}(q,s) & \cdots \end{pmatrix} \tag{A.74}$$

Focusing attention on the lower left element, we obtain an exact equation about $\mathsf{F}^{(s)}(q,t)$, which includes the self-intermediate scattering function, as

$$\partial_t^2 \mathsf{F}^{(s)}(q,t) + \frac{q^2}{m\beta}\mathsf{F}^{(s)}(q,t) + m\beta \int_0^t \mathrm{d}s \left\langle \boldsymbol{R}_{s,q}(t-s) {\boldsymbol{R}_{s,q}}^\dagger \right\rangle \cdot \partial_s \mathsf{F}^{(s)}(q,s) = 0. \tag{A.75}$$

A.2.2 Approximative equation of motion in the mode-coupling theory

The memory term cannot be treated definitely. Some approximations are needed as well as derivation of the mode-coupling equation for the intermediate scattering function. First of all, we consider bilinear projection of the random term onto subspace spanned by $\boldsymbol{\rho}_{s,k_1}\boldsymbol{\delta\rho}_{k_2}$ [90]. We can also consider $\boldsymbol{\rho}_{s,k_1}\boldsymbol{\rho}_{s,k_2}$, $\boldsymbol{\rho}_{s,k_1}\boldsymbol{\rho}_{s',k_2}$ (s' means another particle), and/or $\boldsymbol{\delta\rho}_{k_1}\boldsymbol{\delta\rho}_{k_2}$ as components of the bilinear projection. However, we do not need to consider them because of the following reasons. The first one is equal to $\boldsymbol{\rho}_{s,k_1+k_2}$, so that it is same as a projection onto $\boldsymbol{\rho}_{s,q}$. The second one is in the same concept as $\boldsymbol{\rho}_{s,k_1}\boldsymbol{\delta\rho}_{k_2}$. The third one can be neglected in the thermodynamic limit.

The bilinear projection for the self part is defined by

$$\mathcal{P}_{s,2}\boldsymbol{X}_q := \sum_{\alpha,\beta,\gamma,\epsilon}\sum_{\boldsymbol{k}_1,\boldsymbol{k}_2,\boldsymbol{k}_3,\boldsymbol{k}_4}\left\langle \boldsymbol{X}_q\rho^{(\alpha)}_{s,-2}\delta\rho^{(\beta)}_{-1}\right\rangle\left[\Phi^{(s)-1}_{1,2,3,4}\right]^{(\beta\alpha\gamma\epsilon)}\delta\rho^{(\epsilon)}_3\rho^{(\gamma)}_{s,4}, \tag{A.76}$$

where

$$\Phi^{(s)(\alpha\beta\gamma\epsilon)}_{1,2,3,4} := \left\langle \delta\rho^{(\alpha)}_1\rho^{(\beta)}_{s,2}\rho^{(\gamma)}_{s,-4}\delta\rho^{(\epsilon)}_{s,-3}\right\rangle, \tag{A.77}$$

and

$$\sum_{\eta,\xi}\sum_{\boldsymbol{k}_3,\boldsymbol{k}_4}\Phi^{(s)(\alpha\beta\xi\eta)}_{1,2,3,4}\left[\Phi^{(s)-1}_{3,4,5,6}\right]^{(\eta\xi\gamma\epsilon)} = \sum_{\eta,\xi}\sum_{\boldsymbol{k}_3,\boldsymbol{k}_4}\left[\Phi^{(s)-1}_{1,2,3,4}\right]^{(\alpha\beta\xi\eta)}\Phi^{(s)(\eta\xi\gamma\epsilon)}_{3,4,5,6} = \delta_{\boldsymbol{k}_1,\boldsymbol{k}_5}\delta_{\boldsymbol{k}_2,\boldsymbol{k}_6}\delta_{\beta,\gamma}\delta_{\alpha,\epsilon}. \tag{A.78}$$

Note that $\mathcal{P}_{s,2}(\mathcal{P}_{s,2}\boldsymbol{X}_q) = \mathcal{P}_{s,2}\boldsymbol{X}_q$ is easily shown using the above relationship. The bilinear-projected random term is

$$\mathcal{P}_{s,2}R^{(\eta)}_{s,q} = \sum_{\boldsymbol{k}_3,\boldsymbol{k}_4}\sum_{\alpha,\beta}V^{(\eta\beta\alpha)}_{s,q}(3,4)\delta\rho^{(\alpha)}_3\rho^{(\beta)}_{s,4}, \tag{A.79}$$

where

$$V^{(\eta\beta\alpha)}_{s,q}(3,4) := \sum_{\boldsymbol{k}_1,\boldsymbol{k}_2}\sum_{\gamma,\epsilon}\left\langle R^{(\eta)}_{s,q}\rho^{(\epsilon)}_{s,-2}\delta\rho^{(\gamma)}_{-1}\right\rangle\left[\Phi^{(s)-1}_{1,2,3,4}\right]^{(\gamma\epsilon\beta\alpha)}. \tag{A.80}$$

The above equation is transformed to

$$\sum_{\boldsymbol{k}_3,\boldsymbol{k}_4}\sum_{\alpha,\beta}V^{(\eta\beta\alpha)}_{s,q}(3,4)\Phi^{(s)(\alpha\beta\zeta\xi)}_{3,4,5,6} = \left\langle R^{(\eta)}_{s,q}\rho^{(\zeta)}_{s,-6}\delta\rho^{(\xi)}_{-5}\right\rangle. \tag{A.81}$$

The RHS reduces to

$$\left\langle R^{(\eta)}_{s,q}\rho^{(\zeta)}_{s,-6}\delta\rho^{(\xi)}_{-5}\right\rangle = \left\langle (i\mathcal{L}j^{L(\eta)}_{s,q})\rho^{(\zeta)}_{s,-6}\delta\rho^{(\xi)}_{-5}\right\rangle - \frac{iq}{m\beta}\left\langle \rho^{(\eta)}_{s,q}\rho^{(\zeta)}_{s,-6}\delta\rho^{(\xi)}_{-5}\right\rangle. \tag{A.82}$$

The first term of RHS of eq. (A.82) is

$$\left\langle (i\mathcal{L}j^{L(\eta)}_{s,q})\rho^{(\zeta)}_{s,-6}\delta\rho^{(\xi)}_{-5}\right\rangle = \frac{i\delta_{6,q-5}\tilde{\boldsymbol{q}}}{m\beta\sqrt{N_\eta}}\cdot\left\{(\boldsymbol{q}-\boldsymbol{k}_5)\delta_{\eta,\zeta}S^{(\eta\xi)}(k_5) + \boldsymbol{k}_5\delta_{\eta,\xi}\delta_{\eta,\zeta}\right\} \tag{A.83}$$

in the thermodynamic limit. On the other hand, the second term of RHS of eq. (A.82) is

$$\left\langle \rho^{(\eta)}_{s,q}\rho^{(\zeta)}_{s,-6}\delta\rho^{(\xi)}_{-5}\right\rangle = \delta_{6,q-5}\frac{1}{\sqrt{N_\eta}}\delta_{\eta,\zeta}S^{(\eta\xi)}(k_5) \tag{A.84}$$

in the thermodynamic limit. Thus, the RHS of eq. (A.81) (i.e. eq. (A.82)) reduces to

$$\left\langle R^{(\eta)}_{s,q}\rho^{(\zeta)}_{s,-6}\delta\rho^{(\xi)}_{-5}\right\rangle = \frac{i\delta_{6,q-5}\tilde{\boldsymbol{q}}\cdot\boldsymbol{k}_5}{m\beta\sqrt{N_\eta}}\delta_{\eta,\zeta}\left(\delta_{\eta,\xi}-S^{(\eta\xi)}(k_5)\right). \tag{A.85}$$

Moreover, it is assumed that the four-particle correlation can be decoupled, that is[3],

$$\begin{aligned}\Phi^{(s)(\alpha\beta\zeta\xi)}_{3,4,5,q-5} &= \delta_{4,q-3}\left\langle\delta\rho^{(\alpha)}_3\rho^{(\beta)}_{s,4}\rho^{(\zeta)}_{s,5-q}\delta\rho^{(\xi)}_{-5}\right\rangle \\ &\simeq \delta_{4,q-3}\left[\delta_{3,q-5}\left\langle\delta\rho^{(\alpha)}_3\rho^{(\zeta)}_{s,5-q}\right\rangle\left\langle\rho^{(\beta)}_{s,4}\delta\rho^{(\xi)}_{-5}\right\rangle+\delta_{3,5}\left\langle\delta\rho^{(\alpha)}_3\delta\rho^{(\xi)}_{-5}\right\rangle\left\langle\rho^{(\beta)}_{s,4}\rho^{(\zeta)}_{s,5-q}\right\rangle\right] \\ &= \delta_{4,q-3}\delta_{3,5}\left\langle\delta\rho^{(\alpha)}_3\delta\rho^{(\xi)}_{-5}\right\rangle\left\langle\rho^{(\beta)}_{s,4}\rho^{(\zeta)}_{s,5-q}\right\rangle = \delta_{4,q-3}\delta_{3,5}\delta_{\beta\zeta}S^{(\alpha\xi)}(k_5).\end{aligned} \tag{A.86}$$

The second equality is due to the decoupling approximation and the third one the thermodynamic limit:

$$\delta_{4,q-3}\delta_{3,q-5}\left\langle\delta\rho^{(\alpha)}_3\rho^{(\zeta)}_{s,5-q}\right\rangle\left\langle\rho^{(\beta)}_{s,4}\delta\rho^{(\xi)}_{-5}\right\rangle = \frac{1}{\sqrt{N_\zeta N_\beta}}S^{(\alpha\zeta)}(|\boldsymbol{q}-\boldsymbol{k}_5|)S^{(\beta\xi)}(k_5). \tag{A.87}$$

Thus, we obtain

$$V^{(\eta\zeta\kappa)}_{s,q}(5,6) = -\frac{i\delta_{6,q-5}\tilde{\boldsymbol{q}}\cdot\boldsymbol{k}_5}{m\beta\sqrt{N_\eta}}\delta_{\eta,\zeta}c_2^{(\eta\kappa)}(k_5), \tag{A.88}$$

where $\mathsf{c}(k)$ denotes the direct correlation tensor.

As well as the derivation of the intermediate scattering function in the mode-coupling method, the memory term thus reduces to

$$\begin{aligned}\left\langle R^{(\eta)}_{s,q}(t)R^{(\xi)\dagger}_{s,q}\right\rangle &\simeq \left\langle\left(e^{ti\mathcal{L}}\mathcal{P}_{s,2}R^{(\eta)}_{s,q}\right)\left(\mathcal{P}_{s,2}R^{(\xi)}_{s,q}\right)^\dagger\right\rangle \\ &= \frac{1}{(m\beta)^2\sqrt{N_\eta N_\xi}}\sum_{\boldsymbol{k},\boldsymbol{k}'}\sum_{\alpha,\beta}\left\langle\delta\rho^{(\alpha)}_k(t)\rho^{(\eta)}_{s,q-k}(t)\rho^{(\xi)}_{s,k'-q}\delta\rho^{(\beta)}_{-k'}\right\rangle(\tilde{\boldsymbol{q}}\cdot\boldsymbol{k})(\tilde{\boldsymbol{q}}\cdot\boldsymbol{k}')c_2^{(\eta\alpha)}(k)c_2^{(\xi\beta)}(k') \\ &\simeq \frac{1}{(m\beta)^2\sqrt{N_\eta N_\xi}}\sum_{\boldsymbol{k}}\sum_{\alpha,\beta}\left\langle\delta\rho^{(\alpha)}_k(t)\delta\rho^{(\beta)}_{-k}\right\rangle\left\langle\rho^{(\eta)}_{s,q-k}(t)\rho^{(\xi)}_{s,k-q}\right\rangle(\tilde{\boldsymbol{q}}\cdot\boldsymbol{k})(\tilde{\boldsymbol{q}}\cdot\boldsymbol{k})c_2^{(\eta\alpha)}(k)c_2^{(\xi\beta)}(k)\end{aligned}$$

[3]Equation (A.85) includes $\delta_{6,q-5}$, and then we consider $\boldsymbol{k}_6 = \boldsymbol{q}-\boldsymbol{k}_5$ in what follows.

$$= \frac{\delta_{\eta,\xi}}{(m\beta)^2 N_\eta} \sum_{\boldsymbol{k}} \sum_{\alpha,\alpha'} (\tilde{\boldsymbol{q}} \cdot \boldsymbol{k})^2 c_2^{(\eta\alpha)}(k) c_2^{(\eta\alpha')}(k) F^{(\alpha\alpha')}(k,t) F_s^{(\eta)}(|\boldsymbol{q}-\boldsymbol{k}|,t) \tag{A.89}$$

in the thermodynamic limit. Therefore, we obtain an approximative mode-coupling equation for the self-intermediate scattering function as

$$\partial_t^2 F_s^{(\eta)}(q,t) + \frac{q^2}{m\beta} F_s^{(\eta)}(q,t) + \frac{1}{m\beta N_\eta} \int_0^t \mathrm{d}s \sum_{\boldsymbol{k}} \sum_{\alpha,\alpha'} (\tilde{\boldsymbol{q}} \cdot \boldsymbol{k})^2$$

$$\times c_2^{(\eta\alpha)}(k) F^{(\alpha\alpha')}(k,t-s) c_2^{(\alpha'\eta)}(k) F_s^{(\eta)}(|\boldsymbol{q}-\boldsymbol{k}|,t-s) \partial_s F_s^{(\eta)}(q,s) = 0. \tag{A.90}$$

We should not forget that this equation holds only in the thermodynamic limit. It seems that the third term could be neglected in the thermodynamic limit, but it cannot be allowed to neglect it because summation of $\boldsymbol{k}$ is of order the volume V. It is clearer if summation is replaced by integral:

$$\partial_t^2 F_s^{(\eta)}(q,t) + \frac{q^2}{m\beta} F_s^{(\eta)}(q,t) + \frac{1}{m\beta\rho_\eta} \int_0^t \mathrm{d}s \int \frac{\mathrm{d}\boldsymbol{k}}{(2\pi)^3} \sum_{\alpha,\alpha'} (\tilde{\boldsymbol{q}} \cdot \boldsymbol{k})^2$$

$$\times \left[\mathsf{c}_2(k) \cdot \mathsf{F}(k,t-s) \cdot \mathsf{c}_2(k)\right]^{(\eta\eta)} F_s^{(\eta)}(|\boldsymbol{q}-\boldsymbol{k}|,t-s) \partial_s F_s^{(\eta)}(q,s) = 0. \tag{A.91}$$

where ρ_η is still constant in the thermodynamic limit.

A.2.3 Numerical algorithm of memory term

We consider an algorithm for a mode-coupling equation of the self-intermediate scattering function:

$$\partial_t^2 F_s^{(\eta)}(q,t) + \frac{q^2}{m\beta} F_s^{(\eta)}(q,t) + \int_0^t \mathrm{d}s K_s^{(\eta)}(q,t-s) \partial_s F_s^{(\eta)}(q,s) = 0. \tag{A.92}$$

The memory term $K_s^{(\eta)}(q,t)$ is represented by

$$K^{(\eta)}(q,t) = \frac{1}{m\beta\rho_\eta} \int \frac{\mathrm{d}\boldsymbol{k}}{(2\pi)^3} (\tilde{\boldsymbol{q}} \cdot \boldsymbol{k})^2 \sum_{\alpha,\alpha'} c_2^{(\eta\alpha)}(k) F^{(\alpha\alpha')}(k,t) c_2^{(\alpha'\eta)}(k) F_s^{(\eta)}(|\boldsymbol{q}-\boldsymbol{k}|,t). \tag{A.93}$$

We draw upon the algorithm that we employ in the memory term for the intermediate scattering function. First, the variable of integration is changed from $\boldsymbol{k}$ to $\boldsymbol{p} = \boldsymbol{k} - \boldsymbol{q}/2$ to obtain

$$K_s^{(\zeta)}(q,t) = \frac{1}{m\beta\rho_\zeta}\int\frac{\mathrm{d}\boldsymbol{p}}{(2\pi)^3}\left(\frac{q}{2}+\hat{\boldsymbol{q}}\cdot\boldsymbol{p}\right)^2 \times\sum_{\alpha,\alpha'}c_2^{(\zeta\alpha)}\left(|+|\right)F^{(\alpha\alpha')}\left(|+|,t\right)c_2^{(\alpha'\zeta)}\left(|+|\right)F_s^{(\zeta)}\left(|-|,t\right), \quad \text{(A.94)}$$

where $|\pm|$ are abbreviated expressions of $|\boldsymbol{q}/2\pm\boldsymbol{p}|$, respectively. Let the axis of p_z point to the direction of $\hat{\boldsymbol{q}}$, so that $\hat{\boldsymbol{p}}\cdot\boldsymbol{q} = q\cos\theta$ and $\mathrm{d}\boldsymbol{p} = p^2\sin\theta\mathrm{d}p\mathrm{d}\theta\mathrm{d}\phi$. Moreover, new variables are introduced: $x = |+|$ and $y = |-|$. Since the Jacobian is represented by $|\partial(x,y)/\partial(p,\theta)| = qp^2\sin\theta/xy$, we obtain

$$\begin{aligned}K_s^{(\eta)}(q,t) &= \frac{1}{(2\pi)^2 m\beta\rho_\eta}\int_0^\infty\mathrm{d}x\int_{|x-q|}^{|x+q|}\mathrm{d}y\frac{xy}{q}\left(\frac{q^2+x^2-y^2}{2q}\right)^2 \\ &\quad\times\sum_{\alpha,\alpha'}c_2^{(\eta\alpha)}(x)F^{(\alpha\alpha')}(x,t)c_2^{(\alpha'\eta)}(x)F_s^{(\eta)}(y,t) \\ &= \frac{1}{16\pi^2 m\beta q^3\rho_\eta}\int_0^\infty\mathrm{d}x x\sum_{\alpha,\alpha'}c_2^{(\eta\alpha)}(x)F^{(\alpha\alpha')}(x,t)c_2^{(\alpha'\eta)}(x) \\ &\quad\times\int_{|x-q|}^{|x+q|}\mathrm{d}y y\left(q^2+x^2-y^2\right)^2F_s^{(\eta)}(y,t). \end{aligned} \quad \text{(A.95)}$$

Using the dimensionless variables, the memory term is represented by

$$\begin{aligned}K_s^{(\eta)}(q,t) &= \frac{\varepsilon_{AA}\hat{T}}{16\pi^2 m\hat{q}^3\hat{\rho}_\eta}\int_0^\infty\mathrm{d}\hat{x}\hat{x}\sum_{\alpha,\alpha'}c_2^{(\eta\alpha)}(\hat{x})F^{(\alpha\alpha')}(\hat{x},\hat{t})c_2^{(\alpha'\eta)}(\hat{x}) \\ &\quad\times\int_{|\hat{x}-\hat{q}|}^{|\hat{x}+\hat{q}|}\mathrm{d}\hat{y}\hat{y}\left(\hat{q}^2+\hat{x}^2-\hat{y}^2\right)^2F_s^{(\eta)}(\hat{y},\hat{t}), \end{aligned} \quad \text{(A.96)}$$

where the variables with hat symbol denote the dimensionless variables. On the other hand,

$$\frac{m\beta}{q^2}\partial_t^2F_s^{(\eta)}(q,t) = \frac{48}{\hat{q}^2\hat{T}}\partial_{\hat{t}}^2F_s^{(\eta)}(\hat{q},\hat{t}). \quad \text{(A.97)}$$

in the Lennard-Jones unit. Therefore, we can obtain

$$\partial_{\hat{t}}^2 F_s^{(\eta)}(\hat{q},\hat{t}) + \frac{\hat{q}^2\hat{T}}{48} F_s^{(\eta)}(\hat{q},\hat{t}) + \int_0^{\hat{t}} \mathrm{d}\hat{s}\hat{K}_s^{(\eta)}(\hat{q},\hat{t}-\hat{s})\partial_{\hat{s}} F_s^{(\eta)}(\hat{q},\hat{s}) = 0, \tag{A.98}$$

where

$$\begin{aligned}
\hat{K}_s^{(\eta)}(\hat{q},\hat{t}) &= \frac{\hat{T}}{768\pi^2\hat{q}^3\hat{\rho}_\eta}\int_0^\infty \mathrm{d}\hat{x}\hat{x}\sum_{\alpha,\alpha'} c_2^{(\eta\alpha)}(\hat{x})F^{(\alpha\alpha')}(\hat{x},\hat{t})c_2^{(\alpha'\eta)}(\hat{x}) \\
&\quad \times \int_{|\hat{x}-\hat{q}|}^{|\hat{x}+\hat{q}|} \mathrm{d}\hat{y}\hat{y}\left(\hat{q}^2+\hat{x}^2-\hat{y}^2\right)^2 F_s^{(\eta)}(\hat{y},\hat{t}) \qquad \text{(A.99)} \\
&=: \frac{\hat{T}}{768\pi^2\hat{q}^3\hat{\rho}_\eta}\int_0^\infty \mathrm{d}\hat{x}\hat{x}\sum_{\alpha,\alpha'} c_2^{(\eta\alpha)}(\hat{x})F^{(\alpha\alpha')}(\hat{x},\hat{t})c_2^{(\alpha'\eta)}(\hat{x})\int_{|\hat{x}-\hat{q}|}^{|\hat{x}+\hat{q}|}\mathrm{d}\hat{y}\hat{y}Q_{\hat{q}}^{(\eta)}(\hat{x},\hat{y};\hat{t}) \\
&=: \frac{\hat{T}}{768\pi^2\hat{q}^3\hat{\rho}_\eta}\int_0^\infty \mathrm{d}\hat{x}\hat{x}Y_{\hat{q}}^{(\eta)}(\hat{x};\hat{t}) \qquad \text{(A.100)}
\end{aligned}$$

where

$$\begin{aligned}
Q_q^{(\eta)}(x,y;t) &= \left(q^2+x^2-y^2\right)^2 F_s^{(\eta)}(y,t), \qquad \text{(A.101)} \\
Y_q^{(\eta)}(x,t) &= \sum_{\alpha,\alpha'} c_2^{(\eta\alpha)}(x)F^{(\alpha\alpha')}(x,t)c_2^{(\alpha'\eta)}(x)Q_q^{(\eta)}(x,y;t). \qquad \text{(A.102)}
\end{aligned}$$

The functions are numerically integrated by the Simpson's rule to obtain

$$\begin{aligned}
\int_{|x-q|}^{|x+q|}\mathrm{d}yyQ_q^{(\eta)}(x,y;t) \simeq \frac{\Delta q}{3}\Bigg[&|x-q|Q_q^{(\eta)}(x,|x-q|;t) + 2\sum_{n_y=1}^{n/2}\left\{2y_{2n_y-1}Q_q^{(\eta)}(x,y_{2n_y-1};t)\right. \\
&\left. + y_{2n_y}Q_q^{(\eta)}(x,y_{2n_y};t)\right\} - |x+q|Q_q^{(\eta)}(x,|x+q|;t)\Big] \qquad \text{(A.103)}
\end{aligned}$$

and

$$\begin{aligned}
\int_0^{q_m}\mathrm{d}xxY_q^{(\eta)}(x,t) \simeq \frac{\Delta q}{3}\Bigg[&2\sum_{m_x=1}^{m/2}\left\{x_{2m_x-1}Y_q^{(\eta)}(x_{2m_x-1};t) + x_{2m_x}Y_q^{(\eta)}(x_{2m_x};t)\right\} \\
&- q_m Y_q^{(\eta)}(q_m;t)\Big], \qquad \text{(A.104)}
\end{aligned}$$

where $n = (|x+q| - |x-q|)/\Delta q$, $y_j = j\Delta q + |x-q|$, $m = q_m/\Delta q$, and $x_j = j\Delta q$.

A.2.4 Convolution integral

We discretize the mode-coupling equation for the self-intermediate scattering function. For sake of simplicity, eq. (A.98) is abbreviated to

$$\partial_t^2 F_s(t) + \frac{q^2 T}{48} F_s(t) + \int_0^t \mathrm{d}s K_s(t-s)\partial_s F_s(s) = 0 \tag{A.105}$$

in what follows. The convolution integral reduces to

$$\begin{aligned}\int_0^t \mathrm{d}s K_s(t-s)\partial_s F_s(s) &= K_s(t-t^*)F_s(t^*) - K_s(t) - \int_0^{t^*} \mathrm{d}s \left\{\partial_s K_s(t-s)\right\} F_s(s) \\ &\quad - \int_0^{t-t^*} \mathrm{d}s K_s(s) \left\{\partial_s F_s(t-s)\right\}, \end{aligned} \tag{A.106}$$

where t^* is arbitrary and $F_s(0) = F_s^{(\zeta)}(q,0) = 1$. The discretized convolution integral is represented by

$$\begin{aligned}\int_0^t \mathrm{d}s K_s(t-s)\partial_s F_s(s) &= K_{s,J-J^*}F_{s,J^*} - K_{s,J} - \sum_{j=1}^{J^*}(K_{s,J-j} - K_{s,J-j+1})\mathrm{d}F_{s,j} \\ &\quad - \sum_{j=1}^{J-J^*} \mathrm{d}K_{s,j}(F_{s,J-j} - F_{s,J-j+1}), \end{aligned} \tag{A.107}$$

where the subscript denotes the time index: $j = t_j/\Delta t$, $J = t/\Delta t$, and $J^* = t^*/\Delta t$.

A.2.5 Discretized equation

We obtain the discretized MCT equation for the self-intermediate scattering function as

$$A_s F_{s,J} = B_s K_{s,J} + C_s, \tag{A.108}$$

where the coefficients are

$$A_s = \frac{2}{(\Delta t)^2} + \frac{q^2 T}{48} + \mathrm{d}K_{s,1}, \tag{A.109}$$

$$B_s = 1 - \mathrm{d}F_{s,1}, \tag{A.110}$$

$$C_s = \frac{1}{(\Delta t)^2}\left(F_{s,J-3} - 4F_{s,J-2} + 5F_{s,J-1}\right) - K_{s,J-J^*}F_{s,J^*} + K_{s,J-1}\mathrm{d}F_{s,1} + \mathrm{d}K_{s,1}F_{s,J-1}$$

$$+\sum_{j=2}^{J^*}(K_{s,J-j}-K_{s,J-j+1})\mathrm{d}F_{s,j}+\sum_{j=2}^{J-J^*}\mathrm{d}K_{s,j}(F_{s,J-j}-F_{s,J-j+1}). \tag{A.111}$$

We can solve the mode-coupling equation for the self-intermediate scattering function by using the recursion method for eq. (A.108).

A.3 Dynamics of a tagged particle

A.3.1 Mean-squared displacement and mean-quartic displacement

The self memory function is expanded around $q = 0$ as

$$K_s(\boldsymbol{q},t) = K_0(t) + q^2K_2(t) + O(q^4), \tag{A.112}$$

where

$$K_0(t) = \lim_{q\to 0} K_s(q,t) = \frac{1}{6\pi^2 m\beta\rho}\int_0^\infty \mathrm{d}k k^4 c(k)^2 F(k,t)F_s(k,t) \tag{A.113}$$

and

$$\begin{aligned} K_2(t) &= \frac{1}{2m\beta\rho}\int\frac{\mathrm{d}\boldsymbol{k}}{(2\pi)^3}\left(\frac{\boldsymbol{q}}{q}\cdot\boldsymbol{k}\right)^2 c(k)^2F(k,t)\left(\boldsymbol{q}\cdot\frac{\partial}{\partial\boldsymbol{k}}\right)^2F(k,t) \\ &= \frac{1}{20\pi^2 m\beta\rho}\int_0^\infty \mathrm{d}k k^4 c(k)^2F(k,t)\left\{\frac{2}{3k}\frac{\partial F(k,t)}{\partial k}+\frac{\partial^2F(k,t)}{\partial k^2}\right\}. \end{aligned} \tag{A.114}$$

In addition, the self-intermediate scattering function is expanded as

$$F_s(q,t) = 1-\frac{q^2}{6}M_2(t)+\frac{q^4}{120}M_4(t)+O(q^6). \tag{A.115}$$

We thus obtain equations of motion for mean-square and mean-quartic displacement as

$$\ddot{M}_2(t)+\int_0^t \mathrm{d}sK_0(t-s)\dot{M}_2(s) = \frac{6}{m\beta} \tag{A.116}$$

$$\ddot{M}_4(t)+\int_0^t \mathrm{d}sK_0(t-s)\dot{M}_4(s)-20\int_0^t \mathrm{d}sK_2(t-s)\dot{M}_2(s) = \frac{20}{m\beta}M_2(t) \tag{A.117}$$

As well as the (self) intermediate scattering function, the convolution integral is divided as

$$\int_0^t \mathrm{d}sK_0^{(\eta)}(t-s)\partial_sM_2^{(\eta)}(s) = K_0^{(\eta)}(t-t^*)M_2^{(\eta)}(t^*)-\int_0^{t^*}\mathrm{d}s\left\{\partial_sK_0^{(\eta)}(t-s)\right\}M_2^{(\eta)}(s)$$

$$
\begin{aligned}
& - \int_0^{t-t^*} K_0^{(\eta)}(s) \left\{ \partial_s M_2^{(\eta)}(t-s) \right\} \\
\simeq \; & K_0^{(\eta)}(t-t^*) M_2^{(\eta)}(t^*) - \sum_{j=1}^{J^*} \left(K_0^{(\eta)}(t-t_j) - K_0^{(\eta)}(t-t_{j-1}) \right) \mathrm{d}M_2^{(\eta)}(t_j) \\
& - \sum_{j=1}^{J-J^*} \mathrm{d}K_0^{(\eta)}(t_j) \left(M_2^{(\eta)}(t-t_j) - M_2^{(\eta)}(t-t_{j-1}) \right),
\end{aligned} \tag{A.118}
$$

where $t = J\Delta t$, $t_j = j\Delta t$, and

$$
\mathrm{d}M_2^{(\eta)}(t_j) = \frac{1}{\Delta t} \int_{t_{j-1}}^{t_j} \mathrm{d}s M_2^{(\eta)}(s) \,, \quad \mathrm{d}K_0^{(\eta)}(t_j) = \frac{1}{\Delta t} \int_{t_{j-1}}^{t_j} \mathrm{d}s K_0^{(\eta)}(s). \tag{A.119}
$$

We can obtain the discretized equation for the mean-square displacement[4] by

$$
\begin{aligned}
\left\{ \frac{2}{(\Delta t)^2} + \mathrm{d}K_{0,1} \right\} M_{2,J} \; = \; & \frac{1}{(\Delta t)^2} \left(M_{2,J-3} - 4M_{2,J-2} + 5M_{2,J-1} \right) + \frac{6}{m\beta} \\
& + \Bigg[\mathrm{d}K_{0,1} M_{2,J-1} - K_{0,J-J^*} M_{2,J^*} + \sum_{j=1}^{J^*} \left(K_{0,J-j} - K_{0,J-j+1} \right) \mathrm{d}M_{2,j} \\
& \qquad + \sum_{j=2}^{J-J^*} \mathrm{d}K_{0,j} \left(M_{2,J-j} - M_{2,J-j+1} \right) \Bigg].
\end{aligned} \tag{A.120}
$$

Using the dimensionless parameters, we can alternative discretized equation by

$$
\begin{aligned}
\left\{ \frac{2}{(\Delta \hat{t})^2} + \mathrm{d}\tilde{K}_{0,1} \right\} \hat{M}_{2,J} \; = \; & \frac{1}{(\Delta \hat{t})^2} \left(\hat{M}_{2,J-3} - 4\hat{M}_{2,J-2} + 5\hat{M}_{2,J-1} \right) + \frac{\hat{T}}{8} \\
& + \Bigg[\mathrm{d}\tilde{K}_{0,1} \hat{M}_{2,J-1} - \tilde{K}_{0,J-J^*} \hat{M}_{2,J^*} + \sum_{j=1}^{J^*} \left(\tilde{K}_{0,J-j} - \tilde{K}_{0,J-j+1} \right) \mathrm{d}\hat{M}_{2,j} \\
& \qquad + \sum_{j=2}^{J-J^*} \mathrm{d}\tilde{K}_{0,j} \left(\hat{M}_{2,J-j} - \hat{M}_{2,J-j+1} \right) \Bigg],
\end{aligned} \tag{A.121}
$$

where variables with hat symbol denote the dimension variables,

$$
\tilde{K}_{0,j}^{(\eta)} = \frac{\hat{T}}{288\pi^2 \hat{\rho}_\eta} \int_0^\infty \mathrm{d}\hat{k} \, \hat{k}^4 \sum_{\alpha,\alpha'} c_2^{(\eta\alpha)}(\hat{k}) F^{(\alpha\alpha')}(\hat{k}, t_j) c_2^{(\alpha'\eta)}(\hat{k}) F_s^{(\eta)}(\hat{k}, t_j), \tag{A.122}
$$

and

$$
\mathrm{d}\tilde{K}_{0,j} = \frac{1}{\Delta t} \int_{t_{j-1}}^{t_j} \mathrm{d}s \tilde{K}_0(s). \tag{A.123}
$$

[4]For sake of simplicity, η is omitted in what follows.

In very short time regime ($t \sim \Delta t$), the mean-square displacement is represented by

$$M_2(t) = {v_0}^2 t^2 = \frac{\hat{T}\hat{t}^2}{16}{\sigma_{AA}}^2, \tag{A.124}$$

where v_0 denotes the average speed: $v_0 = \sqrt{3k_BT/m}$. We have employed the equation as the initial condition of the mean-square displacement. Moreover, $\mathrm{d}M_{2,j}$ is calculated as

$$\mathrm{d}M_{2,j} = \frac{\hat{T}{\sigma_{AA}}^2}{16\Delta t}\int_{t_{j-1}}^{t_j} \mathrm{d}s s^2 = \frac{\hat{T}(\Delta t)^2}{16}\left(j^2 - j + \frac{1}{3}\right){\sigma_{AA}}^2. \tag{A.125}$$

We have employed the above equation as the initial condition of $\mathrm{d}M_{2,j}$.

The algorithm to calculation of the mean-quartic displacement is similar to the above method. The non-Gaussian parameter is defined by

$$\alpha_2(t) := \frac{3M_4(t)}{5M_2(t)^2} - 1. \tag{A.126}$$

It is expected that the non-Gaussian parameter be zero in the short-time region because the distribution of the velocity is Gaussian. However, in the short-time region, eq. (A.117) shows

$$\ddot{M}_4(t) \simeq \frac{20}{m\beta}M_2(t) \simeq \frac{60}{(m\beta)^2}t^2, \tag{A.127}$$

$$M_4(t) = \frac{5}{(m\beta)^2}t^4. \tag{A.128}$$

Therefore, in the short-time region, we can obtain

$$\alpha_2(t) \simeq \frac{3\cdot 5t^4/(m\beta)^2}{5\cdot 3^2 t^4/(m\beta)^2} - 1 = -\frac{2}{3}(\neq 0). \tag{A.129}$$

A.3.2 Long-time self-diffusion constant

The long-time Self-Diffusion Constant (LSD) is represented by

$$D_S^{L(\eta)} = \frac{\hat{T}}{48}\left[\int_0^\infty K_0^{(\eta)}(s)\mathrm{d}s\right]^{-1}, \tag{A.130}$$

where

$$K_0^{(\eta)}(t) = \frac{\hat{T}}{288\pi^2\hat{\rho}_\eta}\int_0^\infty \mathrm{d}\hat{k}\ \hat{k}^4 \sum_{\alpha,\alpha'} c_2^{(\eta\alpha)}(\hat{k})F^{(\alpha\alpha')}(\hat{k},t)c_2^{(\alpha'\eta)}(\hat{k})F_s^{(\eta)}(\hat{k},t). \tag{A.131}$$

It should be noted that

$$\lim_{z\to 0} z^2 \tilde{M}_2^{(\eta)}(z) = \lim_{z\to 0} \int_0^\infty \mathrm{d}t \frac{\mathrm{d}}{\mathrm{d}t}\left(\frac{\mathrm{d}M_2^{(\eta)}(t)}{\mathrm{d}t}\right) e^{-zt} = 6D_s^{L(\eta)}, \tag{A.132}$$

where $\tilde{f}(z)$ denotes the Laplace transformed functions represented by

$$\tilde{f}(z) = \int_0^\infty \mathrm{d}t f(t) e^{-zt}. \tag{A.133}$$

According to this representation, let $D_S^{(\eta)}(t)$ denote the time-dependent self-diffusion constant defined by

$$D_S^{(\eta)}(t) = \frac{\hat{T}}{48}\left[\int_0^t K_0^{(\eta)}(s)\mathrm{d}s\right]^{-1}. \tag{A.134}$$

Needless to say, $D_S^{(\eta)}(t) \to D_S^{L(\eta)}$ $(t \to \infty)$.

In numerical calculations, we divide the integral with respect to time into

$$\int_0^\infty \mathrm{d}s = \int_0^{\frac{N_t}{2}\Delta t} \mathrm{d}s + \int_{\frac{N_t}{2}\Delta t}^{N_t\Delta t} \mathrm{d}s + \int_{\frac{N_t}{2}2\Delta t}^{N_t 2\Delta t} \mathrm{d}s + \int_{\frac{N_t}{2}4\Delta t}^{N_t 4\Delta t} \mathrm{d}s + \cdots = \int_0^{\frac{N_t}{2}\Delta t} \mathrm{d}s + \sum_{j=0}^{\infty} \int_{2^j\Delta t\frac{N_t}{2}}^{2^j\Delta t N_t} \mathrm{d}s. \tag{A.135}$$

The initial condition of $K_0^{(\eta)}(t)$ is given by

$$K_0^{(\eta)}(t) = \frac{1}{6\pi^2\hat{\rho}_\eta}\int_0^\infty \mathrm{d}\hat{k}\ \hat{k}^4 \sum_{\alpha,\alpha'} c_2^{(\eta\alpha)}(\hat{k}) S^{(\alpha\alpha')}(\hat{k}) c_2^{(\alpha'\eta)}(\hat{k}) \quad \left(\text{for } 0 \le t \le \frac{N_t}{2}\Delta t\right), \tag{A.136}$$

and then

$$\int_0^{\frac{N_t}{2}\Delta t} \mathrm{d}s K_0^{(\eta)}(s) = \frac{N_t\Delta t}{2}\frac{1}{6\pi^2\hat{\rho}_\eta}\int_0^\infty \mathrm{d}\hat{k}\ \hat{k}^4 \sum_{\alpha,\alpha'} c_2^{(\eta\alpha)}(\hat{k}) S^{(\alpha\alpha')}(\hat{k}) c_2^{(\alpha'\eta)}(\hat{k}). \tag{A.137}$$

Moreover, using the Simpson's rule, we can obtain

$$\begin{aligned}\int_{2^j\Delta t\frac{N_t}{2}}^{2^j\Delta t N_t} \mathrm{d}s K_0^{(\eta)}(s) &= \frac{2^j\Delta t}{3}\left[K_0^{(\eta)}\left(2^j\Delta t\frac{N_t}{2}\right) + 4\sum_{k=1}^{N_t/2} K_0^{(\eta)}\left(2^j\Delta t\left(2k-1+N_t/2\right)\right)\right. \\ &\left. 2\sum_{k=1}^{N_t/2-1} K_0^{(\eta)}\left(2^j\Delta t(2k+N_t/2)\right) + K_0^{(\eta)}(2^j\Delta t N_t)\right].\end{aligned} \tag{A.138}$$

Appendix B

Remarks

B.1 Volume of ν-dimension sphere

The volume of ν-dimension sphere in which the radius is r is defined by

$$V_\nu(r) := \int \cdots \int_{\sqrt{\sum_i^\nu x_i^2} \leq r} \mathrm{d}x_1 \cdots \mathrm{d}x_\nu. \tag{B.1}$$

First of all, we define

$$F(r) = \int \cdots \int_{\sqrt{\sum_i^\nu x_i^2} \leq r} \mathrm{d}x_1 \cdots \mathrm{d}x_\nu f\left(\sqrt{x_1^2 + \cdots + x_\nu}\right), \tag{B.2}$$

where $f(r)$ is an arbitrary function for $r \geq 0$. For imperceptible Δr, we can obtain

$$\begin{aligned} F(r+\Delta r) - F(r) &= \int \cdots \int_{r \leq \sqrt{\sum_i^\nu x_i^2} \leq r+\Delta r} \mathrm{d}x_1 \cdots \mathrm{d}x_\nu \left[f(r) + O(\Delta r)\right] \\ &= \left[V_\nu(r+\Delta r) - V_\nu(r)\right] f(r) + O(\Delta r^2), \end{aligned} \tag{B.3}$$

thus,

$$\frac{\mathrm{d}}{\mathrm{d}r} F(r) = \frac{\mathrm{d}V_\nu(r)}{\mathrm{d}r} f(r) = \nu V_\nu r^{\nu-1} f(r), \tag{B.4}$$

where $V_\nu(r) = V_\nu r^\nu$ where $V_\nu := V_\nu(1)$. Integrating this relationship with respect to r, we can obtain

$$\int \cdots \int \mathrm{d}x_1 \cdots \mathrm{d}x_\nu f\left(\sqrt{x_1^2 + \cdots + x_\nu^2}\right) = \int_0^\infty \mathrm{d}r \nu V_\nu r^{\nu-1} f(r). \tag{B.5}$$

Next, let us consider

$$I_\nu = \int \cdots \int \mathrm{d}x_1 \cdots \mathrm{d}x_\nu \exp\left[-(x_1^2 + \cdots x_\nu^2)\right]. \tag{B.6}$$

Using the property of the gauss integral, the I_ν reduces clearly to

$$I_\nu = \pi^{\nu/2}. \tag{B.7}$$

On the other hand, using eq. (B.5), we can obtain

$$I_\nu = \int_0^\infty \nu V_\nu r^{n-1} e^{-r^2} = V_\nu \frac{\nu}{2}\Gamma\left(\frac{\nu}{2}\right) = V_\nu \Gamma\left(\frac{\nu}{2}+1\right), \tag{B.8}$$

where $\Gamma(x)$ denotes the Gamma function defined by

$$\Gamma(x) := \int_0^\infty \mathrm{d}t\, t^{x-1} e^{-t}.$$

Therefore, the volume of ν-dimension sphere (radius is r) is

$$V_\nu(r) = V_\nu r^\nu = \frac{2\pi^{\nu/2}}{\nu\Gamma(\nu/2)} r^\nu = \frac{\pi^{\nu/2}}{\Gamma\left((\nu/2)+1\right)} r^\nu. \tag{B.9}$$

B.2 Relationship between C_V and C_p

The thermal variation δQ is represented by

$$\delta Q = T\mathrm{d}S = \begin{cases} C_V \mathrm{d}T + T\left(\frac{\partial S}{\partial V}\right)_T \mathrm{d}V \\ C_p \mathrm{d}T + T\left(\frac{\partial S}{\partial p}\right)_T \mathrm{d}p \end{cases},$$

where C_V and C_p denote the specific heat at constant volume and at constant pressure, respectively. They are defined by

$$C_V := \left(\frac{\delta Q}{\mathrm{d}T}\right)_V = \left(\frac{\partial E}{\partial T}\right)_V \tag{B.10}$$

$$C_p := \left(\frac{\delta Q}{\mathrm{d}T}\right)_p = \left(\frac{\partial H}{\partial T}\right)_V, \tag{B.11}$$

where E denotes the internal energy and H the enthalpy. Using the following relationship

$$\mathrm{d}p = \left(\frac{\partial p}{\partial T}\right)_V \mathrm{d}T + \left(\frac{\partial p}{\partial V}\right)_T \mathrm{d}V, \tag{B.12}$$

one can write

$$T\mathrm{d}S = C_p\mathrm{d}T + T\left(\frac{\partial S}{\partial p}\right)_T \left\{\left(\frac{\partial p}{\partial T}\right)_V \mathrm{d}T + \left(\frac{\partial p}{\partial V}\right)_T \mathrm{d}V\right\}. \tag{B.13}$$

Since $\mathrm{d}S$ is exact differential, we can compare the coefficients of the above equations and then obtain the following relationship[1]

$$C_V = C_p + T\left(\frac{\partial S}{\partial p}\right)_T \left(\frac{\partial p}{\partial T}\right)_V. \tag{B.14}$$

We are hard to measure the term $T\left(\frac{\partial S}{\partial p}\right)_T \left(\frac{\partial p}{\partial T}\right)_V$, and then we try to represent the term by measurable variables. Firstly, because of the Maxwell relationship, we obtain

$$\left(\frac{\partial S}{\partial p}\right)_T = -\left(\frac{\partial V}{\partial T}\right)_p =: -\alpha V, \tag{B.15}$$

where $\alpha := V^{-1}(\partial V/\partial T)_p$ denotes the isobaric expansion coefficient. In addition[2],

$$\left(\frac{\partial p}{\partial T}\right)_V = -\frac{\left(\frac{\partial V}{\partial T}\right)_p}{\left(\frac{\partial V}{\partial p}\right)_T} =: \frac{\alpha}{\kappa}, \tag{B.18}$$

where $\kappa := -V^{-1}(\partial V/\partial p)_T$ denotes the isothermal compressibility. Therefore, the relationship between C_V and C_p is given by

$$C_p = C_V + TV\frac{\alpha^2}{\kappa}. \tag{B.19}$$

When the gas is ideal, the above equation reduces to the Mayer's relation

$$C_p = C_V + Nk_B, \tag{B.20}$$

where N denotes the number of particles and k_B the Boltzmann constant. Note that $\alpha = 1/T$ and $\kappa = 1/p$ for the ideal gas.

[1] At the same time, we can prove that the coefficients of $\mathrm{d}V$ are equivalent because $\left(\frac{\partial S}{\partial p}\right)_T \left(\frac{\partial p}{\partial V}\right)_T = \left(\frac{\partial S}{\partial V}\right)_T$.

[2] In general,

$$\left(\frac{\partial X}{\partial Y}\right)_Z \left(\frac{\partial Y}{\partial Z}\right)_X \left(\frac{\partial Z}{\partial X}\right)_Y = -1, \tag{B.16}$$

and

$$\left\{\left(\frac{\partial X}{\partial Y}\right)_Z\right\}^{-1} = \left(\frac{\partial Y}{\partial X}\right)_Z \tag{B.17}$$

B.3 Langevin equation for the one-dimensional Brownian motion with the harmonic potential

Let us consider a simple model proposed by Zwanzig [78]. We consider the one-dimensional dynamics of a Brownian particle in solvent. The Hamiltonian is represented as

$$\mathcal{H} = \frac{P^2}{2M} + \sum_{j=1}^{N} \frac{p_j^2}{2m} + U_0(X) + \sum_{j=1}^{N} \frac{m\omega_j^2}{2} \left(x_j - \frac{\gamma_j}{m\omega_j^2} X \right)^2, \tag{B.21}$$

where X denotes the position of the Brownian particle, P the momentum of that, M the muss of that, $U(X)$ a interaction from external field, x_j the position of the j-th particle of solvent, p_j the momentum of that, m the mass of that, ω_j the frequency of that, and γ_j the friction constant of that. The interaction between the Brownian particle and the particles of solvent is described by the harmonic potential, i.e. fictitious spring, is considered. The equations of motion are

$$\frac{\mathrm{d}X}{\mathrm{d}t} = \frac{P}{M} \quad , \quad \frac{\mathrm{d}P}{\mathrm{d}t} = -\frac{\mathrm{d}U_0}{\mathrm{d}X} + \sum_{j=1}^{N} \gamma_j \left(x_j - \frac{\gamma_j}{m\omega_j^2} X \right) \tag{B.22}$$

$$\frac{\mathrm{d}x_j}{\mathrm{d}t} = \frac{p_j}{m} \quad , \quad \frac{\mathrm{d}p_j}{\mathrm{d}t} = -m\omega_j^2 x_j + \gamma_j X_j \tag{B.23}$$

From the equations of motion, it is straightforward to show

$$x_j - \frac{\gamma_j}{m\omega_j^2} X = \left\{ x_j(0) - \frac{\gamma_j}{m\omega_j^2} \right\} \cos\omega_j t + \frac{\dot{x}_j(0)}{\omega_j} \sin\omega_j t - \int_0^t \mathrm{d}t' \frac{\gamma_j}{m\omega_j^2} \cos\omega_j (t-t') \dot{X}(t'). \tag{B.24}$$

Therefore, we obtain a convolution-type Langevin equation as

$$\frac{\mathrm{d}P}{\mathrm{d}t} = -\frac{\mathrm{d}U_0}{\mathrm{d}X} - \int_0^t \mathrm{d}t' \zeta(t-t') P(t') + \xi(t), \tag{B.25}$$

where

$$\zeta(t) := \sum_{j=1}^{N} \frac{\gamma_j^2}{mM\omega_j^2} \cos\omega_j t \tag{B.26}$$

$$\xi(t) := \sum_{j=1}^{N} \gamma_j \left[\left\{ x_j(0) - \frac{\gamma_j}{m\omega_j^2} X(0) \right\} \cos\omega_j t + \frac{\dot{x}_j(0)}{\omega_j} \sin\omega_j t \right]. \tag{B.27}$$

When the initial distribution of Γ-space is the canonical ensemble, we can prove the fluctuation-dissipation relation

$$\overline{\xi(t)} = 0 \ , \ \overline{\xi(t)\xi(t')} = k_B T \zeta(t - t'), \tag{B.28}$$

where the overbar denotes an average over the initial distribution.

B.4 Integral range of x and y in eq. (A.27)

New variables x and y are represented by

$$x = \sqrt{p^2 + \frac{q^2}{4} + pq\cos\theta} \ , \ y = \sqrt{p^2 + \frac{q^2}{4} - pq\cos\theta}. \tag{B.29}$$

For $\cos\theta \geq -1$, $x \geq |p - q/2|$ and $y \leq p + q/2$, and thus $x \geq |y - q|$. Similarly, $y \geq |x - q|$ for $\cos\theta \leq 1$.

Let us consider the inequalities more closely. Although the inequality $x \geq |y - q|$ describes the range of x, we want to know the range of y. Thus, we transform it as

$$x \geq |y - q| \ \Leftrightarrow \ \begin{cases} x \geq y - q & (y \geq q) \\ x \geq q - y & (y \leq q) \end{cases} \ \Leftrightarrow \ \begin{cases} y \leq x + q & (y \geq q) \\ y \geq -x + q & (y \leq q) \end{cases} . \tag{B.30}$$

At first, we focus on the range of $0 \leq x \leq q$. When $0 \leq y \leq q$, considering both $y \geq |x - q|$ and $y \geq -x + q$, we can get

$$-x + q \leq y \leq q \ \ (\text{for } 0 \leq x \leq q) \ \Leftrightarrow \ \ |x - q| \leq y \leq q \ \ (\text{for } 0 \leq x \leq q). \tag{B.31}$$

Moreover, when $q \leq y$, considering both $y \geq |x - q|$ and $y \leq x + q$, we can also get

$$q \leq y \leq x + q \ \ (\text{for } 0 \leq x \leq q) \tag{B.32}$$

Because of the above results, we obtain the range of y in $0 \leq x \leq q$ as

$$|x - q| \leq y \leq x + q \ \ (\text{for } 0 \leq x \leq q). \tag{B.33}$$

Next, we focus on the range of $q \leq x$. when $0 \leq y \leq q$, considering both $y \geq -x + q$ and $y \geq |x - q|$, we can get

$$|x - q| \leq y \leq q \ \ (\text{for } x \leq q) \tag{B.34}$$

because $-x + q < 0$ in the x-region we consider. Further, when $q \leq y$, considering both $y \leq x + q$ and $y \geq |x - q|$, we can also get

$$q \leq y \leq x + q \ \ (\text{for } x \leq q) \tag{B.35}$$

because $q \geq |x - q|$ in the x-region we consider. Therefore, we obtain the range of y in $q \leq x$ as

$$|x - q| \leq y \leq x + q \ \ (\text{for } q \leq x). \tag{B.36}$$

Summarizing the above results, we obtain the range of y in $0 \leq x$ as

$$x \geq |y - q| \ \text{ and } \ y \geq |x - q| \ \ \Leftrightarrow \ \ |x - q| \leq y \leq x + q \ \ (\text{for } 0 \leq x). \tag{B.37}$$

B.5 Three-point difference formula

The Euler method is usually used as the easiest method of the numerical difference. However, the method includes truncation error of order h where h is a step size. Here, we consider a less-error method; three-point difference formula.

Since

$$f(x - h) = f(x) - hf'(x) + \frac{h^2}{2} f''(x) + O(h^3) \tag{B.38}$$

and

$$f(x - 2h) = f(x) - 2hf'(x) + 2h^2 f''(x) + O(h^3), \tag{B.39}$$

we obtain the three-point backward first difference formula as

$$f'(x) = \frac{1}{h}\left(\frac{3}{2} f(x) - 2f(x - h) + \frac{1}{2} f(x - 2h)\right) + O(h^2). \tag{B.40}$$

Similarly, since

$$f(x-h) = f(x) - hf'(x) + \frac{h^2}{2}f''(x) - \frac{h^3}{6}f'''(x) + O(h^4), \tag{B.41}$$

$$f(x-2h) = f(x) - 2hf'(x) + 2h^2f''(x) - \frac{4h^3}{3}f'''(x) + O(h^4), \tag{B.42}$$

and

$$f(x-3h) = f(x) - 3hf'(x) + \frac{9h^2}{2}f''(x) - \frac{9h^3}{2}f'''(x) + O(h^4), \tag{B.43}$$

we obtain the three-point backward second difference formula as

$$f''(x) = \frac{1}{h^2}\{2f(x) - 5f(x-h) + 4f(x-2h) - f(x-3h)\} + O(h^2). \tag{B.44}$$

Note that the three-point forward difference formula is easily obtained if h is transformed to $-h$. The three-point difference formula includes truncation error of order h^2.

B.6 Simpson's rule

The Simpson's rule is one of theorems to obtain integrals numerically. The idea is that an arbitrary function $f(x)$ is approximated with a quadric[3]. The derivation is straightforward[4]. Let range of an integral that we consider be (x_0, x_2), and x_1 denote the center of the integral range. Moreover, let Δx denote $x_2 - x_1 = x_1 - x_0$. Since a quadric represented by $px^2 + qx + r$ passes through (x_0, y_0), (x_1, y_1), and (x_2, y_2), we obtain

$$p = \frac{y_2 - 2y_1 + y_0}{2\Delta x^2}, \tag{B.45}$$

$$q = \frac{y_2 - y_0}{2\Delta x} - 2x_1 p, \tag{B.46}$$

$$r = \frac{1}{2}(y_2 + y_0) - x_1 q + (x_1^2 - \Delta x^2)p. \tag{B.47}$$

Therefore, an integral of $f(x)$ is approximatively solved as

$$\int_{x_0}^{x_2} \mathrm{d}x f(x) \simeq \int_{x_0}^{x_2} \mathrm{d}x (px^2 + qx + r) = \frac{\Delta x}{3}(y_0 + 4y_1 + y_2). \tag{B.48}$$

[3]The simplest method to calculate integrals is the trapezium rule. The Simpson's rule is more accurate than the trapezium rule.

[4]The Simpson's rule is also obtained by using the Lagrange polynomial interpolation.

Range of an integral should be as narrow as possible because error of the Simpson's rule is smaller as the integral range is narrower. Suppose that the range (a, b) is split up in n subintervals, where n is an even integer. Then, the composite Simpson's rule is represented as

$$\int_a^b \mathrm{d}x f(x) \simeq \frac{\Delta x}{3}\left[f(a) + 4\sum_{j=1}^{n/2} f(x_{2j-1}) + 2\sum_{j=1}^{n/2-1} f(x_{2j}) + f(b)\right], \tag{B.49}$$

where n denotes $(b-a)/\Delta x$.

B.7 Prescription for Multiplicative Random Term

We consider the following type differential equation

$$\frac{\mathrm{d}}{\mathrm{d}t}\boldsymbol{A}(t) = \boldsymbol{h}(\boldsymbol{A}(t)) + \boldsymbol{\Omega}(\boldsymbol{A}(t), t), \tag{B.50}$$

where $\boldsymbol{h}(\boldsymbol{A}(t))$ denotes a nonlinear deterministic function of a set of physical variables $\boldsymbol{A}(t)$ and $\boldsymbol{\Omega}(\boldsymbol{A}(t), t)$ a nonlinear stochastic function containing an additive and/or a multiplicative random term in general. The purpose of this article is to transform the multiplicative type to the additive type stochastic equation using the Tokuyama-Mori (so-called time-convolutionless) type projection method.

B.7.1 Tokuyama-Mori Type Projection Method

We define a generating function as $\Pi_a(t) := \delta(\boldsymbol{A}(t) - \boldsymbol{a}) = \prod_i \delta(A_i(t) - a_i)$ where $A_i(t)$ denotes a dynamical variable and a_i an available value (not variable) of $A_i(t)$. The temporal differentiation of the generating function is

$$\begin{aligned}\frac{\partial}{\partial t}\boldsymbol{\Pi}(t) &= -\frac{\partial}{\partial \boldsymbol{a}} \cdot \dot{\boldsymbol{A}}(t)\boldsymbol{\Pi}(t) = -\frac{\partial}{\partial \boldsymbol{a}} \cdot \{\boldsymbol{h}(\boldsymbol{A}(t)) + \boldsymbol{\Omega}(\boldsymbol{A}(t), t)\}\,\boldsymbol{\Pi}(t) &\text{(B.51)}\\ &= -\frac{\partial}{\partial \boldsymbol{a}} \cdot \{\boldsymbol{h}(\boldsymbol{a}) + \boldsymbol{\Omega}(\boldsymbol{a}, t)\}\,\boldsymbol{\Pi}(t) =: \mathcal{L}(\boldsymbol{a}, t)\boldsymbol{\Pi}(t), &\text{(B.52)}\end{aligned}$$

where the operator $\mathcal{L}(\boldsymbol{a},t)$ is defined[5] as $-\frac{\partial}{\partial \boldsymbol{a}}\cdot\{\boldsymbol{h}(\boldsymbol{a})+\boldsymbol{\Omega}(\boldsymbol{a},t)\}$. Furthermore we obtain the infinite series solution for the generating function

$$\boldsymbol{\Pi}(t)=\exp_+\left[\int_0^t \mathrm{d}\tau\mathcal{L}(\boldsymbol{a},\tau)\right]\boldsymbol{\Pi}(0)=:\mathcal{U}(\boldsymbol{a},t)\boldsymbol{\Pi}(0), \tag{B.53}$$

where $\exp_+$ denotes the time-ordered exponential function of x (see Appendix B.7.3). Using the adjoint operators of $\mathcal{L}(\boldsymbol{a},t)$ and $\mathcal{U}(\boldsymbol{a},t)$ (see Appendix B.7.4 about the adjoint operators), the time derivative of the generating function reduces to

$$\frac{\partial}{\partial t}\boldsymbol{\Pi}(t)=\mathcal{L}(\boldsymbol{a},t)\mathcal{U}(\boldsymbol{a},t)\boldsymbol{\Pi}(0)=\tilde{\mathcal{U}}(\boldsymbol{A}(0),t)\tilde{\mathcal{L}}(\boldsymbol{A}(0),t)\boldsymbol{\Pi}(0). \tag{B.54}$$

Note that

$$\begin{aligned}
\mathcal{U}(\boldsymbol{a},t)\delta(\boldsymbol{a}-\boldsymbol{b}) &= \exp_+\left[\int_0^t \mathrm{d}\tau\mathcal{L}(\boldsymbol{a},\tau)\right]\delta(\boldsymbol{a}-\boldsymbol{b})\\
&= \delta(\boldsymbol{a}-\boldsymbol{b})+\int_0^t \mathrm{d}\tau_1\mathcal{L}(\boldsymbol{a},\tau_1)\delta(\boldsymbol{a}-\boldsymbol{b})\\
&\quad+\int_0^t \mathrm{d}\tau_1\int_0^{\tau_1}\mathrm{d}\tau_2\mathcal{L}(\boldsymbol{a},\tau_1)\mathcal{L}(\boldsymbol{a},\tau_2)\delta(\boldsymbol{a}-\boldsymbol{b})+\cdots\\
&= \delta(\boldsymbol{a}-\boldsymbol{b})+\int_0^t \mathrm{d}\tau_1\tilde{\mathcal{L}}(\boldsymbol{b},\tau_1)\delta(\boldsymbol{a}-\boldsymbol{b})\\
&\quad+\int_0^t \mathrm{d}\tau_1\int_0^{\tau_1}\mathrm{d}\tau_2\tilde{\mathcal{L}}(\boldsymbol{b},\tau_2)\tilde{\mathcal{L}}(\boldsymbol{b},\tau_1)\delta(\boldsymbol{a}-\boldsymbol{b})+\cdots\\
&= \exp_-\left[\int_0^t \mathrm{d}\tau\tilde{\mathcal{L}}(\boldsymbol{b},\tau)\right]\delta(\boldsymbol{a}-\boldsymbol{b}),
\end{aligned} \tag{B.55}$$

$$\therefore\ \tilde{\mathcal{U}}(\boldsymbol{b},t)=\exp_-\left[\int_0^t \mathrm{d}\tau\tilde{\mathcal{L}}(\boldsymbol{b},\tau)\right]. \tag{B.56}$$

Using an identity (B.105) in Appendix B.7.5 about $\tilde{\mathcal{U}}$, eq. (B.54) reduces to

$$\begin{aligned}
\frac{\partial}{\partial t}\boldsymbol{\Pi}(t) &= \tilde{\mathcal{U}}(\boldsymbol{A}(0),t)\mathcal{P}\tilde{\mathcal{L}}(\boldsymbol{A}(0),t)\boldsymbol{\Pi}(0)+\tilde{\mathcal{V}}(\boldsymbol{A}(0),t)\mathcal{Q}\tilde{\mathcal{L}}(\boldsymbol{A}(0),t)\boldsymbol{\Pi}(0)\\
&\quad+\tilde{\mathcal{U}}(\boldsymbol{A}(0),t)\mathcal{P}\tilde{\mathcal{J}}(\boldsymbol{A}(0),t)\mathcal{Q}\left[1-\tilde{\mathcal{J}}(\boldsymbol{A}(0),t)\mathcal{Q}\right]^{-1}\tilde{\mathcal{L}}(\boldsymbol{A}(0),t)\boldsymbol{\Pi}(0)\\
&= \tilde{\mathcal{U}}(\boldsymbol{A}(0),t)\mathcal{P}\left[1-\tilde{\mathcal{J}}(\boldsymbol{A}(0),t)\mathcal{Q}\right]^{-1}\tilde{\mathcal{L}}(\boldsymbol{A}(0),t)\boldsymbol{\Pi}(0)\\
&\quad+\tilde{\mathcal{V}}(\boldsymbol{A}(0),t)\mathcal{Q}\tilde{\mathcal{L}}(\boldsymbol{A}(0),t)\boldsymbol{\Pi}(0),
\end{aligned} \tag{B.57}$$

[5] We must NOT regard $-\frac{\partial}{\partial \boldsymbol{a}}\cdot\{\boldsymbol{h}(\boldsymbol{A}(t))+\boldsymbol{\Omega}(\boldsymbol{A}(t),t)\}\boldsymbol{\Pi}(t)$ as $\mathcal{L}(\boldsymbol{A}(t),t)\boldsymbol{\Pi}(t)$ in eq. (B.51) because both $\boldsymbol{a}$ and $\boldsymbol{A}(t)$ are there.

where

$$1 + \mathcal{X}\left[1 - \mathcal{X}\right]^{-1} \equiv \left[1 - \mathcal{X}\right]^{-1}. \tag{B.58}$$

We define a new operator $\tilde{\mathcal{G}}(\boldsymbol{A}(0), t)$ as

$$\tilde{\mathcal{G}}(\boldsymbol{A}(0), t) := \left[1 - \tilde{\mathcal{J}}(\boldsymbol{A}(0), t)\mathcal{Q}\right]^{-1}.$$

Here,

$$\begin{aligned}
\tilde{\mathcal{G}} &= \left[1 - \tilde{\mathcal{J}}\right]^{-1}\left[1 - \tilde{\mathcal{J}}\right]\left[1 - \tilde{\mathcal{J}}\mathcal{Q}\right]^{-1} \\
&= \left[1 - \tilde{\mathcal{J}}\right]^{-1}\left[1 - \tilde{\mathcal{J}}\mathcal{Q} - \tilde{\mathcal{J}}\mathcal{P}\right]\left[1 - \tilde{\mathcal{J}}\mathcal{Q}\right]^{-1} \\
&= \left[1 - \tilde{\mathcal{J}}\right]^{-1}\left\{1 - \tilde{\mathcal{J}}\mathcal{P}\left[1 - \tilde{\mathcal{J}}\mathcal{Q}\right]^{-1}\right\} \\
&= \left[1 - \tilde{\mathcal{J}}\right]^{-1}\left[1 - \tilde{\mathcal{J}}\mathcal{P}\tilde{\mathcal{G}}\right], \\
\Leftrightarrow \quad \left\{1 + \left[1 - \tilde{\mathcal{J}}\right]^{-1}\tilde{\mathcal{J}}\mathcal{P}\right\}\tilde{\mathcal{G}} &= [1 - \tilde{\mathcal{J}}]^{-1}, \\
\Leftrightarrow \quad \tilde{\mathcal{G}} &= \left\{1 + \left[1 - \tilde{\mathcal{J}}\right]^{-1}\tilde{\mathcal{J}}\mathcal{P}\right\}^{-1}[1 - \tilde{\mathcal{J}}]^{-1}.
\end{aligned}$$

Moreover, we define a new operator $\tilde{\mathcal{W}}(\boldsymbol{A}(0), t)$ as

$$\tilde{\mathcal{W}}(\boldsymbol{A}(0), t) := \left[\tilde{\mathcal{J}}(\boldsymbol{A}(0), t) - 1\right]^{-1}\tilde{\mathcal{J}}(\boldsymbol{A}(0), t),$$

and thus

$$\tilde{\mathcal{G}}(\boldsymbol{A}(0), t) = \left[1 - \tilde{\mathcal{W}}(\boldsymbol{A}(0), t)\mathcal{P}\right]^{-1}\left[1 - \tilde{\mathcal{W}}(\boldsymbol{A}(0), t)\right], \tag{B.59}$$

where for an arbitrary operator $\mathcal{X}$

$$\left[1 - \mathcal{X}\right]^{-1} \equiv -\left[\mathcal{X} - 1\right]^{-1} \equiv 1 - \left[\mathcal{X} - 1\right]^{-1}\mathcal{X}. \tag{B.60}$$

Furthermore, since $\tilde{\mathcal{J}}(\boldsymbol{A}(0), t) := 1 - \tilde{\mathcal{U}}^{-1}(\boldsymbol{A}(0), t)\tilde{\mathcal{U}}_Q(\boldsymbol{A}(0), t)$, we can obtain

$$\tilde{\mathcal{W}} = -\tilde{\mathcal{U}}_Q^{-1}(\boldsymbol{A}(0), t)\tilde{\mathcal{U}}(\boldsymbol{A}(0), t)(1 - \tilde{\mathcal{U}}^{-1}(\boldsymbol{A}(0), t)\tilde{\mathcal{U}}_Q(\boldsymbol{A}(0), t)) = 1 - \tilde{\mathcal{U}}_Q^{-1}(\boldsymbol{A}(0), t)\tilde{\mathcal{U}}. \tag{B.61}$$

Using the following relationship[6]

$$[1-\mathcal{X}]^{-1} = \sum_{n=0}^{\infty} \mathcal{X}^n, \tag{B.63}$$

for an arbitrary variable F we obtain

$$\begin{aligned}
\left[1-\tilde{\mathcal{W}}\mathcal{P}\right]^{-1} F &= F + \sum_{n=1}^{\infty} (\tilde{\mathcal{W}}\mathcal{P})^n F \\
&= F + \left\langle F\mathbf{\Pi}^\dagger(0)\right\rangle \\
&\quad \cdot \left[\sum_{n=0}^{\infty} \left\{ \overleftrightarrow{\phi}^{-1}(0) \cdot \left\langle (\tilde{\mathcal{W}}\mathbf{\Pi}(0))\mathbf{\Pi}^\dagger(0)\right\rangle \right\}^n \cdot \overleftrightarrow{\phi}^{-1}(0) \right] \cdot \tilde{\mathcal{W}}\mathbf{\Pi}(0)
\end{aligned} \tag{B.64}$$

$$= F + \left\langle F\mathbf{\Pi}^\dagger(0)\right\rangle \cdot \left\langle \mathbf{\Pi}(t)\mathbf{\Pi}^\dagger(0)\right\rangle^{-1} \cdot \tilde{\mathcal{W}}\mathbf{\Pi}(0), \tag{B.65}$$

where

$$\overleftrightarrow{\phi}^{-1}(0) \cdot \left\langle (\tilde{\mathcal{W}}\mathbf{\Pi}(0))\mathbf{\Pi}^\dagger(0)\right\rangle = 1 - \overleftrightarrow{\phi}^{-1}(0) \cdot \left\langle \mathbf{\Pi}(t)\mathbf{\Pi}^\dagger(0)\right\rangle,$$

and the relationship eq. (B.62) is used again. Here, we should note that we imposed $\mathcal{P}\tilde{\mathcal{U}}_Q = \mathcal{P} \Leftrightarrow \mathcal{P} = \mathcal{P}\tilde{\mathcal{U}}_Q^{-1}$ on $\mathcal{U}_Q$. In other words, $\mathcal{U}_Q$ must hold $\left\langle (\tilde{\mathcal{U}}_Q F)\mathbf{\Pi}^\dagger(0)\right\rangle = \left\langle (\tilde{\mathcal{U}}_Q^{-1} F)\mathbf{\Pi}^\dagger(0)\right\rangle = \left\langle F\mathbf{\Pi}^\dagger(0)\right\rangle$. One of conflict forms of $\tilde{\mathcal{U}}_Q$ is

$$\tilde{\mathcal{U}}_Q(a,t) := \exp_- \left[\mathcal{Q} \int_0^t \mathrm{d}\tau \tilde{\mathcal{L}}(a,\tau) \right]. \tag{B.66}$$

In the following, we employ eq. (B.66) as $\tilde{\mathcal{U}}_Q$.

The first term of RHS of eq. (B.57) reduces to

$$\begin{aligned}
\tilde{\mathcal{U}}\mathcal{P}\tilde{\mathcal{G}}\tilde{\mathcal{L}}\mathbf{\Pi}(0) &= \left\langle (\tilde{\mathcal{G}}\tilde{\mathcal{L}}\mathbf{\Pi}(0))\mathbf{\Pi}^\dagger(0)\right\rangle \cdot \overleftrightarrow{\phi}^{-1}(0) \cdot \mathbf{\Pi}(t) \\
&= \left\langle \dot{\mathbf{\Pi}}(t)\mathbf{\Pi}^\dagger(0)\right\rangle \cdot \left\langle \mathbf{\Pi}(t)\mathbf{\Pi}^\dagger(0)\right\rangle^{-1} \cdot \mathbf{\Pi}(t).
\end{aligned} \tag{B.67}$$

[6]This relationship corresponds to the summation rule of the geometric series. We can justify that relation as

$$\sum_{n=0}^{\infty} \mathcal{X}(1-\mathcal{X}) = 1 \quad \Leftrightarrow \quad (1-\mathcal{X})^{-1} = \sum_{n=0}^{\infty} \mathcal{X}^n. \tag{B.62}$$

This proof might be incorrect mathematically but we can understand it intuitively.

Therefore, the generalized projection method leads to the linear equation of motion for $\mathbf{\Pi}(t)$ as

$$\frac{\partial}{\partial t}\mathbf{\Pi}(t) = \mathsf{M}(t)\cdot\mathbf{\Pi}(t) + \boldsymbol{G}(t) \quad \text{or} \quad \frac{\partial}{\partial t}\Pi_a(t) = \mathcal{M}(\boldsymbol{a},t)\Pi_a(t) + G_a(t), \tag{B.68}$$

where M denotes a matrix defined as[7]

$$\begin{aligned}[\mathsf{M}(t)]_{ab} &:= \mathcal{M}(\boldsymbol{a},t)\delta(\boldsymbol{a}-\boldsymbol{b}) := \left[\left\langle\dot{\mathbf{\Pi}}(t)\mathbf{\Pi}^\dagger(0)\right\rangle\cdot\left\langle\mathbf{\Pi}(t)\mathbf{\Pi}^\dagger(0)\right\rangle^{-1}\right]_{ab} \\ &= \int \mathrm{d}\boldsymbol{c}\left\langle\dot{\Pi}_a(t)\Pi_c^*(0)\right\rangle\phi_{cb}^{-1}(t)\end{aligned} \tag{B.69}$$

by using the master operator $\mathcal{M}$, and $\boldsymbol{G}(t)$ denotes the master fluctuating force defined by the second term of RHS of eq. (B.57);

$$\boldsymbol{G}(t) := \tilde{\mathcal{V}}(\boldsymbol{A}(0),t)\mathcal{Q}\tilde{\mathcal{L}}(\boldsymbol{A}(0),t)\mathbf{\Pi}(0). \tag{B.70}$$

When we choose $\tilde{\mathcal{U}_Q}$ as eq. (B.66), $\boldsymbol{G}(t)$ satisfies $\langle\boldsymbol{G}(t)\mathbf{\Pi}(0)\rangle = 0$.

Multiplying the equation of motion for $\mathbf{\Pi}(t)$ by a_k from the left side, we obtain the nonlinear Langevin type equation

$$\frac{\partial}{\partial t}A_k(t) = h_k(\boldsymbol{A}(t)) + Z_k(\boldsymbol{A}(t),t) + G_k(t), \tag{B.71}$$

where $Z_k(\boldsymbol{A}(t),t)$ denotes the drift term represented by

$$Z_k(\boldsymbol{A}(t),t) := \int \mathrm{d}\boldsymbol{a}\,\langle\Omega_k(\boldsymbol{a},t)\mathcal{U}(\boldsymbol{a},t);\boldsymbol{a}\rangle\,\mathcal{S}_-(\boldsymbol{a},t)\Pi_a(t) \tag{B.72}$$

and the $G_k(t)$ the master fluctuating term represented by

$$G_k(t) := \tilde{\mathcal{V}}(\boldsymbol{A}(0),t)\mathcal{Q}\dot{A}_k(0). \tag{B.73}$$

Note that the form of the master operator is represented by eq. (B.114) in Appendix B.7.6.

[7] It is not always true that M is a diagonal matrix even though M contains the delta function because $\mathcal{M}$ is an operator.

B.7.2 Drift Term

We consider the drift term (B.72). Using the operator identity (B.119) and (B.120) in appendix B.7.7, $\mathcal{U}$ and $\mathcal{S}_-$ is expanded as

$$\begin{aligned}\mathcal{U}(\boldsymbol{a},t) &= e^{-t\frac{\partial}{\partial \boldsymbol{a}}\cdot\boldsymbol{h}(\boldsymbol{a})}\exp_+\left[-\int_0^t \mathrm{d}\tau e^{\tau\frac{\partial}{\partial \boldsymbol{a}}\cdot\boldsymbol{h}(\boldsymbol{a})}\frac{\partial}{\partial \boldsymbol{a}}\cdot\boldsymbol{\Omega}(\boldsymbol{a},\tau)e^{-\tau\frac{\partial}{\partial \boldsymbol{a}}\cdot\boldsymbol{h}}\right] \\ &= e^{-t\frac{\partial}{\partial \boldsymbol{a}}\cdot\boldsymbol{h}(\boldsymbol{a})} - \int_0^t \mathrm{d}\tau e^{-(t-\tau)\frac{\partial}{\partial \boldsymbol{a}}\cdot\boldsymbol{h}(\boldsymbol{a})}\frac{\partial}{\partial \boldsymbol{a}}\cdot\boldsymbol{\Omega}(\boldsymbol{a},t)e^{-\tau\frac{\partial}{\partial \boldsymbol{a}}\cdot\boldsymbol{h}(\boldsymbol{a})} + O(\Omega^2), \quad \text{(B.74)}\end{aligned}$$

$$\begin{aligned}\mathcal{S}_-(\boldsymbol{a},t) = \exp_-&\left[\int_0^t \mathrm{d}\tau e^{\tau\frac{\partial}{\partial \boldsymbol{a}}\cdot\boldsymbol{h}(\boldsymbol{a})}\frac{\partial}{\partial \boldsymbol{a}}\cdot\langle\boldsymbol{\Omega}(\boldsymbol{a},\tau)\mathcal{U}(\boldsymbol{a},\tau);\boldsymbol{a}\rangle\,\mathcal{S}_-(\boldsymbol{a},\tau)e^{-\tau\frac{\partial}{\partial \boldsymbol{a}}\cdot\boldsymbol{h}(\boldsymbol{a})}\right]e^{t\frac{\partial}{\partial \boldsymbol{a}}\cdot\boldsymbol{h}(\boldsymbol{a})} \\ =&e^{t\frac{\partial}{\partial \boldsymbol{a}}\cdot\boldsymbol{h}(\boldsymbol{a})} + \int_0^t \mathrm{d}\tau e^{\tau\frac{\partial}{\partial \boldsymbol{a}}\cdot\boldsymbol{h}(\boldsymbol{a})}\frac{\partial}{\partial \boldsymbol{a}}\cdot\langle\boldsymbol{\Omega}(\boldsymbol{a},\tau)\mathcal{U}(\boldsymbol{a},\tau);\boldsymbol{a}\rangle\,\mathcal{S}_-(\boldsymbol{a},\tau)e^{(t-\tau)\frac{\partial}{\partial \boldsymbol{a}}\cdot\boldsymbol{h}(\boldsymbol{a})} + O(\Omega^2) \\ =&e^{t\frac{\partial}{\partial \boldsymbol{a}}\cdot\boldsymbol{h}(\boldsymbol{a})} + \int_0^t \mathrm{d}\tau e^{\tau\frac{\partial}{\partial \boldsymbol{a}}\cdot\boldsymbol{h}(\boldsymbol{a})}\frac{\partial}{\partial \boldsymbol{a}}\cdot\left\langle\boldsymbol{\Omega}(\boldsymbol{a},\tau)e^{-\tau\frac{\partial}{\partial \boldsymbol{a}}\cdot\boldsymbol{h}(\boldsymbol{a})};\boldsymbol{a}\right\rangle e^{t\frac{\partial}{\partial \boldsymbol{a}}\cdot\boldsymbol{h}(\boldsymbol{a})} + O(\Omega^2). \quad \text{(B.75)}\end{aligned}$$

These lead us to calculate the drift term of order up to Ω^2 as

$$\begin{aligned}\boldsymbol{Z}(\boldsymbol{b},t) &= \int \mathrm{d}\boldsymbol{a}\,\langle\boldsymbol{\Omega}(\boldsymbol{a},t)\mathcal{U}(\boldsymbol{a},t);\boldsymbol{a}\rangle\,\mathcal{S}_-(\boldsymbol{a},t)\delta(\boldsymbol{a}-\boldsymbol{b}) \\ &= \int \mathrm{d}\boldsymbol{a}\left\langle\boldsymbol{\Omega}(\boldsymbol{a},t)e^{-t\frac{\partial}{\partial \boldsymbol{a}}\cdot\boldsymbol{h}(\boldsymbol{a})};\boldsymbol{a}\right\rangle e^{t\frac{\partial}{\partial \boldsymbol{a}}\cdot\boldsymbol{h}(\boldsymbol{a})}\delta(\boldsymbol{a}-\boldsymbol{b}) \\ &\quad - \int \mathrm{d}\boldsymbol{a}\left\langle\boldsymbol{\Omega}(\boldsymbol{a},t)\int_0^t \mathrm{d}\tau e^{-(t-\tau)\frac{\partial}{\partial \boldsymbol{a}}\cdot\boldsymbol{h}(\boldsymbol{a})}\frac{\partial}{\partial \boldsymbol{a}}\cdot\boldsymbol{\Omega}(\boldsymbol{a},t)e^{-\tau\frac{\partial}{\partial \boldsymbol{a}}\cdot\boldsymbol{h}(\boldsymbol{a})};\boldsymbol{a}\right\rangle e^{t\frac{\partial}{\partial \boldsymbol{a}}\cdot\boldsymbol{h}(\boldsymbol{a})}\delta(\boldsymbol{a}-\boldsymbol{b}) \\ &\quad + \int \mathrm{d}\boldsymbol{a}\left\langle\boldsymbol{\Omega}(\boldsymbol{a},t)e^{-t\frac{\partial}{\partial \boldsymbol{a}}\cdot\boldsymbol{h}(\boldsymbol{a})};\boldsymbol{a}\right\rangle\int_0^t \mathrm{d}\tau e^{\tau\frac{\partial}{\partial \boldsymbol{a}}\cdot\boldsymbol{h}(\boldsymbol{a})} \\ &\qquad\qquad \times\frac{\partial}{\partial \boldsymbol{a}}\cdot\left\langle\boldsymbol{\Omega}(\boldsymbol{a},\tau)e^{-\tau\frac{\partial}{\partial \boldsymbol{a}}\cdot\boldsymbol{h}(\boldsymbol{a})};\boldsymbol{a}\right\rangle e^{t\frac{\partial}{\partial \boldsymbol{a}}\cdot\boldsymbol{h}(\boldsymbol{a})}\delta(\boldsymbol{a}-\boldsymbol{b}) \\ &\quad + O(\Omega^3). \quad \text{(B.76)}\end{aligned}$$

Considering the fact that the adjoint operator of $e^{t\frac{\partial}{\partial \boldsymbol{a}}\cdot\boldsymbol{h}(\boldsymbol{a})}$ denotes $e^{-t\boldsymbol{h}(\boldsymbol{a})\cdot\frac{\partial}{\partial \boldsymbol{a}}}$, the first term reduces to

$$\begin{aligned}\int \mathrm{d}\boldsymbol{a}\left\langle\boldsymbol{\Omega}(\boldsymbol{a},t)e^{-t\frac{\partial}{\partial \boldsymbol{a}}\cdot\boldsymbol{h}(\boldsymbol{a})};\boldsymbol{a}\right\rangle e^{t\frac{\partial}{\partial \boldsymbol{a}}\cdot\boldsymbol{h}(\boldsymbol{a})}\delta(\boldsymbol{a}-\boldsymbol{b}) &= \int \mathrm{d}\boldsymbol{a}\,\langle\boldsymbol{\Omega}(\boldsymbol{a}(-t),t);\boldsymbol{a}\rangle\,\delta(\boldsymbol{a}-\boldsymbol{b}(t)) \\ &= \langle\boldsymbol{\Omega}(\boldsymbol{b},t);\boldsymbol{b}(t)\rangle\,, \quad \text{(B.77)}\end{aligned}$$

where $\boldsymbol{a}(t)$ is defined by (B.127) in Appendix B.7.8. Note that the time-derivative of $\boldsymbol{a}(t)$ holds the differential equation given by

$$\frac{\partial \boldsymbol{a}(t)}{\partial t} = -\boldsymbol{h}(\boldsymbol{a}(t)). \tag{B.78}$$

The second term of eq. (B.76) reduces to

$$\int_0^t \mathrm{d}\tau \left\langle \left\{ \frac{\partial}{\partial \boldsymbol{b}(\tau)} \cdot \boldsymbol{\Omega}(\boldsymbol{b}, t) \right\} \boldsymbol{\Omega}(\boldsymbol{b}(\tau), t-\tau); \boldsymbol{b}(t) \right\rangle, \tag{B.79}$$

and the third term to

$$-\int_0^t \mathrm{d}\tau \left\langle \boldsymbol{\Omega}(\boldsymbol{b}(\tau), t-\tau); \boldsymbol{b}(t) \right\rangle \left\langle \frac{\partial}{\partial \boldsymbol{b}(\tau)} \cdot \boldsymbol{\Omega}(\boldsymbol{b}, t); \boldsymbol{b}(t) \right\rangle, \tag{B.80}$$

where

$$\frac{\partial}{\partial \boldsymbol{a}(t)} := e^{-t\boldsymbol{h}\cdot\frac{\partial}{\partial \boldsymbol{a}}} \frac{\partial}{\partial \boldsymbol{a}} e^{t\boldsymbol{h}\cdot\frac{\partial}{\partial \boldsymbol{a}}}. \tag{B.81}$$

Therefore, we obtain

$$\begin{aligned} \boldsymbol{Z}(\boldsymbol{b}, t) &= \langle \boldsymbol{\Omega}(\boldsymbol{b}, t); \boldsymbol{b}(t) \rangle \\ &+ \int_0^t \mathrm{d}\tau \left[\left\langle \boldsymbol{\Omega}(\boldsymbol{b}(\tau), t-\tau) \left\{ \frac{\partial}{\partial \boldsymbol{b}(\tau)} \cdot \boldsymbol{\Omega}(\boldsymbol{b}, t) \right\}; \boldsymbol{b}(t) \right\rangle \right. \\ &\qquad \left. - \langle \boldsymbol{\Omega}(\boldsymbol{b}(\tau), t-\tau); \boldsymbol{b}(t) \rangle \left\langle \frac{\partial}{\partial \boldsymbol{b}(\tau)} \cdot \boldsymbol{\Omega}(\boldsymbol{b}, t); \boldsymbol{b}(t) \right\rangle \right] \\ &+ O(\Omega^3). \end{aligned} \tag{B.82}$$

B.7.3 Time-Ordered Exponential Function

In general, a differential equation $\mathrm{d}X(t)/\mathrm{d}t = \mathcal{O}(t)X(t)$ is formally solved to give the formal solution

$$X(t) = X(0) + \int_0^t \mathrm{d}\tau \mathcal{O}(\tau) X(\tau). \tag{B.83}$$

Substituting eq. (B.83) to itself, we obtain the infinite series solution

$$X(t) = \exp_+ \left[\int_0^t \mathrm{d}\tau \mathcal{O}(\tau) \right] X(0), \tag{B.84}$$

where $\exp_+$ denotes the time-ordered exponential function defined as

$$\exp_+\left[\int_0^t \mathrm{d}\tau\mathcal{O}(\tau)\right] := 1+\int_0^t \mathrm{d}\tau_1\mathcal{O}(\tau_1)+\int_0^t \mathrm{d}\tau_1\int_0^{\tau_1}\mathrm{d}\tau_2\mathcal{O}(\tau_1)\mathcal{O}(\tau_2) + \int_0^t \mathrm{d}\tau_1\int_0^{\tau_1}\mathrm{d}\tau_2\int_0^{\tau_2}\mathrm{d}\tau_3\mathcal{O}(\tau_1)\mathcal{O}(\tau_2)\mathcal{O}(\tau_3)+\cdots. \quad \text{(B.85)}$$

Likewise, the reversed time-ordered exponential function $\exp_-$ is defined as

$$\exp_-\left[\int_0^t \mathrm{d}\tau\mathcal{O}(\tau)\right] := 1+\int_0^t \mathrm{d}\tau_1\mathcal{O}(\tau_1)+\int_0^t \mathrm{d}\tau_1\int_0^{\tau_1}\mathrm{d}\tau_2\mathcal{O}(\tau_2)\mathcal{O}(\tau_1) + \int_0^t \mathrm{d}\tau_1\int_0^{\tau_1}\mathrm{d}\tau_2\int_0^{\tau_2}\mathrm{d}\tau_3\mathcal{O}(\tau_3)\mathcal{O}(\tau_2)\mathcal{O}(\tau_1)+\cdots. \quad \text{(B.86)}$$

Note that both the time-ordered and reversed time-ordered exponential functions reduce to the ordinary exponential function in case the operators $\mathcal{O}(\tau_1), \mathcal{O}(\tau_2), \mathcal{O}(\tau_3), \ldots$ are commutative each other.

We can prove a useful identity

$$\exp_+\left[\int_0^t \mathrm{d}\tau\mathcal{O}(\tau)\right]\exp_-\left[-\int_0^t \mathrm{d}\tau\mathcal{O}(\tau)\right] = 1. \quad \text{(B.87)}$$

Expanding the LHS of this equation using the definition, we can rewrite it as

$$\sum_{n=1}^{\infty}\left[\sum_{i=0}^{n}(-1)^i\int_0^t \mathrm{d}\tau_1\int_0^{\tau_1}\mathrm{d}\tau_2\cdots\int_0^{\tau_{i-1}}\mathrm{d}\tau_i\int_0^t \mathrm{d}\tau_n\int_0^{\tau_n}\mathrm{d}\tau_{n-1}\cdots\int_0^{\tau_{i+2}}\mathrm{d}\tau_{i+1}\right] \times\mathcal{O}(\tau_1)\cdots\mathcal{O}(\tau_n) = 0. \quad \text{(B.88)}$$

In order to probe it, we focus on the term[8] in which the number of the operator is n ($n \in \mathbb{N}$);

$$\left[\sum_{i=0}^{n}(-1)^i\int_0^t \mathrm{d}\tau_1\int_0^{\tau_1}\mathrm{d}\tau_2\cdots\int_0^{\tau_{i-1}}\mathrm{d}\tau_i\int_0^t \mathrm{d}\tau_n\int_0^{\tau_n}\mathrm{d}\tau_{n-1}\cdots\int_0^{\tau_{i+2}}\mathrm{d}\tau_{i+1}\right] \times\mathcal{O}(\tau_1)\cdots\mathcal{O}(\tau_n). \quad \text{(B.89)}$$

Changing the order of the integral using the following relationship

$$\int_a^b \mathrm{d}x\int_a^x \mathrm{d}y\cdots = \int_a^b \mathrm{d}y\int_y^b \mathrm{d}x\cdots, \quad \text{(B.90)}$$

[8] Strictly speaking, the eq. (B.89) is not correct because when $i = 0$, for example, τ_1 does NOT exist!

the term (B.89) reduces to

$$\left[\sum_{i=0}^{n}(-1)^i\int_0^t \mathrm{d}\tau_1\int_0^{\tau_1}\mathrm{d}\tau_2\cdots\int_0^{\tau_{i-1}}\mathrm{d}\tau_i\int_0^t\mathrm{d}\tau_{i+1}\int_{\tau_{i+1}}^t\mathrm{d}\tau_{i+2}\cdots\int_{\tau_{n-1}}^t\mathrm{d}\tau_n\right]\mathcal{O}(\tau_1)\cdots\mathcal{O}(\tau_n). \tag{B.91}$$

Thus, the first term of (B.91) (i.e. the term of $i=0$) is

$$\int_0^t\mathrm{d}\tau_1\int_{\tau_1}^t\mathrm{d}\tau_2\int_{\tau_2}^t\mathrm{d}\tau_3\cdots\int_{\tau_{n-1}}^t\mathrm{d}\tau_n\mathcal{O}(\tau_1)\cdots\mathcal{O}(\tau_n). \tag{B.92}$$

On the other hand, summing the terms from $i=n$ to $i=1$, you can show that the rest of the terms (i.e. the terms of $i=1,2,3,\dots$) of (B.91) reduces to

$$-\int_0^t\mathrm{d}\tau_1\int_{\tau_1}^t\mathrm{d}\tau_2\int_{\tau_2}^t\mathrm{d}\tau_3\cdots\int_{\tau_{n-1}}^t\mathrm{d}\tau_n\mathcal{O}(\tau_1)\cdots\mathcal{O}(\tau_n). \tag{B.93}$$

Therefore, the term (B.89) is zero for any natural numbers, and then it is proved that eq. (B.88) is true.

B.7.4 Adjoint Operator

We define an adjoint operator $\tilde{\mathcal{O}}(\boldsymbol{b})$ of an operator $\mathcal{O}(\boldsymbol{a})$ as

$$\tilde{\mathcal{O}}(\boldsymbol{b})\delta(\boldsymbol{a}-\boldsymbol{b}) := \mathcal{O}(\boldsymbol{a})\delta(\boldsymbol{a}-\boldsymbol{b}). \tag{B.94}$$

$\tilde{\mathcal{O}}(\boldsymbol{a})$ is called an "adjoint" operator because

$$\begin{aligned}
\int \mathrm{d}\boldsymbol{a} f(\boldsymbol{a})\mathcal{O}(\boldsymbol{a})g(\boldsymbol{a}) &= \int \mathrm{d}\boldsymbol{a} f(\boldsymbol{a})\mathcal{O}(\boldsymbol{a})\int\mathrm{d}\boldsymbol{b}\delta(\boldsymbol{a}-\boldsymbol{b})g(\boldsymbol{b})\\
&= \int\mathrm{d}\boldsymbol{b}\int\mathrm{d}\boldsymbol{a} f(\boldsymbol{a})g(\boldsymbol{b})\mathcal{O}(\boldsymbol{a})\delta(\boldsymbol{a}-\boldsymbol{b})\\
&= \int\mathrm{d}\boldsymbol{b}\int\mathrm{d}\boldsymbol{a} f(\boldsymbol{a})g(\boldsymbol{b})\tilde{\mathcal{O}}(\boldsymbol{b})\delta(\boldsymbol{a}-\boldsymbol{b})\\
&= \int\mathrm{d}\boldsymbol{b}\int\mathrm{d}\boldsymbol{a} g(\boldsymbol{b})\tilde{\mathcal{O}}(\boldsymbol{b})\delta(\boldsymbol{a}-\boldsymbol{b})f(\boldsymbol{a})\\
&= \int\mathrm{d}\boldsymbol{b} g(\boldsymbol{b})\tilde{\mathcal{O}}(\boldsymbol{b})f(\boldsymbol{b}),\\
\therefore \int \mathrm{d}\boldsymbol{a} f(\boldsymbol{a})\mathcal{O}(\boldsymbol{a})g(\boldsymbol{a}) &= \int\mathrm{d}\boldsymbol{a} g(\boldsymbol{a})\tilde{\mathcal{O}}(\boldsymbol{a})f(\boldsymbol{a}).
\end{aligned} \tag{B.95}$$

Moreover, the adjoint operator of product of two operators, $e.g.$ $\mathcal{X}(\boldsymbol{a})\mathcal{Y}(\boldsymbol{a})$, is product of each adjoint operators, $\tilde{\mathcal{Y}}(\boldsymbol{a})\tilde{\mathcal{X}}(\boldsymbol{a})$. In order to prove this relationship, we define an operator $\mathcal{Z}(\boldsymbol{a})$ as $\mathcal{Z}(\boldsymbol{a}) = \mathcal{X}(\boldsymbol{a})\mathcal{Y}(\boldsymbol{a})$. Because of eq. (B.95),

$$\int \mathrm{d}\boldsymbol{a} f(\boldsymbol{a})\mathcal{Z}(\boldsymbol{a})g(\boldsymbol{a}) = \int \mathrm{d}\boldsymbol{a} g(\boldsymbol{a})\tilde{\mathcal{Z}}(\boldsymbol{a})f(\boldsymbol{a}). \tag{B.96}$$

On the other hand,

$$\begin{aligned}
\int \mathrm{d}\boldsymbol{a} f(\boldsymbol{a})\mathcal{X}(\boldsymbol{a})\mathcal{Y}(\boldsymbol{a})g(\boldsymbol{a}) &= \int \mathrm{d}\boldsymbol{a} \left\{\mathcal{Y}(\boldsymbol{a})g(\boldsymbol{a})\right\} \tilde{\mathcal{X}}(\boldsymbol{a})f(\boldsymbol{a}) \\
&= \int \mathrm{d}\boldsymbol{b} \int \mathrm{d}\boldsymbol{a} g(\boldsymbol{b}) \left\{\mathcal{Y}(\boldsymbol{a})\delta(\boldsymbol{a}-\boldsymbol{b})\right\} \tilde{\mathcal{X}}(\boldsymbol{a})f(\boldsymbol{a}) \\
&= \int \mathrm{d}\boldsymbol{b} \int \mathrm{d}\boldsymbol{a} g(\boldsymbol{b}) \left\{\tilde{\mathcal{Y}}(\boldsymbol{b})\delta(\boldsymbol{a}-\boldsymbol{b})\right\} \tilde{\mathcal{X}}(\boldsymbol{a})f(\boldsymbol{a}) \\
&= \int \mathrm{d}\boldsymbol{b} \int \mathrm{d}\boldsymbol{a} g(\boldsymbol{b})\tilde{\mathcal{Y}}(\boldsymbol{b})\delta(\boldsymbol{a}-\boldsymbol{b})\tilde{\mathcal{X}}(\boldsymbol{a})f(\boldsymbol{a}) \\
&= \int \mathrm{d}\boldsymbol{b} g(\boldsymbol{b})\tilde{\mathcal{Y}}(\boldsymbol{b})\tilde{\mathcal{X}}(\boldsymbol{b})f(\boldsymbol{b}).
\end{aligned} \tag{B.97}$$

Therefore, it is confirmed that[9] $\tilde{\mathcal{Z}}(\boldsymbol{a}) = \tilde{\mathcal{Y}}(\boldsymbol{a})\tilde{\mathcal{X}}(\boldsymbol{a})$ where $\mathcal{Z}(\boldsymbol{a}) = \mathcal{X}(\boldsymbol{a})\mathcal{Y}(\boldsymbol{a})$.

B.7.5 Identity of Adjoint Operator $\tilde{\mathcal{U}}(\boldsymbol{A}(0), t)$

A projection operator $\mathcal{P}$ is defined as the following equation[10];

$$\begin{aligned}
\mathcal{P}X(t) &:= \left\langle X(t)\boldsymbol{\Pi}^{\dagger}(0)\right\rangle \cdot \left\langle \boldsymbol{\Pi}(0)\boldsymbol{\Pi}^{\dagger}(0)\right\rangle^{-1} \cdot \boldsymbol{\Pi}(0) \\
&= \int \mathrm{d}\boldsymbol{a} \int \mathrm{d}\boldsymbol{b} \left\langle X(t)\Pi_a^*(0)\right\rangle \phi_{ab}^{-1}(0)\Pi_b(0) = \int \mathrm{d}\boldsymbol{a} \left\langle X(t); \boldsymbol{a}\right\rangle \Pi_a(0),
\end{aligned} \tag{B.98}$$

where the dagger symbol denotes the Hermitian conjugate, the asterisk symbol the complex conjugate, $\phi_{ab}(t) := \langle \Pi_a(t)\Pi_b(0)\rangle$, and $\phi_{ab}^{-1}(t)$ satisfies

$$\int \mathrm{d}\boldsymbol{b}\phi_{ab}^{-1}(t)\phi_{bc}(t) = \delta(\boldsymbol{a}-\boldsymbol{c}). \tag{B.99}$$

We define an equilibrium probability distribution $w(\boldsymbol{a})$ as $w(\boldsymbol{a}) := \langle \Pi_a(0)\rangle$, thus

$$\phi_{ab}(0) = \langle \Pi_a(0)\Pi_b(0)\rangle = \langle \Pi_a(0)\delta(\boldsymbol{a}-\boldsymbol{b})\rangle = w(\boldsymbol{a})\delta(\boldsymbol{a}-\boldsymbol{b}). \tag{B.100}$$

[9] Similarly it is confirmed about three and more operators.

[10] Furthermore, an operator $\mathcal{Q}$ is defined as $\mathcal{Q} := 1 - \mathcal{P}$.

Therefore,

$$\phi_{ab}^{-1}(0) = \frac{\delta(\boldsymbol{a}-\boldsymbol{b})}{w(\boldsymbol{a})}. \tag{B.101}$$

Moreover, a conditional probability, $\langle X;\boldsymbol{a}\rangle$, is defined as

$$\langle X;\boldsymbol{a}\rangle := \frac{\langle X\Pi_a^*(0)\rangle}{w(\boldsymbol{a})}. \tag{B.102}$$

In order to separate the RHS of eq. (B.54), let us consider an identity of $\tilde{\mathcal{U}}(\boldsymbol{A}(0),t)$. It is clear that

$$\tilde{\mathcal{U}} = \tilde{\mathcal{U}}\mathcal{P} + \tilde{\mathcal{U}}\mathcal{Q}. \tag{B.103}$$

Here,

$$\begin{aligned}
\tilde{\mathcal{U}}\mathcal{Q} &= \tilde{\mathcal{U}}_Q\mathcal{Q} + \tilde{\mathcal{U}}\mathcal{Q} - \tilde{\mathcal{U}}\tilde{\mathcal{U}}^{-1}\tilde{\mathcal{U}}_Q\mathcal{Q} \\
&= \tilde{\mathcal{U}}_Q\mathcal{Q} + \tilde{\mathcal{U}}\left[1-\tilde{\mathcal{U}}^{-1}\tilde{\mathcal{U}}_Q\right]\mathcal{Q} \\
&=: \tilde{\mathcal{U}}_Q\mathcal{Q} + \tilde{\mathcal{U}}\tilde{\mathcal{J}}\mathcal{Q} \\
&= \tilde{\mathcal{U}}_Q\mathcal{Q} + \tilde{\mathcal{U}}\mathcal{P}\tilde{\mathcal{J}}\mathcal{Q} + \tilde{\mathcal{U}}\mathcal{Q}\tilde{\mathcal{J}}\mathcal{Q}, \\
\Leftrightarrow\ \tilde{\mathcal{U}}\left[1-\mathcal{Q}\tilde{\mathcal{J}}\right]\mathcal{Q} &= \tilde{\mathcal{U}}_Q\mathcal{Q} + \tilde{\mathcal{U}}\mathcal{P}\tilde{\mathcal{J}}\mathcal{Q}, \\
\Leftrightarrow\ \tilde{\mathcal{U}} &= \tilde{\mathcal{U}}_Q\left[1-\mathcal{Q}\tilde{\mathcal{J}}\right]^{-1} + \tilde{\mathcal{U}}\mathcal{P}\tilde{\mathcal{J}}\left[1-\mathcal{Q}\tilde{\mathcal{J}}\right]^{-1} \\
&=: \tilde{\mathcal{V}} + \tilde{\mathcal{U}}\mathcal{P}\tilde{\mathcal{J}}\left[1-\mathcal{Q}\tilde{\mathcal{J}}\right]^{-1}, \\
\Leftrightarrow\ \tilde{\mathcal{U}}\mathcal{Q} &= \tilde{\mathcal{V}}\mathcal{Q} + \tilde{\mathcal{U}}\mathcal{P}\tilde{\mathcal{J}}\mathcal{Q}\left[1-\tilde{\mathcal{J}}\mathcal{Q}\right]^{-1},
\end{aligned}$$

where the following relation is used;

$$\left[1-\mathcal{X}\mathcal{Y}\right]^{-1}\mathcal{X} \equiv \mathcal{X}\left[1-\mathcal{Y}\mathcal{X}\right]^{-1}. \tag{B.104}$$

Therefore

$$\tilde{\mathcal{U}} \equiv \tilde{\mathcal{U}}\mathcal{P} + \tilde{\mathcal{V}}\mathcal{Q} + \tilde{\mathcal{U}}\mathcal{P}\tilde{\mathcal{J}}\mathcal{Q}\left[1-\tilde{\mathcal{J}}\mathcal{Q}\right]^{-1}. \tag{B.105}$$

Note that the formal operator $\mathcal{U}_Q$ is introduced and the form will be determined.

B.7.6 Master Operator

Multiplying $\phi_{bd}(t)$ to the eq. (B.69) from right side, and integrating it with respect to $\boldsymbol{b}$, we obtain

$$\frac{\mathrm{d}}{\mathrm{d}t}\phi_{ad}(t) = \mathcal{M}(\boldsymbol{a},t)\phi_{ad}(t), \tag{B.106}$$

thus

$$\phi_{ab}(t) = \exp_+ \left[\int_0^t \mathrm{d}\tau \mathcal{M}(\boldsymbol{a}, \tau) \right] \phi_{ab}(0) =: \mathcal{S}_+(\boldsymbol{a}, t)\phi_{ab}(0). \tag{B.107}$$

$\mathcal{S}_+$ has physical meaning that time development of ϕ.

A transition probability $\mathrm{Prob}(\boldsymbol{a}, t|\boldsymbol{b}, 0)$ is defined as

$$\mathrm{Prob}(\boldsymbol{a}, t|\boldsymbol{b}, 0) := \langle \Pi_a(t); \boldsymbol{b} \rangle = \frac{\langle \Pi_a(t)\Pi_b(0) \rangle}{w(\boldsymbol{b})} = \frac{\phi_{ab}(t)}{w(\boldsymbol{b})}. \tag{B.108}$$

From eq. (B.106), we obtain the differential equation about the transition probability

$$\frac{\mathrm{d}}{\mathrm{d}t}\mathrm{Prob}(\boldsymbol{a}, t|\boldsymbol{b}, 0) = \mathcal{M}(\boldsymbol{a}, t)\mathrm{Prob}(\boldsymbol{a}, t|\boldsymbol{b}, 0). \tag{B.109}$$

Considering the equilibrium probability distribution should be the solution of this differential equation, we obtain $\mathcal{M}(\boldsymbol{a}, t)w(\boldsymbol{a}) = 0$ because the ensemble probability distribution is steady-state. Furthermore, eq. (B.107) reduces to

$$\phi_{ab}(t) = w(\boldsymbol{a})\mathcal{S}_+(\boldsymbol{a}, t)\delta(\boldsymbol{a} - \boldsymbol{b}), \tag{B.110}$$

where $\mathcal{S}_+(\boldsymbol{a}, t)w(\boldsymbol{a}) = w(\boldsymbol{a})\mathcal{S}_+(\boldsymbol{a}, t)$ because $\mathcal{M}(\boldsymbol{a}, t)w(\boldsymbol{a}) = 0$. In addition,

$$\phi^{-1}_{ab}(t) = \frac{1}{w(\boldsymbol{a})}\mathcal{S}_-(\boldsymbol{a}, t)\delta(\boldsymbol{a} - \boldsymbol{b}), \tag{B.111}$$

where $\mathcal{S}_-(\boldsymbol{a}, t)$ is represented by

$$\mathcal{S}_-(\boldsymbol{a}, t) = \exp_- \left[- \int_0^t \mathrm{d}\tau \mathcal{M}(\boldsymbol{a}, \tau) \right] \tag{B.112}$$

which satisfies $\mathcal{S}_+(\boldsymbol{a}, t)\mathcal{S}_-(\boldsymbol{a}, t) = 1$ which is proved in Appendix B.7.3 (eq. (B.87)).

Therefore,

$$\begin{aligned}
[\mathsf{M}(t)]_{ab} &= \int \mathrm{d}\boldsymbol{c} \left\langle \left\{ \mathcal{L}(\boldsymbol{a}, t)\Pi_a(t) \right\} \Pi^*_c(0) \right\rangle \phi^{-1}_{cb}(t) \\
&= \int \mathrm{d}\boldsymbol{c} \left\langle \mathcal{L}(\boldsymbol{a}, t)\Pi_a(t)\Pi^*_c(0) \right\rangle \phi^{-1}_{cb}(t) \\
&= -\frac{\partial}{\partial \boldsymbol{a}} \cdot \int \mathrm{d}\boldsymbol{c} \left\langle \left\{ \boldsymbol{h}(\boldsymbol{a}) + \boldsymbol{\Omega}(\boldsymbol{a}, t) \right\} \Pi_a(t)\Pi^*_c(0) \right\rangle \phi^{-1}_{cb}(t)
\end{aligned}$$

$$
\begin{aligned}
&= -\frac{\partial}{\partial \boldsymbol{a}} \cdot \boldsymbol{h}(\boldsymbol{a}) \int \mathrm{d}\boldsymbol{c} \phi_{ac}(t) \phi_{cb}^{-1}(t) \\
&\quad -\frac{\partial}{\partial \boldsymbol{a}} \cdot \langle \boldsymbol{\Omega}(\boldsymbol{a},t) \mathcal{U}(\boldsymbol{a},t) \Pi_a(0) \rangle \int \mathrm{d}\boldsymbol{c} \delta(\boldsymbol{a}-\boldsymbol{c}) \phi_{cb}^{-1}(t) \\
&= -\frac{\partial}{\partial \boldsymbol{a}} \cdot \boldsymbol{h}(\boldsymbol{a}) \delta(\boldsymbol{a}-\boldsymbol{b}) - \frac{\partial}{\partial \boldsymbol{a}} \cdot \langle \boldsymbol{\Omega}(\boldsymbol{a},t) \mathcal{U}(\boldsymbol{a},t) \Pi_a(0) \rangle \, \phi_{ab}^{-1}(t) \\
&= -\frac{\partial}{\partial \boldsymbol{a}} \cdot \left[\boldsymbol{h}(\boldsymbol{a}) + \langle \boldsymbol{\Omega}(\boldsymbol{a},t) \mathcal{U}(\boldsymbol{a},t); \boldsymbol{a} \rangle \, \mathcal{S}_-(\boldsymbol{a},t) \right] \delta(\boldsymbol{a}-\boldsymbol{b}) \qquad \text{(B.113)}
\end{aligned}
$$

Comparing the above equation with eq. (B.69), the master operator reduces to

$$
\therefore \ \mathcal{M}(\boldsymbol{a},t)\delta(\boldsymbol{a}-\boldsymbol{b}) = -\frac{\partial}{\partial \boldsymbol{a}} \cdot \left[\boldsymbol{h}(\boldsymbol{a}) + \langle \boldsymbol{\Omega}(\boldsymbol{a},t) \mathcal{U}(\boldsymbol{a},t); \boldsymbol{a} \rangle \, \mathcal{S}_-(\boldsymbol{a},t) \right] \delta(\boldsymbol{a}-\boldsymbol{b}). \qquad \text{(B.114)}
$$

Note that the above equation is a formal solution because $\mathcal{S}_-(\boldsymbol{a},t)$ is depend on $\mathcal{M}(\boldsymbol{a},t)$.

B.7.7 Identity about the exponential function of operator

We consider the following type operator;

$$
\mathcal{X}_+(t) = \exp_+ \left[t\mathcal{A} + \int_0^t \mathrm{d}\tau \mathcal{B}(\tau) \right]. \qquad \text{(B.115)}
$$

It is assumed that the above operator is transformed to

$$
\exp_+ \left[t\mathcal{A} + \int_0^t \mathrm{d}\tau \mathcal{B}(\tau) \right] = e^{t\mathcal{A}} \mathcal{F}(t). \qquad \text{(B.116)}
$$

Differentiating the both side of the equation with respect to time, we obtain

$$
\begin{aligned}
&(\mathcal{A} + \mathcal{B}(t)) \exp_+ \left[t\mathcal{A} + \int_0^t \mathrm{d}\tau \mathcal{B}(\tau) \right] = \mathcal{A} e^{t\mathcal{A}} \mathcal{F}(t) + e^{t\mathcal{A}} \dot{\mathcal{F}}(t) \\
&\dot{\mathcal{F}}(t) = e^{-t\mathcal{A}} \mathcal{B}(t) e^{t\mathcal{A}} \mathcal{F}(t), \qquad \text{(B.117)}
\end{aligned}
$$

where the time derivative of the time-ordered exponential is given by

$$
\frac{\mathrm{d}}{\mathrm{d}t} \exp_+ \left[\int_0^t \mathrm{d}\tau \mathcal{O}(\tau) \right] = \mathcal{O}(t) \exp_+ \left[\int_0^t \mathrm{d}\tau \mathcal{O}(\tau) \right]. \qquad \text{(B.118)}
$$

Thus, $\mathcal{X}_+(t)$ is represented by

$$
\mathcal{X}_+(t) = e^{t\mathcal{A}} \exp_+ \left[\int_0^t \mathrm{d}\tau e^{-\tau\mathcal{A}} \mathcal{B}(\tau) e^{\tau\mathcal{A}} \right] \qquad \text{(B.119)}
$$

because $\mathcal{F}(0)$ is the unitary operator. Similarly, we can obtain

$$\mathcal{X}_-(t) = \exp_-\left[t\mathcal{A} + \int_0^t \mathrm{d}\tau \mathcal{B}(\tau)\right] = \exp_-\left[\int_0^t \mathrm{d}\tau e^{\tau\mathcal{A}}\mathcal{B}(\tau)e^{-\tau\mathcal{A}}\right] e^{t\mathcal{A}}. \tag{B.120}$$

Note that the time-derivative of the reverse time-ordered exponential is given by

$$\frac{\mathrm{d}}{\mathrm{d}t}\exp_-\left[\int_0^t \mathrm{d}\tau \mathcal{O}(\tau)\right] = \exp_-\left[\int_0^t \mathrm{d}\tau \mathcal{O}(\tau)\right]\mathcal{O}(t). \tag{B.121}$$

B.7.8 Calculation of each term of the drift term

We assume that it is expanded as

$$e^{-t_2\boldsymbol{h}(\boldsymbol{a})\cdot\frac{\partial}{\partial\boldsymbol{a}}}\boldsymbol{\Omega}(\boldsymbol{a},t_1)X = \boldsymbol{\mathcal{A}}^h(\boldsymbol{a},t_1,t_2)e^{-t_2\boldsymbol{h}(\boldsymbol{a})\cdot\frac{\partial}{\partial\boldsymbol{a}}}X, \tag{B.122}$$

where $\boldsymbol{\mathcal{A}}^h$ is an operator represented by

$$\boldsymbol{\mathcal{A}}^h(\boldsymbol{a},t_1,t_2) = e^{-t_2\boldsymbol{h}(\boldsymbol{a})\cdot\frac{\partial}{\partial\boldsymbol{a}}}\boldsymbol{\Omega}(\boldsymbol{a},t_1)e^{t_2\boldsymbol{h}(\boldsymbol{a})\cdot\frac{\partial}{\partial\boldsymbol{a}}}. \tag{B.123}$$

We consider the time-derivative[11] of $\boldsymbol{\mathcal{A}}^h(\boldsymbol{a},t_1,t_2)$ with respect to t_2:

$$\begin{aligned}\frac{\partial\boldsymbol{\mathcal{A}}^h(\boldsymbol{a},t_1,t_2)}{\partial t_2} &= -\boldsymbol{h}(\boldsymbol{a})\cdot\frac{\partial}{\partial\boldsymbol{a}}e^{-t_2\boldsymbol{h}(\boldsymbol{a})\cdot\frac{\partial}{\partial\boldsymbol{a}}}\boldsymbol{\Omega}(\boldsymbol{a},t_1)e^{t_2\boldsymbol{h}(\boldsymbol{a})\cdot\frac{\partial}{\partial\boldsymbol{a}}} \\ &\quad + e^{-t_2\boldsymbol{h}(\boldsymbol{a})\cdot\frac{\partial}{\partial\boldsymbol{a}}}\boldsymbol{\Omega}(\boldsymbol{a},t_1)\boldsymbol{h}(\boldsymbol{a})\cdot\frac{\partial}{\partial\boldsymbol{a}}e^{t_2\boldsymbol{h}(\boldsymbol{a})\cdot\frac{\partial}{\partial\boldsymbol{a}}} \\ &= -\left\{\boldsymbol{h}(\boldsymbol{a})\cdot\frac{\partial}{\partial\boldsymbol{a}}\boldsymbol{\Omega}(\boldsymbol{a}(t_2),t_1)\right\}e^{t_2\boldsymbol{h}(\boldsymbol{a})\cdot\frac{\partial}{\partial\boldsymbol{a}}},\end{aligned} \tag{B.126}$$

where $\boldsymbol{a}(t)$ is defined by

$$\boldsymbol{a}(t) = e^{-t\boldsymbol{h}(\boldsymbol{a})\cdot\frac{\partial}{\partial\boldsymbol{a}}}\boldsymbol{a}e^{t\boldsymbol{h}(\boldsymbol{a})\cdot\frac{\partial}{\partial\boldsymbol{a}}} \tag{B.127}$$

and it is assumed that $\boldsymbol{\Omega}(\boldsymbol{a},t_1)$ is represented by a polynomial of $\boldsymbol{a}$. It should be noted here that we can regard $\boldsymbol{a}(t)$ defined by the above equation as a number not an operator. This will be discussed the following.

[11] $\partial\mathcal{A}(t)/\partial t$ is equal to $\left(\frac{\partial}{\partial t}\mathcal{A}(t)\right)$ but not $\frac{\partial}{\partial t}\mathcal{A}(t)$. The former is the time-derivative of operators and the latter represents that the time-derivative operator operates an operator $\mathcal{A}(t)$. In case $\mathcal{A}(t) = t$ for example,

$$\frac{\partial\mathcal{A}(t)}{\partial t}X(t) = X(t) \tag{B.124}$$

but

$$\frac{\partial}{\partial t}\mathcal{A}(t)X(t) = X(t) + t\dot{X}(t). \tag{B.125}$$

On the other hand, we can obtain

$$\boldsymbol{h}(\boldsymbol{a})\cdot\frac{\partial}{\partial\boldsymbol{a}}\boldsymbol{\mathcal{A}}^h(\boldsymbol{a},t_1,t_2)=\left\{\boldsymbol{h}(\boldsymbol{a})\cdot\frac{\partial}{\partial\boldsymbol{a}}\boldsymbol{\Omega}(\boldsymbol{a}(t_2),t_1)\right\}e^{t_2\boldsymbol{h}(\boldsymbol{a})\cdot\frac{\partial}{\partial\boldsymbol{a}}}+\boldsymbol{\mathcal{A}}^h(\boldsymbol{a},t_1,t_2)\boldsymbol{h}(\boldsymbol{a})\cdot\frac{\partial}{\partial\boldsymbol{a}},$$

$$\begin{aligned}\left\{\boldsymbol{h}(\boldsymbol{a})\cdot\frac{\partial}{\partial\boldsymbol{a}}\boldsymbol{\Omega}(\boldsymbol{a}(t_2),t_1)\right\}e^{t_2\boldsymbol{h}(\boldsymbol{a})\cdot\frac{\partial}{\partial\boldsymbol{a}}} &= \boldsymbol{h}(\boldsymbol{a})\cdot\frac{\partial}{\partial\boldsymbol{a}}\boldsymbol{\mathcal{A}}^h(\boldsymbol{a},t_1,t_2)-\boldsymbol{\mathcal{A}}^h(\boldsymbol{a},t_1,t_2)\boldsymbol{h}(\boldsymbol{a})\cdot\frac{\partial}{\partial\boldsymbol{a}}\\ &= \left\{\boldsymbol{h}(\boldsymbol{a})\cdot\frac{\partial}{\partial\boldsymbol{a}}\mathcal{A}^h(\boldsymbol{a},t_1,t_2)\right\}. \qquad \text{(B.128)}\end{aligned}$$

Therefore, we can obtain

$$\boldsymbol{\mathcal{A}}^h(\boldsymbol{a},t_1,t_2)=e^{-t_2\boldsymbol{h}(\boldsymbol{a})\cdot\frac{\partial}{\partial\boldsymbol{a}}}\boldsymbol{\mathcal{A}}^h(\boldsymbol{a},t_1,0)=\boldsymbol{\Omega}(\boldsymbol{a}(t_2),t_1), \qquad \text{(B.129)}$$

and eq. (B.122) reduces to

$$e^{-t_2\boldsymbol{h}(\boldsymbol{a})\cdot\frac{\partial}{\partial\boldsymbol{a}}}\boldsymbol{\Omega}(\boldsymbol{a},t_1)X=\boldsymbol{\Omega}(\boldsymbol{a}(t_2),t_1)e^{-t_2\boldsymbol{h}(\boldsymbol{a})\cdot\frac{\partial}{\partial\boldsymbol{a}}}X. \qquad \text{(B.130)}$$

We initially defined $\boldsymbol{\mathcal{A}}^h$ as an operator but eq. (B.129) shows that $\boldsymbol{A}^h$ is regarded as just a number. Similarly, we can prove that $\boldsymbol{a}(t)$ is a number not an operator.

B.8 Mode-Coupling Theory for Binary Mixture Suspensions

B.8.1 Fokker-Planck Operator

We derive a stochastic Fokker-Planck equation. The generating function is defined by

$$\Pi_{xp}(t):=\prod_{i=1}^{N}\delta(\boldsymbol{X}_i(t)-\boldsymbol{x}_i)\delta(\boldsymbol{P}_i(t)-\boldsymbol{p}_i). \qquad \text{(B.131)}$$

The time-derivative of the generating function is represented as

$$\partial_t\Pi_{xp}(t)=-\sum_{i=1}^{N}\left[\frac{\boldsymbol{p}_i}{m_i}\cdot\frac{\partial}{\partial\boldsymbol{x}_i}-\frac{\partial}{\partial\boldsymbol{p}_i}\cdot\left(\frac{\gamma_i}{m_i}\boldsymbol{p}_i-\boldsymbol{F}_i\right)\right]\Pi_{xp}(t)-\sum_{i=1}^{N}\frac{\partial}{\partial\boldsymbol{p}_i}\cdot\boldsymbol{R}_i(t)\Pi_{xp}(t). \qquad \text{(B.132)}$$

The last term is a multiplicative random term, and then we can write [91]

$$-\sum_{i=1}^{N}\frac{\partial}{\partial\boldsymbol{p}_i}\cdot\boldsymbol{R}_i(t)\Pi_{xp}(t)\simeq\sum_{i=1}^{N}\gamma_i k_BT\frac{\partial}{\partial\boldsymbol{p}_i}\cdot\frac{\partial}{\partial\boldsymbol{p}_i}\Pi_{xp}(t)+\xi_{xp}(t), \qquad \text{(B.133)}$$

where $\xi_{xp}(t)$ denotes a new random term for the Fokker-Planck equation. The new random term satisfies

$$\begin{aligned} \langle \xi_{xp}(t) \rangle &= 0 \\ \langle \xi_{xp}(t) \xi_{x'p'}(t') \rangle &= \sum_{i=1}^{N} 2\gamma_i k_B T \delta(t-t') \frac{\partial}{\partial \boldsymbol{p}_i} \cdot \frac{\partial}{\partial \boldsymbol{p}_i'} \delta(\boldsymbol{x}-\boldsymbol{x}') \delta(\boldsymbol{p}-\boldsymbol{p}') w(\boldsymbol{x},\boldsymbol{p}), \end{aligned} \tag{B.134}$$

where $w(\boldsymbol{x},\boldsymbol{p})$ denotes the equilibrium distribution function defined by

$$w(\boldsymbol{x},\boldsymbol{p}) := \langle \Pi_{xp}(t) \rangle \,. \tag{B.135}$$

Therefore, we can obtain a stochastic equation of motion for $\Pi_{xp}(t)$ as

$$\partial_t \Pi_{xp}(t) = \Omega(\boldsymbol{x},\boldsymbol{p}) \Pi_{xp}(t) + \xi_{xp}(t), \tag{B.136}$$

where $\Omega(\boldsymbol{x},\boldsymbol{p})$ denotes the Fokker-Planck operator;

$$\Omega(\boldsymbol{x},\boldsymbol{p}) := -\sum_{i=1}^{N} \left[\frac{\boldsymbol{p}_i}{m_i} \cdot \frac{\partial}{\partial \boldsymbol{x}_i} - \frac{\gamma_i}{m_i} \frac{\partial}{\partial \boldsymbol{p}_i} \cdot \boldsymbol{p}_i + \boldsymbol{F}_i(\boldsymbol{x}) \cdot \frac{\partial}{\partial \boldsymbol{p}_i} - \gamma_i k_B T \frac{\partial}{\partial \boldsymbol{p}_i} \cdot \frac{\partial}{\partial \boldsymbol{p}_i} \right]. \tag{B.137}$$

The formal solution of eq. (B.136) is

$$\Pi_{xp}(t) = e^{t\Omega} \Pi_{xp} + \int_0^t \mathrm{d}s e^{(t-s)\Omega} \xi_{xp}(s). \tag{B.138}$$

Thus, the momentum of i-th particle is represented as

$$\boldsymbol{P}_i(t) = \iint \mathrm{d}\boldsymbol{x} \mathrm{d}\boldsymbol{p} \left[\Pi_{xp} e^{t\hat{\Omega}} \boldsymbol{p}_i + \int_0^t \xi_{xp}(t-s) e^{s\hat{\Omega}} \boldsymbol{p}_i \right], \tag{B.139}$$

where $\hat{\Omega}(\boldsymbol{x}',\boldsymbol{p}')$ denotes the adjoint operator of $\Omega(\boldsymbol{x},\boldsymbol{p})$, that is,

$$\hat{\Omega}(\boldsymbol{x}',\boldsymbol{p}') \delta(\boldsymbol{x}-\boldsymbol{x}') \delta(\boldsymbol{p}-\boldsymbol{p}') = \Omega(\boldsymbol{x},\boldsymbol{p}) \delta(\boldsymbol{x}-\boldsymbol{x}') \delta(\boldsymbol{p}-\boldsymbol{p}'). \tag{B.140}$$

Hence, we obtain

$$\langle \boldsymbol{P}_i(t) \boldsymbol{P}_j \rangle = \iiiint \mathrm{d}\boldsymbol{x} \mathrm{d}\boldsymbol{p} \mathrm{d}\boldsymbol{x}' \mathrm{d}\boldsymbol{p}' \langle \Pi_{xp} \Pi_{x'p'} \rangle \left(e^{t\hat{\Omega}} \boldsymbol{p}_i \right) \boldsymbol{p}_j$$

$$= \iint \mathrm{d}\boldsymbol{x}\mathrm{d}\boldsymbol{p} w(\boldsymbol{x},\boldsymbol{p}) \left(e^{t\hat{\Omega}}\boldsymbol{p}_i\right) \boldsymbol{p}_j$$

$$= \langle \boldsymbol{p}_i(t)\boldsymbol{p}_j \rangle \,, \tag{B.141}$$

where $\boldsymbol{p}_i(t)$ is defined by $e^{t\hat{\Omega}}\boldsymbol{p}_i$. The above relationship implies that it is sufficient to consider only $\boldsymbol{p}_i(t)$ as long as we consider correlations of that.

From the definition, the adjoint Fokker-Planck operator is represented by

$$\hat{\Omega}(\boldsymbol{x},\boldsymbol{p}) = \sum_{i=1}^{N} \left[\frac{\boldsymbol{p}_i}{m_i} \cdot \frac{\partial}{\partial \boldsymbol{x}_i} + \boldsymbol{F}_i(\boldsymbol{x}) \cdot \frac{\partial}{\partial \boldsymbol{p}_i} - \frac{\gamma_i}{m_i}\boldsymbol{p}_i \cdot \frac{\partial}{\partial \boldsymbol{p}_i} + \gamma_i k_B T \frac{\partial}{\partial \boldsymbol{p}_i} \cdot \frac{\partial}{\partial \boldsymbol{p}_i} \right]. \tag{B.142}$$

The equation of motion for $\boldsymbol{p}_i(t)$ is obtained by

$$\partial_t \boldsymbol{p}_i(t) = \hat{\Omega}\boldsymbol{p}_i(t) = -\frac{\gamma_i}{m_i}\boldsymbol{p}_i(t) + \boldsymbol{F}_i(\boldsymbol{x}(t)). \tag{B.143}$$

Similarly,

$$\partial_t \boldsymbol{x}_i(t) = \hat{\Omega}\boldsymbol{x}_i(t) = \frac{\boldsymbol{p}_i(t)}{m_i}, \tag{B.144}$$

where $\boldsymbol{x}_i(t) := e^{t\hat{\Omega}}\boldsymbol{x}_i$.

B.8.2 Generalized Langevin Equation

For an arbitrary function $\boldsymbol{A}(\boldsymbol{X}(t),\boldsymbol{P}(t))$, we can write

$$\boldsymbol{A}(\boldsymbol{X}(t),\boldsymbol{P}(t)) = \iint \mathrm{d}\boldsymbol{x}\mathrm{d}\boldsymbol{p} \left[\Pi_{xp}\boldsymbol{A}(\boldsymbol{x},\boldsymbol{p};t) + \int_0^t \mathrm{d}s \xi_{xp}(t-s)\boldsymbol{A}(\boldsymbol{x},\boldsymbol{p};t) \right], \tag{B.145}$$

where $\boldsymbol{A}(\boldsymbol{x},\boldsymbol{p};t) = e^{t\hat{\Omega}}\boldsymbol{A}(\boldsymbol{x},\boldsymbol{p};0)$. The equation of motion for $\boldsymbol{A}(\boldsymbol{x},\boldsymbol{p};t)$ is represented by

$$\partial_t \boldsymbol{A}(\boldsymbol{x},\boldsymbol{p};t) = \hat{\Omega}\boldsymbol{A}(\boldsymbol{x},\boldsymbol{p};t). \tag{B.146}$$

We consider the microscopic number density $\boldsymbol{\delta\rho}_q(t)$ and its current $\boldsymbol{j}_q^{(L)}(t)$ as dynamical variables $\boldsymbol{A}(\boldsymbol{x},\boldsymbol{p};t)$, where

$$\delta\rho_q^{(\alpha)}(t) := \frac{1}{\sqrt{N_\alpha}}\sum_i^{(\alpha)} e^{i\boldsymbol{q}\cdot\boldsymbol{x}_i(t)} - \frac{\rho_\alpha}{\sqrt{N_\alpha}}(2\pi)^3\delta(\boldsymbol{q}), \tag{B.147}$$

$$j_q^{L(\alpha)}(t) := \frac{1}{\sqrt{N_\alpha}}\sum_i^{(\alpha)} \hat{\boldsymbol{q}}\cdot\frac{\boldsymbol{p}_i(t)}{m_i} e^{i\boldsymbol{q}\cdot\boldsymbol{x}_i(t)} \tag{B.148}$$

with $\hat{\boldsymbol{q}} = \boldsymbol{q}/q$. We introduce a projection operator $\mathcal{P}$ defined by

$$\mathcal{P}\boldsymbol{G} := \left\langle \boldsymbol{G}\boldsymbol{A}^\dagger \right\rangle \cdot \phi^{-1} \cdot \boldsymbol{A}, \tag{B.149}$$

where ϕ^{-1} denotes the inverse matrix of the correlation matrix $\phi = \left\langle \boldsymbol{A}\boldsymbol{A}^\dagger \right\rangle$. Using the time-convolution type projection method, we can divide the equation of motion into three parts as

$$\partial_t \boldsymbol{A}(t) = \left\langle \dot{\boldsymbol{A}}\boldsymbol{A}^\dagger \right\rangle \cdot \phi^{-1} \cdot \boldsymbol{A}(t) + \int_0^t \mathrm{d}s \left\langle \left(\hat{\Omega}\boldsymbol{R}(t-s)\right)\boldsymbol{A}^\dagger \right\rangle \cdot \phi^{-1} \cdot \boldsymbol{A}(s) + \boldsymbol{R}(t), \tag{B.150}$$

where $\boldsymbol{R}(t)$ denotes the random term defined by

$$\boldsymbol{R}(t) := e^{t\mathcal{Q}\hat{\Omega}}\mathcal{Q}\hat{\Omega}\boldsymbol{A} \tag{B.151}$$

with $\mathcal{Q} := 1 - \mathcal{P}$.

The temporal differentiation of the dynamical variables is

$$\partial_t \delta\rho_q^{(\alpha)}(t) = iq j_q^{L(\alpha)}(t), \tag{B.152}$$

$$\begin{aligned}\partial_t j_q^{L(\alpha)}(t) &= \frac{1}{\sqrt{N_\alpha}}\sum_i^{(\alpha)} \left[\hat{\boldsymbol{q}}\cdot\frac{\dot{\boldsymbol{p}}_i(t)}{m_i} + iq\hat{\boldsymbol{q}}\cdot\frac{\boldsymbol{p}_i(t)}{m_i}\frac{\boldsymbol{p}_i(t)}{m_i}\cdot\hat{\boldsymbol{q}}\right] e^{i\boldsymbol{q}\cdot\boldsymbol{x}_i(t)} \\ &= \frac{1}{\sqrt{N_\alpha}}\sum_i^{(\alpha)} \left[-\frac{\gamma_i}{m_i}\hat{\boldsymbol{q}}\cdot\frac{\boldsymbol{p}_i(t)}{m_i} + \hat{\boldsymbol{q}}\cdot\frac{\boldsymbol{F}_i(\boldsymbol{x}(t))}{m_i} + iq\hat{\boldsymbol{q}}\cdot\frac{\boldsymbol{p}_i(t)}{m_i}\frac{\boldsymbol{p}_i(t)}{m_i}\cdot\hat{\boldsymbol{q}}\right] e^{i\boldsymbol{q}\cdot\boldsymbol{x}_i(t)}.\end{aligned} \tag{B.153}$$

Thus,

$$\left\langle \dot{\boldsymbol{A}}\boldsymbol{A}^\dagger \right\rangle = \begin{pmatrix} 0 & \frac{iq}{\beta}\frac{\mathbf{1}_2'}{m} \\ \frac{iq}{\beta}\frac{\mathbf{1}_2'}{m} & -\frac{1}{\beta}\frac{\gamma\mathbf{1}_2'}{m^2} \end{pmatrix}, \tag{B.154}$$

where $x\mathbf{1}_2'$ denotes

$$\begin{pmatrix} x^{(A)} & 0 \\ 0 & x^{(B)} \end{pmatrix}. \tag{B.155}$$

It should be here noted that $\left\langle \dot{\boldsymbol{j}}_q^L \boldsymbol{j}_{-q}^L \right\rangle \neq 0$ although it vanishes in molecular systems.

The initial random term reduces to

$$\boldsymbol{R} = \mathcal{Q}\hat{\Omega}\boldsymbol{A} = \begin{pmatrix} 0 \\ \hat{\Omega}\boldsymbol{j}_q^L - \dfrac{iq}{\beta}\dfrac{\mathbf{1}_2'}{m} \cdot \mathsf{S}^{-1}(q) \cdot \boldsymbol{\delta\rho}_q + \dfrac{\gamma \mathbf{1}_2'}{m} \cdot \boldsymbol{j}_q^L \end{pmatrix} =: \begin{pmatrix} 0 \\ \boldsymbol{R}_q \end{pmatrix}, \tag{B.156}$$

where the following relationship is used;

$$\phi^{-1} = \begin{pmatrix} \mathsf{S}^{-1}(q) & 0 \\ 0 & \beta m \mathbf{1}_2' \end{pmatrix}. \tag{B.157}$$

One can also represent $\boldsymbol{R}_q$ as

$$R_q^{(\alpha)} = \frac{1}{\sqrt{N_\alpha}} \sum_i^{(\alpha)} \left[\hat{\boldsymbol{q}} \cdot \frac{\boldsymbol{F}_i(\boldsymbol{x})}{m_i} + iq\hat{\boldsymbol{q}} \cdot \frac{\boldsymbol{p}_i}{m_i}\frac{\boldsymbol{p}_i}{m_i} \cdot \hat{\boldsymbol{q}} \right] e^{i\boldsymbol{q}\cdot\boldsymbol{x}_i} - \frac{iq}{m_\alpha \beta} \sum_\eta \left[\mathsf{S}^{-1}(q)\right]^{(\alpha\eta)} \delta\rho_q^{(\eta)}. \tag{B.158}$$

Note that it is satisfied that $\langle \boldsymbol{R}_q \rangle = 0$.

From the definition of the adjoint operator,

$$\left\langle \left(\hat{\Omega}\boldsymbol{X} \right) \boldsymbol{Y}^\dagger \right\rangle = \left\langle \boldsymbol{X} \left(\Omega \boldsymbol{Y} \right)^\dagger \right\rangle \tag{B.159}$$

with arbitrary variables $\boldsymbol{X}$ and $\boldsymbol{Y}$. The memory term reduces to

$$\begin{aligned} \left\langle \left(\hat{\Omega}\boldsymbol{R}(t) \right) \boldsymbol{A}^\dagger \right\rangle \cdot \phi^{-1} &= \left\langle \boldsymbol{R}(t) \left(\Omega \boldsymbol{A} \right)^\dagger \right\rangle \cdot \phi^{-1} \\ &= \begin{pmatrix} 0 & 0 \\ \left\langle \boldsymbol{R}_q(t) \left(\Omega \boldsymbol{\delta\rho}_q \right)^\dagger \right\rangle & \left\langle \boldsymbol{R}_q(t) \left(\Omega \boldsymbol{j}_q^L \right)^\dagger \right\rangle \end{pmatrix} \cdot \phi^{-1}, \end{aligned} \tag{B.160}$$

where $\boldsymbol{R}_q(t) = e^{t\mathcal{Q}\hat{\Omega}} \mathcal{Q}\hat{\Omega}\boldsymbol{j}_q^L$. The $\delta\rho_q^{(\alpha)}$ and $j_q^{L(\alpha)}$ operated by Ω are represented by

$$\Omega\delta\rho_q^{(\alpha)} = -iqj_q^{L(\alpha)} + \frac{dN\gamma_\alpha}{m_\alpha}\delta\rho_q^{(\alpha)}, \tag{B.161}$$

$$\Omega j_q^{L(\alpha)} = -iq\frac{1}{\sqrt{N_\alpha}} \sum_i^{(\alpha)} \hat{\boldsymbol{q}} \cdot \frac{\boldsymbol{p}_i}{m_i}\frac{\boldsymbol{p}_i}{m_i} \cdot \hat{\boldsymbol{q}} e^{i\boldsymbol{q}\cdot\boldsymbol{x}_i} + \frac{(dN+1)\gamma_\alpha}{m_\alpha} j_q^{L(\alpha)} - \frac{1}{\sqrt{N_\alpha}} \sum_i^{(\alpha)} \frac{\boldsymbol{F}_i}{m_i} \cdot \hat{\boldsymbol{q}} e^{i\boldsymbol{q}\cdot\boldsymbol{x}_i}.$$

(B.162)

We can thus obtain

$$\left\langle \boldsymbol{R}_q(t) \left(\Omega \boldsymbol{\delta\rho}_q\right)^\dagger \right\rangle = 0, \tag{B.163}$$

$$\begin{aligned}
&\left\langle R_q^{(\alpha)}(t) \left(\Omega j_q^{L(\beta)}\right)^\dagger \right\rangle \\
&\quad = \left\langle R_q^{(\alpha)}(t) \left[-\frac{iq}{\sqrt{N_\beta}} \sum_i^{(\beta)} \hat{\boldsymbol{q}} \cdot \frac{\boldsymbol{p}_i}{m_i} \frac{\boldsymbol{p}_i}{m_i} \cdot \hat{\boldsymbol{q}} e^{i\boldsymbol{q}\cdot\boldsymbol{x}_i} - \frac{1}{\sqrt{N_\beta}} \sum_i^{(\beta)} \frac{\boldsymbol{F}_i}{m_i} \cdot \hat{\boldsymbol{q}} e^{i\boldsymbol{q}\cdot\boldsymbol{x}_i} \right]^\dagger \right\rangle \\
&\quad = -\left\langle R_q^{(\alpha)}(t) \left[\frac{1}{\sqrt{N_\beta}} \sum_i^{(\beta)} \left\{ iq\hat{\boldsymbol{q}} \cdot \frac{\boldsymbol{p}_i}{m_i} \frac{\boldsymbol{p}_i}{m_i} \cdot \hat{\boldsymbol{q}} + \frac{\boldsymbol{F}_i}{m_i} \cdot \hat{\boldsymbol{q}} \right\} e^{i\boldsymbol{q}\cdot\boldsymbol{x}_i} \right]^\dagger \right\rangle \\
&\quad = -\left\langle R_q^{(\alpha)}(t) R_q^{(\beta)\dagger} \right\rangle,
\end{aligned} \tag{B.164}$$

and then the memory term reduces to

$$\left\langle \left(\hat{\Omega}\boldsymbol{R}(t)\right) \boldsymbol{A}^\dagger \right\rangle \cdot \phi^{-1} \cdot \boldsymbol{A} = \begin{pmatrix} 0 \\ -\left\langle \boldsymbol{R}_q(t) \boldsymbol{R}_q^\dagger \right\rangle \cdot \beta m \mathbf{1}_2' \cdot \boldsymbol{j}_q^L \end{pmatrix}. \tag{B.165}$$

It leads us to the following differential equations

$$\partial_t \delta\rho_q^{(\alpha)}(t) = iq j_q^{L(\alpha)}(t), \tag{B.166}$$

$$\begin{aligned}
\partial_t j_q^{L(\alpha)}(t) &= \frac{iq}{m_\alpha \beta} \sum_\eta \left[\mathsf{S}^{-1}(q)\right]^{(\alpha\eta)} \delta\rho_q^{(\eta)} - \frac{1}{t_B^{(\alpha)}} j_q^{L(\alpha)}(t) \\
&\quad - \sum_\eta m_\eta \beta \int_0^t \mathrm{d}s \left\langle R_q^{(\alpha)}(t-s) R_q^{(\eta)*} \right\rangle j_q^{L(\eta)}(s) + R_q^{(\alpha)}(t) \\
\Leftrightarrow \quad \partial_t^2 \delta\rho_q^{(\alpha)}(t) &= -\frac{q^2}{m_\alpha \beta} \sum_\eta \left[\mathsf{S}^{-1}(q)\right]^{(\alpha\eta)} \delta\rho_q^{(\eta)} - \frac{1}{t_B^{(\alpha)}} \partial_t \delta\rho_q^{(\alpha)}(t) \\
&\quad - \sum_\eta m_\eta \beta \int_0^t \mathrm{d}s \left\langle R_q^{(\alpha)}(t-s) R_q^{(\eta)*} \right\rangle \partial_t \delta\rho_q^{(\eta)}(s) + iq R_q^{(\alpha)}(t)
\end{aligned} \tag{B.167}$$

$$\begin{aligned}
\Rightarrow \quad \partial_t^2 F^{(\alpha\beta)}(q,t) &= -\frac{q^2}{m_\alpha \beta} \sum_\eta \left[\mathsf{S}^{-1}(q)\right]^{(\alpha\eta)} F^{(\eta\beta)}(q,t) - \frac{1}{t_B^{(\alpha)}} \partial_t F^{(\alpha\beta)}(q,t) \\
&\quad - \sum_\eta m_\eta \beta \int_0^t \mathrm{d}s \left\langle R_q^{(\alpha)}(t-s) R_q^{(\eta)*} \right\rangle \partial_t F^{(\eta\beta)}(q,s),
\end{aligned} \tag{B.168}$$

where t_B denotes the Brownian relaxation time $t_B := m/\gamma$ and $\mathsf{F}(q,t)$ the matrix of the intermediate scattering function defined by

$$\mathsf{F}(q,t) := \langle \boldsymbol{\delta\rho}_q(t)\boldsymbol{\delta\rho}_{-q}\rangle = \begin{pmatrix} F^{(AA)}(q,t) & F^{(AB)}(q,t) \\ F^{(BA)}(q,t) & F^{(BB)}(q,t) \end{pmatrix}. \tag{B.169}$$

B.8.3 Approximation of Memory Term

Let us introduce bilinear projection operator $\mathcal{P}_2$ as

$$\mathcal{P}_2 X := \sum_{k_1,k_2,k_3,k_4} \sum_{\alpha,\beta,\gamma,\epsilon} \delta\rho_{k_1}^{(\alpha)}\delta\rho_{k_2}^{(\beta)} \left[\Phi^{-1}_{1,2,3,4}\right]^{(\beta\alpha\gamma\epsilon)} \left\langle \delta\rho_{-k_4}^{(\epsilon)}\delta\rho_{-k_3}^{(\epsilon)} X \right\rangle, \tag{B.170}$$

where $\Phi^{(\alpha\beta\gamma\epsilon)}_{1,2,3,4}$ denotes

$$\Phi^{(\alpha\beta\gamma\epsilon)}_{1,2,3,4} := \left\langle \delta\rho_{-k_2}^{(\alpha)}\delta\rho_{-k_1}^{(\beta)}\delta\rho_{k_3}^{(\gamma)}\delta\rho_{k_4}^{(\epsilon)} \right\rangle \tag{B.171}$$

and the inverse tensor satisfies

$$\sum_{\eta,\xi}\sum_{k_3,k_4} \left[\Phi^{-1}_{1,2,3,4}\right]^{(\alpha\beta\xi\eta)} \Phi^{(\eta\xi\gamma\epsilon)}_{3,4,5,6} = \delta_{k_1,k_5}\delta_{k_2,k_6}\delta_{\beta,\gamma}\delta_{\alpha\epsilon}. \tag{B.172}$$

The initial random term operated by $\mathcal{P}_2$ is

$$\begin{aligned} \mathcal{P}_2 R_q^{(\eta)} &= \sum_{k_1,k_2,k_3,k_4} \sum_{\alpha,\beta,\gamma,\epsilon} \delta\rho_{k_1}^{(\alpha)}\delta\rho_{k_2}^{(\beta)} \left[\Phi^{-1}_{1,2,3,4}\right]^{(\beta\alpha\gamma\epsilon)} \left\langle \delta\rho_{-k_4}^{(\epsilon)}\delta\rho_{-k_3}^{(\gamma)} R_q^{(\eta)} \right\rangle \\ &=: \sum_{k_1,k_2}\sum_{\alpha,\beta} \delta\rho_{k_1}^{(\alpha)}\delta\rho_{k_2}^{(\beta)} V_{1,2}^{(\beta\alpha\eta)}, \end{aligned} \tag{B.173}$$

where the vertex $V_{1,2}^{(\beta\alpha\eta)}$ is defined by

$$V_{1,2}^{(\beta\alpha\eta)} := \sum_{k_3,k_4}\sum_{\gamma,\epsilon} \left[\Phi^{-1}_{1,2,3,4}\right]^{(\beta\alpha\gamma\epsilon)} \left\langle \delta\rho_{-k_4}^{(\epsilon)}\delta\rho_{-k_3}^{(\gamma)} R_q^{(\eta)} \right\rangle, \tag{B.174}$$

therefore,

$$\sum_{k_1,k_2}\sum_{\alpha,\beta} \Phi^{(\epsilon\gamma\alpha\beta)}_{3,4,1,2} V_{1,2}^{(\beta\alpha\eta)} = \left\langle \delta\rho_{-k_4}^{(\epsilon)}\delta\rho_{-k_3}^{(\gamma)} R_q^{(\eta)} \right\rangle. \tag{B.175}$$

RHS of the above equation reduces to

$$\left\langle \delta\rho_{-k_4}^{(\epsilon)}\delta\rho_{-k_3}^{(\gamma)} R_q^{(\eta)} \right\rangle = \left\langle \delta\rho_{-k_4}^{(\epsilon)}\delta\rho_{-k_3}^{(\gamma)} \hat{\Omega} j_q^{L(\eta)} \right\rangle - \frac{iq}{m_\eta \beta} \sum_{\xi} \left[\mathsf{S}^{-1}(q)\right]^{(\eta\xi)} \left\langle \delta\rho_{-k_4}^{(\epsilon)}\delta\rho_{-k_3}^{(\gamma)}\delta\rho_q^{(\xi)} \right\rangle$$

$$= i\frac{\delta_{k_4,q-k_3}\hat{\boldsymbol{q}}}{m_\eta\beta\sqrt{N_\eta}}\cdot\left[\boldsymbol{k}_4\delta_{\epsilon\eta}S^{(\gamma\eta)}(k_3)+\boldsymbol{k}_3\delta_{\gamma\eta}S^{(\epsilon\eta)}(k_4)-\boldsymbol{q}S^{(\epsilon\eta)}(k_4)S^{(\gamma\eta)}(k_3)\right]$$

$$= i\frac{\delta_{k_4,q-k_3}\hat{\boldsymbol{q}}}{m_\eta\beta\sqrt{N_\eta}}\cdot\left[\boldsymbol{k}_4\left(\delta_{\epsilon\eta}-S^{(\epsilon\eta)}(k_4)\right)S^{(\gamma\eta)}(k_3)+\boldsymbol{k}_3\left(\delta_{\gamma\eta}-S^{(\gamma\eta)}(k_3)\right)S^{(\epsilon\eta)}(k_4)\right], \tag{B.176}$$

where we employ the convolution approximation without a three-body correlation term [30]

$$\left\langle\delta\rho^{(\epsilon)}_{-k_4}\delta\rho^{(\gamma)}_{-k_3}\delta\rho^{(\xi)}_{q}\right\rangle\simeq\delta_{k_4,q-k_3}\sum_\zeta\frac{1}{\sqrt{N_\zeta}}S^{(\epsilon\zeta)}(k_4)S^{(\gamma\zeta)}(k_3)S^{(\xi\zeta)}(q). \tag{B.177}$$

Using the decoupling approximation

$$\begin{aligned}\delta_{k_4,q-k_3}&\left\langle\delta\rho^{(\epsilon)}_{-k_4}\delta\rho^{(\gamma)}_{-k_3}\delta\rho^{(\alpha)}_{k_1}\delta\rho^{\beta)}_{k_2}\right\rangle\\&\simeq\ \delta_{k_4,q-k_3}\left[\left\langle\delta\rho^{(\epsilon)}_{-k_4}\delta\rho^{(\alpha)}_{k_1}\right\rangle\left\langle\delta\rho^{(\gamma)}_{-k_3}\delta\rho^{(\beta)}_{k_2}\right\rangle+\left\langle\delta\rho^{(\epsilon)}_{-k_4}\delta\rho^{(\beta)}_{k_2}\right\rangle\left\langle\delta\rho^{(\gamma)}_{-k_3}\delta\rho^{(\alpha)}_{k_1}\right\rangle\right],\end{aligned} \tag{B.178}$$

we can obtain[12]

$$\begin{aligned}V^{(\alpha\beta\eta)}_{3,4}&=-\frac{i\delta_{k_4,q-k_3}\hat{\boldsymbol{q}}}{2m_\eta\beta\sqrt{N_\eta}}\cdot\left\{(\boldsymbol{q}-\boldsymbol{k}_3)\delta_{\beta\eta}c_2^{(\alpha\eta)}(|\boldsymbol{q}-\boldsymbol{k}_3|)+\boldsymbol{k}_3\delta_{\alpha\eta}c_2^{(\beta\eta)}(k_3)\right\}\\&=:-\frac{i\delta_{k_4,q-k_3}\hat{\boldsymbol{q}}}{2m_\eta\beta\sqrt{N_\eta}}\cdot\boldsymbol{V}_q^{(\alpha\beta\eta)}(\boldsymbol{k}_3),\end{aligned} \tag{B.179}$$

where $\mathsf{c}_2(q)$ denotes the matrix of the direct correlation function defined by

$$\mathsf{c}_2(q):=\mathbf{1}_2-\mathsf{S}^{-1}(q) \tag{B.180}$$

and

$$\boldsymbol{V}_q^{(\alpha\beta\eta)}(\boldsymbol{k}):=\boldsymbol{k}\delta_{\alpha\eta}c_2^{(\beta\eta)}(k)+(\boldsymbol{q}-\boldsymbol{k})\delta_{\beta\eta}c_2^{(\alpha\eta)}(|\boldsymbol{q}-\boldsymbol{k}|). \tag{B.181}$$

The memory term thus reduces to

$$\left\langle R_q^{(\xi)}(t)R_q^{(\zeta)*}\right\rangle\ \simeq\ \left\langle\left\{e^{t\hat{\Omega}}\left(\mathcal{P}_2R_q^{(\xi)}\right)\right\}\left(\mathcal{P}_2R_q^{(\zeta)}\right)^*\right\rangle$$

[12]Note that $V^{(\alpha\beta\eta)}_{1,2}=V^{(\beta\alpha\eta)}_{2,1}$ from the definition.

$$
\begin{aligned}
&= \frac{1}{4m_\xi m_\zeta \beta^2 \sqrt{N_\xi N_\zeta}} \sum_{k_1,k_3} \sum_{\alpha,\beta,\gamma,\epsilon} \left(\hat{\boldsymbol{q}} \cdot \boldsymbol{V}_q^{(\beta\alpha\xi)}(\boldsymbol{k}_1)\right) \left(\hat{\boldsymbol{q}} \cdot \boldsymbol{V}_q^{(\epsilon\gamma\zeta)}(\boldsymbol{k}_3)\right) \\
&\quad \times \left\langle \delta\rho_{k_1}^{(\alpha)}(t)\delta\rho_{q-k_1}^{(\beta)}(t)\delta\rho_{-k_3}^{(\gamma)}\delta\rho_{k_3-q}^{(\epsilon)} \right\rangle \\
&\simeq \frac{1}{4m_\xi m_\zeta \beta^2 \sqrt{N_\xi N_\zeta}} \sum_{k_1,k_3} \sum_{\alpha,\beta,\gamma,\epsilon} \left(\hat{\boldsymbol{q}} \cdot \boldsymbol{V}_q^{(\beta\alpha\xi)}(\boldsymbol{k}_1)\right) \left(\hat{\boldsymbol{q}} \cdot \boldsymbol{V}_q^{(\epsilon\gamma\zeta)}(\boldsymbol{k}_3)\right) \\
&\quad \times \left\{ \delta_{k_3,k_1} F^{(\alpha\gamma)}(k_1,t) F^{(\beta\epsilon)}(|\boldsymbol{q}-\boldsymbol{k}_1|,t) + \delta_{k_3,q-k_1} F^{(\alpha\epsilon)}(k_1,t) F^{(\beta\gamma)}(|\boldsymbol{q}-\boldsymbol{k}_1|,t) \right\} \\
&= \frac{1}{2m_\xi m_\zeta \beta^2 \sqrt{N_\xi N_\zeta}} \sum_{k} \sum_{\alpha,\alpha',\beta,\beta'} \hat{V}_q^{(\alpha\beta\xi)}(\boldsymbol{q}-\boldsymbol{k}) \hat{V}_q^{(\beta'\alpha'\zeta)}(\boldsymbol{k}) F^{(\alpha\alpha')}(|\boldsymbol{q}-\boldsymbol{k}|,t) F^{(\beta\beta')}(k,t),
\end{aligned}
\tag{B.182}
$$

where

$$
\hat{V}_q^{(\alpha\beta\xi)}(\boldsymbol{k}) := \hat{\boldsymbol{q}} \cdot \boldsymbol{k} \delta_{\beta\xi} c_2^{(\alpha\xi)}(k) + \hat{\boldsymbol{q}} \cdot (\boldsymbol{q}-\boldsymbol{k}) \delta_{\alpha\xi} c_2^{(\beta\xi)}(|\boldsymbol{q}-\boldsymbol{k}|) = \hat{\boldsymbol{q}} \cdot \boldsymbol{V}_q^{(\beta\alpha\xi)}(\boldsymbol{k}). \tag{B.183}
$$

We finally obtain an approximative MCT equation for the intermediate scattering function as

$$
\begin{aligned}
&\partial_t^2 F^{(\alpha\beta)}(q,t) + \frac{q^2}{m_\alpha \beta} \sum_\eta \left[\mathsf{S}^{-1}(q)\right]^{(\alpha\eta)} F^{(\eta\beta)}(q,t) + \frac{1}{t_B^{(\alpha)}} \partial_t F^{(\alpha\beta)}(q,t) \\
&\qquad + \sum_\eta \frac{1}{2m_\alpha \beta \sqrt{N_\alpha N_\eta}} \int_0^t \mathrm{d}s M_q^{(\alpha\eta)}(t-s) \partial_s F^{(\eta\beta)}(q,s) \;=\; 0,
\end{aligned}
\tag{B.184}
$$

where

$$
M_q^{(\alpha\eta)}(t) := \sum_{\gamma,\gamma',\epsilon,\epsilon'} \sum_k \hat{V}_q^{(\gamma\epsilon\alpha)}(\boldsymbol{q}-\boldsymbol{k}) \hat{V}_q^{(\gamma'\epsilon'\eta)}(\boldsymbol{k}) F^{(\gamma\gamma')}(|\boldsymbol{q}-\boldsymbol{k}|,t) F^{(\epsilon\epsilon')}(k,t). \tag{B.185}
$$

When we focus on the time scale $t_D^{(A)} := {\sigma_{AA}}^2/4D_0^A = \gamma {\sigma_{AA}}^2/4k_BT$ of the diffusive motion (i.e. the time is scaled by $t_D^{(A)}$), the above differential-integral equation reduces to

$$
\begin{aligned}
&\frac{t_B^{(A)}}{t_D^{(A)}} \partial_{\hat{t}}^2 F^{(\alpha\beta)}(\hat{q},\hat{t}) + \frac{\hat{q}^2}{4} \sum_\eta \left[\mathsf{S}^{-1}(\hat{q})\right]^{(\alpha\eta)} F^{(\eta\beta)}(\hat{q},\hat{t}) + \partial_{\hat{t}} F^{(\alpha\beta)}(\hat{q},\hat{t}) \\
&\qquad + \sum_\eta \frac{1}{8\sqrt{N_\alpha N_\eta}} \int_0^{\hat{t}} \mathrm{d}\hat{s} \hat{M}_{\hat{q}}^{(\alpha\eta)}(\hat{t}-\hat{s}) \partial_{\hat{s}} F^{(\eta\beta)}(\hat{q},\hat{s}) \;=\; 0,
\end{aligned}
\tag{B.186}
$$

where

$$\hat{M}_q^{(\alpha\eta)}(t) := \sum_{\gamma,\gamma',\epsilon,\epsilon'} \sum_k \hat{\hat{V}}_q^{(\gamma\epsilon\alpha)}(\boldsymbol{q}-\boldsymbol{k})\hat{\hat{V}}_q^{(\gamma'\epsilon'\eta)}(\boldsymbol{k})F^{(\gamma\gamma')}(|\boldsymbol{q}-\boldsymbol{k}|,t)F^{(\epsilon\epsilon')}(k,t). \tag{B.187}$$

In case that $t_B^{(A)} \ll t_D^{(A)}$, we can obtain an overdamped approximative MCT equation as

$$\begin{aligned}\partial_{\hat{t}}F^{(\alpha\beta)}(\hat{q},\hat{t}) + \frac{\hat{q}^2}{4}\sum_\eta \left[\mathsf{S}^{-1}(\hat{q})\right]^{(\alpha\eta)} F^{(\eta\beta)}(\hat{q},\hat{t}) \\ + \sum_\eta \frac{1}{8\sqrt{N_\alpha N_\eta}}\int_0^{\hat{t}} \mathrm{d}\hat{s}\hat{M}_{\hat{q}}^{(\alpha\eta)}(\hat{t}-\hat{s})\partial_{\hat{s}}F^{(\eta\beta)}(\hat{q},\hat{s}) = 0.\end{aligned} \tag{B.188}$$

B.9 Percus-Yevick approximation

In homogeneous systems, the Ornstein-Zernike equation [92] is represented by

$$h(r) = c(r) + \rho\int c(|\boldsymbol{r}-\boldsymbol{r}'|)h(r')\mathrm{d}\boldsymbol{r}', \tag{B.189}$$

where ρ denotes the number density, $h(r) = g(r) - 1$ the total correlation function with the radial distribution function $g(r)$, and $c(r)$ the direct correlation function. The Ornstein-Zernike equation should be regarded as the definition of the direct correlation function. We can obtain

$$h(r) = c(r) + \rho\int c(|\boldsymbol{r}-\boldsymbol{r}'|)c(r')\mathrm{d}\boldsymbol{r}' + \rho^2\iint c(|\boldsymbol{r}-\boldsymbol{r}'|)c(|\boldsymbol{r}'-\boldsymbol{r}''|)c(r'')\mathrm{d}\boldsymbol{r}'\mathrm{d}\boldsymbol{r}'' + \cdots, \tag{B.190}$$

and this equation implies that the "total" correlation is described by sum over the "direct" correlation and propagated "indirect" correlations. The Ornstein-Zernike equation is an equation linking $h(r)$ and $c(r)$, and we need one more equation to obtain them. The Percus-Yevick approximation is a closure relation for solving the Ornstein-Zernike equation [93]. It is represented by

$$c(r) \simeq g(r)\left[1 - \exp\left(\frac{u(r)}{k_BT}\right)\right], \tag{B.191}$$

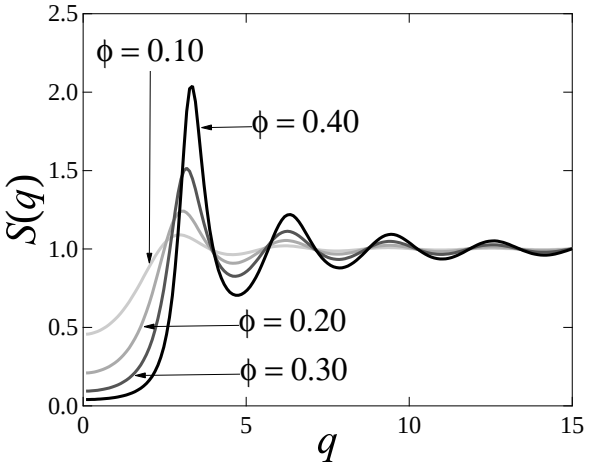

Figure B.1: Plot of the static structure factor from Percus-Yevick approximation for $\phi = 0.1, 0.2, 0.3,$ and 0.4 (from light gray to black). The wave number q is normalized by the inverse radius of a hard sphere.

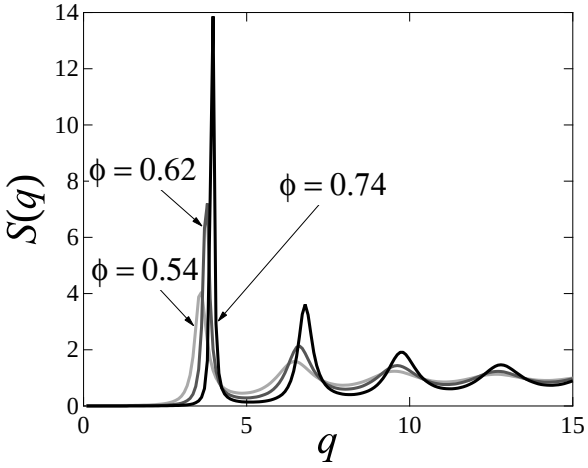

Figure B.2: Plot of the static structure factor from Percus-Yevick approximation for ϕ =0.54, 0.62, and 0.70 (from light gray to black). The wave number q is normalized by the inverse radius of a hard sphere.

where $u(r)$ denotes the pair potential. In order to consider the meaning of the Percus-Yevick approximation, let $\psi(r)$ denote the potential of mean force [94]:

$$g(r) = \exp\left[-\psi(r)/k_BT\right].$$

Note that $\psi(r)$ is equivalent to $u(r)$ for much dilute systems.

The Percus-Yevick approximation reduces to

$$c(r) \simeq \exp\left[-\frac{\psi(r)}{k_BT}\right] - \exp\left[-\frac{\psi(r)-u(r)}{k_BT}\right] =: g(r) - g_{\text{indirect}}(r). \tag{B.192}$$

The Percus-Yevick approximation thus means that the direct correlation is difference between the radial distribution function including total interaction and that without the direct interaction described by $u(r)$. An analytic solution was suggested by Wertheim [95];

$$c(r) = \begin{cases} -\left[\alpha + \beta\left(\frac{r}{\sigma}\right) + \gamma\left(\frac{r}{\sigma}\right)^3\right] & (r < \sigma) \\ 0 & (r > \sigma) \end{cases}, \tag{B.193}$$

where σ denotes the radius of a hard sphere,

$$\alpha = (1+2\phi)^2/(1-\phi)^4, \tag{B.194}$$

$$\beta = -6\phi(1+\phi/2)^2/(1-\phi)^4, \tag{B.195}$$

$$\gamma = \phi\alpha/2, \tag{B.196}$$

with the volume fraction $\phi = \pi\sigma^3\rho/6$. We straightforwardly derive the Fourier transformed direct correlation as [96]

$$c(x) = -4\pi\sigma^3 \int_0^1 \mathrm{d}s\ s^2 \frac{\sin sx}{sx}(\alpha + \beta s + \gamma s^3) \tag{B.197}$$

with $x := k\sigma$ and the wave number k. Note that the detail of equation is mentioned in Ref. [97] but there are some typos. One can calculate the static structure factor from the direct correlation function

$$S(k) = \frac{1}{1-\rho c(k)}. \tag{B.198}$$

Figures B.1 and B.2 show $S(q)$ analytically calculated from the Percus-Yevick approximations. We can calculate it even high volume fractions. Any double peaks at the second peak do not appear while they appear in real systems.

References

[1] P. W. Anderson, Science **267**, 1615 (1995).

[2] M. D. Ediger, C. A. Angell, and S. R. Nagel, J. Phys. Chem. **100**, 13200 (1996).

[3] C. Angell, K. Ngai, G. McKenna, P. McMillan, and S. Martin, Journal of Applied Physics **88**, 3113 (2000).

[4] P. G. Debenedetti and F. H. Stillinger, Nature **410**, 259 (2001).

[5] K. Binder and W. Kob, *Glassy Materials and Disordered Solids*, World Scientific, 2005.

[6] A. Inoue, Acta. Matter. **48**, 279 (2000).

[7] C. A. Angell, J. Phys. Chem. Solids **49**, 863 (1988).

[8] M. Tokuyama, Physica A **364**, 23 (2006).

[9] R. Kubo, M. Toda, and N. Hashitume, *Statistical Physics II: Nonequilibrium Statistical Mechanics*, Springer, 1991.

[10] S.-K. Ma, *Modern Theory of Critical Phenomena*, Westview press, 1976.

[11] E. Rabani, D. J. Gezelter, and B. J. Berne, J. Chem. Phys. **107**, 6867 (1997).

[12] B. Doliwa and A. Heuer, Phys. Rev. Lett. **80**, 4915 (1998).

[13] A. Kasper, E. Bartsch, and H. Sillescu, Langmuir **14**, 5004 (1998).

[14] E. R. Weeks and D. A. Weitz, Phys. Rev. Lett. **89**, 095704 (2002).

[15] E. R. Weeks and D. A. Weitz, Chem. Phys. **284**, 361 (2002).

[16] P. M. Reis, R. A. Ingale, and M. D. Shattuck, Phys. Rev. Lett. **98**, 188301 (2007).

[17] K. Schmidt-Rohr and H. W. Spiess, Phys. Rev. Lett. **66**, 3020 (1991).

[18] M. T. Cicerone and M. D. Ediger, J. Chem. Phys. **103**, 5684 (1995).

[19] B. Schiener, R. V. Chamberlin, G. Diezemann, and R. Böhmer, J. Chem. Phys. Rev. **107**, 7746 (1997).

[20] W. K. Kegel and A. v. Blaaderen, Science **287**, 290 (2000).

[21] M. D. Ediger, Annu. Rev. Phys. Chem. **51**, 88 (2000).

[22] E. R. Weeks, J. C. Crocker, A. C. Levitt, A. Schofield, and D. A. Weitz, Science **287**, 627 (2000).

[23] G. Adam and J. H. Gibbs, J. Chem. Phys. **43**, 139 (1965).

[24] K. Kawasaki, Ann. Phys. **61**, 1 (1970).

[25] H. E. Stanley, *Introduction to Phase transitions and Critical Phenomena*, Oxford University Press, 1971.

[26] U. Bengtzelius, W. Gotze, and A. Sjolander, J. Phys. C: Solid State Phys. **17**, 5915 (1984).

[27] E. Leutheusser, Phys. Rev. A **29**, 2765 (1984).

[28] W. Götze, *Complex Dynamics of Glass Forming Liquids - A Mode-Coupling Theory*, Oxford Science Publications, 2009.

[29] M. Fuchs, W. Gotze, I. Hofacker, and A. Latz, J. Phys: Condens. Matter **3**, 5047 (1991).

[30] M. Nauroth and W. Kob, Phys. Rev. E **55**, 657 (1997).

[31] M. H. Nauroth, *Die Dynamik von normalen und unterkühlten Flüssigkeiten Ein Vergleich von analytischen Theorien mit Computersimulationen*, PhD thesis, Institut für Theoretische Physik der Technischen Universität München, 1999.

[32] F. Sciortino and W. Kob, Phys. Rev. Lett. **86**, 648 (2001).

[33] G. Foffi, W. Götze, F. Sciortino, P. Tartaglia, and T. Voigtmann, Phys. Rev. E **69**, 011505 (2004).

[34] K. Miyazaki, B. Bagchi, and A. Yethira, J. Chem. Phys. **121**, 8120 (2004).

[35] T. Voigtmann, A. M. Puetas, and M. Fuchs, Phys. Rev. E **70**, 061506 (2004).

[36] E. Flenner and G. Szamel, Phys. Rev. E **72**, 031508 (2005).

[37] M. Tokuyama, Physica A **387**, 1926 (2008).

[38] H. Mori, Prog. Theor. Phys. **33**, 423 (1965).

[39] R. Kubo, J. Math. Phys. **4**, 174 (1963).

[40] D. Ahn, Prog. Quant. Electr. **21**, 249 (1997).

[41] T. Renger and R. A. Marcus, J. Chem. Phys **116**, 9997 (2002).

[42] U. Kleinekathöfer, G. Li, and M. Schreiber, J. Lumin. **119–120**, 91 (2006).

[43] E. R. Weeks, J. C. Crocker, and D. A. Weitz, J. Phys.: Condens. Matter **19**, 205131 (2007).

[44] W. Kob and H. C. Andersen, Phys. Rev. Lett. **73**, 1376 (1994).

[45] M. Tokuyama, Physica A **389**, 951 (2010).

[46] P. N. Pusey and W. van Magen, Phys. Rev. Lett. **59**, 2083 (1987).

[47] V. Prasad, D. Semwogerere, and E. R. Weeks, J. Phys.: Cond. Matt. **19**, 113102 (2007).

[48] J. C. Crocker and D. J. Grier, J. Colloid Interf. Sci. **179**, 298 (1996).

[49] P. N. Pusey and W. van Megen, Nature **320**, 340 (1986).

[50] C. R. Nugent, K. V. Edmond, H. N. Patel, and E. R. Weeks, Phys. Rev. Lett. **99**, 025702 (2007).

[51] P. H. Poole, C. Donati, and S. C. Glotzer, Physica A **261**, 51 (1998).

[52] B. Doliwa and A. Heuer, Phys. Rev. E **61**, 6898 (2000).

[53] C. Toninelli, M. Wyart, L. Berthier, G. Biroli, and J.-P. Bouchaud, Phys. Rev. E **71**, 041505 (2005).

[54] L. Berthier et al., Science **310**, 1797 (2005).

[55] J. M. Lynch, G. C. Cianci, and E. R. Weeks, Phys. Rev. E **78**, 031410 (2008).

[56] R. E. Courtland and E. R. Weeks, J. Phys.: Condens. Matter **15**, S359 (2003).

[57] G. C. Cianci, R. E. Courtland, and E. R. Weeks, Solid State Comm. **139**, 599 (2006).

[58] W. Kob, C. Donati, S. J. Plimpton, P. H. Poole, and S. C. Glotzer, Phys. Rev. Lett. **79**, 2827 (1997).

[59] A. Rahman, Phys. Rev. **136**, A405 (1964).

[60] C. Donati et al., Phys. Rev. Lett. **80**, 2338 (1998).

[61] A. Widmer-Cooper, P. Harrowell, and H. Fynewever, Phys. Rev. Lett. **93**, 135701 (2004).

[62] J. C. Conrad, F. W. Starr, and D. A. Weitz, J. Phys. Chem. B **109**, 21235 (2005).

[63] R. L. Hoffman, J. Rheol. **36**, 947 (1992).

[64] P. D'Haene and J. Mewis, Rheologica Acta **33**, 165 (1994).

[65] S. R. Williams and W. van Megen, Phys. Rev. E **64**, 041502 (2001).

[66] A. H. Marcus, J. Schofield, and S. A. Rice, Phys. Rev. E **60**, 5725 (1999).

[67] A. D. Dinsmore, E. R. Weeks, V. Prasad, A. C. Levitt, and D. A. Weitz, App. Optics **40**, 4152 (2001).

[68] T. Kawasaki, T. Araki, and H. Tanaka, Phys. Rev. Lett. **99**, 215701 (2007).

[69] T. Narumi and M. Tokuyama, Philos. Mag. **88**, 4169 (2008).

[70] T. A. Weber and F. H. Stillinger, Phys. Rev. B **31**, 1954 (1985).

[71] J. L. Lebowitz, J. K. Percus, and L. Verlet, Phys. Rev. **153**, 250 (1967).

[72] B. Wunderlich, J. Phys. Chem. **64**, 1052 (1960).

[73] S. S. Chang and A. B. Bestul, J. Chem. Phys. **56**, 503 (1972).

[74] A. V. Granato, J. Non-Cryst. Solids. **307–310**, 376 (2002).

[75] M. Tokuyama, T. Narumi, and E. Kohira, Physica A **385**, 439 (2007).

[76] T. Narumi, S. V. Franklin, M. Tokuyama, and E. R. Weeks, to be submitted .

[77] M. E. Cates, Arrest and flow of colloidal glasses, Invited plenary talk, Th2002, 2003.

[78] R. Zwanzig, J. Stat. Phys. **9**, 215 (1973).

[79] M. Tokuyama and H. Mori, Prog. Theor. Phys. **55**, 411 (1976).

[80] M. Tokuyama, Physica A **388**, 3083 (2009).

[81] M. Tokuyama, Phys. Rev. E **80**, 031503 (2009).

[82] T. Narumi and M. Tokuyama, Rep. Inst. Fluid Science **19**, 73 (2007).

[83] D. R. Reichman and P. Charbonneau, J. Stat. Mech. **5**, P05013 (2005).

[84] E. Kohira, Y. Terada, and M. Tokuyama, Rep. Inst. Fluid Science **19**, 91 (2007).

[85] M. Tokuyama and Y. Terada, J. Phys. Chem. B **109**, 21357 (2005).

[86] P. Gallo, R. Pellarin, and M. Rovere, Phys. Rev. E **67**, 041202 (2003).

[87] M. Tokuyama, AIP Conf. Proc. **982**, 3 (2008).

[88] T. Narumi and M. Tokuyama, to be submitted (2010).

[89] G. Biroli and J. P. Bouchaud, Europhys. Lett. **67**, 21 (2004).

[90] G. Nägele and J. K. G. Dhont, J. Chem. Phys. **108**, 9566 (1998).

[91] M. Tokuyama, Physica A **109**, 128 (1981).

[92] L. S. Ornstein and F. Zernike, Proc. Acad. Sci. Amsterdam **17**, 793 (1914).

[93] J. K. Percus and G. J. Yevick, Phys. Rev. **110**, 1 (1958).

[94] J. P. Hansen and I. R. McDonald, *Theory of Simple Liquids*, Academic Press, 2nd edition, 1986.

[95] M. S. Wertheim, J. Math. Phys **5**, 643 (1964).

[96] N. W. Ashcroft and J. Lekner, Phys. Rev. **145**, 83 (1966).

[97] J. P. Boon and S. Yip, *Molecular Hydrodynamics*, McGraw-Hill International Book Co., 1980.

List of Figures

Acknowledgement

This study was strongly inspired by Prof. Michio Tokuyama. Discussions with him was very useful and exciting. He also supported my entire student life in graduate school. I am profoundly grateful for him.

Prof. Taku Ohara, Prof. Hiroo Yugami, and Prof. Akira Takeuchi gave me a lot of meaningful suggestions at the examining meeting for doctor's degree. In addition, Prof. Seiichiro Izawa, Prof. Takashi Tokumasu, and Prof. Shigeru Yonemura also gave me a lot of useful comments at the sectoral seminar. I express cordial gratitude.

When I have been to Emory university (Georgia, U.S.A.), I stayed in the Soft Condensed Matter Group of the Physics Department in Emory University for three months. Prof. Eric R. Weeks took care of me and helped doing experiments. Prof. Scott V. Franklin, who visited to the Soft Condensed Matter Group on sabbatical leave, also helped me and did experiments with me. Doing experiments and writing paper with them are extremely useful experience for me. In addition, I thank the member of the group, especially Ms. Jennifer M. Lynch and Dr. Gianguido C. Cianci.

I would like to thank Dr. Yayoi Terada, Dr. Limei Xu, Dr. YongSeok Cho, Dr. Arunabhiram Chutia, Dr. Takaaki Furubayashi, Mr. Kuniaki Hidaka, Mr. Yuto Kimura, Mr. Hiroyuki Fujii, and all of members in Tokuyama laboratory. Not only the academic activities but also daily life with them were very significant. In addition, the staff persons, Mr. Masayoshi Takahashi (technician), Ms. Saiko Yumura, Ms. Yumiko Sasaki (previous office administrators), and

Ms. Yukako Endo (present office administrator), work (or worked) in Tokuyama laboratory. I was supported by them. I feel greateful for their help.

I was financially supported by the department of engineering in Tohoku University, the 21st Century COE Program ”International COE of Flow Dynamics” of Institute of Fluid Science, the global COE Program ”World Center of Education and Research for Trans-disciplinary Flow Dynamics” of Institute of Fluid Science, and the World Premier International Research Center Advanced Institute for Materials Research.

These simulations mainly performed on the SGI Origin2000 of Institute of Fluid Science. If the super computer was not high-spec, we would have not done this research.

At the tail of this thesis, I would like to thank all people associated with me, especially my father and mother.